PhD Dissertation

통합형 무인 수상선 - 케이블 - 수중선 시스템의 다물체동역학 거동 및 제어

Multi-Body Dynamic Behaviors and Control of the Integrated Unmanned Surface Vehicle-Cable-Underwater Vehicle Systems

Supervisor
Professor. Hyeung-Sik Choi

August 2019

Graduate School of Ocean Science and Technology
Korea Maritime and Ocean University

Department of Convergence Study on the Ocean Science and Technology

MAI THE VU

We certify that we have read this dissertation and that, in our opinion, it is satisfactory in scope and quality as a dissertation for the degree of doctor of philosophy in Mechanical Engineering, submitted by **MAI THE VU**.

DISSERTATION COMMITTEE

Chairperson: Professor Sam-Sang You
Department of Refrigeration and Air-Conditioning Engineering, Korea Maritime and Ocean University

_____

Supervisor: Professor Hyeung-Sik Choi
Department of Mechanical Engineering, Korea Maritime and Ocean University

_____

Reviewer: Professor Joon-Young Kim
Department of Marine Equipment Engineering, Korea Maritime and Ocean University

_____

Reviewer: Professor Sung-Wook Lee
Department of Naval Architecture and Marine Engineering, Korea Maritime and Ocean University

_____

Reviewer: Professor Yong-Seong Cho
Department of Electronics Engineering, Dong-A University

_____

August, 2019

Graduate School of Ocean Science and Technology

Korea Maritime and Ocean University

본 논문을 MAI THE VU의 공학박사 학위논문으로 인준함.

위원장: 공학박사 유삼상 (인)

위 원: 공학박사 최형식 (인)

위 원: 공학박사 김준영 (인)

위 원: 공학박사 이성욱 (인)

위 원: 공학박사 조용성 (인)

2019 년 06 월 28 일

한국해양대학교 대학원

Acknowledgement

This dissertation is the product of the culmination of years of research that required the collective abilities only found in a group of skilled researchers. Many people guided me through the higher level decision-making and advising process as well as implementation efforts. Without these people, I would not have been able to finish a dissertation, even approaching this quality. It is my great pleasure to thank the many people who enabled me to perform this work.

First and foremost, I am extremely grateful to my advisor, Professor Hyeung-Sik Choi, for his excellent guidance, support, and patience throughout the course of this research. Under his tutelage, I have been guided towards interesting controls tasks. Furthermore, he always gives me the best of mental and material conditions for the making of this research becomes possible. His enthusiasm, dedication, and the dazzling sense of humor have been an invaluable source of inspiration and motivation for me during the last five years.

I also would like to show my gratitude to members of my dissertation committee, Professor Sam-Sang You, Professor Joon-Young Kim, Professor Sung-Wook Lee, and Professor Yong-Seong Cho, for all the knowledge they shared with me through coursework, evaluation steps, and discussions has immensely added to the richness and applicability of the content of my dissertation.

I would like to say thank you to all members of KIAL Laboratory for all scientific discussions and helped when I studied in Korea Maritime and Ocean University. Thanks and best wishes to the new KIAL generation.

Thanks are due to all members of the Vietnamese Student Community in Korea Maritime and Ocean University for their active supports.

To my parents, my sisters, my brother, my sincere thanks for their love, encouragement, and sympathy for me not only in this dissertation time but also in the whole of my life. Their belief and support only made my small achievements ever possible.

Last but not least, I would like to thank my wife, Pham Thi Sin, with all my love. Thanks for sharing not only joyful moments but also disappointments with me, and keeping our hope alive. Her endless love and support were immeasurable, and her presence in my life changed my entire life much more vibrant and happier

Korea Maritime and Ocean University, Pusan, Korea

July 10th 2019

Mai The Vu

Multi-Body Dynamic Behaviors and Control of the Integrated Unmanned Surface Vehicle-Cable-Underwater Vehicle Systems

Mai The Vu

Department of Convergence Study on the Ocean Science and Technology
Graduate School of Ocean Science and Technology
Korea Maritime and Ocean University

Abstract

Underwater exploration is becoming more and more important, since a vast range of unknown resources in the deep ocean remain undeveloped. This dissertation thus presents a modeling of the coupled dynamics of an Unmanned Surface Vehicle (USV) system with an Underwater Vehicles (UV) connected by an underwater cable (UC). The complexity of this multi-body dynamics system and ocean environments is very difficult to model. First, for modeling this, dynamics analysis was performed on each subsystem and further total coupled system dynamics were studied. The UV which is towed by a UC is modeled with 6-DOF equations of motion that reflects its hydrodynamic characteristic was studied. The 4th-order Runge–Kutta numerical method was used to analyze the motion of the USV with its hydrodynamic coefficients which were obtained through experiments and from the literature. To analyze the effect of the UC, the complicated nonlinear and coupled UC dynamics under currents forces, the governing equations of the UC dynamics are established based on the catenary equation method, then it is solved by applying the shooting method. The new formulation and solution of the UC dynamics yields the three dimensional position and forces of the UC end point under the current forces. Also, the advantage of the proposed method is that the

catenary equations using shooting method can be solved in real time such that the calculated position and forces of UC according to time can be directly utilized to calculate the UV motion. The proposed method offers advantages of simple formulation, convenient use, and fast calculation time with exact result. Some simple numerical simulations were conducted to observe the dynamic behaviors of AUV with cable effects. The simulations results clearly reveal that the UC can greatly influence the motions of the vehicles, especially on the UV motions. Based on both the numerical model and simulation results developed in the dissertation, we may offer some valuable information for the operation of the UV and USV.

Secondly, for the design controller, a PD controller and its application to automatic berthing control of USV are also studied. For this, a nonlinear mathematical model for the maneuvering of USV in the presence of environmental forces was firstly established. Then, in order to control rudder and propeller during automatic berthing process, a PD control algorithm is applied. The algorithm consists of two parts, the forward velocity control and heading angle control. The control algorithm was designed based on the longitudinal and yaw dynamic models of USV. The desired heading angle was obtained by the so-called “Line of Sight” method. To support the validity of the proposed method, the computer simulations of automatic USV berthing are carried out. The results of simulation showed good performance of the developed berthing control system.

Also, a hovering-type AUV equipped with multiple thrusters should maintain the specified position and orientation in order to perform given tasks by applying a dynamic positioning (DP) system. Besides, the control allocation algorithm based on a scaling factor is presented for distributing the forces required by the control law onto the available set of actuators in the most effective and energy efficient way. Thus, it is necessary for the robust control algorithm to conduct successfully given missions in spite of a model uncertainty and a disturbance. In this dissertation, the robust DP control algorithm based on a sliding mode theory is also addressed to guarantee the stability and better performance despite the model uncertainty and disturbance of current and cable effects. Finally, a series of simulations are conducted to verify the availability of the generated trajectories and performance of the designed robust controller.

Thirdly, for the navigation of UV, a method for designing the path tracking controller using a Rapidly-exploring Random Trees (RRT) algorithm is proposed. The RRT algorithm is firstly used for the generation of collision free waypoints. Next, the unnecessary waypoints are removed by a simple path pruning algorithm generating a piecewise linear path. After that, a path smoothing algorithm utilizing

cubic Bezier spiral curves to generate a continuous curvature path that satisfies the minimum radius of curvature constraint of underwater is implemented. The angle between two waypoints is the only information required for the generation of the continuous curvature path. In order to underwater vehicle follow the reference path, the path tracking controller using the global Sliding Mode Control (SMC) approach is designed. To verify the performance of the proposed algorithm, some simulation results are performed. Simulation results showed that the RRT algorithm could be applied to generate an optimal path in a complex ocean environment with multiple obstacles.

KEY WORDS: Underwater Vehicle (UV), Umbilical Cable (UC), Catenary Equation, Sliding Mode Control, Rapidly-exploring Random Trees (RRT), Maneuvering.

Contents

Nomenclature

x, y, z	Axes of body fixed reference frame
X, Y, Z	Axes of earth fixed reference frame
$\dot{x}$	Linear velocity along the North-South axis (earth)
$\dot{y}$	Linear velocity along the East- West axis (earth)
$\dot{z}$	Linear velocity along the vertical axis (earth)
φ	Euler angle in North-South axis. Positive sense is clockwise as seen from back of the vehicle (earth)
θ	Euler angle in pitch plane. Positive sense is clockwise as seen from port of the vehicle (earth)
ψ	Euler angle in yaw plane. Positive sense is clockwise as seen from above (earth)
$\dot{\varphi}$	Roll Euler rate about North-South axis (earth)
$\dot{\theta}$	Pitch Euler rate about East-West axis (earth)
$\dot{\psi}$	Yaw Euler rate about North-South axis (earth)
u	Linear velocity along longitudinal axis (body)
v	Linear velocity along horizontal plane (body)
w	Linear velocity along depth (body)
p	Angular velocity component about body longitudinal axis
q	Angular velocity component about body lateral axis
r	Angular velocity component about body vertical axis
$\dot{u}$	Time rate of change of velocity along the body longitudinal axis
$\dot{v}$	Time rate of change of velocity along the body lateral axis
$\dot{w}$	Time rate of change of velocity along the body vertical axis
$\dot{p}$	Time rate of change of body roll angular velocity about the body longitudinal axis
$\dot{q}$	Time rate of change of body pitch angular velocity about the body lateral axis

$\dot{r}$	Time rate of change of body yaw angular velocity about the body vertical axis
W	Weight of the vehicle
B	Buoyancy of the vehicle
L	Length of the vehicle.
g	Acceleration due to gravity
ρ	Density of fluid
m	mass of the vehicle
I_{xx}	Mass Moment of Inertia about x-axis
I_{yy}	Mass Moment of Inertia about y-axis
I_{zz}	Mass Moment of Inertia about z-axis
I_{xy}	Cross Product of Inertia about xy-axes
I_{yz}	Cross Product of Inertia about yz-axes
I_{xz}	Cross Product of Inertia about xz-axes
CG	Center of gravity
x_G	x Coordinate of CG From Body Fixed Origin
y_G	y Coordinate of CG From Body Fixed Origin
z_G	z Coordinate of CG From Body Fixed Origin
CB	Center of buoyancy
x_B	x Coordinate of CB From Body Fixed Origin
y_B	y Coordinate of CB From Body Fixed Origin
z_B	z Coordinate of CB From Body Fixed Origin
W_c	The weight per length of the cable
D_c	Diameter of cable
L_c	Length of cable

E_c	Modulus of elasticity of cable
$X_{\dot{u}}$	Added mass in surge movement
$Y_{\dot{v}}$	Added mass in sway movement
$Z_{\dot{w}}$	Added mass in heave movement
$K_{\dot{p}}$	Added mass in roll movement
$M_{\dot{q}}$	Added mass in pitch movement
$N_{\dot{r}}$	Added mass in yaw movement
X_u	Linear damping in surge movement
Y_v	Linear damping in sway movement
Z_w	Linear damping in heave movement
K_p	Linear damping coefficient for roll movement
M_q	Linear damping coefficient for pitch movement
N_r	Linear damping coefficient for yaw movement
X_{uu}	Quadratic damping in surge movement
Y_{vv}	Quadratic damping in sway movement
Z_{ww}	Quadratic damping in heave movement
K_{pp}	Quadratic damping coefficient for roll movement
M_{qq}	Quadratic damping coefficient for pitch movement
N_{rr}	Quadratic damping coefficient for yaw movement
D_{prop}	Propeller diameter
F_{prop}	Force due to propeller
K_D	Derivative gain
K_I	Integral gain
K_P	Proportional gain

$K_{T,th}$	Thrust coefficient for the propeller model
L_{los}	Line-of-sight distance
V	Lyapunov candidate function
$C(v)$	System Coriolis-centripetal matrix
$C_A(v)$	Added Coriolis-centripetal matrix
C_{RB}	Rigid-body Coriolis-centripetal matrix
$D(v)$	System damping coefficient matrix
D_l	Linear damping coefficient matrix
$D_q(v)$	Quadratic damping coefficient matrix
$I_{n\times n}$	Identity matrix with dimension n x n
J	Matrix for transforming velocity vector in b-frame, v, to an equivalent velocity vector in NED-frame, $\dot{\eta}$
M	System inertia matrix
M_A	Added inertia matrix
M_{RB}	Rigid-body inertia matrix
S	Skew-symmetry matrix
T	Matrix for transforming actuator forces on the local frame into the equivalent forces on the b-frame
$g(\eta)$	Hydrostatic force vector
p_{los}	Line-of-sight position
s	Sliding variable
η	Position and orientation vector expressed in NED-frame
∇	Volumetric displacement of the vehicle
v	Velocity vector expressed in b-frame
ψ_{los}	Line-of-sight angle
τ	Generalized force vector due to actuators

u	Actuator demand vector

List of Abbreviations

3D	Three Dimensional
AUV	Autonomous Underwater Vehicle
ASV	Autonomous Surface Vehicle
ASC	Autonomous Surface Craft
AHRS	Attitude and Heading Reference System
BVP	Boundary Value Problem
BNode	Begin Node
CB	Center of Buoyancy
CFD	Computation Fluid Dynamic
CG	Center of Gravity
DOF	Degree of Freedom
DP	Dynamic Positioning
DVL	Doppler Velocity Logger
ENode	End Node
FDM	Finite Difference Method
FEM	Finite Element Method
FSA	Finite Segment Approach
GNSS	Global Navigation Satellite System
GPS	Global Positioning System
INS	Inertial Navigation System
IVP	Initial Value Problem
LBL	Long Baseline
LMM	Lumped Mass Method
LMS	Lump-Mass-Spring Formulation
LOS	Line of Sight
LP	Linear Programming
MPC	Model Predictive Control

MIMO	Multiple Inputs and Multiple Outputs
NED	North East Down
NSS	Non-Steady State
ODE	Ordinary Differential Equation
P	Proportional
PD	Proportional Differential
PI	Proportional Integral
PID	Proportional Integral Differential
PMM	Planar Motion Mechanism
QP	Quadratic Programming
RF	Radio Frequency
RLS	Recursive Least Square
ROV	Remotely Operated Vehicle
RRT	Rapidly-exploring Random Trees
SBL	Short Baseline
SLAM	Simultaneous Localization and Mapping
SMC	Sliding Mode Control
UC	Underwater Cable
USBL	Ultimate Short Base Line
USV	Unmanned Surface Vehicle
UUV	Unmanned Surface Vehicle
UV	Underwater Vehicle
VSS	Variable System Structure

List of Tables

List of Figures

Chapter 1: Introduction

This chapter will present the motivation behind this dissertation and make the reader better acquainted with the problem to be solved. Some parts of the complete control system presented here are the result of previous research, and the distinction between this material and that which belongs to the dissertation will be made clear. A short literature review is also given, where some existing knowledge relevant to the contents of the dissertation is presented.

1.1 Background

Nowadays we are capable of investigating the surface of the earth and exploring outer space, but we have minimal knowledge about the deep sea world. Oceans contain numerous natural and mineral resources. The depletion of resources on land has accelerated the development of resources in the ocean. Oceans cover about 70% of surface area of the earth, and enormous wealth and resources are buried in seas. As the world's population and resource consumption increase, more and more attention has been focused on the oceans. At present, techniques for undersea development are still very limited and awkward. The need and desire to explore the vast oceanic environment has contributed with a significant momentum towards the development of advanced oceanographic systems. Some of those oceanographic systems consist of robotic systems such as Autonomous Underwater Vehicles (AUV), Remotely Operated Vehicles (ROV) or Autonomous Surface Vehicles (ASV).

1.1.1 Unmanned Surface Vehicles (USVs)

In today's commercial, scientific, and military communities there exists an ever growing interest for the development of Autonomous surface vehicles (ASVs). ASVs are unmanned vessels which travel on the surface of the water and perform missions without human intervention. ASVs are sometimes called autonomous surface vessels, autonomous surface craft (ASC), or unmanned surface vehicles (USVs). These unmanned vehicles are defined through their capability of performing tasks and missions, in a variety of cluttered environments without any human intervention. ASVs are used in a variety of missions, including mapping underwater terrain, studying the environment both above and below the water

surface, and communicating with other autonomous vehicles. Recently ASVs have been gaining more attention as vessels which can travel into areas that were previously unreachable by autonomous vehicles. The possible applications for these vehicles are many and include scientific research, environmental missions, transportation and ocean resource exploration. The further development of ASVs are expected to provide several benefits, as compared to other manned vehicles, such as lower development and operational costs, improved personal safety, and extended operational range. ASVs are also expect to be able to perform more hazardous missions and exhibit enhanced maneuverability in sophisticated environments. Several countries have done extensive research and development, and come up with a number of different designs.

The Norwegian University of Science and Technology in conjunction with Maritime Robotics has three types of research vessels at their disposal. The aluminum planning monohull Kaasboll USV shown in Fig. 1.1(a) measures 5.75 m in length and is equipped with a 50 hp Evinrude outboard E-tec motor propelling the vessel to up to 20 kts. Fully actuated throttle and rudder are controlled using proportional controllers. Vessel position, heading, velocity, and turn rate are all output from a Seapath 20 navigation system. An onboard computer directly interfaces with MATLAB/Simulink software. The Viknes USV pictured in Fig. 1.1(b) provides all weather capability with its encapsulated cockpit. The vessel is an 8.3 m long semi-displacement vessel with an inboard Yanmar 184 hp motor propelling the vessel to 20 kts. The Viknes USV and Kaasboll USV contain the same sensor and computer suite. The 6.6 m long planning hull Mariner USV shown in Fig. 1.1(c) seeks to bridge the gap between research and application. The Mariner USV uses the same software and hardware as its predecessors, though, with a top speed of 38 kts due to its 150 hp Evinrude E-tec, the vessel clearly has a performance edge. The primary research purposes for these vessels involve a variety of waypoint control, target tracking, path following, and trajectory tracking algorithms [1].

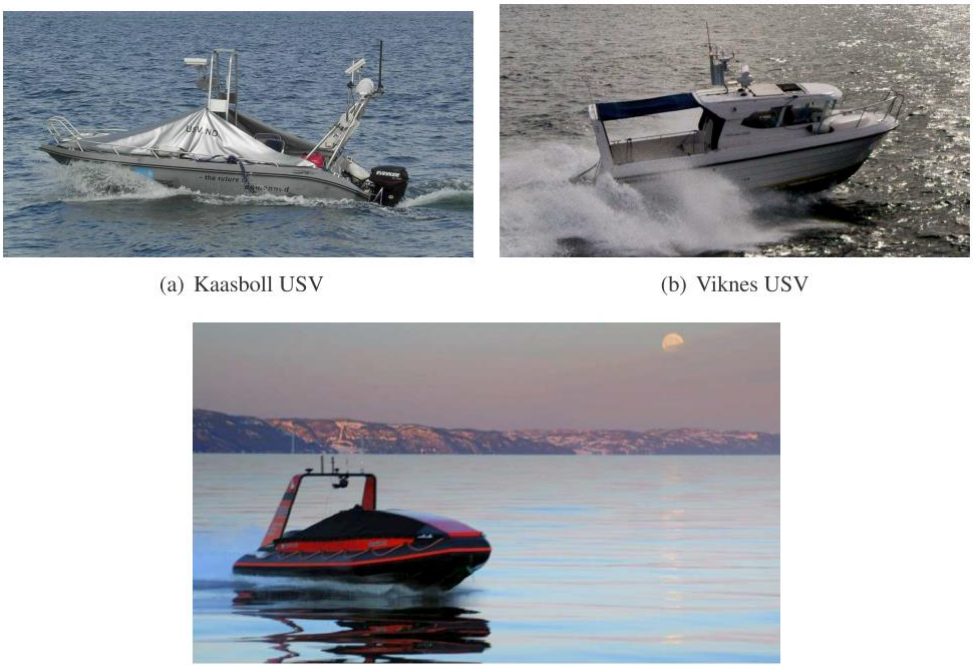

(a) Kaasboll USV (b) Viknes USV

(c) Mariner USV

Fig. 1.1 Maritime Robotics/NTNU USVs (Permission granted by Maritime Robotics)

The Institute of Intelligent Systems for Automation (ISSIA), part of the National Research Council (CNR) located in Italy, uses their two USVs to test a variety system identification [2 , 3], control [4, 5], and path planning algorithms [6]. The Aluminum Autonomous Navigator for Intelligent Sampling (ALANIS) shown in Fig. 1.2(a) collects water samples and monitors the sea floor at sites deemed interesting by its control logic [7]. This vehicle, measuring 4.5 m in length, is equipped with a 50 hp Honda outboard motor. Rudder and throttle actuation is accomplished through the use of two brushless motors coupled with simple proportional control. ALANIS uses a Garmin 152 GPS for localization, a Navicontrol smart compass SC1G measuring yaw and Applied Geomechanics IRIS MD900-TWWide-Angle clinometer measuring pitch and roll. An automatic winch deploys and recovers the scientific instrumentation necessary for taking water samples. The Charlie USV shown in Fig. 1.2(b) is a purpose built catamaran USV [8, 9]. Two DC motors powered by four lead acid batteries replenished by solar cells drive the 2.4 m vessel to a top speed of 2 m/s. The Charlie USV has a GPS Ashtech GG24C for localization, a Kvh Azimuth Gyrotrac for yaw information, and an Applied Geomechanics IRIS MD900-TW Wide-Angle clinometer measuring pitch and roll. The vessel is also equipped with an anemometer, altimeter echo sounder, and side scan sonar. C++ control code runs on a single

board computer with a Linux operating system (OS). Research on the Charlie USV includes modeling and identification [3], regulation tasks like speed and yaw control, line following [4], path following [10, 5], and path planning algorithms for tasks like mine hunting [6].

(a) ALANIS USV (b) Charlie USV

Fig. 1.2 ISSIA-CNR USVs (Permission granted by ISSIA-CNR)

1.1.2 Umbilical Cable

The motion of a long flexible buoyant cable in water is very complex; in addition to the non-linear dynamic motion of the AUV, it makes the motion analysis of the coupled system even more challenging. The cable is treated as a long, thin, flexible circular cylinder. It is assumed that the dynamics of a cable are determined by gravity, hydrodynamic loading and inertial forces, no bending or torsional stiffness is taken into account in this study. The UC that connects the UV to the vessel can be affected by many parameters, including the motions of either the UV or the vessel, the current along the cable and the total length of the cable itself. The UC configuration can be optimized by numerical simulations.

There are several methods with different assumptions and considerations for the motion study of a cable-tethered vehicle system, which include analytical method, experimental method, Lumped Mass method (LMM), catenary method and Finite Difference method (FDM). The analytical method was initially studied by Casarella and Parsons [11]; however, the application of this method is very limited as it can only be used to solve the simple problem when the studied system is at rest. Experimental method can be considered as the most reliable method to predict the dynamic behavior of the cable-tethered vehicle system [12, 13]; however, experimental method is very time-consuming and costly, and the conduction of the experiment in the field has many limitations and difficulties. LMM considers the cable as a discretized system consisting of micro units connected by elastic non-

mass spring [14, 15]. In this chain-connected spring system, although all the forces are considered for each node, the bending stiffness of the cable is neglected, which is less realistic. Burgess [16] indicated the internal forces generated by the cable curvature could avoid the singular behavior of the implicit finite difference scheme, which was made by implementing three additional rotational equations of motion. Recently Feng and Allen [17] extended the numerical scheme developed by Milinazzo et al. [18] and presented a finite difference method to evaluate the effects of the umbilical cable on an underwater flight vehicle, which showed that the numerical scheme was effective and provided a means for developing a feed-forward controller to compensate for the cable effects. It means that the proposed numerical scheme can handle the dynamics of an underwater flight vehicle with cables of non-fixed length.

In this dissertation, we will apply catenary equation to conduct motion analysis of the AUV and cable coupling system; and the shooting method will be used to solve the nonlinear finite differential equations in our numerical simulation scheme to obtain more reliable solving results.

1.1.3 Unmanned Underwater Vehicles (UUVs)

There are many various kinds of the underwater vehicles for variety of tasks in current use, as shown in Fig. 1.3. Most of the early commercial scientific work under the oceans was done by manned underwater submersibles. Unmanned underwater vehicles describe all vehicles that can operate underwater without a human operator in them. They are typically divided into two categories: AUVs and ROVs.

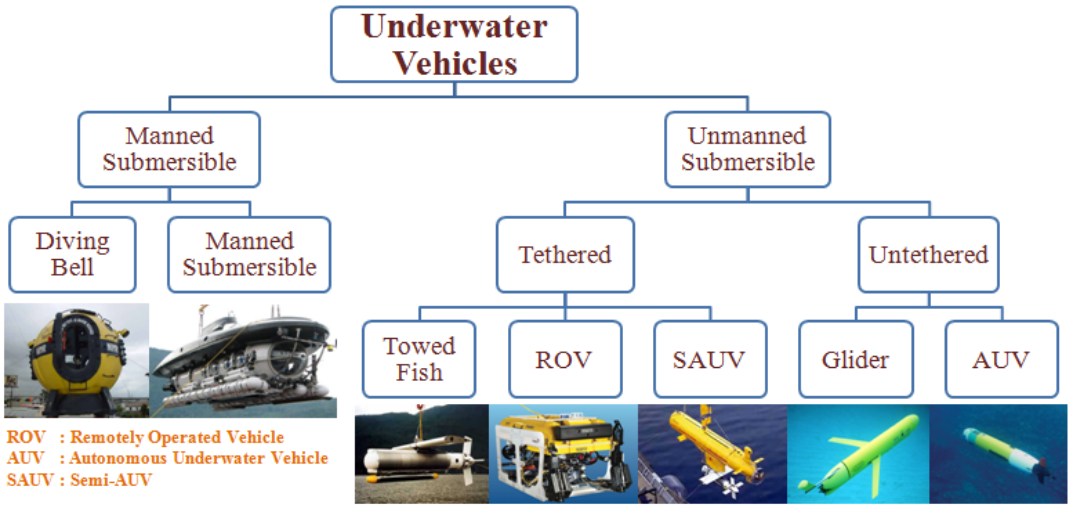

Fig. 1.3 Classification of underwater robots

1.1.3.1 Autonomous Underwater Vehicles

The Autonomous Underwater Vehicle is a device that can operate underwater without any connection to the surface, with all the systems installed onboard, including a power supply. Such a configuration greatly improves the flexibility of such a vehicle, since it is not bound by constraints to a point in the sea, and can operate over longer distances, and in more complex environments. However, development and usage of AUVs provides additional challenges. An AUV must be able to host a power source with sufficiently high capacity to perform long duration operations. Additionally, the operating system of an AUV must be sophisticated enough to ensure completely autonomous operation. AUVs are most often shaped to have minimal damping and to maximize battery life, and are often under-actuated, which limits the hover capabilities. Typical tasks for an AUV can be monitoring of cables and seabed surveys. Autonomous underwater vehicles (AUVs) usually have only one thruster that is located at the backside of the vehicle. Steering of the vehicle is provided by the fins. A number of sensory systems are located on the vehicle. These sensors are inertial measurement units that contain linear acceleration and angular velocity sensors, pressure-meter to observe vehicle depth, sonar systems; front sonar to measure distance from obstacles, ground speed sonar to measure the speed of the vehicle relative to ground. Global Positioning System (GPS) is used to learn the exact location of the vehicle at the sea surface. The positioning through GPS can only be achieved when the vehicle surfaced. AUVs may also consist of acoustic systems that are used to learn the exact location

of the vehicle in pre-defined areas. Also, the acoustic communication can be used for data transfer between the base station and the vehicle. AUVs are supposed to be completely autonomous, consequently relying on onboard power systems and intelligence. There are several examples of operational underwater vehicles designed for commercial use or for scientific reasons.

Fig. 1.4 HUGIN 1000.

Fig. 1.4 shows the photo of HUGIN 1000. The Hugin AUV is developed by Kongsberg Maritime and Forsvarets Forskningsinstiutt (FFI) in Norway. It is intended for high accuracy seabed mapping and surveillance and mine reconnaissance. The HUGIN survey vehicles have demonstrated endurance in excess of 72 hours, and they have depth ratings of 3000-4500 m. These attractive features come in addition to providing high qualitative sonar images of the seabed. Very few others can report equivalent capabilities. Six commercial survey vehicles are currently in operational use around the world. From the first commercial survey in 1997, HUGIN survey vehicles have covered a distance exceeding 120,000 km of commercial survey work. See [19, 20] for more details regarding the HUGIN AUV. The MARIUS AUV has been developed under the Marine Science and Technology (MAST) Programme of the Commission of the European Communities, see Fig. 1.5. The primary envisioned missions of the prototype AUV are environmental surveying and oceanographic data acquisition in coastal waters. The vehicle is 4.5m long, 1.1 m wide and 0.6m high. It is equipped with two main rear thrusters for cruising, four tunnel thrusters for hovering, and rudders, bow, and stern planes for vehicle steering and diving. See [21, 22].

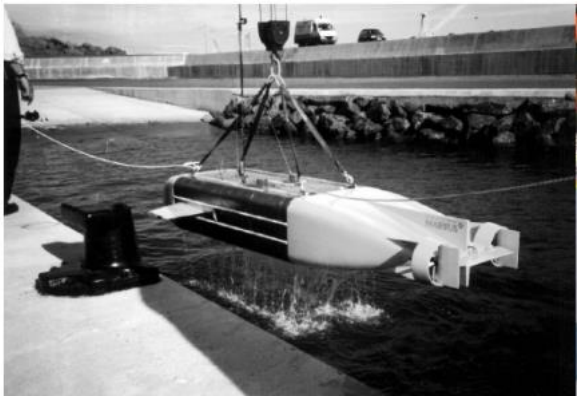

Fig. 1.5 The MARIUS AUV.

1.1.3.2 Remotely Operated Vehicles

In contrast to AUVs, Remotely Operated Vehicles are underwater vehicles that are connected to the operator on the surface by an umbilical cable. This cable carries the electrical power and data from operator to the vehicle or vice versa. There is also less concern as to the shape of the ROV, since the power to the vehicle is provided through the umbilical cable, and thus the only concern is maximum movement speed. Since the ROV is controlled by a human operator, it is often equipped with a wide assortment of tools, cameras and lights, which makes it possible to perform a wide variety of tasks. ROVs are also fully actuated, meaning that it can be controlled in all degrees of freedom (DOFs), and are thus better suited than AUVs to performing tasks that require high precision. These vehicles are usually used in deep water application such as, offshore extraction of oil, and natural gases.

Fig. 1.6 The C-ROV manufactured by Hallin Marine.

These days are a lot of submersible remote operated vehicles (ROV) are used frequently. They tend to be highly specialized for their specific task. Some are designed for scanning wide swaths of the ocean floor while others are designed for photography and recovery. A number of deep-sea animals and plants have been discovered or studied in their natural environment only through the use of ROVs. Fig. 1.6 shows the C-ROV (manufactured by Hallin Marine), and the typical box shape design which is a clear distinction from the AUV. Fig. 1.7 shows ROV Minerva with the basic equipment. Minerva is a SUB-fighter 7500 ROV made by Sperre AS in 2003 for NTNU.

Fig. 1.7 The ROV Minerva.

1.1.4 Literature on Modeling of Marine Vehicles

Modeling of marine vehicles involves the study of statics and dynamics. Statics is concerned with the equilibrium of bodies at rest or moving with constant velocity, whereas dynamics is concerned with bodies having accelerated motion. The foundation of hydrostatic force analysis is the Archimedes' principle. The study of dynamics can be divided into two parts: kinematics, which treats only geometrical aspect of motion, and kinetics, which is the analysis of the forces causing the motion [23]. The increasing needs for AUV have brought about corresponding demands of accurate control of AUV and consequently, models which control laws are based on. Abkowitz [24] addressed issues pertaining to the stability and motion control of marine vehicle. He derived the dynamics of marine vehicles, and also studied and analyzed the external forces and moments acting on the vehicles. Ship hydrodynamics, steering and maneuverability are well discussed. Fossen [23] has also described the modeling of marine vehicles. He described the details of vehicles' kinematics and rigid body dynamics. Based on these, the compact forms of equations of vehicle motion were explained specifically. In addition, he divided the hydrodynamic forces and moments into two parts: radiation-induced forces and Froude-Kriloff and diffraction forces. The equations of motion are nonlinear. The

forces and moments acting on a vehicle moving through a fluid medium are dependent on many factors. These include the properties of the vehicle (length, geometry, etc.), the properties of motion (linear and angular velocities, etc.), and the properties of the fluid (density, viscosity, etc.). Among these forces and moments, the hydrodynamics forces are the most difficult part to model. Newman [25] has presented the marine hydrodynamics in detail, especially the derivation of the added mass.

While many literatures deal with surface ships, articles pertaining to autonomous underwater vehicles are not as common. Yuh [26] is one of the earliest to describe AUV modeling. In [26], he re-emphasized the importance of added mass and introduced functional terms which are essential in describing the equations of motion of an AUV. Since then, many papers and books which further extend this work have appeared. While almost all reports on control of AUVs invariably list all or part of the six degree of freedom (DOF) equations of motion, any newcomer to the topic will most likely be unable to decipher the various terms involved. Fossen offers the most comprehensive treatment on AUV modeling in [27, 28]. Interested readers can find detailed explanations of the various terms that form the equations of motion. After deriving general equations of AUV motion, the next step is to determine the relevant coefficients in these equations and then obtain the whole dynamics model. In these coefficients, the hydrodynamic derivatives are the most difficult terms to model. Therefore, according to the methods of modeling hydrodynamic forces, Goheen [29] has categorized 2 methods of modeling AUV dynamics: test-based method and predictive method.

The test-based method requires direct experiments to obtain relevant data from a prototype of the AUV in a tow-tank or free waters. Abkowitz [24] and Clayton and Bishop [30] have discussed some of the steps and calculations involved in tow-tank testing. The hydrodynamic testing of the MARIUS AUV is outlined in [31]. In addition, the system identification techniques are a less direct, but perhaps more efficient test-based method. However, a disadvantage of this method is the need for a vehicle, as well as laboratory or in-field testing facilities. Considering the cost of the direct method or unavailability of the vehicle especially during vehicle design stage, a predictive method is an attractive alternative. This method calculates the parameters of AUV dynamic model from the vehicle's dimension and shape, control surfaces (fins), weight distribution and other physical components [32]. These techniques make use of potential flow theory, computational fluid dynamics (CFD) or empirical formulas to model the dynamics. In [33], Nahon proposed a component build-up method. It decomposes the vehicle into basic elements, determines drag and lift force for each part, then finds points of force application,

computes moments and finally sums them to get the whole model. This method is easy to apply but may not be accurate enough. Prestero's model [34, 35] adopted the component build-up idea. But with different methods to model forces and moments acting on the vehicle, this model is more accurate.

1.1.5 Literature on Control and Guidance of Marine Vehicles

The main factors that make control process difficult can be stated as: highly nonlinear, time varying dynamic behavior of the vehicle, uncertainties in hydrodynamic coefficients, disturbances by sea environment (especially high frequency waves near surface), unpredicted underwater currents, for our case changes in the gravity and buoyancy. Considering the difficulty to fine-tune the control gains during operations, it will be advantageous to have a control system that will tune itself if the control performance decreases [36].

Different control techniques have been applied to underwater vehicles in recent years. Jalving used classical PID control methods for Norwegian Defence Research Establishment-AUV. He decoupled the system into three lightly interacting subsystems and designed three autopilots for steering, diving and speed control. The design of the each controller was based on PID techniques [37]. Yoerger and Slotine [38] designed a sliding mode controller for an underwater vehicle. In their study they neglected cross-coupling terms and investigated the uncertainties of the hydrodynamic coefficients. Meanwhile, preferring SMC for controlling their vehicle, Healey and Lienard [39] were the ones who decoupled the system into three subsystems first time. Each autopilot was again designed using SMC with exploiting the advantage and ease of decoupled system. Nakamura and Savant [40] urged a nonlinear tracking control of an AUV pondering kinematic motion. They achieved the control by thinking the nonholonomic nature of the system without considering the dynamics of the system. Cristi, Papoulias and Healey [41] designed a robust adaptive SMC such that in the presence of dynamical uncertainties, controllers can adjust to the changing dynamics and operating conditions. A hybrid adaptive controller using both continuous and discrete operations was mentioned by Tabaii et al [42].

In guidance of UUVs not so many studies have been performed. Healey and Lineard [39] worked on the waypoint guidance by line of sight principle where the guidance is accomplished by a heading command to the vehicle's steering system to approach the line of sight between the present position of the vehicle and the waypoint to be reached. In missile guidance this is related to "proportional navigation". Caccia and Veruggio [43] introduced a PI- type task functions which

enables a Lyapunov-based guidance system to compensate the effects of both un-modeled interactions between vehicle and environment.

1.2 Our System Architecture

The relationship between the USV, umbilical cable and AUV is shown in Fig. 1.8. The environmental influences are also shown. Below follows a description of the system architecture.

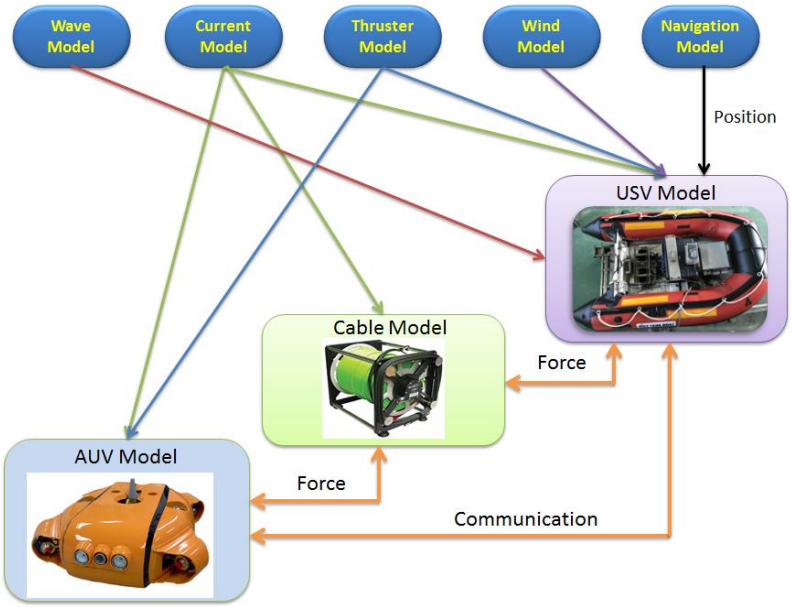

Fig. 1.8 Our complete system.

Description of the System Architecture:

AUV Model:

- ***Purpose:*** The purpose of this model is to conduct tasks such as oceanographic data measurements, bottom imagery, bathymetric imaging, cable-laying, mine-detection, and so on. During a mission, an AUV is expected to carry sensors, such as scanning sonar, bathymetry, track a certain planned trajectory, and even make on-line decisions allowing for mission reconfiguration.
- ***Connection:*** This model is directly connected to the cable. It is also connected to the current-model in term of pressure and current forces. Moreover, the AUV model has a thruster model to generate a force in each direction then to force the AUV follow the desired trajectories.

Cable Model:

- ***Purpose:*** The purpose of this model is to connect the USV to the AUV. It is to have some dynamic in case the AUV runs the survey mission underwater.
- ***Connection:*** This model is directly connected to the USV and the AUV. It is also connected to the current-model in term of pressure and current acting on the cable. This is assumed to be disturbances.

USV Model:

- ***Purpose:*** The purpose of this model is to increase the moving speed of system. The AUV is to follow a specified route determined by the waypoints. It is possible to work for a long time and easy to obtain the real time navigation information and underwater information. The USV sometimes also pull the AUV in the desired direction. The USV must also maintain a correct heading and course.
- ***Connection:*** This model is connected to the navigation-model which measures the exact location of the surface vessel. The USV model is also connected to the disturbances model such as come from the ocean model, wind model and wave model. The USV model is directly connected to the cable. Similar to AUV model, the USV model also has a thruster model to generate a force in each direction. Finally, the USV model has a communication line to the AUV. The AUV tells the USV its position, speed, direction and other possible information that the USV requires to control the AUV.

1.3 Motivation

The guidance and control of marine vessels is an area of focus within the research community. The use of marine vehicles is increasing rapidly within several fields, such as marine biology, seafloor mapping, oceanography, military use and in oil and gas industry, and the autonomy of such vehicles are increasing rapidly. A basic and highly applicable task for such marine vessels, both surface and underwater, are to follow a general path to perform some mission. There are still challenges related to autonomous path following and tracking tasks, and as such the preliminary goal of this dissertation is to develop a method that allows a marine vessel to follow a general path in the presence of unknown ocean currents. This is a very relevant issue for real-life applications.

Dynamic modeling of systems such as marine surface vessels, underwater vehicles, robotic manipulators and more, have become increasingly important the last decades due to, among other things, the increased use of model based motion control. These systems can however be complicated to model, especially when

several systems are interconnected, such an underwater vehicle with robotic manipulators. Furthermore, the dynamics of these systems are typically subject to various external loads such as waves, wind and actuator systems. It is as such important to develop a modeling approach for the dynamics of such systems which allows for both effective production of the models, and flexibility in interfacing other systems and external loads to the model. Fig. 1.9 shows that in general, the deep-sea-operated vehicle systems typically consist of a support vessel, winch, UC, and UV. The UC is widely used in the ocean environment, and plays an important role in supplying power and communications between the UV and the support vessel. However, the management and attachment of the UC and the drag relative to the current cause some restrictions on the maneuverability of the UV. Therefore, while analyzing the UV's maneuvering behaviors, estimation of the corresponding effect caused by the UC and the current will be helpful. However, most researchers neglect the effect of the UC, because the UC effect will cause the numerical model to become very complicated and difficult to solve. Therefore, only a few authors deal with this kind of problem by including the effects due to the UC.

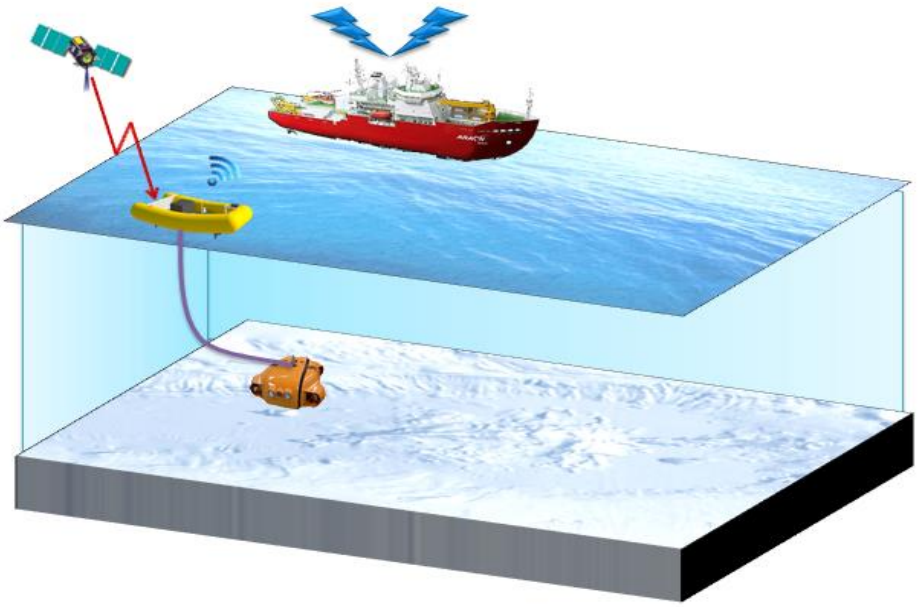

Fig. 1.9 A typical deep-sea-operated vehicle systems.

As mentioned before, several methods with different properties exist for this purpose: Experimental study, Finite Element Methods (FEM), Finite Difference Methods (FDM), Catenary Equations, Lump-Mass-Spring Formulations (LMS), and Finite Segment Approaches (FSA). While all of these methods are based on a particular and generalized mathematical formulation of the problem, experimental study will remain the most reliable method to predict the dynamic behavior of the

UC systems. Yoerger et al. [44] and Hover and Yoerger [45] measured the motion of a deep UV system. However, the experimental study was time-consuming, costly, and the experiment faced some limitations and difficulties. Buckham et al. [46] applied the FEM to calculate the tension and bending force on the slack tether attached to the ROV. However, the computational load of this approach is heavy, and it is difficult to incorporate such packages into control system designs. Ablow and Schechter [47] proposed an implicit FDM to simulate a UC, which has frequently been referenced in the relevant literature. However, if the tension in the UC is lost, their algorithm will become singular. The LMS formulation has a clear physical interpretation, and does not require a large amount of computing. Chai and Varyani [48] presented a general LMS formulation that allowed static and dynamic analysis of a variety of slender structures. Wingnet and Huston [49] discussed the FSA for cable dynamics. They modeled the cable as a series of links connected to each other by ball-and-sockets joints. Although some researches on the hydrodynamics of a UC system have been conducted, they have various limitations. Most of them are one- or two-dimensional, and usually they do not discuss the kinematic properties of the UV in detail. Many of these studies require much computer effort, and are certainly not capable of solving the equations in real time, as is required in model-based estimation and control. In fact, existing researches commonly do not consider hydrodynamic loading on the main body of a UV caused by ocean disturbing effects, such as current agitation and motion velocity of the UV itself during UC operation.

Clearly, the UC motion is very complex, but addition of non-linear motion of the UV makes the system more complex. There are many researchers work on modeling and simulating dynamic behavior of UC. However, until now, almost previous studies still exist a knotty problem that how to implement the dynamic analysis of the complete UV and UC system, since the dynamic interaction between UV and the UC is uncertain, complex and difficult to describe; unfortunately, it is not fully studied and carefully analyzed. So, new efficient and reliable modeling methods for the UC and further for the complete UV and UC system should be considered and developed. Thus, in this dissertation, we present the governing dynamic equation on combined motions of the UV and the UC based on the catenary equation, and apply the shooting method to solve the two-point boundary value problem of the catenary equation. Catenary equations provide a static representation of cables [50]. It is easier to gain insight into the mechanisms that govern the solution than to understand the FEM representation. Also, catenary equations provide a simple representation of the forces acting on the supports where the cable is attached. The equations are solved faster than FEM equations,

and the result is exact. Therefore, this dissertation proposes a new method that combines catenary equations and the shooting method, which is based on the search method developed by Sagatun [51] for simulation of the UC in space. The basic theory of catenaries is well established, and the catenary equations provide a simple representation of the forces acting on the supports where the cable is attached. We apply the shooting method to solve the two-point boundary value problem. The shooting method is a mathematical procedure applied to boundary value problems with unknown initial states. Another advantage of the proposed method is that we obtain the dynamic model as a function of physical variables such as positions and forces, and this allows greater ease of interaction with other dynamics, such as a UV at the free end of the UC.

The hydrodynamic numerical model for simulating the UV maneuvering behavior is very important. A general non-linear model for the dynamics of the UV can be derived either using a Newtonian or a Lagrangian method. In order to understand the behavior of the UV maneuvering in an ocean current, we formulate the mathematical model with the UC effect based on the formulae with 6 degrees of freedom (6 DOF) motions formulated in the dissertation with hydrodynamic coefficients of the UV that we obtained through experiments, and from the literature. We use the catenary equation method to calculate the configuration simulation of the UC connecting to the UV, and solve the corresponding two-end boundary-value problem by using the shooting method. We also apply the 4th Runge–Kutta method to solve the 6 DOF motions of the UV with the UC effect. We describe the compact hydrodynamic model with 6 DOF motions and the numerical solution technique in this dissertation.

1.4 Contribution

The main contributions of this dissertation can be summarized as follows:

- Robust control for the over-actuated, hover-capable nonlinear and highly coupled USV-cable-AUV under uncertainties in the hydrodynamic forces and ocean current effects is always an open research area. To best of our knowledge, the work on such complete USV-cable-AUV systems is not found in the present literature. Clearly, dynamic modeling of USV-cable-AUV systems is a complicated task, mainly due to the several degrees of freedom needed to represent a very complex dynamics, especially when considering movements in 3D space. Thus, knowledge of the dynamic interaction between the USV and cable is required to effectively build and safely operate AUV systems. Knowing the effects of AUV motion on cable motion and

tension in the cable is necessary to allow selection of AUV with compatible motion characteristics as well as USV motion, so we need to model the motions of the system as a multi-body system.

- The problem of thrust allocation for dynamic positioning of AUV with 7 thrusters has been formulated and addressed with consideration of the constraints of thrust forces.
- Applying both PID and sliding mode controls for solving the external disturbance problems such as ocean currents and especially cable effects for controlling an AUV.
- Some simulations of complete model including USV-cable-AUV system are performed to demonstrate the performance of the controllers.
- The research aim is also to enhance a navigation system for over-actuated, hover-capable AUVs with a primary focus on interconnections between the path planning, guidance and control systems. It is assumed that the environment is static and known a priori. Given a start location and a destination, the AUV must be able to plan a valid path connecting the two locations automatically and then navigate along the path without human intervention. The navigation system must be proficient in utilizing available actuators, maintaining better performance.

1.5 Publications Associated to the Dissertation

- **Journals**
  - M.T. Vu, H.S. Choi, J.I. Kang, D.H. Ji and S. K. Jeong, “A study on hovering motion of the underwater vehicle with umbilical cable,” Ocean Engineering, vol. 135, pp. 137-157, 2017.
  - M.T. Vu, H.S. Choi, J.Y. Oh, and S. K. Jeong, “A study on automatic berthing control of an unmanned surface vehicle,” Journal of Advanced Research in Ocean Engineering, vol. 2, pp. 192-201, 2016.
  - D.W. Jung, S.M. Hong, J.H. Lee, H.J. Cho, H.S. Choi and M.T, “A study on unmanned surface vehicle combined with remotely operated vehicle system,” Proceedings of Engineering and Technology Innovation, vol. 9, pp. 17-24, 2018.
  - M.T. Vu, H.S. Choi, J.Y. Ohm, N.D. Nguyen and S. K. Kim, “Analysis on dynamics of USV-linked-ROV system for underwater exploration,”. Submitted to International Journal of Engineering and Technology Innovation.
- **Conference**

- M.T. Vu, H.S. Choi, T.Q.M. Nhat, D.H. Ji and H. J. Son, “Study on the dynamic behaviors of an USV with a ROV,” OCEANS-Anchorage, IEEE Press, pp. 1-7, September 2017.
- M.T. Vu, H.S. Choi, J.Y. Kim, and D.H. Ji, “Study on the dynamic of marine umbilical cable for underwater vehicle,” AETA 2015: Recent Advances in Electrical Engineering and Related Sciences, September 2017.

1.6 Structure of the Dissertation

This dissertation consists of nine chapters. The content and summary of contribution in each chapter is summarized as follows:

Chapter 1 - Introduction

In this chapter, the background of the issue is provided so the necessary of this research is set up. Some previous researches about the same field are summarized for showing the context of the problem and the trend of the other nearby problems. The summary of the motivation and the contributions of this dissertation as well as the outline of the dissertation content are also shown in this chapter.

Chapter 2 – Mathematical Model of Unmanned Surface vehicle (USV)

This chapter discusses the modeling, starting with a general nonlinear six degree of freedom model. The marine vessel is modeled as a rigid body with six degrees of freedom under the excitations of wind, wave, current and cable effects. This most general model is distilled to a three degree of freedom planar motion model, which is then further simplified by observing symmetries present on the research test-bed. A vectored thruster model describes the input forces and moments.

Chapter 3 – Mathematical Model of the Umbilical Cable (UC)

This chapter presents the mathematical modeling of umbilical cable system and how to apply the cable effects to vehicle. The catenary equations and shooting method that are applied on cable are also explained.

Chapter 4 – Mathematical Model of Underwater Vehicle (UV)

In this chapter, the coordinate systems used to model the AUV are displayed and kinematic relations are presented. Furthermore, the complete AUV model is presented step by step. The effects of rigid-body kinetics, hydrostatics, hydrodynamics and the AUV’s actuators are modeled separately and then combined to produce the complete 6-DOF model. The nonlinear equations of motion are written in a compact form intended for nonlinear control system design

and simulation. Especially, the interaction force between the vehicles and the cable is presented in this chapter.

Chapter 5 – Guidance Theory

This chapter acquaints about a guidance strategy which generates suitable reference trajectories for tackling the path tracking (trajectory tracking) problem. Guidance is divided into two parts such as; way point guidance by line-of-sight and way point guidance by cubic polynomial.

Chapter 6 – Control Algorithm Design and Analysis

This chapter describes how nonlinear control design techniques can be applied to underwater vehicle autopilot design. Both PID control and sliding mode control are discussed in detail. Computer simulations are used to illustrate the different control design techniques.

Chapter 7 – Obstacle Avoidance and Path Planning for vehicle using Rapidly-Exploring Random Trees Algorithm

A methodology for getting useful paths from the roadmaps initially generated by the RRT method is presented in this chapter. The main goal was to generate paths which are safe, smooth, and do not require unnecessary heading changes. For this reason, the RRT algorithm is employed in order to initially generate a roadmap where the edges are waypoint candidates for a path connecting one point (departure point) on the map to another (arrival point). A process consisting of several steps is designed so as to choose the waypoints in a way such as the problem requirements are met. Simulation studies are performed to test the proposed approach with different levels of environment complexity.

Chapter 8 – Simulation of Complete USV-UC-UV Systems

This chapter contains a series of numerical simulation that is used to show the efficacy of the proposed path generation algorithm. The results from simulations show the dynamic behaviors of the complete USV-cable-AUV under ocean current effects. Also, a SMC controller is specifically designed to offer consistent tracking performance of the complete system.

Chapter 9 – Conclusions and Future Works

This chapter provides the conclusions of the work presented throughout this dissertation, as well as some suggestions for the future development.

Chapter 2: Mathematical Model of Unmanned Surface Vehicle (USV)

A mathematical model is required for designing the controller of a dynamical system. This chapter presents the numerical modeling of a marine USV; the models are expressed in a vectorial form in order to simplify the control design. The study of dynamics can be divided into two parts: kinematics and kinetics, which is also discussed separately in the following sub chapters. The ocean environment (wind, waves, and currents) affects the surface vessel's dynamics and creates highly nonlinear motion. Further the final maneuvering model will be presented.

2.1 Basic Assumptions

The horizontal motion of an USV moving in a horizontal plane is often described by the motion components in surge, sway, and yaw. Fig. 2.2 illustrates the motion variables in this case. This model is obtained from the general model under the following assumption.

- The motion in roll, pitch, and heave is ignored.
- The vessel has homogeneous mass distribution and *xz*-plane of symmetry so that $I_{xy} = I_{yz} = 0$.
- The center of gravity CG and the center of buoyancy CB are located vertically on the *z*-axis.
- The vessel has three planes of symmetry.
- Disturbances induced by waves, wind, and ocean currents are ignored.

2.2 Three Coordinate Systems

To analyze the motion of the UC as well as its effect on the UUV, it is convenient to define three coordinate systems, i.e., the earth-fixed frame *(X, Y, Z)*, the local cable frames along the UC *(t, n, b)*, and the vehicle-fixed frame *(x, y, z)*. Fig. 2.1(a) shows that we select the earth-fixed frame with *Z* pointing vertically downwards. We choose the orientation of the local cable frame so that *t* is tangent

to the UC in the direction of increasing the UC length coordinate *s*, *b* is in the plane of *X* and *Y*, and *t* and *n* lie in a vertical plane. We locate the vehicle-fixed frame *(x, y, z)* at the mass center of the hull, with *x* coinciding with the longitudinal axis, and *y* pointing to starboard.

We can express the relationship between the vehicle-fixed frame and the earth-fixed frame regarding Euler angles [23]:

$$\begin{bmatrix} x & y & z \end{bmatrix} = \begin{bmatrix} X & Y & Z \end{bmatrix} R(\phi,\theta,\psi) \tag{2.1}$$

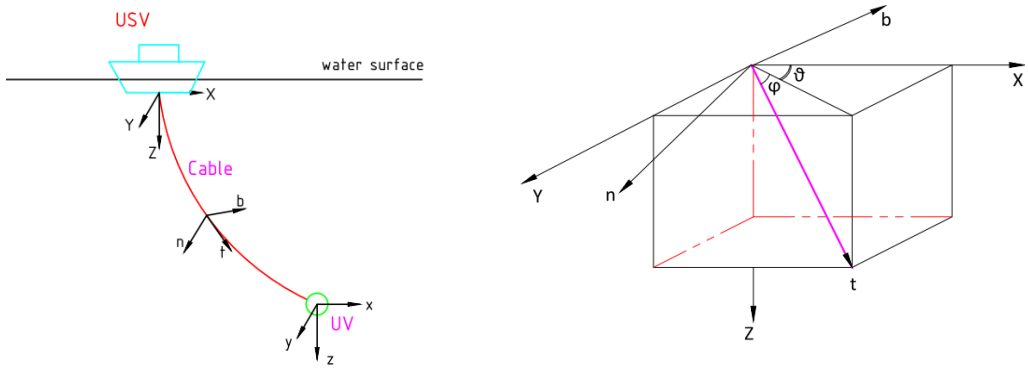

(a) Coordinates of complete system (b) Coordinate of the UC

Fig. 2.1 Three coordinates of the system.

$$R(\phi,\theta,\psi) = \begin{bmatrix} c\theta c\psi & s\phi s\theta c\psi - c\phi s\psi & c\phi s\theta c\psi + s\phi s\psi \\ c\theta s\psi & s\phi s\theta s\psi + c\phi c\psi & c\phi s\theta s\psi - s\phi c\psi \\ -s\theta & s\phi c\theta & c\phi c\theta \end{bmatrix} \tag{2.2}$$

where, ϕ, θ and ψ are the roll, pitch, and heading angle of the vehicle, respectively.

The relationship between the local cable frame and the earth-fixed frame can be expressed as follows [47]:

$$\begin{bmatrix} t & n & b \end{bmatrix} = \begin{bmatrix} X & Y & Z \end{bmatrix} W(\vartheta,\varphi) \tag{2.3}$$

Where,

$$W(\vartheta,\varphi) = \begin{bmatrix} c\vartheta c\varphi & -c\vartheta s\varphi & s\vartheta \\ -s\vartheta c\varphi & s\vartheta s\varphi & c\vartheta \\ -s\varphi & -c\varphi & 0 \end{bmatrix} \tag{2.4}$$

Fig. 2.1(b) shows the relative position of the two coordinate systems. Considering Eqs. (2.1)-(2.4), the relationship between the local cable frame and the vehicle-fixed frame can be written as:

$$\begin{bmatrix} t & n & b \end{bmatrix} = \begin{bmatrix} x & y & z \end{bmatrix} R^T(\phi,\theta,\psi) W(\vartheta,\varphi) \tag{2.5}$$

where, we have used the orthogonal property of *R*.

2.3 Variable Notation

For an ocean vessel moving in six degrees of freedom, six independent coordinates are required to determine its position and orientation. The first three coordinates (x, y, z) and their first time derivatives correspond to the position and translational motion along the x-, y- and z-axes, while the last three coordinates (ϕ,θ,ψ) and their first time derivatives describe orientation and rotational motion.

Table 2.1. SNAME notation [52]

Degree of freedom	Motion	Force and moment	Linear and angular velocity	Position and Euler angles
1	Surge	X	u	x
2	Sway	Y	v	y
3	Heave	Z	w	z
4	Roll	K	p	ϕ
5	Pitch	M	q	θ
6	Yaw	N	r	ψ

According to SNAME, the six different motion components are defined as surge, sway, heave, roll, pitch, and yaw. To determine the equations of motion, two reference frames are considered: the inertial or fixed to earth frame $O_E X_E Y_E Z_E$ that may be taken to coincide with the vessel fixed coordinates in some initial condition and the body-fixed frame $O_b X_b Y_b Z_b$ see Fig. 2.2. Since the motion of the Earth hardly affects ocean vessels (different from air vehicles), the earth-fixed frame $O_E X_E Y_E Z_E$ can be considered to be inertial. For ocean vessels in general, the most commonly adopted position for the body-fixed frame is such that it gives hull

symmetry about the $O_bX_bZ_b$ -plane and approximate symmetry about the $O_bX_bZ_b$ plane. In this sense, the body axes O_bX_b, O_bY_b, and O_bZ_b coincide with the principal axes of inertia and are usually defined as follows: O_bX_b is the longitudinal axis (directed from aft to fore); O_bY_b is the transverse axis (directed to starboard); and O_bZ_b is normal axis (directed from top to bottom. Based on the notion in Table 2.1, the general motion of an ocean vessel can be described by the following vectors.

$$\eta = [\eta_1 \quad \eta_2]^T, \eta_1 = [x \quad y \quad z]^T, \eta_2 = [\phi \quad \theta \quad \psi]^T \tag{2.6}$$

$$\upsilon = [\upsilon_1 \quad \upsilon_2]^T, \upsilon_1 = [u \quad v \quad w]^T, \upsilon_2 = [p \quad q \quad r]^T \tag{2.7}$$

$$\tau = [\tau_1 \quad \tau_2]^T, \tau_1 = [X \quad Y \quad Z]^T, \tau_2 = [K \quad M \quad N]^T \tag{2.8}$$

where η denotes the position and orientation vector with coordinates in the earth-fixed frame, υ denotes the linear and angular velocity vector with coordinates in the body-fixed frame, and τ denotes the forces and moments acting on the vessel in the body-fixed frame.

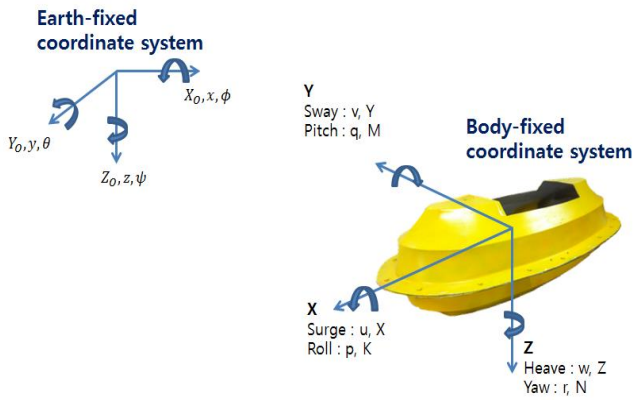

Fig. 2.2 Motion variables for an USV.

In deriving equations of motion of the ocean vessels, we divide the study of vessel dynamics into two parts kinematics, which treats only geometrical aspects of motion, and kinetics, which is the analysis of the forces resulting in the motion.

2.4 Kinematics

The USV is modeled as a rigid hull with an articulated outboard motor. Define a body-fixed reference frame whose x-axis (denoted by the unit vector b_x) points forward along the longitudinal axis of the boat, whose y-axis (denoted by the unit vector b_y) points to starboard, and whose z-axis (denoted $b_z = b_x \times b_y$) points

downward, completing the orthonormal triad. We assume that the USV is symmetric about its longitudinal plane and that the body reference frame is chosen such that the inertia tensor is diagonal: $I = diag(I_{xx}, I_{yy}, I_{zz})$.

Suppose that the vector x denotes the position of the body coordinate origin with respect to some inertially fixed reference frame, denoted by the unit vectors i_x, i_y, and i_z. Let R denote the proper rotation matrix which maps free vectors from the body frame to the inertial frame. Let the body vector $v = (u, \upsilon, w)^T$ represents the translational velocity of the body reference frame with respect to the inertial reference frame. Similarly, let $\omega = (p, q, r)^T$ represents the body angular rate relative to the inertial reference frame shown in Fig. 2.3.

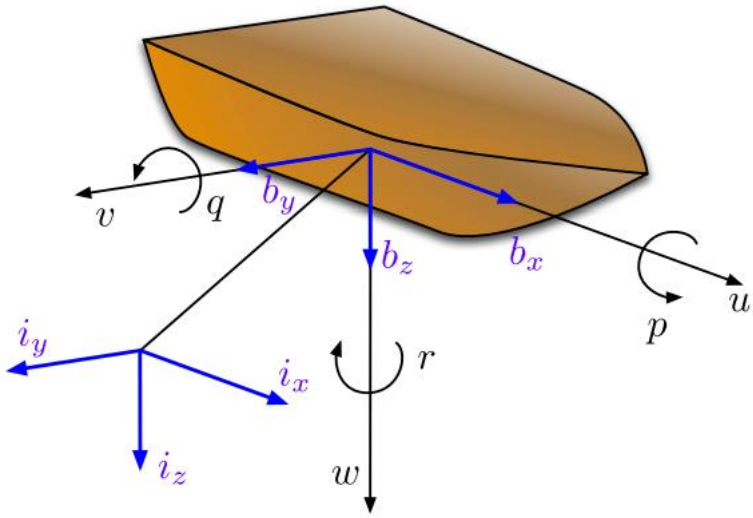

Fig. 2.3 Body fixed 6 DOF reference frame.

The rigid body kinematic equations are

$$\dot{x} = Rv \tag{2.9}$$

$$\dot{R} = R\hat{\omega} \tag{2.10}$$

where the notation $\hat{\cdot}$ denotes the 3 × 3 skew-symmetric matrix satisfying $\hat{a}b$ = a × b for vectors a and b. These equations relate the body's translational and rotational velocity to the rate of change of position and attitude. The matrix R is typically expressed in coordinates, using the conventional Euler angles ϕ, θ, and ψ, for example. In this case, the matrix differential Eq. (2.10) is replaced by three equations relating $\dot{\phi}$, $\dot{\theta}$, and $\dot{\psi}$ to ω. Specifically,

$$\dot{\eta} = J(\eta)v \tag{2.11}$$

The first time derivative of the position vector η_1 is related to the linear velocity vector υ_1 via the following transformation:

$$\dot{\eta}_1 = J_1(\eta_2)\upsilon_1 \tag{2.12}$$

where $J_1(\eta_2)$ is a transformation matrix, which is related through the functions of the Euler angles: roll ϕ, pitch θ, and yaw ψ. This matrix is given by:

$$J_1(\eta_2) = \begin{bmatrix} c\psi c\theta & -s\psi c\phi + s\phi s\theta c\psi & s\psi s\phi + s\theta c\psi c\phi \\ s\psi c\theta & c\psi c\phi + s\phi s\theta s\psi & -c\psi s\phi + s\theta s\psi c\phi \\ -s\theta & s\phi c\theta & c\phi c\theta \end{bmatrix} \tag{2.13}$$

Where s(.) = sin (.) and c(.) = cos (.). It is noted that the matrix $J_1(\eta_2)$ is globally invertible since $J_1^{-1}(\eta_2) = J_1^T(\eta_2)$

On the other hand, the first time derivative of the Euler angle vector η_2 is related to the body-fixed velocity vector υ_2 through the following transformation:

$$\dot{\eta}_2 = J_2(\eta_2)\upsilon_2 \tag{2.14}$$

where the transformation matrix $J_2(\eta_2)$ is given by:

$$J_2(\eta_2) = \begin{bmatrix} 1 & \sin\phi\tan\theta & \cos\phi\tan\theta \\ 0 & \cos\phi & -\sin\phi \\ 0 & \sin\phi/\cos\theta & \cos\phi/\cos\theta \end{bmatrix} \tag{2.15}$$

Note that the transformation matrix $J_2(\eta_2)$ is singular at $\theta = \pm\frac{\pi}{2}$. However, during practical operations ocean vessels are not likely to enter the neighborhood of $\theta = \pm\frac{\pi}{2}$ because of the metacentric restoring forces. For the case where it is essential to consider a region containing $\theta = \pm\frac{\pi}{2}$, a four-parameter description based on Euler parameters can be used instead. The interested reader is referred to [23] for more details. Combining Eq. (2.12) and Eq. (2.14) results in the kinematics of the ocean vessels:

$$\begin{bmatrix} \dot{\eta}_1 \\ \dot{\eta}_2 \end{bmatrix} = \begin{bmatrix} J_1(\eta_2) & 0_{3\times3} \\ 0_{3\times3} & J_2(\eta_2) \end{bmatrix} \begin{bmatrix} \upsilon_1 \\ \upsilon_2 \end{bmatrix} \Leftrightarrow \dot{\eta} = J(\eta)\upsilon \tag{2.16}$$

2.5 Kinetics

2.5.1 Rigid Body Equations of Motion

Let us define the following vectors:

- $f_{Ob} = \begin{bmatrix} X & Y & Z \end{bmatrix}^T$: force decomposed in the body-fixed frame.
- $m_{Ob} = \begin{bmatrix} K & M & N \end{bmatrix}^T$ moment decomposed in the body-fixed frame.
- $v_{Ob} = \begin{bmatrix} u & v & w \end{bmatrix}^T$: linear velocity decomposed in the body-fixed frame.
- $\omega^E{}_{Ob} = \begin{bmatrix} p & q & r \end{bmatrix}^T$: angular velocity of the body-fixed frame relative to the earth-fixed frame.
- $r_{Ob} = \begin{bmatrix} x_g & y_g & z_g \end{bmatrix}^T$: vector from Ob to CG (center of gravity of the vessel) decomposed in the body-fixed frame.

By the Newton–Euler formulation for a rigid body with a mass of m, we have the following balancing forces and moments:

$$m\left[\dot{v}_{Ob} + \dot{\omega}^E_{Ob} \times r_{Ob} + \omega^E_{Ob} \times v_{Ob} + \omega^E_{Ob} \times \left(\omega^E_{Ob} \times r_{Ob}\right)\right] = f_{Ob} \tag{2.17}$$

$$I_o \dot{\omega}^E_{Ob} + \omega^E_{Ob} \times I_o \omega^E_{Ob} + m r_{Ob} \times \left(\dot{v}_{Ob} + \omega^E_{Ob} \times v_{Ob}\right) = m_{Ob} \tag{2.18}$$

where I_o is the inertia matrix about O_b defined by

$$I_o = \begin{bmatrix} I_x & -I_{xy} & -I_{xz} \\ -I_{yx} & I_y & -I_{yz} \\ -I_{zx} & -I_{zy} & I_z \end{bmatrix} \tag{2.19}$$

Here I_x, I_y, and I_z are the moments of inertia about the $O_b X_b$, $O_b Y_b$, and $O_b Z_b$ axes, and , $I_{xy} = I_{yx}$, $I_{xz} = I_{zx}$ and $I_{yz} = I_{zy}$ are the products of inertia. These quantities are defined as:

$$I_x = \int_V \left(y^2 + z^2\right)\rho_m dV, I_{xy} = \int_V xy\rho_m dV \tag{2.20}$$

$$I_y = \int_V \left(x^2 + z^2\right)\rho_m dV, I_{xz} = \int_V xz\rho_m dV \tag{2.21}$$

$$I_z = \int_V \left(x^2 + y^2\right)\rho_m dV, I_{zy} = \int_V zy\rho_m dV \tag{2.22}$$

where ρ_m and V are, respectively, the mass density and the volume of the rigid body. Substituting the definitions of f_{Ob}, m_{Ob}, v_{Ob}, $\omega^E{}_{Ob}$, and r_{Ob} into Eqs. (2.17) and (2.18) results in the following equations of motion of a rigid body:

$$M_{RB}\dot{\nu} + C_{RB}(\nu)\nu = \tau_{RB} \tag{2.23}$$

where $\nu = [u \quad v \quad w \quad p \quad q \quad r]^T$ is the generalized velocity vector decomposed in the body-fixed frame, $\tau_{RB} = [X \quad Y \quad Z \quad K \quad M \quad N]^T$ is the generalized vector of external forces and moments, the rigid body system inertia matrix M_{RB} is given by:

$$M_{RB} = \begin{bmatrix} m & 0 & 0 & 0 & mz_G & -my_G \\ 0 & m & 0 & -mz_G & 0 & mx_G \\ 0 & 0 & m & my_G & -mx_G & 0 \\ 0 & -mz_G & my_G & I_{xx} & -I_{xy} & -I_{xz} \\ mz_G & 0 & -mx_G & -I_{yx} & I_{yy} & -I_{yz} \\ -my_G & mx_G & 0 & -I_{zx} & -I_{zy} & I_{zz} \end{bmatrix} \tag{2.24}$$

where m is the total mass, $(x_G, y_G, z_G)^T$ is the vector between the center of gravity and vehicle origin, and the inertial tensor that accounts for lack of symmetry with off-diagonal terms is as:

$$I = \begin{bmatrix} I_{xx} & -I_{xy} & -I_{xz} \\ -I_{yx} & I_{yy} & -I_{yz} \\ -I_{zx} & -I_{zy} & I_{zz} \end{bmatrix} \tag{2.25}$$

Using the parallel axis theorem gives the terms containing the mass variable combined with elements of the center of gravity vector, which adds to the rotational inertia. The corresponding rigid body Coriolis and centripetal matrix $C_{RB}(\nu)$ is:

$$C_{RB}(v) = -\begin{bmatrix} 0 & 0 & 0 & m(y_G q + z_G r) & -m(x_G q - w) & -m(x_G r + v) \\ 0 & 0 & 0 & -m(y_G q + w) & m(z_G r + x_G p) & -m(y_G r - u) \\ 0 & 0 & 0 & -m(z_G p - v) & -m(z_G q + u) & m(x_G p + y_G q) \\ -m(y_G q + z_G r) & m(y_G q + w) & m(z_G p - v) & 0 & -I_{yz}q - I_{xz}p + I_z r & I_{yz}r + I_{xy}p - I_y q \\ m(x_G q - w) & -m(z_G r + x_G p) & m(z_G q + u) & I_{yz}q + I_{xz}p - I_z r & 0 & -I_{xz}r - I_{xy}q + I_x p \\ m(x_G r + v) & m(y_G r - u) & -m(x_G p + y_G q) & -I_{yz}r - I_{xy}p + I_y q & I_{xz}r + I_{xy}q - I_x p & 0 \end{bmatrix} \tag{2.26}$$

The generalized external force and moment vector, τ_{RB} , is a sum of hydrodynamic force and moment vector τ_H , external disturbance force and moment vector τ_E , and propulsion force and moment vector τ . Each of these vectors is detailed in the following sections.

2.5.2 Hydrodynamic Forces and Moments

In hydrodynamics, it is usually assumed that the hydrodynamic forces and moments on a rigid body can be linearly superimposed, see [53]. The hydrodynamic forces and moments are forces and moments on the body when the body is forced to oscillate with the wave excitation frequency and there are no incident waves. These forces and moments can be identified as the sum of three components: (1) added mass due to the inertia of the surrounding fluid, (2) radiation-induced potential damping due to the energy carried away by generated surface waves, and (3) restoring forces due to Archimedian forces (weight and buoyancy). The hydrodynamic force and moment vector τ_H is given by:

$$\tau_H = -M_A \dot{\nu} - C_A(\nu)\nu - D(\nu)\nu - g(\eta) \tag{2.27}$$

where M_A is the added mass matrix, $C_A(\nu)$ is the hydrodynamic Coriolis and centripetal matrix, $D(\nu)$ is the damping matrix, and $g(\eta)$ is the position and orientation depending vector of restoring forces and moments.

The vessel accelerates nearby fluid around its body during motion, effectively adding inertia to the system, which is accounted for by including added mass terms. All vehicles moving in a fluid (including heavier-than-air aircraft) have added mass,

but its effects become more pronounced when the density of the fluid approaches as the density of the vehicle. The added mass matrix M_A is defined as.

$$M_A = -\begin{bmatrix} X_{\dot{u}} & X_{\dot{v}} & X_{\dot{w}} & X_{\dot{p}} & X_{\dot{q}} & X_{\dot{r}} \\ Y_{\dot{u}} & Y_{\dot{v}} & Y_{\dot{w}} & Y_{\dot{p}} & Y_{\dot{q}} & Y_{\dot{r}} \\ Z_{\dot{u}} & Z_{\dot{v}} & Z_{\dot{w}} & Z_{\dot{p}} & Z_{\dot{q}} & Z_{\dot{r}} \\ K_{\dot{u}} & K_{\dot{v}} & K_{\dot{w}} & K_{\dot{p}} & K_{\dot{q}} & K_{\dot{r}} \\ M_{\dot{u}} & M_{\dot{v}} & M_{\dot{w}} & M_{\dot{p}} & M_{\dot{q}} & M_{\dot{r}} \\ N_{\dot{u}} & N_{\dot{v}} & N_{\dot{w}} & N_{\dot{p}} & N_{\dot{q}} & N_{\dot{r}} \end{bmatrix}. \tag{2.28}$$

Knowing the added mass matrix of a system allows for the immediate derivation of the corresponding added mass Coriolis and centripetal matrix. Using the equation for fluid kinetic energy:

$$T_A = \frac{1}{2} v^T M_A v \tag{2.29}$$

with Kirchhoff's equations for a rigid body moving through an incompressible fluid gives:

$$\begin{aligned} \frac{d}{dt}\frac{\partial T_A}{\partial u} &= r\frac{\partial T_A}{\partial v} - q\frac{\partial T_A}{\partial w} + X_A \\ \frac{d}{dt}\frac{\partial T_A}{\partial v} &= -p\frac{\partial T_A}{\partial w} - r\frac{\partial T_A}{\partial u} - Y_A \\ \frac{d}{dt}\frac{\partial T_A}{\partial r} &= q\frac{\partial T_A}{\partial u} - p\frac{\partial T_A}{\partial v} + Z_A \\ \frac{d}{dt}\frac{\partial T_A}{\partial u} &= w\frac{\partial T_A}{\partial v} - v\frac{\partial T_A}{\partial w} + r\frac{\partial T_A}{\partial q} - q\frac{\partial T_A}{\partial r} - K_A \\ \frac{d}{dt}\frac{\partial T_A}{\partial v} &= u\frac{\partial T_A}{\partial w} - w\frac{\partial T_A}{\partial r} - r\frac{\partial T_A}{\partial p} - M_A \\ \frac{d}{dt}\frac{\partial T_A}{\partial r} &= v\frac{\partial T_A}{\partial u} - u\frac{\partial T_A}{\partial v} + q\frac{\partial T_A}{\partial p} - p\frac{\partial T_A}{\partial q} - N_A \end{aligned} \tag{2.30}$$

Applying assumptions of port/starboard symmetry considerably simplifies the added mass matrix giving:

$$M_A = -\begin{bmatrix} X_{\dot{u}} & 0 & X_{\dot{w}} & 0 & X_{\dot{q}} & 0 \\ 0 & Y_{\dot{v}} & 0 & Y_{\dot{p}} & 0 & Y_{\dot{r}} \\ Z_{\dot{u}} & 0 & Z_{\dot{w}} & 0 & Z_{\dot{q}} & 0 \\ 0 & K_{\dot{v}} & 0 & K_{\dot{p}} & 0 & K_{\dot{r}} \\ M_{\dot{u}} & 0 & M_{\dot{w}} & 0 & M_{\dot{q}} & 0 \\ 0 & N_{\dot{v}} & 0 & N_{\dot{p}} & 0 & N_{\dot{r}} \end{bmatrix}. \tag{2.31}$$

In its current state the added mass matrix is positive definite but not symmetric. In the presence of waves and forward vessel motion this matrix will stay asymmetric, but for slow speeds on inland bodies of water the waves can be assumed to be small enough to allow for symmetry. This gives:

$$M_A = -\begin{bmatrix} X_{\dot{u}} & 0 & Z_{\dot{u}} & 0 & M_{\dot{u}} & 0 \\ 0 & Y_{\dot{v}} & 0 & K_{\dot{v}} & 0 & N_{\dot{v}} \\ Z_{\dot{u}} & 0 & Z_{\dot{w}} & 0 & M_{\dot{w}} & 0 \\ 0 & K_{\dot{v}} & 0 & K_{\dot{p}} & 0 & N_{\dot{p}} \\ M_{\dot{u}} & 0 & M_{\dot{w}} & 0 & M_{\dot{q}} & 0 \\ 0 & N_{\dot{v}} & 0 & N_{\dot{p}} & 0 & N_{\dot{r}} \end{bmatrix}. \tag{2.32}$$

Extracting the added mass Coriolis and centripetal matrix we have:

$$C_A(v) = -\begin{bmatrix} 0 & 0 & 0 & 0 & -a_3 & a_2 \\ 0 & 0 & 0 & a_3 & 0 & -a_1 \\ 0 & 0 & 0 & -a_2 & a_1 & 0 \\ 0 & -a_3 & a_2 & 0 & -b_3 & b_2 \\ a_3 & 0 & -a_1 & b_3 & 0 & -b_1 \\ -a_2 & a_1 & 0 & -b_2 & b_1 & 0 \end{bmatrix} \tag{2.33}$$

Where

$$\begin{aligned} a_1 &= X_{\dot{u}}u + X_{\dot{v}}v + X_{\dot{w}}w + X_{\dot{p}}p + X_{\dot{q}}q + X_{\dot{r}}r, \\ a_2 &= Y_{\dot{u}}u + Y_{\dot{v}}v + Y_{\dot{w}}w + Y_{\dot{p}}p + Y_{\dot{q}}q + Y_{\dot{r}}r, \\ a_3 &= Z_{\dot{u}}u + Z_{\dot{v}}v + Z_{\dot{w}}w + Z_{\dot{p}}p + Z_{\dot{q}}q + Z_{\dot{r}}r, \\ b_1 &= K_{\dot{u}}u + K_{\dot{v}}v + K_{\dot{w}}w + K_{\dot{p}}p + K_{\dot{q}}q + K_{\dot{r}}r, \\ b_2 &= M_{\dot{u}}u + M_{\dot{v}}v + M_{\dot{w}}w + M_{\dot{p}}p + M_{\dot{q}}q + M_{\dot{r}}r, \\ b_3 &= N_{\dot{u}}u + N_{\dot{v}}v + N_{\dot{w}}w + N_{\dot{p}}p + N_{\dot{q}}q + N_{\dot{r}}r, \end{aligned} \tag{2.34}$$

In general, hydrodynamic damping for ocean vessels is mainly caused by potential damping, skin friction, wave drift damping, and damping due to vortex shedding. It is difficult to give a general expression of the hydrodynamic damping matrix $D(v)$. However, it is common to write the hydrodynamic damping matrix $D(v)$ as:

$$D(v) = D_l + D_q(v) \tag{2.35}$$

The linear damping matrix arrises due to laminar friction on the body of the boat and takes the form:

$$D_l = -\begin{bmatrix} X_u & X_v & X_w & X_p & X_q & X_r \\ Y_u & Y_v & Y_w & Y_p & Y_q & Y_r \\ Z_u & Z_v & Z_w & Z_p & Z_q & Z_r \\ K_u & K_v & K_w & K_p & K_q & K_r \\ M_u & M_v & M_w & M_p & M_q & M_r \\ N_u & N_v & N_w & N_p & N_q & N_r \end{bmatrix}. \tag{2.36}$$

The quadratic damping matrix comes about due to pressure drag off of the hull of the boat and is shown as:

$$D_q(v) = \begin{bmatrix} X_{u|u|}|u| & X_{v|v|}|v| & X_{w|w|}|w| & X_{p|p|}|p| & X_{q|q|}|q| & X_{r|r|}|r| \\ Y_{u|u|}|u| & Y_{v|v|}|v| & Y_{w|w|}|w| & Y_{p|p|}|p| & Y_{q|q|}|q| & Y_{r|r|}|r| \\ Z_{u|u|}|u| & Z_{v|v|}|v| & Z_{w|w|}|w| & Z_{p|p|}|p| & Z_{q|q|}|q| & Z_{r|r|}|r| \\ K_{u|u|}|u| & K_{v|v|}|v| & K_{w|w|}|w| & K_{p|p|}|p| & K_{q|q|}|q| & K_{r|r|}|r| \\ M_{u|u|}|u| & M_{v|v|}|v| & M_{w|w|}|w| & M_{p|p|}|p| & M_{q|q|}|q| & M_{r|r|}|r| \\ N_{u|u|}|u| & N_{v|v|}|v| & N_{w|w|}|w| & N_{p|p|}|p| & N_{q|q|}|q| & N_{r|r|}|r| \end{bmatrix}. \tag{2.37}$$

2.5.3 Restoring Forces and Moments

In this section, a model for $g(\eta)$ is described. Effects of buoyancy's interaction with gravity, manifested in g(η), give the metacentric stability properties of a ship. Simplifying to bodies with symmetry in the xz-plane gives:

$$g(\eta) = -\begin{pmatrix} -\rho g \int_0^z A_{wp}(\tau) d\tau \sin\theta \\ \rho g \int_0^z A_{wp}(\tau) d\tau \cos\theta \sin\phi \\ \rho g \int_0^z A_{wp}(\tau) d\tau \cos\theta \cos\phi \\ \rho g \nabla \overline{GM}_L \sin\phi \cos\theta \cos\phi \\ \rho g \nabla \overline{GM}_L \sin\theta \cos\theta \cos\phi \\ \rho g \nabla \left(-\overline{GM}_L \cos\theta + \overline{GM}_T\right) \sin\phi \sin\theta \end{pmatrix} \tag{2.38}$$

where ρ is water density, g is gravity, z is the depth at the lowest point of the vehicle, ∇ is displaced water volume, A_{wp} is the water plane area, $\overline{GM}_T$ is the transverse metacentric height, and $\overline{GM}_L$ is the longitudinal metacentric height.

2.5.4 Environmental Disturbances

The ocean environmental disturbance can be separated into high- and low-frequency forces and moments affecting the vessel. The high-frequency part is filtered by a low-pass filter, and the low-frequency part is counteracted using only the control input. Furthermore, in this study, only the low-frequency part is considered, and the implementation of low-pass filtering is assumed.

2.5.4.1 Wind Effects

Wind forces and moments directly affect the vessel's part above the sea surface. Wind is characterized by the velocity V_w and direction β_w. In order to apply the wind effect on a DP vessel, wind should be redefined in terms of the relative wind speed V_{rw} and angle of attack γ_{rw}.

$$u_w = V_w \cos(\beta_w - \psi) \tag{2.39}$$

$$v_w = V_w \sin(\beta_w - \psi) \tag{2.40}$$

$$u_{rw} = u - u_w \tag{2.41}$$

$$v_{rw} = v - v_w \tag{2.42}$$

$$V_{rw} = \sqrt{u_{rw}^2 + v_{rw}^2} \tag{2.43}$$

$$\gamma_{rw} = -a\tan 2(v_{rw}, u_{rw}) \tag{2.44}$$

And wind forces and moments τ_{wind} can compute as follows:

$$\tau_{wind} = \begin{bmatrix} X_w & Y_w & N_w \end{bmatrix}^T \tag{2.45}$$

Or

$$\tau_{wind} = \begin{bmatrix} \frac{1}{2}\rho_{air} V_{rw}^2 C_{Xw}(\gamma_{rw}) A_{Fw} \\ \frac{1}{2}\rho_{air} V_{rw}^2 C_{Yw}(\gamma_{rw}) A_{Lw} \\ \frac{1}{2}\rho_{air} V_{rw}^2 C_{Nw}(\gamma_{rw}) A_{Lw} L_{oa} \end{bmatrix} \tag{2.46}$$

where ρ_{air} is the density of air; A_{Fw} and A_{Lw} are the frontal and lateral wind projection areas; L_{oa} is the overall length of the vessel; and $C_{Xw}(\gamma_{rw})$, $C_{Yw}(\gamma_{rw})$, and $C_{Nw}(\gamma_{rw})$ are the non-dimensional wind coefficients in surge, sway, and yaw, respectively.

Many researchers derived various sets of wind coefficients to apply the wind effect to different ocean platforms. These coefficients are often found through a model test or by employing empirical formulas. The wind load coefficients reported in [54] are used for this study.

2.5.4.2 Waves Effects

The ocean waves' effect on the vessel can divide the 1st- and 2nd-order wave-induced forces. The 1st-order term is a wave-frequency motion that is represented by zero-mean oscillatory motions. The 2nd-order term is a wave drift force that is represented by a nonzero slowly varying component.

For a low-frequency model such as a DP vessel, the wave drift forces are more dominant than the oscillatory motions. Therefore, by using a low-pass filter, the oscillation component can be removed for control efficiency on the horizontal motion. The wave drift forces can be simply expressed as a random walk process.

$$\tau_{wave2} = \begin{bmatrix} d_X & d_Y & d_N \end{bmatrix}^T \tag{2.47}$$

$$\dot{d}_X = w_1 \tag{2.48}$$

$$\dot{d}_Y = w_2 \tag{2.49}$$

$$\dot{d}_N = w_3 \tag{2.50}$$

where d_X, d_Y, and d_N are wave 2nd-order drift forces and moments, and w_i $(i = 1, 2, 3)$ are Gaussian white noise.

2.5.4.3 Ocean Currents Effects

For surface vessel modeling, a two-dimensional current model is considered. The ocean current is denoted by the current speed V_c and direction β_c . The variation of the current can be implemented by a first-order Gauss-Markov process.

$$\dot{V}_c = -\varepsilon_v V_c + w_v \tag{2.51}$$

$$\dot{\beta}_c = -\varepsilon_\beta \beta_c + w_\beta \tag{2.52}$$

where $\varepsilon_v \geq 0$ and $\varepsilon_\beta \geq 0$ are constants, and w_v and w_β are Gaussian white noise.

The current forces and moments acting on a vessel are generally applied by using a relative velocity v_r in hydrodynamic terms.

$$v_r = \begin{bmatrix} u - u_c & v - v_c & r \end{bmatrix}^T \tag{2.53}$$

For low-speed DP vessel applications, the current forces and moments can be described using the current coefficients C_{Xc} , C_{Yc} and C_{Nc} , which can be experimentally obtained by using scale models in wind tunnels. These current loads can be represented as follows:

$$u_c = V_c \cos(\beta_c - \psi) \tag{2.54}$$

$$v_c = V_c \sin(\beta_c - \psi) \tag{2.55}$$

$$u_{rc} = u - u_c \tag{2.56}$$

$$v_{rc} = v - v_c \tag{2.57}$$

$$V_{rc} = \sqrt{u_{rc}^2 + v_{rc}^2} \tag{2.58}$$

$$\gamma_{rc} = -a \tan 2(v_{rc}, u_{rc}) \tag{2.59}$$

$$X_c = \frac{1}{2} \rho A_{Fc} C_{Xc}(\gamma_{rc}) V_{rc}^2 \tag{2.60}$$

$$Y_c = \frac{1}{2} \rho A_{Lc} C_{Yc}(\gamma_{rc}) V_{rc}^2 \tag{2.61}$$

$$N_c = \frac{1}{2} \rho A_{Lc} L_{oa} C_{Nc}(\gamma_{rc}) V_{rc}^2 \tag{2.62}$$

where, ρ is the density of sea water, A_{Fc} and A_{Lc} are respectively the frontal and lateral projected current areas, and L_{oa} is the length over the entire vessel.

2.5.4.4 Cable Effects

The umbilical connecting the AUV to the USV can be modeled as a long slender pipe, and it will experience forces from drag on the cable from the relative velocity of the USV. Moreover, dependent on the current velocity and the depth of the AUV, the forces and moments due to the umbilical can have a large impact. The current induces a drag force on the cable-run from the surface to the AUV. Forces on the umbilical will also affect the USV, so they must be included in the equations of motion through the force vector τ umbilical. Generally speaking, the dynamics of the mooring lines need to be coupled to the dynamics of the USV for accurate simulation. As the umbilical is comparatively thin compared to the wavelength and amplitude Morison's equation for drag force might be used to calculate the forces acting on it. This is described in more detail in Chapter 3.

2.5.5 Propulsion Forces and Moments

The vector, τ , of propulsion forces and moments depends on a specific configuration of actuators such as propellers. In the next section where τ is specified, we consider some classes of the ocean vessels that are common in practice. In this chapter, we neglect the dynamics of the actuators that provide the propulsion forces and moments since the response of the actuators such as hydraulic systems and electrical motors is much faster than the response of the vessel.

2.6 Nonlinear 6DOF Dynamics

The nonlinear 6 DOF dynamics of a USV can be described as:

$$M\dot{v} + C(v)v + D(v)v + g(\eta) = \tau \tag{2.63}$$

$$\dot{\eta} = J^T(\eta)v \tag{2.64}$$

where M is the mass matrix, C is the Coriolis and centripetal matrix, D is the damping matrix, g is a vector of restoring forces and moments due to the interaction between buoyancy and gravity.

And τ is a vector of control forces and moments as:

$$\tau = \tau_{wind} + \tau_{wave} + \tau_{current} + \tau_{cable} \tag{2.65}$$

The mass matrix M and Coriolis and centripetal matrix C can be decomposed to:

$$M = M_A + M_{RB} \tag{2.66}$$

And

$$C(v) = C_A(v) + C_{RB}(v) \tag{2.67}$$

where the subscript "RB" denotes rigid body contributions and the subscript "A" represents added mass and inertia.

Even with some simplifications, the ship dynamic models contain too many parameters for feasible parameter identification. Since the primary goal of this ship modeling discussion is to provide a suitable structure for a maneuvering model, the roll, pitch, and heave dynamics are ignored in all of the following modeling sections.

2.7 Mathematical Model of USV in 3 DOF

2.7.1 Planar Kinematics

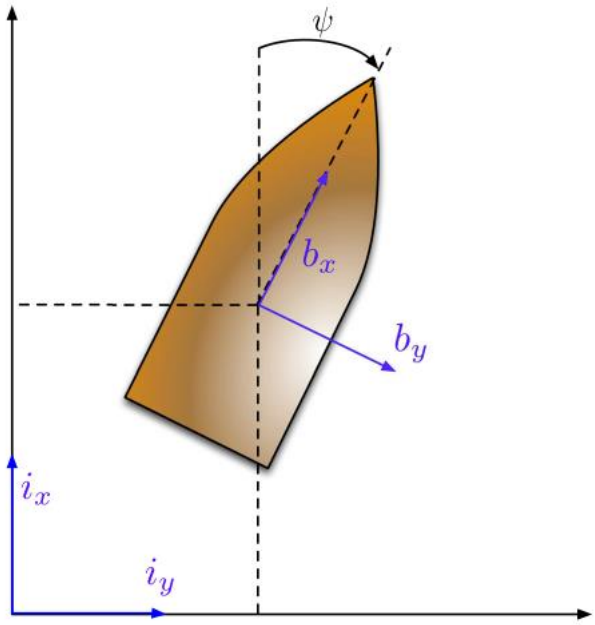

Fig. 2.4 Schematic depiction of a USV.

To simplify matters, we will ignore the roll, pitch, and heave dynamics and consider USV motion in the horizontal plane. Fig. 2.4 illustrates the state and input variables for a planar USV model with a gimbaled thruster (e.g., an outboard engine). Thus, the kinematic model for a USV in planar motion in the absence of currents is:

$$\begin{bmatrix} \dot{x} \\ \dot{y} \\ \dot{\psi} \end{bmatrix} = \begin{bmatrix} \cos\psi & -\sin\psi & 0 \\ \sin\psi & \cos\psi & 0 \\ 0 & 0 & 1 \end{bmatrix} \begin{bmatrix} u \\ v \\ r \end{bmatrix} \tag{2.68}$$

With the total velocity $V = \sqrt{u^2 + v^2}$, we define the sideslip angle β and the course angle χ as follows:

$$\beta = \arcsin(\frac{v}{V}) \tag{2.69}$$

And

$$\chi = \psi + \beta \tag{2.70}$$

These definitions are illustrated in Fig. 2.5. Note that the course angle and the heading angle are equal unless the vehicle is slipping. Recognizing that:

$$\begin{bmatrix} u \\ v \end{bmatrix} = \begin{bmatrix} \cos\beta & -\sin\beta \\ \sin\beta & \cos\beta \end{bmatrix} \begin{bmatrix} V \\ 0 \end{bmatrix} \tag{2.71}$$

We may write:

$$\begin{bmatrix} \dot{x} \\ \dot{y} \\ \dot{\psi} \end{bmatrix} = \begin{bmatrix} \cos\psi & -\sin\psi & 0 \\ \sin\psi & \cos\psi & 0 \\ 0 & 0 & 1 \end{bmatrix} \begin{bmatrix} \cos\beta & -\sin\beta & 0 \\ \sin\beta & \cos\beta & 0 \\ 0 & 0 & 1 \end{bmatrix} \begin{bmatrix} V \\ 0 \\ r \end{bmatrix} \tag{2.72}$$

Or

$$\begin{bmatrix} \dot{x} \\ \dot{y} \\ \dot{\chi} \end{bmatrix} = \begin{bmatrix} \cos\chi & -\sin\chi & 0 \\ \sin\chi & \cos\chi & 0 \\ 0 & 0 & 1 \end{bmatrix} \begin{bmatrix} V \\ 0 \\ r + \dot{\beta} \end{bmatrix} \tag{2.73}$$

Where

$$V\cos\beta\dot{\beta} = \dot{v} - \dot{V}\sin\beta \tag{2.74}$$

The speed-and-sideslip representation provides a useful alternative view, despite the ambiguity in the definition of β when V → 0. Note that Eq. (2.73) is not really a kinematic model, though, because $\dot{\beta}$ depends on acceleration as well as velocity.

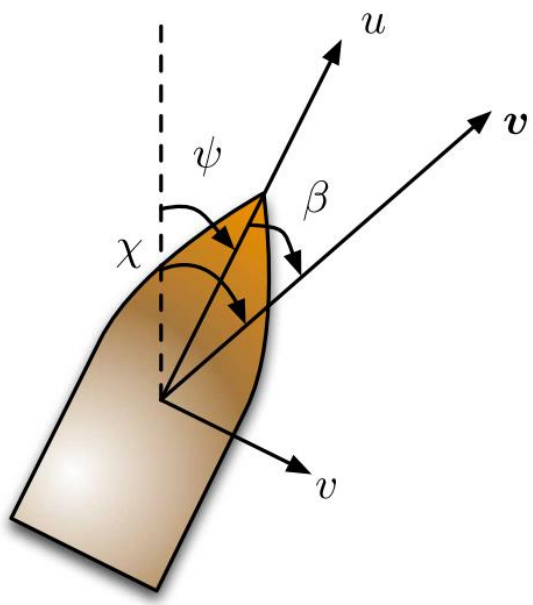

Fig. 2.5 Definitions of side slip and course angles.

2.7.2 Planar Nonlinear 3 DOF Dynamics

By truncating the 6DOF nonlinear model to the 3DOF that define maneuvering motion we inevitably loose fidelity while gaining simplicity. For instance, thrust line effects, which makes smaller boats lean into turns, are neglected. Since the thrust is coming from below the center of gravity and the turning moment is due to a force opposing the direction of the turn, the boat naturally leans into the turn. "Sea-keeping" behavior describing motion due to waves and metacentric stability is also neglected. With these effects ignored the pitch, roll, and heave equations of motion become.

$$\begin{aligned} &Z = K = M = 0 \\ &p = q = w = 0 \\ &g(\eta) = 0 \end{aligned} \tag{2.75}$$

with the 3 DOF state vectors

$$\begin{aligned} &v = \begin{bmatrix} u & v & r \end{bmatrix}^T \\ &\eta = \begin{bmatrix} x & y & \psi \end{bmatrix}^T \end{aligned} \tag{2.76}$$

In some cases, we ignore the off-diagonal terms of the matrices *M* and *D*, all elements of the nonlinear damping matrix $D_n(v)$. These assumptions hold when the USV has three planes of symmetry, for which the axes of the body-fixed

reference frame are chosen to be parallel to the principal axis of the displaced fluid, which equal to the principal axis of the vessel. USV fore/aft non-symmetry implies that the off-diagonal terms of the inertia and damping matrices are nonzero. However, these terms are small compared to the main diagonal terms. Furthermore, disturbances induced by waves, wind, and ocean currents are ignored. Under the just-mentioned assumptions, the dynamics of a surface USV or an underwater vehicle moving in a horizontal plane is simplified from the three degrees of freedom model as follows:

$$\dot{\eta} = J(\eta)v \tag{2.77}$$

$$M\dot{v} = -C(v)v - \left(D + D_n(v)\right)v + \tau + \tau_E + \tau_{C1} \tag{2.78}$$

where the matrices $J(\eta)$, M; $C(v)$; D, and $D_n(v)$ are given by

$$J(\eta) = \begin{bmatrix} \cos\psi & -\sin\psi & 0 \\ \sin\psi & \cos\psi & 0 \\ 0 & 0 & 1 \end{bmatrix} \tag{2.79}$$

$$M = \begin{bmatrix} m - X_{\dot{u}} & 0 & 0 \\ 0 & m - Y_{\dot{v}} & mx_g - Y_{\dot{r}} \\ 0 & mx_g - Y_{\dot{r}} & I_z - N_{\dot{r}} \end{bmatrix} \tag{2.80}$$

$$C(v) = \begin{bmatrix} 0 & 0 & -m\left(x_g r + v\right) + Y_{\dot{v}}v + Y_{\dot{r}}r \\ 0 & 0 & mu - X_{\dot{u}}u \\ m\left(x_g r + v\right) - Y_{\dot{v}}v - Y_{\dot{r}}r & -mu + X_{\dot{u}}u & 0 \end{bmatrix} \tag{2.81}$$

$$D = -\begin{bmatrix} X_u & 0 & 0 \\ 0 & Y_v & Y_r \\ 0 & N_v & N_r \end{bmatrix} \tag{2.82}$$

$$D_n(v) = -\begin{bmatrix} X_{|u|u}|u| & 0 & 0 \\ 0 & Y_{|v|v}|v| + Y_{|r|v}|r| & Y_{|v|r}|v| \\ 0 & N_{|v|v}|v| + N_{|r|v}|r| & N_{|v|r}|v| + N_{|r|v}|r| \end{bmatrix} \tag{2.83}$$

The propulsion force and moment vector τ, the environmental disturbance vector τ_E, and the cable force and moment τ_{C1} are given by

$$\tau = \begin{bmatrix} \tau_u \\ \tau_v \\ \tau_r \end{bmatrix} \tag{2.84}$$

$$\tau_E = \begin{bmatrix} \tau_{uE} \\ \tau_{vE} \\ \tau_{rE} \end{bmatrix} \tag{2.85}$$

$$\tau_{C1} = \begin{bmatrix} \tau_{uC1} \\ \tau_{vC1} \\ \tau_{rC1} \end{bmatrix} \tag{2.86}$$

where, τ_u , τ_{uE} and τ_{uC1} are forces acting in surge, τ_v , τ_{vE} and τ_{vC1} sway, and τ_r , τ_{rE} and τ_{rC1} is moment acting in yaw, respectively.

2.8 Configuration of Thrusters

The USV to control its 3DOF motion has three thrusters i.e., the two stern thrusters and the bow one, to create the forces applied to counteract the environmental forces. Fig. 2.6 shows the configuration of thrusters.

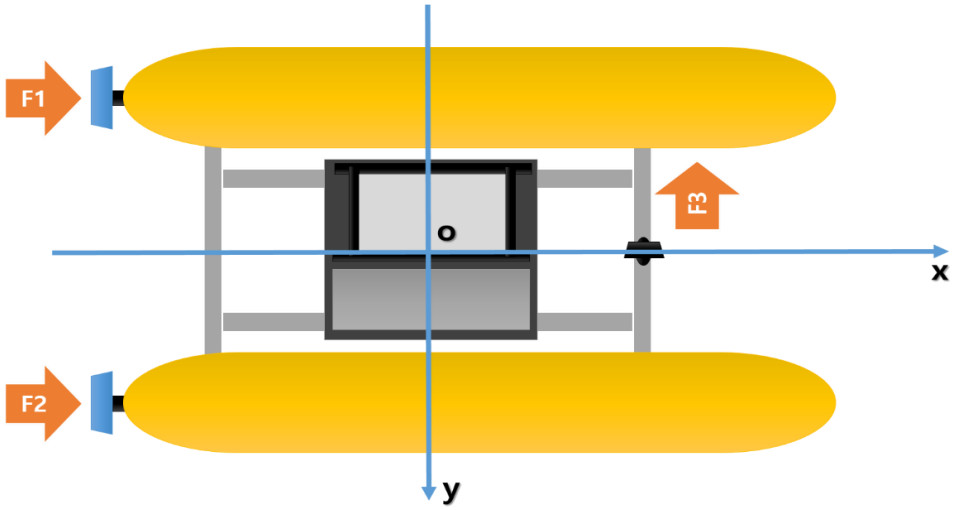

Fig. 2.6 Top view for the thruster arrangement of USV.

Based on the revolution speeds n_i, the thrust forces can be calculated by:

$$T_i = \rho n_i^2 D_P^4 K_T \tag{2.87}$$

where n=RPS, ρ , D_P and K_T are the water density, the propeller diameter and thrust coefficient, respectively. Then the thruster allocation can be obtained by:

$$\tau_c = \mathbf{T} \cdot F_T \tag{2.88}$$

$$\tau_c = \begin{bmatrix} F_x & F_y & M_z \end{bmatrix}^T \tag{2.89}$$

$$F_T = \begin{bmatrix} F_1 & F_2 & F_3 \end{bmatrix}^T \tag{2.90}$$

$$T = \begin{bmatrix} 1-t_p & 1-t_p & 0 \\ 0 & 0 & 1-t_p \\ (1-t_p)\dfrac{RB}{2} & -(1-t_p)\dfrac{RB}{2} & (1-t_p)\dfrac{RL}{2} \end{bmatrix} \tag{2.91}$$

where τ_c is the control forces and moments vector acting on the vehicle due to eight thrusters and F_T is the thrust vector; T is the thruster configuration matrix, t_p (=0.06) is the thrust deduction coefficient, d is the draft; RB (= *5 m*) is the distance between two forward stern thrusters, and RL (= *15.24 m*) is the distance between two port or starboard thrusters.

2.9 General Structure and Model Parameters

2.9.1 Structure of USV

The USV is designed to have three propellers to control yaw, sway, and surge motion. Two propellers is mounted horizontally in the direction of track and one propeller is mounted vertically to perform dynamic positioning functions. The communication between USV and operator is made up of RF and LTE, and the communication between USV and UUV is made by serial communication through tether cable.

Fig. 2.7 System structure of Hybrid System.

The structure is shown in Fig. 2.7. Use GPS to measure the position of USV, and use USBL to determine relative position between UUV and USV. In addition, real-time monitoring is possible on the ground with RF communication. The USV

consists of a main control system for position, attitude and speed control, a winch system for controlling the depth of UUV, and a communication system for data transmission/ reception and UUV control. Mechanism specification and parameters for simulation of the USV are given in Table 2.2.

Table 2.2. Mechanism specification of the USV

Classification	USV
Length	$L = 3.063\ m$
Breadth	$L = 0.633\ m$
Draft	$L = 0.201\ m$
Mass	$m = 220.4\ kg$
Z-axis inertia	$I_z = 330.49\ kgm^2$
Mass center	$x_G = -0.076m$
Propeller diameter	$D_p = 0.122m$

2.9.2 Control System of USV

The control system consists of a control system for the USV operation and a winch control system for controlling the depth of the UUV. This will be described in detail as shown in Fig. 2.8.

Fig. 2.8 The control box of control system.

The USV's control system is shown in Fig. 2.9. AHRS and GPS sensors are used to control USV position and attitude and control the path by line-of sight method.

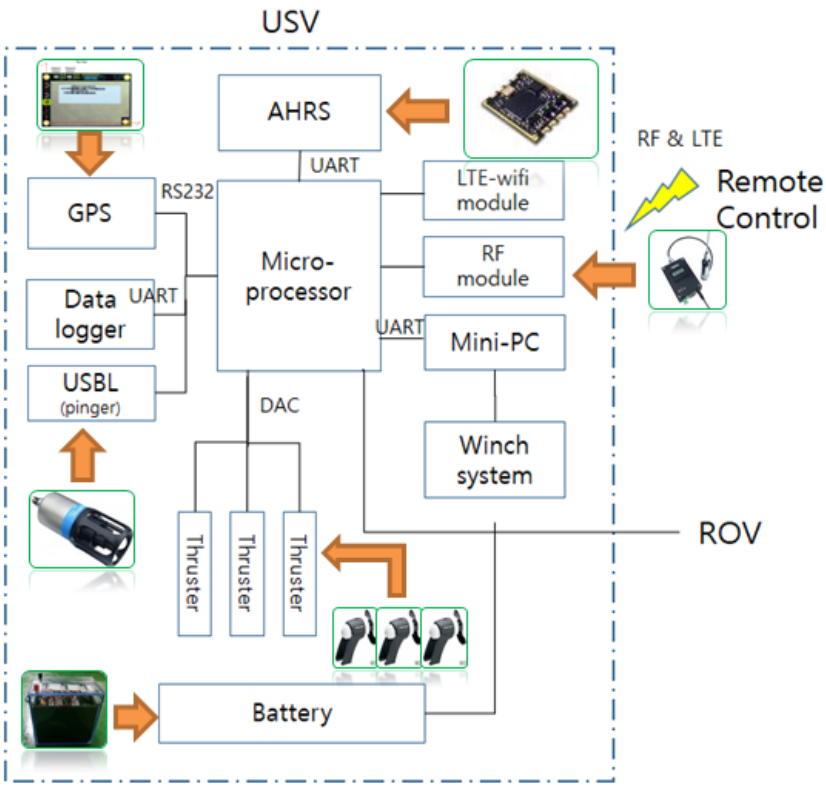

Fig. 2.9 Control system of USV.

UUV is controlled by serial communication through tether cable. Also, by installing a winch system, it is possible to control the depth of the UUV and to Launch and Recover the UUV.

The winch system was installed in USV to control the depth of UUV steadily as shown in Fig. 2.7. A tether cable is designed with stainless steel wire to withstand the tension caused by the weight and wave of UUV.

2.9.3 Winch Control System

The winch system was installed in USV to control the depth of UUV steadily. A tether cable is designed with stainless steel wire to withstand the tension caused by the weight and wave of UUV. Fig. 2.10 shows the winch control system mounted on the USV.

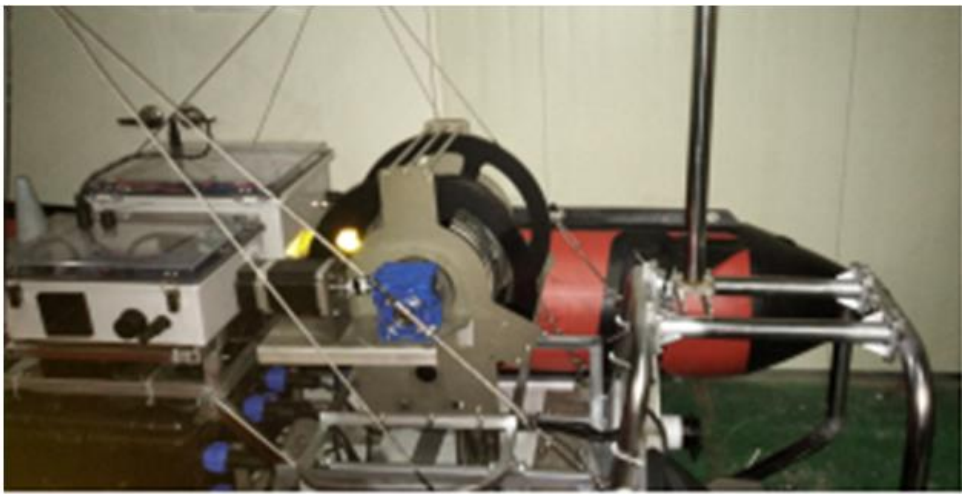

Fig. 2.10 Winch system.

The control system for driving the winch system is shown in Fig. 2.11. The main controller receives UUV depth information and controls the rotation of the winch to reach the target depth.

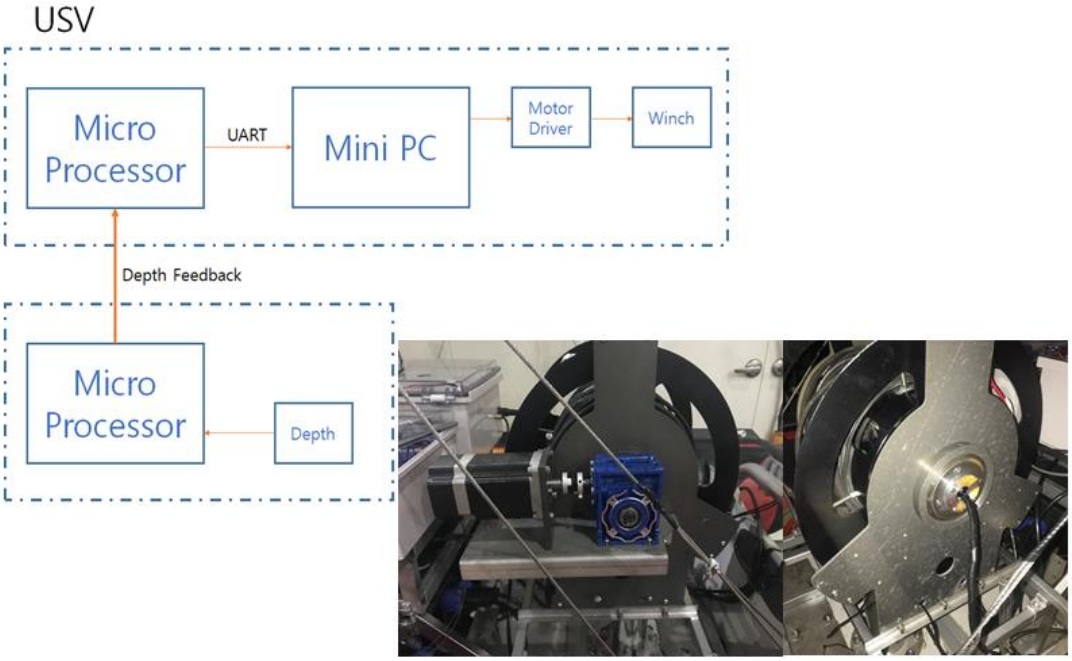

Fig. 2.11 Winch control algorithm.

Chapter 3: Mathematical Model of the Umbilical Cable (UC)

The UC plays an important role in supplying power and communication between the UV and the support vessel. However, the drag and the UC management and attachment cause some restrictions on the maneuverability of the UV. Therefore, estimation of the corresponding effect caused by the UC and the current will help our analysis of the UV's maneuvering behaviors. However, most researchers neglect the effect of the UC because of the complexity, especially regarding current effects. In this dissertation, we analyze UV dynamic affected by the UC motion.

3.1 Basic Assumptions for UC

We assume that the axial tension in the cable is small enough to allow us to operate in the linear range of stress/strain relationship. This is reasonable for metallic cables and synthetic cables under normal tension. We may consider the cable as a continuum with one Lagrangian (or material) dimension. Starting from one end of the un-stretched cable, we measure this material axis using the Lagrangian coordinate $s \in [0, L]$, where L is the cable's length. The position of the un-stretched coordinate s is by the vector $r^i(s,t)$: [0, L] $[t_0, \infty) \rightarrow R^3$. The Lagrangian coordinate $p \in [0, \infty)$ measures the stretched cable length. For an infinitesimal cable segment ds that is stretched to the length *dp*, we define the strain ε as:

$$\varepsilon = \frac{dp - ds}{ds} \tag{3.1}$$

Within the scope of this dissertation, the main underlying assumption for cables is that there is no bending, shear or torsional stiffness, and this is denoted as an ideal cable.

Definition 3.1.1 (Ideal cable) An ideal cable is a slender continuum in one Lagrangian dimension where only axial stiffness is present and active in both tension and compression.

Certainly, the definition of an ideal cable will not hold for all applications. It turns out that when we keep the tension at a low level, inclusion of bending stiffness and in some cases torsional stiffness are important to describe the motion of the cable. With such properties included, the model is said to describe a physical cable.

Definition 3.1.2 (Physical cable) A physical cable is a slender continuum in one Lagrangian dimension where bending, torsional, shear and/or axial stiffness are present and active in both tension and compression.

When working with cable models, we assume that the material is isotropic. Anisotropic material properties are independent of direction by definition, and have only two independent variables (i.e. elastic constants) in their stiffness and compliance matrices. Some materials have a linear stress-strain relationship. We can describe this by Hooke's law for axial strain as:

$$\sigma = E\varepsilon \tag{3.2}$$

where, σ is axial stress, E is Young's modulus, and ε is axial strain. We may also write the axial stress as:

$$\sigma = \frac{T}{A} \tag{3.3}$$

where, T is the axial tension, and A is the cross-sectional area of the cable. Combining the equations gives the relation between axial strain and axial tension,

$$\varepsilon = \frac{T}{EA} \tag{3.4}$$

In our study, we make the following assumptions to analyze the corresponding configuration and tension of the UC attached to the UV:

(1) The UC is continuous, inextensible, and flexible.

(2) The UC is affected by axial tension force, but bending stiffness, shear, and torsional stiffness is neglected.

(3) The UC is not very long cable (L<300m) and the length of the UC is constant L=100m.

(4) The cross-sectional area of the UC, A, will not undergo significant changes due to axial deformation of the UC.

(5) The forces acting on the UC are the self-weight, buoyancy, tension force, and the hydrodynamic force on the UC due to uniform current effect that can be resolved into a tangential component and a normal component.

(6) Furthermore, the water flow velocity is uniform along the cable while the effect of wave on the UC is neglected in this study.

Assumption (1) can be justified since the cable with high Young's modulus E will not stretch appreciably so the tension remains moderate and has relatively high axial stiffness. Therefore, we consider the tether as inextensible. Besides, for most applications, we assume that the submarine cable is continuous in the analysis and flexible because bending stiffness is neglectful. Assumption (2) is in line with assumption (1) because we neglect bending stiffness in the model due to the extreme flexibility of the cable. This is reasonable for cable which has both curvature and its derivative with respect to the arc length are small. Consequently, it is very reasonable to neglect the bending stiffness, shear, and torsional stiffness. Assumption (3) means that the cable length is fixed at the value L =100 m. So that in this case, the UV speed needs to maintain a suitable distance between the support vessel and a UV during maneuvering. Assumption (4) is a direct consequence of assumption (1) because we assume the cable to be inextensible, which also means the cross section of the cable does not change due to Poisson ratio effects. Assumption (5) is made because the cable has a small diameter, thin and, therefore, the fluid loading is drag dominated. Assumption (6) is made in order to decrease implementation complexity and computation time.

3.2 Analysis on Forces of UV

When we suspend the UC between support vessel and UV, there are at least four components that contribute to the tensional forces along the submarine cable:

- Gravity forces, which is due to submarine cable self-weight;
- Buoyancy force, which is equal to the weight of its dis-placed fluid;
- Drag forces, which are due to steady current and current profile;
- Residual bottom tension, which translates to an extra tensional force during the laying operations.

We also convert these forces to concentrated loads at the nodes. Also, we calculate the hydrodynamic forces at the element centroid and assume constant along the element. There is no Froude-Kriloff force acting on the cable as we assume that the fluid medium is at constant velocity and the effects of wave kinematics on the cable's global configuration are negligible.

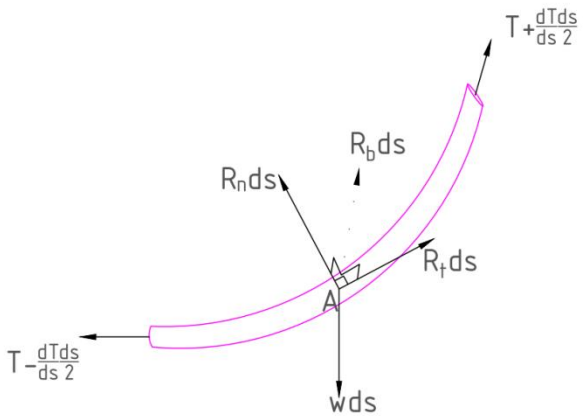

Fig. 3.1 Forces acting on a segment of a UC profile.

Considering a cable infinitesimal element, Fig. 3.1 shows UC equilibrium state. We denote the cable's weight per unit length in air is $w_a = mg$, where, g is the acceleration gravity, and m is the mass per length unit. When the cable is submerged a hydrostatic force will appear according to:

$$B = \rho_w g A \tag{3.5}$$

where, ρ_w is the density of water and A is the cross-sectional area.

This leads to the following definition of the stretched cable's weight in water w_1:

$$w_1 = w_a - B \tag{3.6}$$

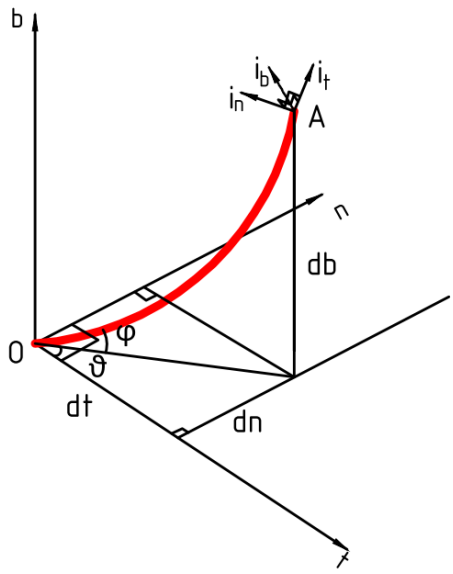

Fig. 3.2 Coordinate system for the UC.

Fig. 3.2 shows the coordinate system for analyzing the UC. The origin O coincides with the end point of the UC. ϑ is the angle between the tOb plane, and the plane that includes the tangential line passing through point A that is perpendicular to the tOn plane. φ is the angle between the tangential line passing through the point A and the tOn plane. i_t, i_b, and i_n are the unit vectors along s, ϑ, and φ, respectively, and are perpendicular to each other. i_t and i_n are located on the vertical plane.

Fig. 3.1 shows the current acting on a small UC element dp. The drag force has two components, namely, the normal drag force R_n, and the tangential drag force R_t as follows:

$$R_n = \frac{1}{2}\rho t C_n V^2 \sin\psi_c \left|\sin\psi_c\right| \tag{3.7}$$

$$R_t = \frac{1}{2}\rho t C_f V^2 \cos\psi_c \left|\cos\psi_c\right| \tag{3.8}$$

where, ρ is the water density, t is the diameter of the UC, C_n is the normal drag coefficient, C_f is the tangential drag coefficient, V is the current velocity relative to the UC, ψ_c is the angle between current and the UC. R_t, R_ϑ, and R_φ are the fluid force per unit length along i_t, i_b, and i_n directions, respectively and their respective formulas are shown below:

$$R_\varphi = R_{nx}\cos\vartheta\cos(\varphi+\frac{\pi}{2}) + R_{ny}\sin\vartheta\sin(\varphi+\frac{\pi}{2}) + R_{nz}\sin(\varphi+\frac{\pi}{2}) \tag{3.9}$$

$$R_t = \frac{1}{2}\rho t\pi C_f V^2 \cos\psi_c \left|\cos\psi_c\right| \tag{3.10}$$

$$R_\vartheta = R_{nx}\cos(\vartheta+\frac{\pi}{2}) + R_{ny}\sin(\vartheta+\frac{\pi}{2}) \tag{3.11}$$

in which,

$$R_{nx} = R_n\cos(\psi_c - \frac{\pi}{2}) \tag{3.12}$$

$$R_{ny} = R_n\sin(\psi_c - \frac{\pi}{2})\cos\gamma \tag{3.13}$$

$$R_{nz} = R_n\sin(\psi_c - \frac{\pi}{2})\sin\gamma \tag{3.14}$$

where, γ is the angle between the tOn plane and the plane composed of i_t direction and current direction. We assume the direction of the current to be along

the t-axis. We can express the relationship between all the angles of the UC system frame as:

$$\cos\psi_c = \cos\varphi \times \cos\vartheta \tag{3.15}$$

$$\tan\gamma = \frac{\tan\varphi}{\sin\vartheta} \tag{3.16}$$

As the cable moves in water, large hydrodynamic forces are generated resisting motion to prevent lines from reaching the instantaneous static-catenary configuration. The value of the drag coefficient can affect the computational dynamic tension of the cable. The tension T acts along the tangent of the average cable configuration, where we define the average cable configuration as the smoothest profile of the cable**.** Given a cable tension, T_c, Triantafyllou [55] shows that the effective tension, T_e may be written as:

$$T_e = T_c + p_e A \tag{3.17}$$

where, p_e is the hydrostatic pressure at the specific point of the cable.

3.3 Relation for UC Equilibrium

Considering the configuration of the UC shown in Fig. 3.2, we can obtain the following three linear differential equations:

$$dt = ds \times \cos\varphi \times \cos\vartheta \tag{3.18}$$

$$dn = ds \times \cos\varphi \times \sin\vartheta \tag{3.19}$$

$$db = ds \times \sin\varphi \tag{3.20}$$

Considering the equilibrium state of the external force on the UC shown in Figs. 3.1 and 3.2, we can obtain more three linear differential equations:

By balancing the forces of direction of i_t, a UC segment, we have:

$$R_t ds - w\sin\varphi ds + (T + \frac{dT}{2})\cos(\frac{1}{2}\frac{d\varphi}{ds}ds)\cos(\frac{1}{2}\frac{d\vartheta}{ds}ds) - (T - \frac{dT}{2})\cos(\frac{1}{2}\frac{d\varphi}{ds}ds)\cos(\frac{1}{2}\frac{d\vartheta}{ds}ds) = 0 \tag{3.21}$$

Alternatively, Eq. (3.21) becomes:

$$dT = w\sin\varphi ds - R_t ds \tag{3.22}$$

By balancing the forces of direction of i_b, a UC segment, we have:

$$R_\vartheta ds + (T + \frac{dT}{2})\sin\frac{d\vartheta}{2}\cos(\varphi + \frac{d\varphi}{2}) + (T - \frac{dT}{2})\sin\frac{d\vartheta}{2}\cos(\varphi - \frac{d\varphi}{2}) = 0 \tag{3.23}$$

Assuming $\sin\frac{d\vartheta}{2} \approx \frac{d\vartheta}{2}$ and $\cos\frac{d\vartheta}{2} \approx 1$, we can rewrite Eq. (3.23) as follows:

$$d\vartheta = -\frac{R_\vartheta ds}{T\cos\varphi} \tag{3.24}$$

By balancing the forces of direction of i_n, a UC segment, we have:

$$d\varphi = \frac{(-R_\varphi ds + w\cos\varphi ds)}{T} \tag{3.25}$$

Finally, from Eq. (3.18)-(3.20), Eq. (3.22), Eq. (3.24) and Eq. (3.25), we can obtain the full linear differential equations of the UC as follows:

$$\frac{dt}{ds} = \cos\varphi \times \cos\vartheta \tag{3.26}$$

$$\frac{dn}{ds} = \cos\varphi \times \sin\vartheta \tag{3.27}$$

$$\frac{db}{ds} = \sin\varphi \tag{3.28}$$

$$\frac{dT}{ds} = w\sin\varphi - R_t \tag{3.29}$$

$$\frac{d\vartheta}{ds} = -\frac{R_\vartheta}{T\cos\varphi} \tag{3.30}$$

$$\frac{d\varphi}{ds} = \frac{(-R_\varphi + w\cos\varphi)}{T} \tag{3.31}$$

where, s is the arc length from the origin to the point A on the UC, T is the tension force along the UC, w is the weight of the UC per unit length in water. R_t, R_ϑ, and R_φ are the fluid force per unit length along i_t, i_b, and i_n directions, respectively.

Since Eqs. (3.26)-(3.31) are a set of first order ordinary differential equations with two-end boundary value problem, it is rather difficult to solve the solution. Here, based on the direct search method, we apply a multi-step shooting method which uses the catenary equations to solve this problem, and the method is described as below (Section 3.4).

3.4 Catenary Equation in the Space Case

In this section, we present a detailed procedure for finding the general elastic catenary equations in space. We compute the UC forces in space by the method reported by Sagatun [56], which uses the catenary equations with end forces estimates. Consider a UC of length L with one end fixed in space, and the other end free. The UC may have varying axial stiffness EA along its length. Moreover, divide the UC into *n* equal length elements, and propagate the result of one element

into the next, till it reaches the end point of the UV. The force vector f_0 represents the reaction forces from the UC on its termination point. The force vector f_i represents a concentrated force acting on an arbitrary point i along the UC, and the distributed load vector p_i force per unit length acts on the UC segment between points i and i-1. The result of the proposed method is an analytical piecewise continuous static solution of the form $F(s)=\begin{bmatrix} F_x & F_y & F_z \end{bmatrix}^T$, where, the symbol s represents the Lagrangian coordinate along the unstrained UC, and F is the local forces in X, Y, Z within the UC's element. Considering the UC with unidimensional strain along the Lagrangian variable s, Hooke's law is:

$$T = EA\left(\frac{dp}{ds}-1\right) \tag{3.32}$$

Seeking a solution in Cartesian coordinates of the UC as a function of s, the identity $\frac{dF}{ds}=\frac{dF}{dp}\frac{dp}{ds}$ will be useful. This leads to the relation:

$$\frac{dF}{ds}=\frac{dF}{dp}\left(\frac{T}{EA}+1\right) \tag{3.33}$$

Assume that the UC terminates in point 0, the concentrated forces f_i may act as discrete points (cable nodes), and there exists axial tension T in the end point. We have the following equation for the forces acting on the UC's terminating point:

$$f_o = T\left.\frac{dr}{dp}\right|_{s=L} + \sum_{i=1}^{n}\overline{f}_i + wL \tag{3.34}$$

where, $\{s\in[0,L]\rightarrow R, k\in[1,n]\rightarrow N \,|\, s\in[s_{k-1},s_k]\}$. n is the number of the UC segments, and L is the UC's un-stretched length. $w=\begin{bmatrix} w_x & w_y & w_z \end{bmatrix}^T$ indicates the constantly distributed force along the UC.

We want to find the tension vector as a function of s. Moreover, the following relation must hold:

$$T\frac{dF}{dp}(s) = f_o - \sum_{i=1}^{k}\overline{f}_i - ws \tag{3.35}$$

where, $\{s\in[0,L]\rightarrow R, k\in[1,n]\rightarrow N \,|\, s\in[s_{k-1},s_k]\}$. We define:

$$T(p) = T\frac{dF}{dp} \tag{3.36}$$

where, $T \in R^3, F = \begin{bmatrix} F_x & F_y & F_z \end{bmatrix}^T$. The substitution is:

$$f_k = f_0 - \sum_{i=1}^{k} \overline{f_i} \tag{3.37}$$

where, $\{k \in [0,n] \to N, s \in [1,L] \to R | s \in [s_{k-1}, s_k]\}$. We also have:

$$T_s = \sqrt{(f_k - ws)^T (f_k - ws)} \tag{3.38}$$

By Eq. (3.33), we obtain:

$$T \frac{dF}{dp}(s) = \left(\frac{1}{EA} + \frac{1}{T} \right)^{-1} \frac{dF}{ds} = f_k - ws \tag{3.39}$$

Reordering and substituting Eq. (3.38) gives the final differential equation as:

$$\frac{dF}{ds} = (f_k - ps) \left(\frac{1}{\sqrt{(f_k - ps)^T (f_k - ps)}} + \frac{1}{EA} \right) \tag{3.40}$$

where, k is the actual UC segment, s is the distance in m, EA is the axial stiffness of the UC in N, p is the weight per length of the UC in N/m, f_k is the force exerted on the UC's element i in N, and F is the local forces in X, Y, Z within the UC's element i. By integration of Eq. (3.40), we can obtain the resulting force F, which is an expression for the local solution within segment k of the end point of the UC. We use the differential equation derived in Eq. (3.40) to solve the forces at each element. We solve it numerically using the Matlab routine. Note that even if the initial guess for the estimated force deviates from the correct value, the routine can still find a good estimate.

While we could have utilized numerical methods to solve the ordinary differential equations (ODE)/ initial value problems (IVP), Sagatun [56] gives the following solution:

$$\begin{aligned} F_k(s) = {} & \frac{\alpha(s)}{\beta^3}(f_k \beta^2 - f_k \otimes w \otimes w - f_k \otimes (P(f_k \otimes w))) - w \frac{1}{\beta^2} \sqrt{(f_k - ws)^T (f_k - ws)} \\ & + \frac{1}{EA}\left(f_k s - \frac{1}{2} w s^2 \right) + C_i \end{aligned} \tag{3.41}$$

where, $\otimes$ denotes component-wise multiplication, and:

$$\beta = \sqrt{w^T w} = \|w\|_2, \alpha = \ln\left(\left(\beta s - \frac{1}{\beta} f_k^T w \right) + \sqrt{(f_k - ws)^T (f_k - ws)} \right), P = \begin{bmatrix} 0 & 1 & 1 \\ 1 & 0 & 1 \\ 1 & 1 & 0 \end{bmatrix}$$

Assume that we want segment no.1 of the global solution F(s) to start in the origin. We also want to ensure continuity between the segments. The following conditions should be fulfilled:

$$\begin{aligned} &F(0)=0, \\ &F(s_i)^- = F(s_i)^+, \{i \in [1, n-1] \to N\} \end{aligned} \tag{3.42}$$

We may calculate the integration constants, $C_i, i \in [0, n-1]$ from:

$$C_{k-1} = \begin{cases} -F_1(0), & for \quad k=1 \\ F_{k-1}(s_{k-1}) - F_k(s_{k-1}), & for \quad k \in [2,n] \to N, \quad for \quad n \geq 2 \end{cases} \tag{3.43}$$

If s belongs to a segment with the index higher than 1, we must calculate C_{k-1} iteratively before we can find the solution of F(s). We can now calculate the final global solution from:

$$\begin{aligned} F(s) = &\frac{\alpha(s)}{\beta^3}(f_k\beta^2 - f_k \otimes w \otimes w - f_k \otimes (P(f_k \otimes w))) - w\frac{1}{\beta^2}\sqrt{(f_k - ws)^T (f_k - ws)} \\ &+ \frac{1}{EA}\left(f_k s - \frac{1}{2}ws^2\right) + C_{k-1}, \end{aligned} \tag{3.44}$$

where, $\{s \in [0, L] \to R, k \in [1, n] \to N | s \in [s_{k-1}, s_k]\}$

Notice that the solution in Eq. (3.44) collapses into a simple Lagrangian catenary solution for constant axial stiffness, when the distributed load is constant and no concentrated loads are acting on the cable [56]. However, in our study, we consider the forces acting on cable including the distributed load and concentrated force as well. We assume that we have considered catenaries as a cable with known properties and known loads. The goal is to achieve a solution for the end point. To find the force components when the two end points are known, the governing differential equations are still known, see Eq. (3.40). We now change the problem from an ODE/IVP to an ODE/BVP (Boundary Value Problems) and can find an analytical solution to this problem if f_k is solved from Eq. (3.40). However, the analytical solution is not obtained yet, and we try numerical approach for the problem.

Sometimes other problems arise when we are dealing with boundary value problems. We may for instance know the boundary coordinates, but want to find the end force to yield this solution. The ODE/BVP has now applied to include an estimation of the parameter $\overline{f_1}$. We can apply a shooting method based on the accurate analytical solution to compute the static equilibrium configuration of the single composite cable with the boundary conditions specified at both ends.

Mathematically the problem is a two-point BVP. If we specify all boundary conditions at one end, the configuration is uniquely determined. We can find this reduces the problem to an IVP and the static configuration by catenary computations, element by element, starting at the end with all specified boundary conditions. In this study, we use Matlab's routine to estimate this force.

3.5 Shooting Method

We define the cable as a constant length L_0 and suspend between two fixed supports at support vessel and UV, which are Cartesian coordinates (0, 0, 0) m and (x_L, y_L, z_L) respectively. We apply guessed end force at its one end. With minor changes, we can solve this problem using the shooting method. The shooting method takes the boundary values at one end as initial values and solves the problem as an IVP. If the solution does not satisfy the boundary values at the other end, we should do a tuning of the initial values or some other parameters of the system before another "shot" from the first end is performed. In this way an iterative approach may solve the problem. Matlab provides a routine for two-point BVP. The shooting method shows promise as a robust solver, even when we supply bad initial guesses [57].

We adopt the shooting method for solution of two-point BVP for composite lines in the following main steps:

Step 1: Guess (estimate) start values of unknown boundary conditions at 1st end.

Step 2: Compute configuration, element by element starting at 1st end.

Step 3: Compare computed boundary conditions at 2nd end with specified values.

Step 4: If result is satisfactory go to Step 6.

Step 5: Compute improved estimate of unknown boundary conditions at 1st end. Go to Step 2.

Step 6: Computations completed.

This approach reflects the basic principle of the shooting methods: iterative correction of unknown boundary conditions at 1st end to satisfy specified boundary conditions at 2nd end by repeated solution of the IVP (Step 2).

In the case of no current loading, we can solve the IVP using catenary equilibrium calculations, segment by segment, which will give the exact catenary solution with a minimum of computational effort. We can find an approximate

solution of the IVP when current loading is present. Each segment is in this case subdivided into elements to obtain an adequate representation of the current loading. Then, we can solve the initial problem by application of catenary equilibrium calculations element by element assuming constant current loading in tangential and normal chord directions for each element, see Fig. 3.3. We find the static configuration of each element by application of the catenary equations in space where the local z-axis is opposite to the resulting load vector governed by weight, buoyancy and drag forces. Then, we transform local force components and coordinates to the global system by standard rules for transformation. Finally, we need an iterative approach since the chord direction is not known prior to the catenary computations.

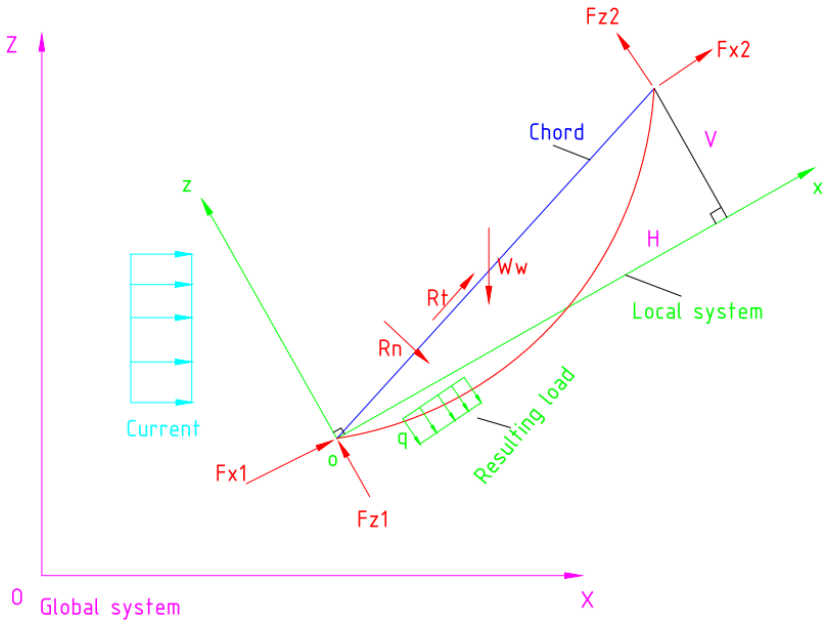

Fig. 3.3 Catenary calculations in local system.

Direction of local z-axis is opposite to resulting load direction governed by weight and buoyancy, W_w, and drag loads tangential and normal to the cable chord denoted R_t^h and R_n^h, respectively. We use the following recalculation procedure for calculation of current loading for each element (see Fig. 3.3).

(1) Assume that the initial chord direction is equal to the direction of the cable tension at 1st element end.

(2) Compute the drag forces based on current estimate of the chord direction.

(3) Compute coordinates, forces and updated chord direction by use of the catenary equations.

(4) If the change in the chord direction is "small" then stop, solution is accepted.

Otherwise, go to 2.

3.6 Boundary Conditions

In establishing the mathematical formulation of the complete system UV and UC, governing equation for UC is given first (see Eq. (3.40)), we take the kinematic condition at the up end of cable above water surface and the dynamic equations of underwater robot conjunct with the lower end of cable as the boundary conditions for the governing equations of the UC. After determining the boundary conditions at the both ends of the UC, we can establish the governing equations for the tethered UV system. Different types of boundary conditions may occur depending on the types of physical conditions at the two ends. Usually, we consider three boundary conditions for an ideal cable. These are:

- FREE-FREE boundary conditions: Both ends of the cable are free and possibly influenced of external end forces.
- FIXED-FREE boundary conditions: We fix one end of the cable, or at a prescribed point in time, and the other is free or influenced by an external force.
- FIXED-FIXED boundary conditions: We fix both ends of the cable, or at a prescribed point in time.

Because bending stiffness is not present for an ideal cable, a fixed boundary condition means that the boundary is pinned. Although different authors use different boundary conditions, probably the most natural set of conditions for catenary equation problems are the positions of both ends of the UC. In the present case, we place boundary conditions at both ends of the UC (upper end and lower end). With one end of the cable attached to the support vessel, we connect the other end to moving UV which has its own propulsion control system. For a controller design, we will assume that we design a dynamic positioning (DP) system for the support vessel. Further, we can assume in analysis that the DP system is perfect such that we can ignore the support vessel-induced motion, so the first boundary condition is given by fixing the position of the support vessel. At the lower end, the UC is connected to the UV. So, the second boundary condition of lower end of the UC $X_0 = X_0(t)$ is given as a function of time. We can express these two conditions as follows:

$$x_0(0,t) = 0\,,\ y_0(0,t) = 0\,,\ z_0(0,t) = 0\,, \tag{3.45}$$

$$\text{and } x_L(L,t) = x_L\,,\ y_L(L,t) = y_L\,,\ z_L(L,t) = z_L \tag{3.46}$$

where, x_L, y_L, and z_L denote the position of the UV during its motion.

3.7 Cable Effects

The tension of the UC at the two-point, i.e., T results in additional forces and moments that affect the motion of the UV. The components of the tension force with respect to the earth-fixed coordinate system X-axis, Y-axis, and Z-axis are:

$$T_E(t) = \begin{bmatrix} T_{Ex} \\ T_{Ey} \\ T_{Ez} \end{bmatrix} = -W(\vartheta, \varphi) \begin{bmatrix} T \\ 0 \\ 0 \end{bmatrix} = \begin{bmatrix} -T \times \cos\varphi \times \cos\vartheta \\ T \times \cos\varphi \times \sin\vartheta \\ T \times \sin\varphi \end{bmatrix} \tag{3.47}$$

Thus, we can obtain the UC forces by expressing the UC tension in the vehicle-fixed frame.

$$F_c(t) = \begin{bmatrix} F_{cX} \\ F_{cY} \\ F_{cZ} \end{bmatrix} = R^T(\phi, \theta, \psi) \begin{bmatrix} T_{Ex} \\ T_{Ey} \\ T_{Ez} \end{bmatrix} \tag{3.48}$$

Where,

$$F_{cX} = T(\cos\psi\cos\theta\cos\vartheta\cos\varphi - \sin\psi\cos\theta\sin\vartheta\cos\varphi + \sin\theta\sin\varphi) \tag{3.49}$$

$$\begin{aligned} F_{cY} = T(&-\cos\theta\sin\phi\sin\varphi + \sin\phi\cos\psi\sin\theta\cos\vartheta\cos\varphi - \sin\phi\sin\psi\sin\theta\sin\vartheta\cos\varphi \\ &-\cos\psi\cos\phi\sin\vartheta\cos\varphi - \sin\psi\cos\phi\cos\vartheta\cos\varphi) \end{aligned} \tag{3.50}$$

$$\begin{aligned} F_{cZ} = T(&-\cos\theta\cos\phi\sin\varphi + \sin\phi\sin\psi\cos\vartheta\cos\varphi + \sin\phi\cos\psi\sin\vartheta\cos\varphi \\ &+\cos\psi\sin\theta\cos\phi\cos\vartheta\cos\varphi - \sin\psi\sin\theta\cos\phi\cos\vartheta\cos\varphi) \end{aligned} \tag{3.51}$$

In terms of the position of the tow-point in the vehicle-fixed frame, the UC which induced moments are:

$$M_c(t) = \begin{bmatrix} M_{cX} \\ M_{cY} \\ M_{cZ} \end{bmatrix} = r_c \times F_c(t) = \begin{bmatrix} x_c \\ y_c \\ z_c \end{bmatrix} \times \begin{bmatrix} F_{cX} \\ F_{cY} \\ F_{cZ} \end{bmatrix} = \begin{bmatrix} y_c F_{cZ} - z_c F_{cY} \\ z_c F_{cX} - x_c F_{cZ} \\ x_c F_{cY} - y_c F_{cX} \end{bmatrix} \tag{3.52}$$

in which,

$$\begin{aligned} M_{cX} = y_c T(&-\cos\theta\cos\phi\sin\varphi + \sin\phi\sin\psi\cos\vartheta\cos\varphi + \sin\phi\cos\psi\sin\vartheta\cos\varphi \\ &+\cos\psi\sin\theta\cos\phi\cos\vartheta\cos\varphi - \sin\psi\sin\theta\cos\phi\cos\vartheta\cos\varphi) \\ -z_c T(&-\cos\theta\sin\phi\sin\varphi + \sin\phi\cos\psi\sin\theta\cos\vartheta\cos\varphi - \sin\phi\sin\psi\sin\theta\sin\vartheta\cos\varphi \\ &-\cos\psi\cos\phi\sin\vartheta\cos\varphi - \sin\psi\cos\phi\cos\vartheta\cos\varphi) \end{aligned} \tag{3.53}$$

$$\begin{aligned} M_{cY} = z_c T(&\cos\psi\cos\theta\cos\vartheta\cos\varphi - \sin\psi\cos\theta\sin\vartheta\cos\varphi + \sin\theta\sin\varphi) \\ -x_c T(&-\cos\theta\cos\phi\sin\varphi + \sin\phi\sin\psi\cos\vartheta\cos\varphi + \sin\phi\cos\psi\sin\vartheta\cos\varphi \\ &+\cos\psi\sin\theta\cos\phi\cos\vartheta\cos\varphi - \sin\psi\sin\theta\cos\phi\cos\vartheta\cos\varphi) \end{aligned} \tag{3.54}$$

$$
\begin{aligned}
M_{cZ} = {} & x_c T(-\cos\theta\sin\phi\sin\varphi + \sin\phi\cos\psi\sin\theta\cos\vartheta\cos\varphi - \sin\phi\sin\psi\sin\theta\sin\vartheta\cos\varphi \\
& -\cos\psi\cos\phi\sin\vartheta\cos\varphi - \sin\psi\cos\phi\cos\vartheta\cos\varphi) \\
& -y_c T(\cos\psi\cos\theta\cos\vartheta\cos\varphi - \sin\psi\cos\theta\sin\vartheta\cos\varphi + \sin\theta\sin\varphi)
\end{aligned}
\tag{3.55}
$$

and $\vec{r_c} = \left(x_c, y_c, z_c\right)$ is the vector from the center of gravity of the UV to the connected point between the UC and the UV.

3.8 Model Parameters and Simulation

To this point we have considered catenaries as a cable with known properties and known loads. The goal has been to achieve a solution for the end point. Let us revert this and try to find the force components when the two end points are known. The governing differential equations are still known, see Eq. (3.40). The problem has now changed from an ODE (Ordinary Differential Equations)/IVP (Initial Value Problems) to an ODE/BVP (Boundary Value Problems). An analytical solution to this problem could be found if f_k was solved from Eq. (3.40). Nobody has published such analytical solution, and we will have to deal with numerical solutions of the problem. The MATLAB's function bvp4c or e.g. a finite element solution will do if the cable's geometry is of particular interest.

Sometimes other problems arise when we are dealing with boundary value problems. We may for instance know the boundary coordinates, but want to find the end force to yield this solution. The ODE/BVP has now increased to include an estimation of the parameter $\overline{f_1}$. A shooting method based on the accurate analytical solution might be applied. Shooting method is used to compute the static equilibrium configuration of a composite single cable with boundary conditions specified at both ends. Mathematically the problem is a two point boundary value problem. If all boundary conditions are specified at one end, the configuration is uniquely determined. This reduces the problem to an initial value problem and the static configuration can be found by catenary computations, element by element, starting at the end with all boundary conditions specified.

We will now give an example where we use MATLAB's routine to estimate this force. A cable of length 100 meters is fastened in $\begin{bmatrix}0 & 0 & 0\end{bmatrix}$.The UC is divided into 100 equal length elements and the result from one element is propagated into next till it reaches the final end point at the UV. The initial guess for the forces in N is $\begin{bmatrix}4 & 5 & 180\end{bmatrix}^T$, cable's length is 100m, cable's weight is $W_c = -0.5N/m$, diameter $d_c = 0.025m$, modulus of elasticity $E_c = 200\times10^9 N/m^2$, axial stiffness $EA = 3\times10^4 N$ and density $\rho_c = 662.2kg/m^3$.The inertial reference

frame (X, Y, Z) is defined at surface of waterline and the first cable's element is attached to the supported vessel. The UC forces in three-dimensional (3D) are computed by the method in Sagatun [56] that uses Catenary equations with end forces estimates. MATLAB's routine bvp4c was applied to these parameters, and an estimate of the end force was found. The results are shown in Figs. 3.5 and 3.6. Even if the initial guess for the estimated force deviated from the correct value, the routine managed to find very good estimates. The results were dependent on the numerical option and the mesh in the variable s. The UC's parameters for simulation are shown in Table 3.1. Fig. 3.4 shows profile of 3-D forces acting on the UC.

Table 3.1. UC's parameters for simulation

Cable parameters	
Length of cable (m)	L=100
3-D forces on cable (N/m)	$W = [3 \quad 3 \quad -5]$
Diameter of cable (m)	$d = 0.025$
Axial stiffness (N)	$EA = 3.10^4$
Position of end point (calculated from equation) (m)	$E_p = [86.4 \quad 0 \quad -45.42]$
Guess for end force (N)	$F_g = [4 \quad 5 \quad 10]$

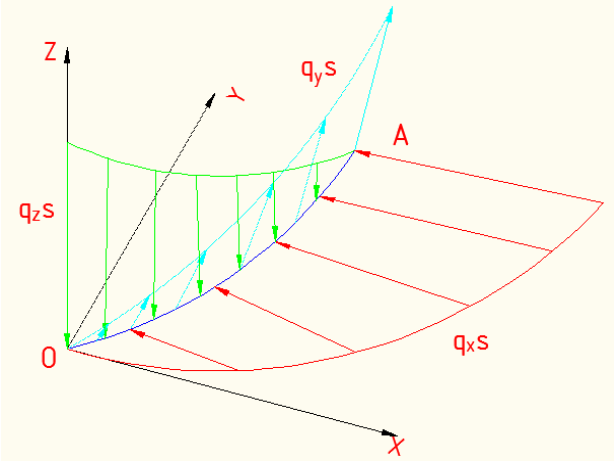

Fig. 3.4 The all forces acting on the UC.

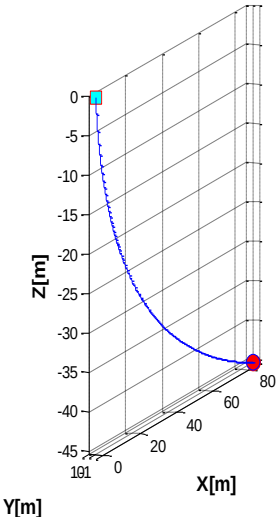

(a) Static

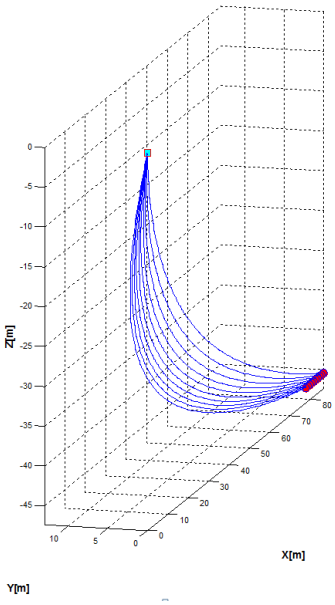

(b) Dynamic

Fig. 3.5 Static and dynamic configurations of UC.

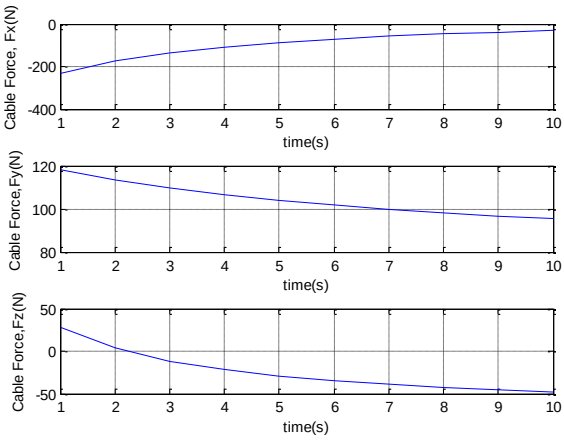

Fig. 3.6 The end point forces of UC.

Fig. 3.5(a) shows a cable of length L attached to a blue point and a red point. These points are defined as the cable supports and they are fixed in space. Here, as in the simulation, the top end or blue point is assumed to be fixed to the support ship, the bottom or red point is attached to the UV. Starting from support blue point and moving along the cable profile, each point on the cable is described by the Lagrangian coordinate s with respect to the origin. *s* is defined as the un-stretched Lagrangian coordinate. And the flow across the cable is determined by the relative velocity between UV and current. When the current is turned on, the cable is pushed to the left and during this motion, under the influence of the side current, and provided there is slack in the cable, the umbilical will form a curve. For calculating the position of the red point, Eq. (3.44) was used to determine this point and calculated value is $E_p = \begin{bmatrix} 86.4 & 0 & -45.42 \end{bmatrix} m$. Eq. (3.40) gives the end force equal $\mathrm{f}_{\mathrm{end}} = \begin{bmatrix} 230.55 & -117.94 & -27.97 \end{bmatrix}^T N$

The dynamic configuration of UC and the end point forces of cable are shown in Fig. 3.5(b) and Fig. 3.6, respectively. It is observed from Fig. 3.5(b) that the trajectory of the red point move backward for about 10m in 10 seconds because the speed of red point is 1m/s. The end point forces in 3D of UC when the red point moves backward is shown in Fig. 3.6. As we can see from this figure that the end point forces increases gradually with increasing in time in three components F_x, F_y, F_z.

Chapter 4: Mathematical Model of Underwater Vehicle (UV)

A detailed dynamics model of the AUV may be used to estimate the vehicle response in difference situations. This is particularly important for simulation studies and control system development. In this chapter, a detailed 6DOF equation of motion is developed based on the physics of an over-actuated AUV and its actuators. The dynamic study typically consists of two aspects: kinematic and kinetic. The former mainly pays attention to geometrical aspects of rigid-body that is subjected to the motion. The latter, on the other hand, analyses the forces and moments that cause the motion. These two aspects are discussed in this section.

4.1 Background

4.1.1 Basic Assumptions

Generating mathematical model of UV is very challenging because of the nature of underwater dynamics mainly due to the non-linear and coupled character of plant equations. The challenge also dues to the lack of precise model of UV dynamics and parameters, as well as the appearance of environment disturbances. It is possible to simplify the number of parameter making the certain assumption related with UV's construction. The following assertions were made for the dynamics of the UV in order to simplify the modeling. These assumptions are:

- UV is away from the free surface, walls and the bottom.
- The mass and distribution mass of the vehicle do not change during its operation.
- The UV travels at low speeds, that is, less than 2m/s.
- The UV is considered to be symmetrical about its three planes.
- The UV's degrees of freedom are decoupled.
- UV is a rigid body and is fully submerged once in water.
- Water is assumed to be ideal fluid that is incompressible, inviscid (frictionless) and irrotational.
- The earth-fixed frame of reference is inertial.

- The off-diagonal elements of the dynamic model matrices are much smaller than their counterparts.
- The hydrodynamic damping coupling is negligible at low speeds.
- Hydrodynamic coefficients are not variable.

The above assertions not only have important ramifications for the modeling of the UV, but also for its control.

4.1.2 Reference Frames

There are two coordinate systems involved in a dynamic study of an underwater vehicle (see Fig. 4.1). The first coordinate system is North-East-Down (NED) frame or NED-frame. As its name implies, this reference frame is defined relative to the surface of the Earth in a way that x-, y- and z-axis is pointing northward, eastward and downward respectively. In this reference frame, two important assumptions have been made: 1) the earth's surface is flat, and the vehicle is operating in a small area where the curvature of the earth can be ignored; 2) the reference frame is inertial such that Newton's laws still apply.

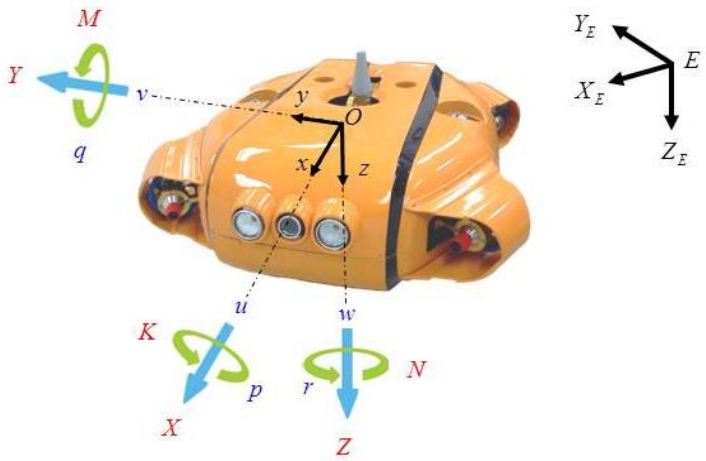

Fig. 4.1 Body-fixed and earth-fixed reference frames.

The second coordinate system is a moving reference frame that is fixed to the body of the vehicle; hence, it is called the body-fixed frame or the b-frame. In this frame, the x-axis is a longitudinal axis that directs from aft to fore, the y-axis points to starboard, and the z-axis points downwards perpendicularly to the xy-plane.

4.1.3 Notations

A vehicle state and forces acting on the vehicle are denoted according to the SNAME (1952) convention. They are summarised in Table 4.1. The position and orientation expressed in the NED-frame are:

$$\eta = \left[\eta_1^T, \eta_2^T\right]^T \in R^6 \tag{4.1}$$

where $\eta_1 = [x, y, z]^T$ denotes the vehicle's position and $\eta_2 = [\phi, \theta, \psi]^T$ denotes the vehicle's orientation. The velocities of the vehicle expressed in the b-frame are as follows:

$$\nu = \left[\nu_1^T, \nu_2^T\right]^T \in R^6 \tag{4.2}$$

where $\nu_1 = [u, v, w]^T$ denotes the translational velocities in surge, sway and heave, and $\nu_2 = [p, q, r]^T$ denotes the rotational velocities in roll, pitch and yaw, respectively.

Generalised forces and moments acting on the vehicle are defined with respect to the b-frame as follows:

$$\tau = \left[\tau_1^T, \tau_2^T\right]^T \in R^6 \tag{4.3}$$

where $\tau_1 = [X, Y, Z]^T$ corresponds to the forces along the x-, y- and z-axis, while $\tau_1 = [K, M, N]^T$ corresponds to the moments about the x-, y- and z-axis, respectively.

Table 4.1. The notation used for describing an AUV's motion (SNAME, 1952)

DOF		Forces and Moments	Linear and Angular Velocities	Position and Orientation
1	Along x-axis (surge)	X	u	x
2	Along y-axis (sway)	Y	v	y
3	Along z-axis (heave)	Z	w	z
4	About x-axis (roll)	K	p	ϕ
5	About y-axis (pitch)	M	q	θ
6	About z-axis (yaw)	N	r	ψ

4.2 Kinematics Equations

This section presents the kinematic equations relating the body-fixed reference frame to the earth-fixed reference frame.

If we define:

$$\eta = \begin{bmatrix} \eta_1^T & \eta_2^T \end{bmatrix}^T \tag{4.4}$$

$$\nu = \begin{bmatrix} \nu_1^T & \nu_2^T \end{bmatrix}^T \tag{4.5}$$

Where

$$\eta_1 = [x, y, z]^T \text{ and } \eta_2 = [\phi, \theta, \psi]^T \tag{4.6}$$

$$\nu_1 = [u, v, w]^T \text{ and } \nu_2 = [p, q, r]^T \tag{4.7}$$

where η is the position and orientation of the vehicle expressed in the earth-fixed reference frame, and ν is the linear and angular velocities of the vehicle in the body-fixed reference frame. The relation between η_1 and ν_1 is given by

$$\dot{\eta}_1 = J_1(\eta_2)\nu_1 \tag{4.8}$$

where $J_1(\eta_2)$ is a transformation matrix which is related with the Euler angles: roll (ϕ), pitch (θ) and yaw (ψ):

$$J_1(\eta_2) = \begin{bmatrix} c\psi c\theta & -s\psi c\phi + s\phi s\theta c\psi & s\psi s\phi + s\theta c\psi c\phi \\ s\psi c\theta & c\psi c\phi + s\phi s\theta s\psi & -c\psi s\phi + s\theta s\psi c\phi \\ -s\theta & s\phi c\theta & c\phi c\theta \end{bmatrix} \tag{4.9}$$

Where s(.) = sin (.) and c(.) = cos (.).

The relation between the body-fixed angular velocity vector ν_2, and the rate of change of the Euler angles η_2 is given by:

$$\dot{\eta}_2 = J_2(\eta_2)\nu_2 \tag{4.10}$$

where $J_2(\eta_2)$ is also a transformation matrix related to the Euler angles, and is expressed by:

$$J_2(\eta_2) = \begin{bmatrix} 1 & s\phi t\theta & c\phi t\theta \\ 0 & c\phi & -s\phi \\ 0 & s\phi / c\theta & c\phi / c\theta \end{bmatrix} \tag{4.11}$$

Where s(.) = sin(.) and c(.) = cos(.) and t(.) = tan(.). It is important to emphasize that $J_2(\eta_2)$ has a singularity at θ = ± 90◦. However, this does not constitute a problem for our system, because the vehicles never reach this operational point. Nonetheless, to overcome this situation, one could use a quaternion approach [59].

In conclusion we have defined the kinematic equations:

$$\dot{\eta} = \begin{bmatrix} J_1(\eta_2) & 0 \\ 0 & J_2(\eta_2) \end{bmatrix} \nu \tag{4.12}$$

4.3 Kinetic Equations

Kinetics is a study of the motions of a rigid body that is subjected to the excitation forces and moments as well as analysing the course of these excitations that may be due to hydrostatics, hydrodynamics and actuators.

4.3.1 Rigid-Body Kinetics

A dynamics model is formulated by initially focussing on how an AUV would move when it is exposed to the external excitations, τ_{RB}, without concerning of where these excitations come from. The equations of motion may be derived using the Newton-Euler formulation based on the conservation of both linear and angular momentum, or using the Lagragian formulation based on the conservation of energy [23].

This work considers only on the Newton-Euler formulation. To this end, two important assumptions must be made. First, the AUV is assumed to be a rigid body; thus, internal forces between individual elements of the AUV's mass can be omitted. Second, the NED-frame is an inertial reference frame where Newton's laws apply.

Equations for linear and angular momentum which are reformed to have the symbols comply with the notations by SNAME (1952) are recalled:

$$m\dot{\nu}_1 + m(\nu_2 \times \nu_1) + m(\dot{\nu}_2 \times r_g) + m(\nu_2 \times (\nu_2 \times r_g)) = \tau_1 \tag{4.13}$$

$$mr_g \times \dot{\nu}_1 + mr_g \times (\nu_2 \times \nu_1) + I_b\dot{\nu}_2 + \nu_2 \times I_b\nu_2 = \tau_2 \tag{4.14}$$

Where

$r_g = \vec{r}_g = \left[x_g, y_g, z_g\right]^T$: location for the centre of gravity expressed in the b-frame.

These equations may be expanded as expressed below:

$$
\begin{aligned}
&m\left[\dot{u}-vr+wq-x_G\left(q^2+r^2\right)+y_G\left(pq-\dot{r}\right)+z_G\left(pr+\dot{q}\right)\right]=X\\
&m\left[\dot{v}-wp+ur+x_G\left(pq+\dot{r}\right)-y_G\left(p^2+r^2\right)+z_G\left(qr-\dot{p}\right)\right]=Y\\
&m\left[\dot{w}-uq+vp+x_G\left(pr-\dot{q}\right)+y_G\left(qr+\dot{p}\right)-z_G\left(p^2+q^2\right)\right]=Z\\
&I_{xx}\dot{p}+\left(I_{zz}-I_{yy}\right)qr+I_{xy}\left(pr-\dot{q}\right)-I_{yz}\left(q^2-r^2\right)-I_{xz}\left(pq+\dot{r}\right)\\
&\qquad -m\left[-y_G\left(\dot{w}-uq+vp\right)+z_G\left(\dot{v}-wp+ur\right)\right]=K\\
&I_{yy}\dot{q}+\left(I_{xx}-I_{zz}\right)pr-I_{xy}\left(qr+\dot{p}\right)+I_{yz}\left(pq-\dot{r}\right)+I_{xz}\left(p^2-r^2\right)\\
&\qquad +m\left[-x_G\left(\dot{w}-uq+vp\right)+z_G\left(\dot{u}-vr+wq\right)\right]=M\\
&I_{zz}\dot{r}+\left(I_{yy}-I_{xx}\right)pq-I_{xy}\left(p^2-q^2\right)-I_{yz}\left(pr+\dot{q}\right)+I_{xz}\left(qr-\dot{p}\right)\\
&\qquad +m\left[x_G\left(\dot{v}-wp+ur\right)-y_G\left(\dot{u}-vr+wq\right)\right]=N
\end{aligned}
\tag{4.15}
$$

The cross products in Eqs. (4.13) and (4.14) may be alterred by the skew-symmetry matrix multiplications and the following is obtained:

$$m\dot{v}_1+mS(v_2)v_1-mS(r_g)\dot{v}_2-mS(v_2)S(r_g)v_2=\tau_1 \tag{4.16}$$

$$mS(r_g)\dot{v}_1+mS(r_g)S(v_2)v_1+I_b\dot{v}_2+S(v_2)I_bv_2=\tau_2 \tag{4.17}$$

By doing so, the equations of motion can be rearranged and expressed in a matrix form as follows:

$$M_{RB}\dot{v}+C_{RB}(v)v=\tau_{RB} \tag{4.18}$$

where $v=\left[v_1^T,v_2^T\right]^T$, and $M_{RB}=M_{RB}^T$ is a symmetric rigid-body inertia matrix that is unique:

$$
\begin{aligned}
M_{RB}&=\begin{bmatrix} mI_{3\times3} & -mS(r_g)\\ mS(r_g) & I_b\end{bmatrix}\\
&=\begin{bmatrix}
m & 0 & 0 & 0 & mz_g & -my_g\\
0 & m & 0 & -mz_g & 0 & mx_g\\
0 & 0 & m & my_g & -mx_g & 0\\
0 & -mz_g & my_g & I_{xx} & I_{xy} & I_{xz}\\
mz_g & 0 & -mx_g & I_{yx} & I_{yy} & I_{yz}\\
-my_g & mx_g & 0 & I_{zx} & I_{zy} & I_{zz}
\end{bmatrix}
\end{aligned}
\tag{4.19}
$$

$C_{RB}(v)$ contains the terms that involve the Coriolis vector and the centripetal vector. This matrix is not unique since it can be rearranged into many forms.

However, it is common to express this matrix such that it is skew symmetric, i.e., $C_{RB}(v) = -C_{RB}^{T}(v)$. Fossen [60] has suggested one possible form of this matrix:

$$C_{RB}(v) = \begin{bmatrix} 0_{3\times3} & -mS(v_1) - S(v_2)S(r_g) \\ -mS(v_1) - mS(v_2)S(r_g) & -S(I_b v_2) \end{bmatrix}$$

$$= \begin{bmatrix} 0 & 0 & 0 & m\left(y_g q + z_g r\right) & -m\left(x_g q - w\right) & -m\left(x_g r + v\right) \\ 0 & 0 & 0 & -m\left(y_g q + w\right) & m\left(z_g r + x_g p\right) & -m\left(y_g r - u\right) \\ 0 & 0 & 0 & -m\left(z_g p - v\right) & -m\left(z_g q + u\right) & m\left(x_g p + y_g q\right) \\ -m\left(y_g q + z_g r\right) & m\left(y_g q + w\right) & m\left(z_g p - v\right) & 0 & -I_{yz}q - I_{xz}p + I_{zz}r & I_{yz}r + I_{xy}p - I_{yy}q \\ m\left(x_g q - w\right) & -m\left(z_g r + x_g p\right) & m\left(z_g q + u\right) & I_{yz}q + I_{xz}p - I_{zz}r & 0 & -I_{xz}r - I_{xy}q + I_{xx}p \\ m\left(x_g r + v\right) & m\left(y_g r - u\right) & -m\left(x_g p + y_g q\right) & -I_{yz}r - I_{xy}p + I_{yy}q & I_{xz}r + I_{xy}q - I_{xx}p & 0 \end{bmatrix} \tag{4.20}$$

The external forces and moments acting on the body defined relative to the b-frame are denoted in a vector form as:

$$\tau_{RB} = \left[X, Y, Z, K, M, N\right]^T \tag{4.21}$$

Note that τ_{RB} in this case includes hydrostatic forces, τ_{hs}, hydrodynamic forces, τ_{hd}, and actuators forces, τ. Each of these terms is explained in the following sections.

4.3.2 Hydrostatic Terms

The hydrostatic force vector, τ_{hs}, denotes the forces and moments that are caused by an interaction between gravitational force and buoyancy force acting on the vehicle at a certain orientation. Respectively, an AUV weight and buoyancy are expressed as

$$W = mg \tag{4.22}$$

And

$$B = \rho g \nabla \tag{4.23}$$

where m denotes the mass of the vehicle including flooding water, ∇ denotes the volume of the AUV, g is the gravitational acceleration, and ρ denotes the water density. Respectively, these two forces are acting through the centre of gravity, defined by $r_g = \left[x_g, y_g, z_g\right]^T$, and the centre of buoyancy, defined by $r_b = \left[x_b, y_b, z_b\right]^T$

The gravitational and buoyancy force vector expressed in the NED-frame are denoted by: $f_g^n = \left[0,0,W\right]^T$ and $f_b^n = \left[0,0,-B\right]^T$. The rotation matrix is employed to transform these vectors into the equivalent vectors expressed in the b-frame:

$$f_g^b = R_n^b f_g^n \tag{4.24}$$

And

$$f_b^b = R_n^b f_b^n \tag{4.25}$$

It is defined that $\tau_{hs} = -$ g(η). The hydrostatic forces and moments that are expressed in the body-frame are therefore:

$$g(\eta) = -\begin{bmatrix} f_g^b + f_b^b \\ r_g \times f_g^b + r_b \times f_b^b \end{bmatrix}$$

$$= \begin{bmatrix} (W-B)\sin\theta \\ -(W-B)\cos\theta\sin\phi \\ -(W-B)\cos\theta\cos\phi \\ -\left(y_g W - y_b B\right)\cos\theta\cos\phi + (z_g W - z_b B)\cos\theta\sin\phi \\ (z_g W - z_b B)\sin\theta + (x_g W - x_b B)\cos\theta\cos\phi \\ -(x_g W - x_b B)\cos\theta\sin\phi - \left(y_g W - y_b B\right)\sin\theta \end{bmatrix} \tag{4.26}$$

4.3.3 Hydrodynamic Terms

The hydrodynamic force vector, τ_{hd}, denote the forces and moments that are caused by the AUV motion relative to the fluid. These are categorised into terms involving added-inertia, added Coriolis-centripetal and hydrodynamic damping:

$$\tau_{hd} = -\left[M_A \dot{v} + C_A(v)v + D(v)v\right] \tag{4.27}$$

4.3.3.1 Added-Inertia Forces and Moments

Imlay [61] described forces and moments with equations consisting of 6 parts corresponding to the generalised force or moment in each DOF:

$$
\begin{aligned}
X_A = {} & X_{\dot{u}}\dot{u} + X_{\dot{w}}\left(\dot{w} + uq\right) + X_{\dot{q}}\dot{q} + Z_{\dot{w}}wq + Z_{\dot{q}}q^2 \\
& + X_{\dot{v}}\dot{v} + X_{\dot{p}}\dot{p} + X_{\dot{r}}\dot{r} - Y_{\dot{v}}vr - Y_{\dot{p}}rp - Y_{\dot{r}}r^2 \\
& - X_{\dot{v}}ur - Y_{\dot{w}}wr \\
& + Y_{\dot{w}}vq + Z_{\dot{p}}pq - (Y_{\dot{q}} - Z_{\dot{r}})qr,
\end{aligned} \tag{4.28}
$$

$$
\begin{aligned}
Y_A = {} & X_{\dot{v}}\dot{u} + Y_{\dot{w}}\dot{w} + Y_{\dot{q}}\dot{q} \\
& + Y_{\dot{v}}\dot{v} + Y_{\dot{p}}\dot{p} + Y_{\dot{r}}\dot{r} + X_{\dot{v}}vr - Y_{\dot{w}}vp + X_{\dot{r}}r^2 + (X_{\dot{p}} - Z_{\dot{r}})rp - Z_{\dot{p}}p^2 \\
& - X_{\dot{w}}(up - wr) + X_{\dot{u}}ur - Z_{\dot{w}}wp \\
& + Z_{\dot{q}}pq + X_{\dot{p}}qr,
\end{aligned} \tag{4.29}
$$

$$
\begin{aligned}
Z_A = {} & X_{\dot{w}}(u - wq) + Z_{\dot{w}}\dot{w} + Z_{\dot{q}}\dot{q} - X_{\dot{u}}uq - X_{\dot{q}}q^2 \\
& + Y_{\dot{w}}\dot{v} + Z_{\dot{p}}\dot{p} + Z_{\dot{r}}\dot{r} + Y_{\dot{v}}vp + Y_{\dot{r}}rp - Y_{\dot{p}}p^2 \\
& + X_{\dot{v}}up + Y_{\dot{w}}wp \\
& - X_{\dot{v}}vq - (X_{\dot{p}} - Y_{\dot{q}})pq - X_{\dot{r}}qr,
\end{aligned} \tag{4.30}
$$

$$
\begin{aligned}
K_A = {} & X_{\dot{p}}\dot{u} + Z_{\dot{p}}\dot{w} + K_{\dot{q}}\dot{q} - X_{\dot{v}}wu + X_{\dot{r}}uq - Y_{\dot{w}}w^2 - (Y_{\dot{q}} - Z_{\dot{r}})wq + M_{\dot{r}}q^2 \\
& + Y_{\dot{p}}\dot{v} + K_{\dot{p}}\dot{p} + K_{\dot{r}}\dot{r} + Y_{\dot{w}}v^2 - (Y_{\dot{q}} - Z_{\dot{r}})vr + Z_{\dot{p}}vp - M_{\dot{r}}r^2 - K_{\dot{q}}rp \\
& - X_{\dot{w}}uv - (Y_{\dot{v}} - Z_{\dot{w}})vw - (Y_{\dot{r}} + Z_{\dot{q}})wr - Y_{\dot{p}}wp - Y_{\dot{q}}ur \\
& + (Y_{\dot{r}} - Z_{\dot{q}})vq - K_{\dot{r}}pq - (M_{\dot{q}} - N_{\dot{r}})qr,
\end{aligned} \tag{4.31}
$$

$$
\begin{aligned}
M_A = {} & X_{\dot{q}}(\dot{u} + wq) + Z_{\dot{q}}(\dot{w} - uq) + M_{\dot{q}}\dot{q} - X_{\dot{w}}(u^2 - w^2) - (Z_{\dot{w}} - X_{\dot{u}})wu \\
& + Y_{\dot{q}}\dot{v} + K_{\dot{q}}\dot{p} + M_{\dot{r}}\dot{r} + Y_{\dot{p}}vr - Y_{\dot{r}}vp - K_{\dot{p}}(p^2 - r^2) + (K_{\dot{p}} - N_{\dot{r}})rp \\
& - Y_{\dot{w}}uv + X_{\dot{v}}vw - (X_{\dot{r}} + Z_{\dot{p}})(up - wr) + (X_{\dot{p}} - Z_{\dot{r}})(wp + ur) \\
& - M_{\dot{r}}pq + K_{\dot{q}}qr,
\end{aligned} \tag{4.32}
$$

$$
\begin{aligned}
N_A = {} & X_{\dot{r}}\dot{u} + Z_{\dot{r}}\dot{w} + M_{\dot{r}}\dot{q} - X_{\dot{v}}u^2 + X_{\dot{w}}wu - (X_{\dot{p}} - Y_{\dot{q}})uq - Z_{\dot{p}}wq - K_{\dot{q}}q^2 \\
& + Y_{\dot{r}}\dot{v} + K_{\dot{r}}\dot{p} + N_{\dot{r}}\dot{r} + X_{\dot{v}}v^2 - X_{\dot{r}}vr - (X_{\dot{p}} - Y_{\dot{q}})vp + M_{\dot{r}}rp - K_{\dot{q}}p^2 \\
& - (X_{\dot{u}} - Y_{\dot{v}})uv - X_{\dot{w}}vw + (X_{\dot{q}} + Y_{\dot{p}})up + Y_{\dot{r}}ur + Z_{\dot{q}}wp \\
& - (X_{\dot{q}} + Y_{\dot{p}})vq - (K_{\dot{p}} - M_{\dot{q}})pq - K_{\dot{r}}qr,
\end{aligned} \tag{4.33}
$$

The coefficients in the above equations are called hydrodynamic derivatives that are defined according to the SNAME (1952) notation. Each part is arranged into four lines. The first line involves components of forces or moments due to longitudinal motion while the second line involves component of forces or moments due to lateral motion. The third line contains mixed terms involving u or *w* as one factor. The fourth line includes mixed components of motion that are commonly neglected as second order terms.

The terms that involve accelerations are isolated from Eqs. (4.28) - (4.33) and contained in the added-inertia matrix as expressed below:

$$M_A = \begin{bmatrix} X_{\dot{u}} & X_{\dot{v}} & X_{\dot{w}} & X_{\dot{p}} & X_{\dot{q}} & X_{\dot{r}} \\ Y_{\dot{u}} & Y_{\dot{v}} & Y_{\dot{w}} & Y_{\dot{p}} & Y_{\dot{q}} & Y_{\dot{r}} \\ Z_{\dot{u}} & Z_{\dot{v}} & Z_{\dot{w}} & Z_{\dot{p}} & Z_{\dot{q}} & Z_{\dot{r}} \\ K_{\dot{u}} & K_{\dot{v}} & K_{\dot{w}} & K_{\dot{p}} & K_{\dot{q}} & K_{\dot{r}} \\ M_{\dot{u}} & M_{\dot{v}} & M_{\dot{w}} & M_{\dot{p}} & M_{\dot{q}} & M_{\dot{r}} \\ N_{\dot{u}} & N_{\dot{v}} & N_{\dot{w}} & N_{\dot{p}} & N_{\dot{q}} & N_{\dot{r}} \end{bmatrix}. \tag{4.34}$$

It is a common assumption to ignore the off-diagonal elements as they are significantly smaller compared to the diagonal elements.

All the remaining terms in Eqs. (4.28) - (4.33) are grouped into the added Coriolis-centripetal matrix $C_A(v)$ that is skew-symmetric, i.e., $C_A(v) = -C_A(v)^T$.

Sagatun and Fossen [62] have suggested a form of $C_A(v)$ that satisfies above requirement by deriving from added inertia matrix. To this end, the added inertia matrix may be referred to as:

$$M_A = \begin{bmatrix} M_{11} & M_{12} \\ M_{21} & M_{22} \end{bmatrix} \tag{4.35}$$

The Coriolis-centripetal matrix is derived from M_A as presented:

$$\begin{aligned} C_A(v) &= \begin{bmatrix} 0_{3\times3} & -S(M_{11}v_1 + M_{12}v_2) \\ -S(M_{11}v_1 + M_{12}v_2) & -S(M_{21}v_1 + M_{22}v_2) \end{bmatrix} \\ &= \begin{bmatrix} 0 & 0 & 0 & 0 & -a_3 & a_2 \\ 0 & 0 & 0 & a_3 & 0 & -a_1 \\ 0 & 0 & 0 & -a_2 & a_1 & 0 \\ 0 & -a_3 & a_2 & 0 & -b_3 & b_2 \\ a_3 & 0 & -a_1 & b_3 & 0 & -b_1 \\ -a_2 & a_1 & 0 & -b_2 & b_1 & 0 \end{bmatrix} \end{aligned} \tag{4.36}$$

Where

$$
\begin{aligned}
a_1 &= X_{\dot{u}}u + X_{\dot{v}}v + X_{\dot{w}}w + X_{\dot{p}}p + X_{\dot{q}}q + X_{\dot{r}}r, \\
a_2 &= Y_{\dot{u}}u + Y_{\dot{v}}v + Y_{\dot{w}}w + Y_{\dot{p}}p + Y_{\dot{q}}q + Y_{\dot{r}}r, \\
a_3 &= Z_{\dot{u}}u + Z_{\dot{v}}v + Z_{\dot{w}}w + Z_{\dot{p}}p + Z_{\dot{q}}q + Z_{\dot{r}}r, \\
b_1 &= K_{\dot{u}}u + K_{\dot{v}}v + K_{\dot{w}}w + K_{\dot{p}}p + K_{\dot{q}}q + K_{\dot{r}}r, \\
b_2 &= M_{\dot{u}}u + M_{\dot{v}}v + M_{\dot{w}}w + M_{\dot{p}}p + M_{\dot{q}}q + M_{\dot{r}}r, \\
b_3 &= N_{\dot{u}}u + N_{\dot{v}}v + N_{\dot{w}}w + N_{\dot{p}}p + N_{\dot{q}}q + N_{\dot{r}}r,
\end{aligned}
\tag{4.37}
$$

In many cases, it is possible to assume that the AUV has three planes of symmetry: port-starboard, fore-aft, and top-bottom. As a consequence, the off-diagonal elements in the added-inertia matrix, M_A, as well as the coupling elements in the added Coriolis-centripetal matrix, $C_A(v)$, can be omitted, yielding much simpler forms as expressed below:

$$
M_A = M_A^T = -diag\left\{X_{\dot{u}}, Y_{\dot{v}}, Z_{\dot{w}}, K_{\dot{p}}, M_{\dot{q}}, N_{\dot{r}}\right\} \tag{4.38}
$$

$$
C_A(v) = -C_A(v)^T = \begin{bmatrix}
0 & 0 & 0 & 0 & -Z_{\dot{w}}w & Y_{\dot{v}}v \\
0 & 0 & 0 & Z_{\dot{w}}w & 0 & -X_{\dot{u}}u \\
0 & 0 & 0 & -Y_{\dot{v}}v & X_{\dot{u}}u & 0 \\
0 & -Z_{\dot{w}}w & Y_{\dot{v}}v & 0 & -N_{\dot{r}}r & M_{\dot{q}}q \\
Z_{\dot{w}}w & 0 & -X_{\dot{u}}u & N_{\dot{r}}r & 0 & -K_{\dot{p}}p \\
-Y_{\dot{v}}v & X_{\dot{u}}u & 0 & -M_{\dot{q}}q & K_{\dot{p}}p & 0
\end{bmatrix} \tag{4.39}
$$

4.3.3.2 Hydrodynamic Damping Forces and Moments

The hydrodynamic damping terms denote the forces and moments that are mainly caused by the potential damping, skin friction, and vortex shedding [60]. For the slender-body AUVs, it is common to assume a lack of coupling between the longitudinal motion (u, w and q) and the lateral motion (v, p and r). The 6DOF fluid actions expressed in the b-frame may be considered as antisymmetric and symmetric actions with respect to xz-plane. To this end, it is convenient to do Taylor expansion for the hydrodynamic damping terms as a function of linear and angular velocities. The terms relating to antisymmetric fluid actions are:

$$
\begin{aligned}
Y &= Y_{\phi}\phi + Y_v v + Y_{|v|v}|v|v + Y_p p + Y_{|p|p}|p|p + Y_r r + Y_{|r|r}|r|r \ldots \\
K &= K_{\phi}\phi + K_v v + K_{|v|v}|v|v + K_p p + K_{|p|p}|p|p + K_r r + K_{|r|r}|r|r \ldots \\
N &= N_{\phi}\phi + N_v v + N_{|v|v}|v|v + N_p p + N_{|p|p}|p|p + N_r r + N_{|r|r}|r|r \ldots
\end{aligned}
\tag{4.40}
$$

And the symmetric fluid actions are:

$$
\begin{aligned}
X &= X_\theta \theta + X_u u + X_{|u|u}|u|u + X_w w + X_{|w|w}|w|w + X_q q + X_{|q|q}|q|q ... \\
Z &= Z_\theta \theta + Z_u u + Z_{|u|u}|u|u + Z_w w + Z_{|w|w}|w|w + Z_q q + Z_{|q|q}|q|q ... \\
M &= M_\theta \theta + M_u u + M_{|u|u}|u|u + M_w w + M_{|w|w}|w|w + M_q q + M_{|q|q}|q|q ...
\end{aligned}
\tag{4.41}
$$

The coefficients above are also denoted according the SNAME (1952) notation. For example, a component of the damping force Y along the y-axis arises from that sway velocity v is expressed as:

$$
Y = Y_v v, \text{ where } Y_v = \frac{\partial Y}{\partial v} \tag{4.42}
$$

In practice, Eqs. (4.40) and (4.41) are truncated to second order terms since the higher order terms are relatively small. Terms involving accelerations are dropped off since they are already included in the added inertia matrix and added Coriolis-centripetal matrix. For the slender-body vehicle that is top-bottom and port-starboard symmetric, surge dynamics can be assumed to be independent of the other degrees of freedom. The terms involving ϕ and θ may be ignored by assuming that the vehicle is passively stable in roll and is operating at a zero-pitch condition, respectively. The remaining terms are the hydrodynamic damping terms that may be grouped into linear and quadratic terms, respectively. This is given by the form:

$$
D(v) = D_l + D_q(v), \tag{4.43}
$$

Where

$$
D_l = -\begin{bmatrix} X_u & 0 & 0 & 0 & 0 & 0 \\ 0 & Y_v & 0 & Y_p & 0 & Y_r \\ 0 & 0 & Z_w & 0 & Z_q & 0 \\ 0 & K_v & 0 & K_p & 0 & K_r \\ 0 & 0 & M_w & 0 & M_q & 0 \\ 0 & N_v & 0 & N_p & 0 & N_r \end{bmatrix} \tag{4.44}
$$

And

$$D_q(\nu) = -\begin{bmatrix} X_{|u|u}|u| & 0 & 0 & 0 & 0 & 0 \\ 0 & Y_{|v|v}|v| & 0 & Y_{|p|p}|p| & 0 & Y_{|r|r}|r| \\ 0 & 0 & Z_{|w|w}|w| & 0 & Z_{|q|q}|q| & 0 \\ 0 & K_{|v|v}|v| & 0 & K_{|p|p}|p| & 0 & K_{|r|r}|r| \\ 0 & 0 & M_{|w|w}|w| & 0 & M_{|q|q}|q| & 0 \\ 0 & N_{|v|v}|v| & 0 & 0 & 0 & N_{|r|r}|r| \end{bmatrix} \tag{4.45}$$

For the stable AUV, both the linear and quadratic diagonal elements are expected to be negative as to damp out the motion.

4.3.4 Actuator Modeling

The external force and torque vector produced by the thrusters is defined as:

$$\tau = \begin{bmatrix} X & Y & Z & K & M & N \end{bmatrix}^T = LU. \tag{4.46}$$

With,

$$U = \begin{bmatrix} T_1 & T_2 & \ldots & T_n \end{bmatrix}^T. \tag{4.47}$$

where L is a mapping matrix and U is a thrust vector. U is the vector of thrusts produced by the vehicle's thrusters. The number of thrust values in U depends on the number of thrusters on the vehicle. The mapping matrix L is essentially a 6 × n matrix that uses U to find the overall forces and moments acting on the vehicle.

4.3.5 Umbilical Cable Forces

Generally, the deep-sea-operated vehicle systems typically consist of a supported vessel umbilical cable (UC) and UV. However, most of researches on the numerical model of predicting the motion of the UV neglect the UC effect. The main reason is that including the UC effect will cause the numerical model to be very complicated and difficult to solve. Therefore, only few authors dealt with such kind of problem. UC is used for both power supply and communication to UV. The cable is treated as a long, thin, flexible circular cylinder. It is assumed that the dynamics of a cable are determined by gravity, hydrodynamic loading and inertial forces, no bending or torsional stiffness is taken into account in this study. The UC that connects the UV to the vessel can be affected by many parameters, including the motions of either the UV or the vessel, the current along the cable and the total length of the cable itself. The UC configuration can be optimized by numerical simulations. This is described in more detail in Chapter 3.

4.4 Nonlinear Equations of Motion (6DOF)

For a submerged vehicle operating in calm water, wave current, and wind factors can be neglected. Such that the rigid-body force vector, τ_{RB}, is presented as a sum of hydrostatic, hydrodynamic and actuator force vectors as follows:

$$\tau_{RB} = \tau_{hs} + \tau_{hd} + \tau_{th} + \tau_{cable} \tag{4.48}$$

Consequently, Eq. (4.18) becomes:

$$M_{RB}\dot{v} + C_{RB}v = \tau_{hs} + \tau_{hd} + \tau_{th} + \tau_{cable} \tag{4.49}$$

The following is obtained by substituting Eqs. (4.26) and (4.27) into the above equation:

$$\underbrace{M_{RB}\dot{v} + C_{RB}v}_{rigid-body} + \underbrace{M_A\dot{v} + C_A v + D(v)v}_{hydrodynamic} + \underset{hydrostatic}{g(\eta)} = \tau_{th} + \tau_{cable} \tag{4.50}$$

By grouping the corresponding terms together, the equation collapses into the following form:

$$M\dot{v} + C(v)v + D(v)v + g(\eta) = \tau = \tau_{th} + \tau_{cable} \tag{4.51}$$

Where

$M = M_{RB} + M_A$: inertia matrix of the system

$C(v) = C_{RB} + C_A(v)$: Coriolis-centripetal matrix of the system,

$D(v)$: damping matrix, and

$g(\eta)$: restoring vector due to weight and buoyancy.

We should note that the dynamics equations of motion are not mathematically expressed in earth-fixed frame but in body-fixed frame. It means that interactions between a vehicle and the ocean environment are defined from the perspective of the vehicle, i.e. within the body coordinate system. This is because all actions and reactions between vehicle and environment are dependent on the orientation, shape, velocity and acceleration of the vehicle body, with the sole exceptions of gravity, waves and current. Also, moment if inertia terms in the mass matrix M can only be constant in a body-fixed frame, further making the body frame attractive for dynamics calculations. The following properties can be observed for the body coordinates vector representation [23]:

Property 1: For a rigid body, the inertia matrix is strictly positive if and only if $M_A > 0$. That is:

$$M = M_{RB} + M_A > 0 \tag{4.52}$$

In addition, we require that the body is at rest or low speed, under the assumption of an ideal fluid, the inertia matrix will also be symmetrical and positive definite. That is:

$$M = M^T > 0 \tag{4.53}$$

Property 2: For a rigid body moving through and ideal fluid, the Coriolis and centripetal matrix C(v) can always be parameterized such that C(v) is skew-symmetrical, that is:

$$C(v) = -C^T(v) \quad \forall \ v \in R^6 \tag{4.54}$$

Property 3: For a rigid body moving through an ideal fluid the hydrodynamic damping matrix will be real, non-symmetric and strictly positive:

$$D(v) > 0 \quad \forall \ v \in R^6 \tag{4.55}$$

The dynamic model equation in earth-fixed frame can also be obtained by using following kinematic transformations:

$$\dot{\eta} = J(\eta)v \Leftrightarrow v = J^{-1}(\eta)\dot{\eta} \tag{4.56}$$

$$\ddot{\eta} = \dot{J}(\eta)v + J(\eta)\dot{v} \Leftrightarrow \dot{v} = J^{-1}(\eta)\left[\ddot{\eta} - \dot{J}(\eta)J^{-1}(\eta)\dot{\eta}\right] \tag{4.57}$$

To eliminate v and $\dot{v}$ in Eq. (4.51). Hence we can get the following earth-fixed vector expression of dynamic model:

$$M_\eta(\eta)\ddot{\eta} + C_\eta(\eta, v)\dot{\eta} + D_\eta(\eta, v)\dot{\eta} + g_\eta(\eta) = \tau_\eta \tag{4.58}$$

Where

$$\begin{aligned}
&M_\eta(\eta) = J^{-T}(\eta)MJ^{-1}(\eta) \\
&C_\eta(v,\eta) = J^{-T}(\eta)\left[C(v) - MJ^{-1}(\eta)\dot{\eta}\right]J^{-1}(\eta) \\
&D_\eta(v,\eta) = J^{-T}(\eta)D(v)J^{-1}(\eta) \\
&g_\eta(\eta) = J^{-T}(\eta)g(\eta) \\
&\tau_\eta(\eta) = J^{-T}(\eta)\tau
\end{aligned} \tag{4.59}$$

4.5 Simplification of UV Dynamic Model

The dynamic model presented in the previous section is quite complex and needs many parameters thus it will be very time consuming and difficult process. Therefore, simplification of the model was required. In order to simplify the UV dynamic, several assertions below are needed.

- The vehicle travels at low speeds (less than 2m/s).
- The vehicle is considered to be symmetrical about its three planes.
- The off-diagonal elements of the dynamic model matrices are much smaller than their counterparts.
- The hydrodynamic damping coupling is negligible when the vehicle travels at low speed.

If the decoupling is valid thus the Coriolis and centripetal terms matrices become negligible and consequently can be eliminated from the dynamic model. The dynamic model in Eq. (4.51) can be simplified as:

$$M\dot{V} + D(V)V + G(\eta_2) = \tau, \tag{4.60}$$

4.5.1 Simplifying the Mass and Inertia Matrix

With the vehicle fixed-body frame is positioned at the center of gravity and since the vehicle is assumed fairly symmetrical about all axes, then UV rigid-body mass M_{RB} can be simplified to a good approximation to,

$$M_{RB} = \begin{bmatrix} m & 0 & 0 & 0 & 0 & 0 \\ 0 & m & 0 & 0 & 0 & 0 \\ 0 & 0 & m & 0 & 0 & 0 \\ 0 & 0 & 0 & I_x & 0 & 0 \\ 0 & 0 & 0 & 0 & I_y & 0 \\ 0 & 0 & 0 & 0 & 0 & I_z \end{bmatrix} \tag{4.61}$$

$$M_{RB} = diag\left\{m, m, m, I_x, I_y, I_z\right\}, \tag{4.62}$$

with m is the mass of the UV, I_x , I_y I_y and I_z is the inertial force in x, y and z axis respectively.

Since the vehicle travels at low speed, thus added mass from Eq. (4.34) can be simplified as:

$$M_A = \begin{bmatrix} X_{\dot{u}} & 0 & 0 & 0 & 0 & 0 \\ 0 & Y_{\dot{u}} & 0 & 0 & 0 & 0 \\ 0 & 0 & Z_{\dot{w}} & 0 & 0 & 0 \\ 0 & 0 & 0 & K_{\dot{p}} & 0 & 0 \\ 0 & 0 & 0 & 0 & M_{\dot{q}} & 0 \\ 0 & 0 & 0 & 0 & 0 & N_{\dot{r}} \end{bmatrix} \tag{4.63}$$

$$M_A = diag\left\{X_{\dot{u}}, Y_{\dot{u}}, Z_{\dot{v}}, K_{\dot{p}}, M_{\dot{q}}, N_{\dot{r}}\right\}, \tag{4.64}$$

with $X_{\dot{u}}$, $Y_{\dot{u}}$, $Z_{\dot{w}}$, $K_{\dot{p}}$, $M_{\dot{q}}$ and $N_{\dot{r}}$ are added mass in the surge, sway, heave, roll, pitch and yaw movement respectively.

4.5.2 Simplifying the Hydrodynamic Damping Matrix

The matrix $D(v)$ is the hydrodynamic damping matrix consisting of both linear and quadratic terms. This hydrodynamic damping is caused by potential damping due to skin friction (linear damping) drag and vortex shedding (quadratic damping). The sum of these individual components gives the overall hydrodynamic damping effect on the UV. The hydrodynamic damping matrix can be simplified by using the following assumptions:

- As the UV is operating at around linear speed of 0.2 m/s (or angular speed of 0.2 rad/s), it is well within the linear damping region of maximum 2m/s. Hence, the linear hydrodynamic damping is used.
- The off-diagonal elements in $D(v)$ on an underwater vehicle are small compared to the diagonal elements.

Hence the hydrodynamic damping $D(v)$ from Eq. (4.43) also can be simplified as:

$$D(v) = -\begin{bmatrix} X_u & 0 & 0 & 0 & 0 & 0 \\ 0 & Y_v & 0 & 0 & 0 & 0 \\ 0 & 0 & Z_w & 0 & 0 & 0 \\ 0 & 0 & 0 & K_p & 0 & 0 \\ 0 & 0 & 0 & 0 & M_q & 0 \\ 0 & 0 & 0 & 0 & 0 & N_r \end{bmatrix} \tag{4.65}$$

$$D(v) = -diag\left\{X_u, Y_v, Z_w, K_p, M_q, N_r\right\}, \tag{4.66}$$

4.5.3 Simplifying the Gravitational and Buoyancy Vector

In designing UV, it is desirable to make the UV neutrally buoyant or slightly positive buoyant by adding additional float or balancing mass. With that, the UV becomes neutrally buoyant, W = B. The center of gravity is located at $r_G = \begin{bmatrix} 0 & 0 & 0 \end{bmatrix}^T$, while the center of buoyancy r_B was found to be $r_B = \begin{bmatrix} 0 & 0 & z_B \end{bmatrix}^T$ for a good approximation, since z_B is not aligned to the center of the gravity in z axis. So, the gravitational force from Eq. (4.26) that can be simplified as:

$$g(\eta) = \begin{bmatrix} 0 \\ 0 \\ 0 \\ -z_B W \cos\theta \sin\phi \\ -z_B W \sin\theta \\ 0 \end{bmatrix} \tag{4.67}$$

4.6 Thruster Modeling

The UV model considered in the present study is equipped with seven thrusters as shown in Fig. 4.2; that is, four horizontal thrusters T_1, T_2, T_3 and T_4 which are installed at the bow and the stern part with inclined angle θ_T, are operated to control the surge, sway, and yaw motions. While three vertical thrusters T_5, T_6 and T_7 enable the AUV to have 3-DOF behaviors of the heave, roll, and pitch motions. Assume $\left(x_{ci}, y_{ci}, z_{ci}\right)_{i=1,2,3,4}$ is the center of the i-th thruster, where θ_T is set to be 30^0 in the present study.

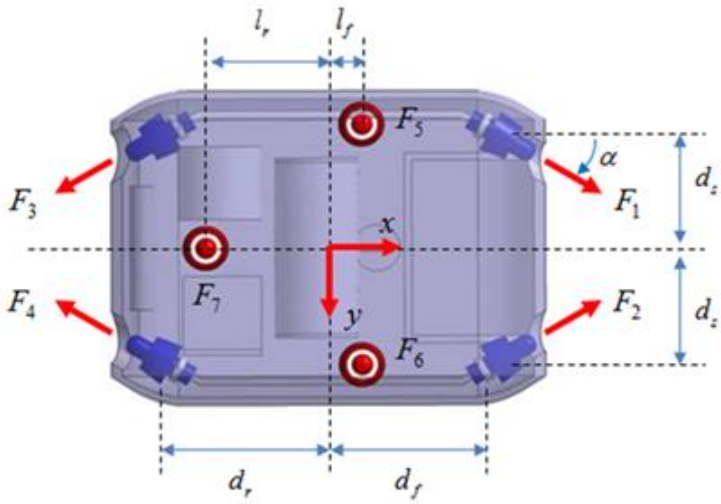

Fig. 4.2 UV frame reference and torque vector.

The center of the 1st thruster T_1 is $x_{c1} = 0.3m$, $y_{c1} = -0.2m$, $z_{c1} = 0m$ and the moment induced by thruster T_1 can be obtained by:

$$\vec{r}_1 \times \vec{F}_1 = \begin{bmatrix} x_{c1} \\ y_{c1} \\ z_{c1} \end{bmatrix} \times \begin{bmatrix} F_1 \cos\theta \\ F_1 \sin\theta \\ 0 \end{bmatrix} = \begin{bmatrix} x_{c1} \\ y_{c1} \\ 0 \end{bmatrix} \times \begin{bmatrix} F_1 \cos\theta \\ F_1 \sin\theta \\ 0 \end{bmatrix} = (x_{c1} F_1 \sin\theta - y_{c1} F_1 \cos\theta)\vec{k} \tag{4.68}$$

The center of the 2nd thruster T_2 is $x_{c2} = 0.3m$, $y_{c2} = 0.2m$, $z_{c2} = 0m$ and the moment induced by thruster T_2 can be obtained by:

$$\vec{r}_2 \times \vec{F}_2 = \begin{bmatrix} x_{c2} \\ y_{c2} \\ z_{c2} \end{bmatrix} \times \begin{bmatrix} F_2 \cos\theta \\ -F_2 \sin\theta \\ 0 \end{bmatrix} = \begin{bmatrix} x_{c2} \\ y_{c2} \\ 0 \end{bmatrix} \times \begin{bmatrix} F_2 \cos\theta \\ -F_2 \sin\theta \\ 0 \end{bmatrix} = (-x_{c2} F_2 \sin\theta - y_{c2} F_2 \cos\theta)\vec{k} \tag{4.69}$$

The center of the 3rd thruster T_3 is $x_{c3} = -0.3m$, $y_{c3} = -0.2m$, $z_{c3} = 0m$ and the moment induced by thruster T_3 can be obtained by:

$$\vec{r}_3 \times \vec{F}_3 = \begin{bmatrix} x_{c3} \\ y_{c3} \\ z_{c3} \end{bmatrix} \times \begin{bmatrix} -F_3 \cos\theta \\ F_3 \sin\theta \\ 0 \end{bmatrix} = \begin{bmatrix} x_{c3} \\ y_{c3} \\ 0 \end{bmatrix} \times \begin{bmatrix} -F_3 \cos\theta \\ F_3 \sin\theta \\ 0 \end{bmatrix} = (x_{c3} F_3 \sin\theta + y_{c3} F_3 \cos\theta)\vec{k} \tag{4.70}$$

The center of the 4-th thruster T_4 is $x_{c4} = -0.3m$, $y_{c4} = 0.2m$, $z_{c4} = 0m$ and the moment induced by thruster T_4 can be obtained by:

$$\vec{r}_4 \times \vec{F}_4 = \begin{bmatrix} x_{c4} \\ y_{c4} \\ z_{c4} \end{bmatrix} \times \begin{bmatrix} -F_4 \cos\theta \\ -F_4 \sin\theta \\ 0 \end{bmatrix} = \begin{bmatrix} x_{c4} \\ y_{c4} \\ 0 \end{bmatrix} \times \begin{bmatrix} -F_4 \cos\theta \\ -F_4 \sin\theta \\ 0 \end{bmatrix} = (-x_{c4}F_4 \sin\theta + y_{c4}F_4 \cos\theta)\vec{k} \tag{4.71}$$

The center of the 5-th thruster T_5 is $x_{c5} = 0.1m$, $y_{c5} = -0.18m$, $z_{c5} = 0m$ and the moment induced by thruster T_5 can be obtained by:

$$\vec{r}_5 \times \vec{F}_5 = \begin{bmatrix} x_{c5} \\ y_{c5} \\ z_{c5} \end{bmatrix} \times \begin{bmatrix} 0 \\ 0 \\ F_5 \end{bmatrix} = \begin{bmatrix} x_{c5} \\ y_{c5} \\ 0 \end{bmatrix} \times \begin{bmatrix} 0 \\ 0 \\ F_5 \end{bmatrix} = (y_{c5}F_5)\vec{i} - (x_{c5}F_5)\vec{j} \tag{4.72}$$

The center of the 6-th thruster T_6 is $x_{c6} = 0.1m$, $y_{c6} = 0.18m$, $z_{c6} = 0m$ and the moment induced by thruster T_6 can be obtained by:

$$\vec{r}_6 \times \vec{F}_6 = \begin{bmatrix} x_{c6} \\ y_{c6} \\ z_{c6} \end{bmatrix} \times \begin{bmatrix} 0 \\ 0 \\ F_6 \end{bmatrix} = \begin{bmatrix} x_{c6} \\ y_{c6} \\ 0 \end{bmatrix} \times \begin{bmatrix} 0 \\ 0 \\ F_6 \end{bmatrix} = (y_{c6}F_6)\vec{i} - (x_{c6}F_6)\vec{j} \tag{4.73}$$

The center of the 7-th thruster T_7 is $x_{c7} = -0.25m$, $y_{c7} = 0m$, $z_{c7} = 0m$ and the moment induced by thruster T_7 can be obtained by:

$$\vec{r}_7 \times \vec{F}_7 = \begin{bmatrix} x_{c7} \\ y_{c7} \\ z_{c7} \end{bmatrix} \times \begin{bmatrix} 0 \\ 0 \\ F_7 \end{bmatrix} = \begin{bmatrix} x_{c7} \\ y_{c7} \\ 0 \end{bmatrix} \times \begin{bmatrix} 0 \\ 0 \\ F_7 \end{bmatrix} = (y_{c7}F_7)\vec{i} - (x_{c7}F_7)\vec{j} \tag{4.74}$$

Finally, the corresponding resultant force and moment induced by each thruster can be obtained by:

$$\begin{aligned} F_{thrust} &= F_{Tx}\vec{i} + F_{Ty}\vec{j} + F_{Tz}\vec{k} \\ &= (F_1 + F_2 - F_3 - F_4)\cos\theta\vec{i} + (F_1 - F_2 + F_3 - F_4)\sin\theta\vec{j} + (F_5 + F_6 + F_7)\vec{k} \end{aligned} \tag{4.75}$$

$$\begin{aligned} M_{thrust} &= M_{Tx}\vec{i} + M_{Ty}\vec{j} + M_{Tz}\vec{k} \\ &= (y_{c5}F_5 + y_{c6}F_6 + y_{c7}F_7)\vec{i} + (-x_{c5}F_5 - x_{c6}F_6 - x_{c7}F_7)\vec{j} + (x_{c1}F_1 \sin\theta - y_{c1}F_1 \cos\theta \\ &\quad - x_{c2}F_2 \sin\theta - y_{c2}F_2 \cos\theta + x_{c3}F_3 \sin\theta + y_{c3}F_3 \cos\theta - x_{c4}F_4 \sin\theta + y_{c4}F_4 \cos\theta)\vec{k} \end{aligned} \tag{4.76}$$

In other way, the thruster allocation can be defined as follows:

$$\mathbf{U}_v = LU \tag{4.77}$$

$$\mathbf{U}_v = \begin{bmatrix} F_{Tx} & F_{Ty} & F_{Tz} & M_{Tx} & M_{Ty} & M_{Tz} \end{bmatrix}^T \tag{4.78}$$

$$U = \begin{bmatrix} F_1 & F_2 & F_3 & F_4 & F_5 & F_6 & F_7 \end{bmatrix}^T \tag{4.79}$$

$$L=\begin{bmatrix} c\alpha & c\alpha & -c\alpha & -c\alpha & 0 & 0 & 0 \\ s\alpha & -s\alpha & s\alpha & -s\alpha & 0 & 0 & 0 \\ 0 & 0 & 0 & 0 & 1 & 1 & 1 \\ 0 & 0 & 0 & 0 & -l_s & l_s & 0 \\ 0 & 0 & 0 & 0 & -l_f & l_f & l_r \\ \begin{matrix} d_s c\alpha \\ +d_f s\alpha \end{matrix} & \begin{matrix} -d_s c\alpha \\ -d_f s\alpha \end{matrix} & \begin{matrix} -d_s c\alpha \\ -d_r s\alpha \end{matrix} & \begin{matrix} d_s c\alpha \\ +d_r s\alpha \end{matrix} & 0 & 0 & 0 \end{bmatrix} \tag{4.80}$$

where U_v is the control forces and moments vector acting on the vehicle due to seven thrusters and U is the thrust vector; L is the thruster configuration matrix and θ is the angle between the longitudinal axis and direction of the propeller thrust; $l_f = x_{c5} = -x_{c6}$ and $l_r = -x_{c7}$ are the distance from the center of buoyancy to the vertical thruster at the bow and stern respectively and $l_s = -y_{c5} = y_{c6}$ is the distance from the center line to the vertical thrusters; $d_s = y_{c2} = y_{c4} = -y_{c1} = -y_{c3}$ is the distance from the center of buoyancy to the port and starboard thruster, $d_f = x_{c1} = x_{c2}$ and $d_r = -x_{c3} = -x_{c4}$ are the distance from the center of buoyancy to the horizontal thruster at the bow and stern respectively.

4.7 Current Modeling

The current velocity can be modeled as a Gauss-Markov process as follows [63]:

$$\dot{V}_c + \mu_c V_c = w_c \tag{4.81}$$

where w_c is Gaussian white noise, and $\mu_c > 0$ is a suitable constant. A saturating element is usually used in the integration process to limit the current speed.

$$V_{\min} \le V_c(t) \le V_{\max} \tag{4.82}$$

Assuming that the fluid is irrotational, the current velocity vector in the NED-frame is given by:

$$v_c^e = \begin{bmatrix} v_x & v_y & v_z & 0 & 0 & 0 \end{bmatrix}^T \tag{4.83}$$

Where $V_c = \sqrt{v_x^2 + v_y^2 + v_z^2}$, and:

$$v_x = V_c \cos\psi_c \cos\theta_c \tag{4.84}$$

$$v_y = V_c \sin\psi_c \cos\theta_c \tag{4.85}$$

$$v_z = V_c \sin\theta_c \tag{4.86}$$

Denote the current vector components in North, East and down directions, respectively. Moreover, ψ_c and θ_c are the horizontal and vertical current angle, respectively. In underwater environments with large variety in depth and bottom topology, a vertical current component needs to be included. The NED-frame current velocity is rotated into the body-frame as:

$$v_c = \begin{bmatrix} u_c & v_c & w_c & 0 & 0 & 0 \end{bmatrix}^T \tag{4.87}$$

$$v_c = diag\left[R^T(\eta), 0_{3\times3} \right] v_c^e \tag{4.88}$$

where u_c , v_c and w_c denote the current velocity in surge, sway and heave, respectively. This results in the following relative velocity.

$$v_r = v - v_c = \begin{bmatrix} u_r & v_r & w_r & p & q & r \end{bmatrix}^T \tag{4.89}$$

For notational convenience we also define the current vectors $\rho_c, \rho_c^e \in R^3$ defined as follows:

$$\rho_c = \left[u_c, \upsilon_c, w_c \right]^T, \rho_c^e = \left[v_x, v_y, v_z \right]^T \tag{4.90}$$

$$\rho_c^e = R(\eta)\rho_c \tag{4.91}$$

Ocean current has significant impact on the vehicle's motion and stability. It generates a relative velocity between the water flow and the vehicle, and it thus has a hydrodynamic effect on the vehicle. The following three factors are important:

- Relative speed between current and vehicle.
- Relative angle between current and vehicle.
- Vehicle shape and size.

These factors are inherently captured by the hydrodynamic forces and moments vector τ_H , provided that the argument to the equation is the relative velocity between the vehicle and the current.

4.8 Dynamic Model Including Ocean Currents

The dynamic model in Eq. (4.51) of the AUV did not include ocean currents. This dynamic model is sufficient to model the AUV for swimming pool experiments. But the final goal is to use the AUV in harbors and for this purpose it is interesting to see how the AUV will respond to environmental disturbances. The environmental disturbances of an AUV are ocean currents. Here wave induced currents are neglected because an AUV is deeply submerged. Ocean currents are horizontal and vertical circulating systems of ocean water, produced by gravity, wind friction and water density variation in different parts of the ocean. Note that if

the AUV is used in a sea harbor also tides can form a current. This section presents a method to include the current-induced forces and moments in the dynamic equations of motions. This method assumes that the equations of motion can be represented in terms of the velocity of the vehicle relative to the ocean currents, expressed in the body-fixed reference frame.

Let

$$v_r = v - v_c \tag{4.92}$$

where $v_c = [u_c, v_c, w_c, 0, 0, 0]^T$ is a vector of non-rotational body-fixed current velocities.

The effect of ocean currents in six DOFs can be expressed with the use of relative motion in.

$$v_r = \begin{bmatrix} u - u_c^b & v - v_c^b & w - w_c^b & p & q & r \end{bmatrix}^T \tag{4.93}$$

where u_c^b , v_c^b and w_c^b are body-fixed current velocities. The dynamic model including the ocean currents is given in

$$\underbrace{M_{RB}\dot{v} + C_{RB}(v)v}_{rigid-body\ terms} + \underbrace{M_A\dot{v}_r + C_A(v_r)v_r + D(v_r)v_r}_{hydrodynamic\ terms} + \underset{hydrostatic\ terms}{g(\eta)} = \tau \tag{4.94}$$

It is common to assume that the current velocity vector is slowly varying, which means that $\dot{v}_r \approx 0$. This simplifies the dynamic model Eq. (4.94) into:

$$M\dot{v} + C_{RB}(v)v + C_A(v_r)v_r + D(v_r)v_r + g(\eta) = \tau \tag{4.95}$$

The ocean current speed is normally defined in the W-frame but can be transformed into the B-frame with the use of the transposed Euler angle rotation matrix given in Eq. (4.9). Thus, this results in the following model for underwater vehicles including ocean current:

$$\begin{aligned} &\dot{\eta} = J(\eta)v \\ &M\dot{v} + C_{RB}(v)v + C_A(v_r)v_r + D(v_r)v_r + g(\eta) = \tau \end{aligned} \tag{4.96}$$

The ocean current effect on the motion of AUV system is performed as shown in Figs. 4.3-4.5. In this simulation, the ocean currents are assumed irrotational fluid, constant or slowly varying and it is generated by the first Gauss-Markov process expressed in two current models with an average velocity of current is 0.5 m / s (about 1 knot) and angle of attack is 60°. As shown in Fig. 4.5, the ocean current significantly affects to all states of AUV motion.

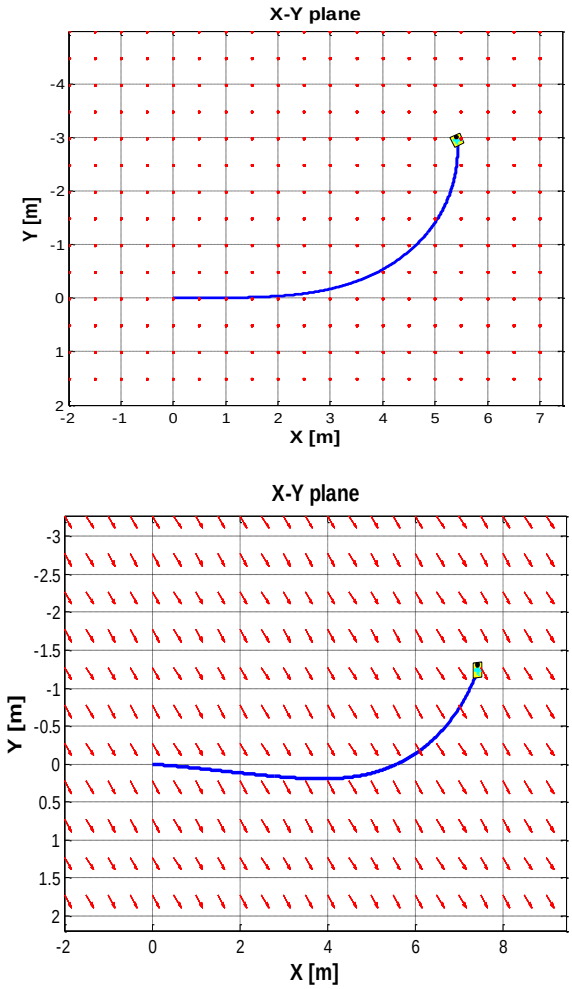

Fig. 4.3 2D trajectories of UV in both cases: with and without current effects.

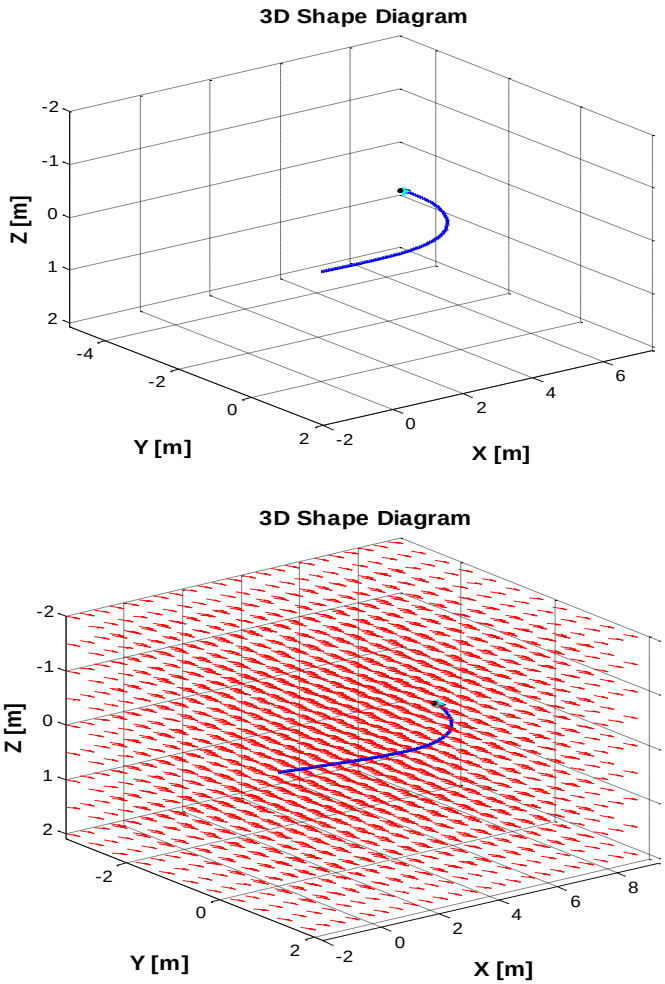

Fig. 4.4 3D trajectories of UV in both cases: with and without current effects.

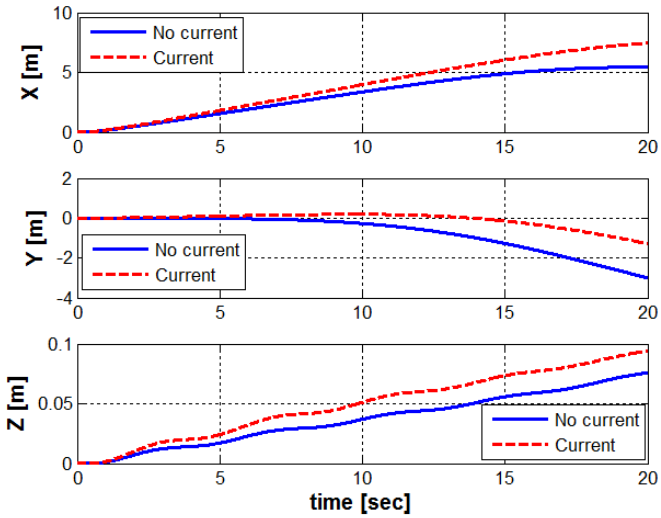
X [m]
Y [m]
Z [m]
No current
Current
time [sec]

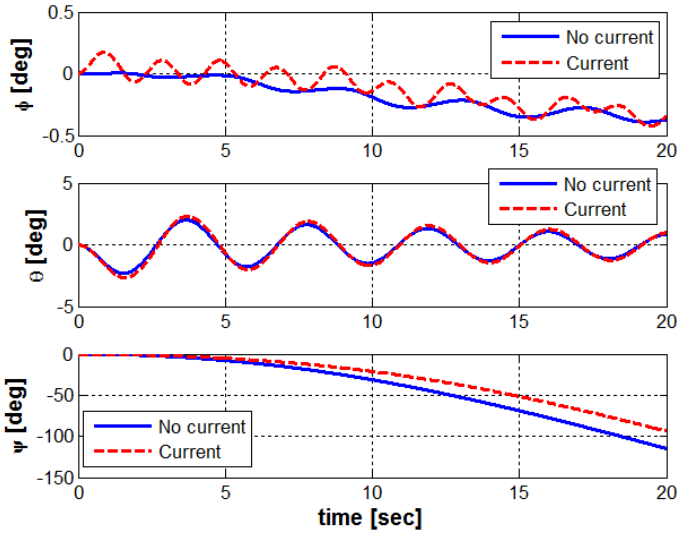
ϕ [deg]
θ [deg]
ψ [deg]
No current
Current
time [sec]

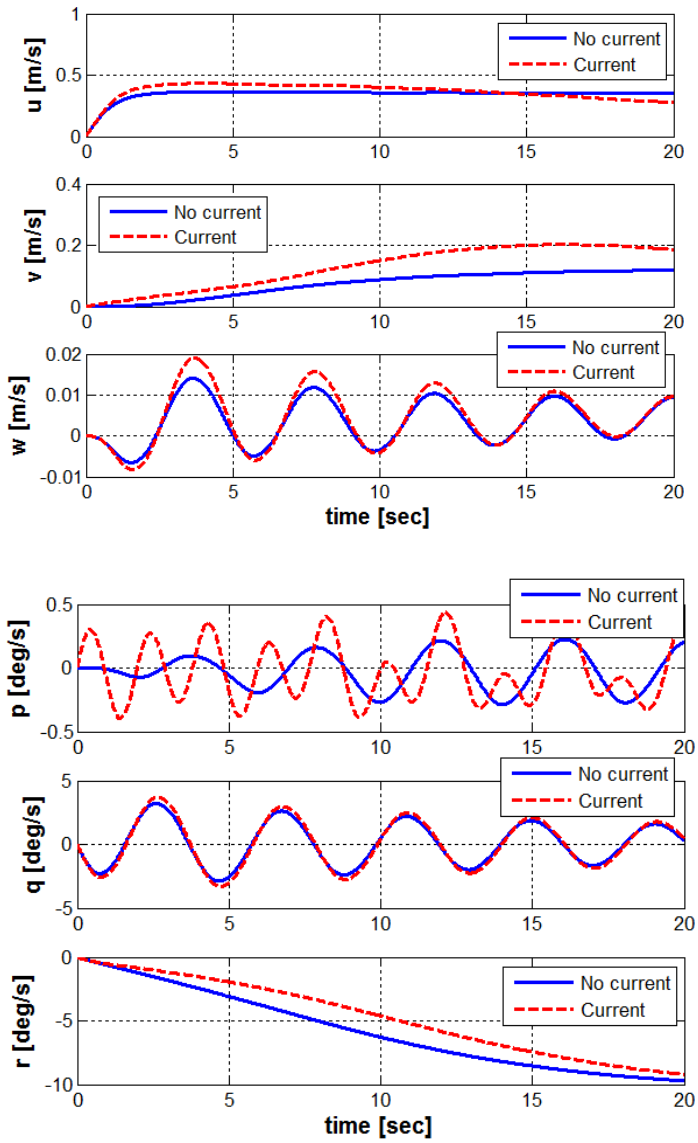

Fig. 4.5 UV dynamic behaviors in both cases: with and without current effects.

4.9 Complete Motion Equations of AUV (6DOF)

Now that we have defined the required transformations between the body-fixed and earth-fixed coordinate systems for the velocities, orientations, and positions, we can detail the equations of motion for this UV. These equations of motion are adopted from work done originally by Healey [39] to derive this 6-DOF model. The technique used to derive these equations and relationships is founded on the Newton-Euler approach.

The following equations fully describe a vehicle's motion with 6-DOF, which include three translational and three rotational all in the body-fixed coordinate frame.

Surge Motion

$$
\begin{aligned}
&(m - X_{\dot{u}})\dot{u} = (-m + Z_{\dot{w}})wq + (m - Y_{\dot{v}})vr + (X_u + X_{u|u|}|u|)u + F_{xthr} + F_{xcable} \\
&\dot{u} = [(-m + Z_{\dot{W}})wq + (m - Y_{\dot{v}})vr + (X_u + X_{u|u|}|u|)u + F_{xthr} + F_{xcable}] / (m - X_{\dot{u}})
\end{aligned}
\tag{4.97}
$$

Sway Motion

$$
\begin{aligned}
&(m - Y_{\dot{v}})\dot{v} = wp(m - Z_{\dot{w}}) + (-m - X_{\dot{u}})ur + (Y_v + Y_{v|v|}|v|)v + F_{ythr} + F_{ycable} \\
&\dot{v} = [pw(m - Z_{\dot{w}}) + (-m - X_{\dot{u}})ur + (Y_v + Y_{v|v|}|v|)v + F_{ythr} + F_{ycable}] / (m - Y_{\dot{v}})
\end{aligned}
\tag{4.98}
$$

Heave Motion

$$
\begin{aligned}
&(m - Z_{\dot{w}})\dot{w} = vp(-m + Y_{\dot{v}}) + qu(m - X_{\dot{u}}) + (Z_w + Z_{w|w|}|w|)w + F_{zthr} + F_{zcable} \\
&\dot{w} = [pv(-m + Y_{\dot{v}}) + qu(m - X_{\dot{u}}) + (Z_w + Z_{w|w|}|w|)w + F_{zthr} + F_{zcable}] / (m - Z_{\dot{w}})
\end{aligned}
\tag{4.99}
$$

Roll Motion

$$
\begin{aligned}
&(I_x - K_{\dot{p}})\dot{p} = vw(Z_{\dot{w}} - Y_{\dot{v}}) + (N_{\dot{r}} - I_z + I_y - M_{\dot{q}})rq + (K_p + K_{p|p|}|p|)p \\
&+ z_B B\cos\theta\sin\phi + M_{xthr} + M_{xcable} \\
&\dot{p} = [vw(Z_{\dot{w}} - Y_{\dot{v}}) + (N_{\dot{r}} - I_z + I_y - M_{\dot{q}})rq + (K_p + K_{p|p|}|p|)p + z_B B\cos\theta\sin\phi \\
&+ M_{xthr} + M_{xcable}] / (I_x - K_{\dot{p}})
\end{aligned}
\tag{4.100}
$$

Pitch Motion

$$
\begin{aligned}
&(I_y - M_{\dot{q}})\dot{q} = uw(X_{\dot{u}} - Z_{\dot{w}}) + (I_z - I_x + K_{\dot{p}} - N_{\dot{r}})rp + (M_q + M_{q|q|}|q|)q \\
&- z_B B\sin\theta + M_{ythr} + M_{ycable} \\
&\dot{q} = [uw(X_{\dot{u}} - Z_{\dot{w}}) + (I_z - I_x + K_{\dot{p}} - N_{\dot{r}})rp + (M_q + M_{q|q|}|q|)q - z_B B\sin\theta \\
&+ M_{ythr} + M_{ycable}] / (I_y - M_{\dot{q}})
\end{aligned}
\tag{4.101}
$$

Yaw Motion

$$
\begin{aligned}
&(I_z - N_{\dot{r}})\dot{r} = uv(Y_{\dot{v}} - X_{\dot{u}}) + (M_{\dot{q}} - I_y + I_x - K_{\dot{p}})qp + (N_r + N_{r|r|}|r|)r \\
&+ M_{zthr} + M_{zcable} \\
&\dot{r} = [uv(Y_{\dot{v}} - X_{\dot{u}}) + (M_{\dot{q}} - I_y + I_x - K_{\dot{p}})qp + (N_r + N_{r|r|}|r|)r \\
&+ M_{zthr} + M_{zcable}] / (I_z - N_{\dot{r}})
\end{aligned}
\tag{4.102}
$$

4.10 Dynamics Model Parameter Identification

The dynamics model for AUVs, Eq. (4.51), involves a large number of the parameters that can be categorised into three groups: rigid-body parameters, added inertia, and damping terms.

In most cases, the parameters in the first group are available a priori. A direct observation and measurement are used for obtaining the net buoyancy, W − B, the center of gravity, $r_g = \left[x_g, y_g, z_g\right]^T$, and the center of buoyancy, $r_b = \left[x_b, y_b, z_b\right]^T$. Volumetric displacement, ∇, and moments of inertia may be determined using CAD software. A flooded mass, m, can be inferred from the following relationship: $W - B = (m - \rho\nabla)g$. The second group denotes extra forces and moments that are generated when a vehicle accelerates along or about a particular axis. This is because when the vehicle accelerates, it needs to overcome not only the inertia of itself but also the inertia of some volume of the surrounding fluid that moves with the vehicle. The added inertia can be determined mathematically using 2D-strip theory or 3D-potential theory or commercial programs that work based on these theories [64]. For a simple shaped vehicle, these terms can also be determined using empirical formulae, see the book by Korotkin [65] for instance. For the complex shaped vehicle, Tang [66] has suggested considering the vehicle body as multiple simple-shaped components. Then the added inertia is estimated for each component separately.

The parameters in the third group, damping terms, may be determined experimentally using the rotating-arm tests and the planar motion mechanism (PMM) tests [67]. These tests also yield added masses and moments of inertia. Skjetne et al. [68] have proposed towing tank tests at different surge and sway speeds. Forces and moments correspond to each case were measured for identifying the diagonal surge and sway cross-flow damping terms, $\left\{X_u, X_{|u|u}\right\}$ and $\left\{Y_v, Y_{|v|v}, N_v, N_{|v|v}\right\}$, respectively. Computational fluid dynamics (CFD) approaches have been employed by Yang et al. [69], avoiding the need for the expensive experimental facility.

Fossen and Ross [64] have suggested an alternative approach to identify the damping terms using the least squares optimization approach. Initially, a priori information of the actual vehicle was exploited, and the partially known model was constructed accordingly. The damping terms were then regulated so that the model response matched to the reference vehicle response that had already been obtained through experiments. An infield automated system identification has been presented by Hong et al. [70] for a yaw dynamics modeling. The vehicle was

demanded to undergo a set of actuator settings, providing a newly measured response that was fitted in situ into the model parameters using the recursive least square (RLS) technique. These model parameters are detailed in Tables 4.3 and 4.4.

Hydrodynamic coefficients of AUV system are shown as in Table 4.2.

Table 4.2. Hydrodynamic coefficients of UV

Notation	Definition	Value	Unit
$X_{\dot{u}}$	*Added mass in surge movement*	*-18.5*	*kg*
$Y_{\dot{v}}$	*Added mass in sway movement*	*-28.0*	*kg*
$Z_{\dot{w}}$	*Added mass in heave movement*	*-46.0*	*kg*
$K_{\dot{p}}$	*Added mass in roll movement*	*-1.3*	$\mathrm{kg.m^2}$
$M_{\dot{q}}$	*Added mass in pitch movement*	*-6.8*	$\mathrm{kg.m^2}$
$N_{\dot{r}}$	*Added mass in yaw movement*	*-5.9*	$\mathrm{kg.m^2}$
X_u	*Linear damping in surge movement*	*-10*	$\mathrm{kg/sec}$
Y_v	*Linear damping in sway movement*	*0*	$\mathrm{kg/sec}$
Z_w	*Linear damping in heave movement*	*0*	$\mathrm{kg/sec}$
K_p	*Linear damping coefficient for roll movement*	*-0.223*	$\mathrm{Nm\,sec/rad}$
M_q	*Linear damping coefficient for pitch movement*	*-1.918*	$\mathrm{Nm\,sec/rad}$
N_r	*Linear damping coefficient for yaw movement*	*-1.603*	$\mathrm{Nm\,sec/rad}$
X_{uu}	*Quadratic damping in surge movement*	*-227.18*	$\mathrm{kg/m}$
Y_{vv}	*Quadratic damping in sway movement*	*-405.41*	$\mathrm{kg/m}$
Z_{ww}	*Quadratic damping in heave movement*	*-478.03*	$\mathrm{kg/m}$
K_{pp}	*Quadratic damping coefficient for roll movement*	*-3.212*	$\mathrm{Nm\,sec^2/rad^2}$
M_{qq}	*Quadratic damping coefficient for pitch movement*	*-14.002*	$\mathrm{Nm\,sec^2/rad^2}$

N_{rr}	*Quadratic damping coefficient for yaw movement*	*-12.937*	$\mathrm{Nm\,sec^2/rad^2}$

4.11 Numerical Solution for Equations of Motion

The *m* DOF dynamics model in a matrix formation are recalled as expressed:

$$\dot{\eta} = J(\eta)v, \tag{4.103}$$

$$M\dot{v} + C(v)v + D(v)v + g(\eta) = \tau - \Delta\tau \tag{4.104}$$

Eq. (4.104) can be re-arranged to yield the following:

$$\dot{v} = M^{-1}\left[\tau - \Delta\tau - C(v)v - D(v)v - g(\eta)\right] \tag{4.105}$$

Eqs. (4.103) and (4.105) may be combined and expressed as one set of first-order ordinary differential equations (ODEs) as follows:

$$\begin{bmatrix} \dot{v} \\ \dot{\eta} \end{bmatrix} = \begin{bmatrix} -M^{-1}\left(C(v) + D(v)\right) & 0_{m\times m} \\ J(\eta) & 0_{m\times m} \end{bmatrix} \begin{bmatrix} v \\ \eta \end{bmatrix} + \begin{bmatrix} M^{-1}\left(\tau - \Delta\tau - g(\eta)\right) \\ 0_{m\times 1} \end{bmatrix} \tag{4.106}$$

Given a vehicle's current state and control forces as an initial condition, a next state of the vehicle can be computed using one of the ODE solvers. According to Fossen [60], The Runge–Kutta 4th order method has the largest stability region among other candidate methods; hence, it is adopted for solving the equations of motion. For further details on the stability region of ODE numerical methods, see Butcher [71].

The current time step and the next time step are denoted by subscripts *i* and *i + 1*, respectively. All terms on the right hand side of Eq. (4.106) at i^{th} time step is referred to as a whole by $\Omega(v_i, \eta_i, \tau_i)$. Therefore, the equation becomes:

$$\begin{bmatrix} \dot{v} \\ \dot{\eta} \end{bmatrix} = \Omega(v_i, \eta_i, \tau_i) \tag{4.107}$$

It is assumed that control forces vector, τ_i, at i^{th} time step remains a constant throughout the time interval, Δt. With Runge–Kutta 4th order technique, a closed-form solution for the equations is expressed in a discrete form as follows:

$$\begin{bmatrix} v_{i+1} \\ \eta_{i+1} \end{bmatrix} = \begin{bmatrix} v_i \\ \eta_i \end{bmatrix} + \frac{\Delta t}{6}\left(k_1 + k_2 + k_3 + k_4\right) \tag{4.108}$$

Where

$$
\begin{aligned}
k_1 &= \Omega\left(\left[v_i, \eta_i\right]^T, \tau_i\right) \\
k_2 &= \Omega\left(\left[v_i, \eta_i\right]^T + \frac{\Delta t}{2} k_1, \tau_i\right) \\
k_3 &= \Omega\left(\left[v_i, \eta_i\right]^T + \frac{\Delta t}{2} k_2, \tau_i\right) \\
k_4 &= \Omega\left(\left[v_i, \eta_i\right]^T + \Delta t k_3, \tau_i\right)
\end{aligned}
\tag{4.109}
$$

4.12 General Structure and Model Parameters

4.12.1 Structure of AUV

The hull of the UV is streamlined for minimization of the effect of ocean currents. The shape of UUV is shown in Fig. 4.6. By using three thrusters, it can control surge, sway and yaw. The seven thrusters are deployed at a symmetric angle, suitable for six DOF motion control for dynamic positioning and attitude control in the UUV as shown in Fig. 4.6. The four horizontal thrusters are used to generate autonomous navigation, and the three vertical thrusters are designed for heaving, pitching, and rolling motion.

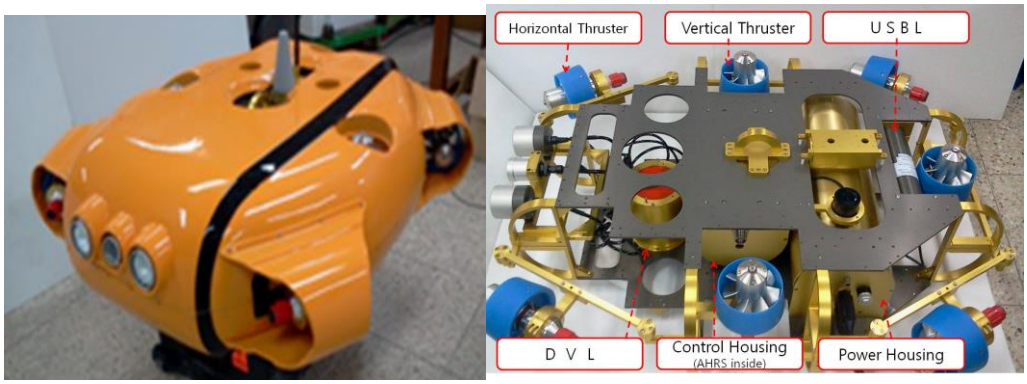

Fig. 4.6 The developed 6-DOF of UUV.

The key components of the hull are largely composed of the body, control housing, power housing, battery housing, tether cable, manipulator, thrusters, sensors as in the Doppler Velocity Logger (DVL), and ultimate short base line (USBL), as shown in Fig. 4.6. The architecture of the UV is designed. Its size is designed to have a midium size and light weight as possible. The frame is made of an alluminum plate. Mechanism specification and parameters for simulation of the UV are given in Table 4.3 and Table 4.4.

Table 4.3. Mechanism specification of the UV

Classification	UV
Size	*560×750×280 mm*
Weight	*80kgf*
Max depth	*200m*
actuators	*300W BLDC motor× 7*
Degree of Freedom (D.O.F)	*6*
Battery housing	*1*
Power housing	*1*
Controller housing	*1*

Table 4.4. UV Parameters

Notation	Definition	Value	Unit
L_H	*Length of UV*	*0.75*	*m*
B_H	*Width of UV*	*0.56*	*m*
H_H	*Height of UV*	*0.28*	*m*
m_H	*Mass of UV*	*80*	*kgf*
g	*Gravity Acceleration*	*9.81*	m/s^2
ρ	*Density of water*	*1025*	kg/m^3
W_H	*Weight of UV*	*784.8*	*N*
B	*Buoyancy force*	*784.8*	*N*
CB	*Center of buoyancy*	$(0,0,-0.06)$	*m*
CG	*Center of gravity*	$(0,0,0)$	*m*
I_{xx}	*Mass Moment of Inertia about x-axis*	*6.9*	$kg.m^2$

I_{yy}	*Mass Moment of Inertia about y-axis*	*26.1*	$kg.m^2$
I_{zz}	*Mass Moment of Inertia about z-axis*	*23.2*	$kg.m^2$
I_{xy}	*Cross Product of Inertia about xy-axes*	*0*	$kg.m^2$
I_{yz}	*Cross Product of Inertia about yz-axes*	*0*	$kg.m^2$
I_{xz}	*Cross Product of Inertia about xz-axes*	*0*	$kg.m^2$

4.12.2 Control System of AUV

The USV's control system is shown in Fig. 4.7. DVL and USBL sensors are used to control AUV position and attitude and control the path by line-of sight method.

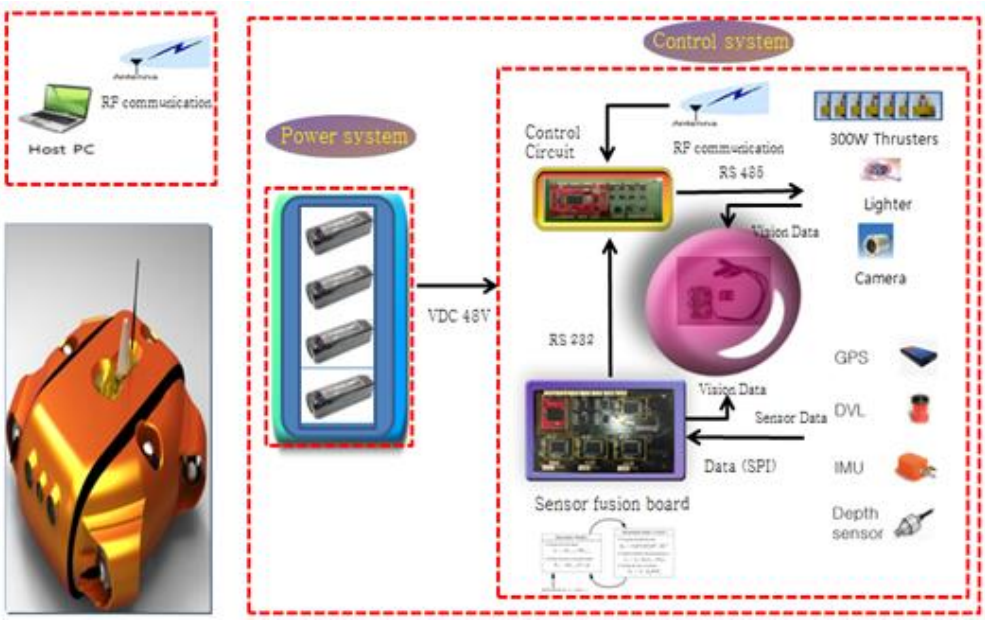

Fig. 4.7 Control system of AUV.

Chapter 5: Guidance Theory

Guidance laws are typically equivalent to kinematic controllers which consider the geometrical aspects of motion, without reference to forces and moments. When considering motion of a vehicle it is useful to distinguish between two types of operation spaces, namely work space and configuration space [72]. The work space represents the physical space which the vehicle moves. This contains a 2-dimensional work space for planar motion such as a USV, while a 3-dimensional work space for spatial position such as an AUV. The configuration space is the set of variables sufficient to specify the location of every point on a rigid-body vehicle. The guidance system receives desired waypoints and surge speed as inputs, and then calculates the desired path. The maneuvering problem and how the guidance system works together with the control law are explained below with a polynom of lower degree for simplicity (see [73] for a complete description of the guidance system). There are several guidance methods for marine vehicles. However, in this dissertation, two methods are presented: way point guidance by line-of-sight and way point guidance based cubic polynomial theory.

5.1 Configuration of GNC System

A marine vehicle control system consists of three independent blocks denoted as a GNC system. The word of GNC is a reference system (guidance), a sensor system (navigation) and a feedback control system [63]. Performance of the vehicle is restricted by capability and reliability of the GNC system [74]. In this section, a typical GNC system is introduced briefly. These three blocks interact with each other through data and signal transmission as illustrated in Fig. 5.1. This figure shows a conventional vehicle autopilot.

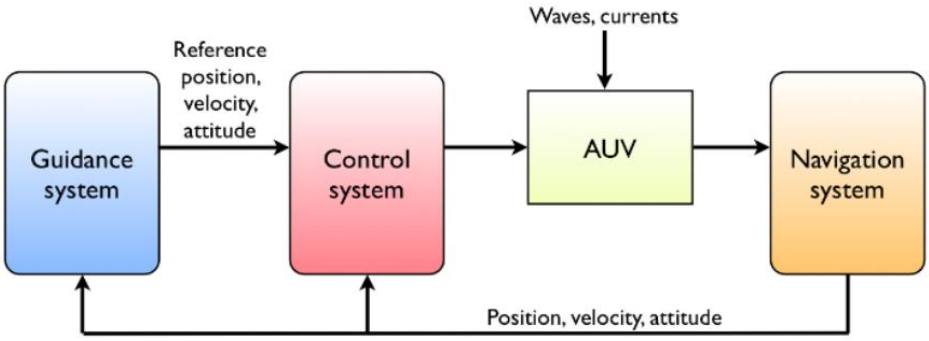

Fig. 5.1 Typical GNC for vehicle.

5.1.1 Guidance

Definition: The action or the system that continuously computes the reference (desired) position, velocity and acceleration of a vessel to be used the control system.

The guidance system generates references where to go. Cost functions can be adopted to make the optimal references with respect to fuel, time, weather conditions and etc. According to the vehicle's tasks, way-points, trajectory or path may be generated.

5.1.2 Navigation

Definition: Providing estimates of its position, course, and distance traveled (velocity and acceleration are determined as well).

Position, attitude, velocity are measured or estimated for localization, mapping or SLAM (Simultaneous Localization and Mapping) by the navigation system. Moreover, states of targets (ex. Docking station) are also measured by the navigation system. The most difficult problem for localization of the AUV is that there is no single proprioceptive position sensor [75]. GPS systems cannot be applied in underwater. In many cases, a system consisted of multi-sensors is demanded for localization. For underwater navigation, LBL (Long baseline), SBL (Short baseline), USBL (Ultra-short baseline) which are based on acoustic sensors are mainly used.

5.1.3 Control

Definition: The action of determining the necessary control forces and moments to be provided by the vessel in order to satisfy a certain control objectives.

The control system generates control inputs for the vehicle to follow references. A precise and low-uncertainty model is required to achieve control objectives efficiently and exactly. However, in the case of the AUV, getting a precise mathematical model is not easy. It is very difficult to obtain precise hydrodynamic coefficients and uncertainties are imposed caused by fluid motion [76]. Moreover, dynamic characteristics are varying with respect to advance speed. Many nonlinear terms exist in the equations of motion. But, fortunately, many terms of nonlinearity can be negligible according to the shape of the vehicle or speed [77]. Therefore, a simplified model that reflects the most important and dominant parts of the dynamics are usually adopted for the control plant model. For prediction and motion simulation, the most accurate model of the vehicle should be used [75]. When the simplified model is used, the stability and performance are guaranteed near operating points only [77]. In the case of an under-actuated vehicle, Brockett's

necessary condition is not satisfied [78]. Then, a time-invariant continuous state feedback controller is not able to guarantee stability.

5.2 Maneuvering Problem Statement

In maneuvering, time t is not used to parametrize the desired motion. Instead, the objective is twofold. The main task is to converge to and follow a desired path. The second task is to satisfy a desired dynamic behaviour along the path [79]. This motivates the following definitions.

Definition 1: A parametrized path is a geometric curve continuously parametrized by a variable θ.

Definition 2: The maneuvering problem is to design a controller that solves the following two tasks:

Geometric task: The main goal for this controller is to have the ship follow a parameterized path. The position of the ship is given by $\eta_s(t)$ and the desired position is given by $\eta_d(\theta(t))$. The geometric task is concerned with reducing the distance between the position of the ship and desired path over time, thus the task can be expressed as:

$$\lim_{t\to\infty}\left|\eta_s(t)-\eta_d(\theta(t))\right|=0 \tag{5.1}$$

Dynamic task: The ship should also follow a given dynamic behavior. Skjetne [80] mentions three different desired dynamic behaviors:

- **Time assignment**: With the time assignment the ship has to be at specific points along the path at specific time instants.
- **Speed assignment:** With the speed assignment the ship should try to obtain a specific speed along the path. The desired speed is expressed by the function $\upsilon_s(\theta,t)$.
- **Acceleration assignment:** With the acceleration assignment the ship should obtain a desired acceleration along the path.

The speed assignment is considered the most suitable dynamic assignment for this task. The dynamic task can therefore be expressed as:

$$\lim_{t\to\infty}\left|\dot{\theta}(t)-\upsilon_s(\theta(t),t)\right|=0 \tag{5.2}$$

Where, $\dot{\theta}(t)$ is the path speed and $\upsilon_s(\theta(t),t)$ is the desired speed.

Note that in order to solve the maneuvering problem, the controller decides the dynamics of the variable, i.e. the desired position $\eta_d(\theta)$ for the surface vessel to follow. The maneuvering problem is turned into an ordinary tracking problem by letting.

$$\dot{\theta}(t) = \upsilon_s(\theta, t) \tag{5.3}$$

Then the desired position moves independently along the path with respect to the controller.

5.3 Guidance Objectives

5.3.1 Target Tracking

If the objective of a marine craft is to follow a target where no information about the targets path is available beforehand, a target tracking scenario should be considered. Advances in this topic traces back to missile guidance, in which a missile is controlled to destroy a given target. In marine applications, missile is substituted for interceptor, where the objective is for the interceptor to converge to a target. The objective is formulated as:

$$\lim_{t\to\infty} \left| p(t) - p_t(t) \right| = 0 \tag{5.4}$$

where $p(t) = \left[x(t), y(t), z(t) \right]^T$ is the position of the craft, while $p_t(t) = \left[x_t(t), y_t(t), z_t(t) \right]$ is the position of the target at time *t*. This definition is consistent with [81, 82].

5.3.2 Trajectory Tracking

A control system that forces the system output $y(t) \in R^m$ to track a desired output $y_d(t) \in R^m$ solves a trajectory tracking problem.

This means that in order to solve the trajectory tracking problem we want to generate a trajectory such that

$$\lim_{t\to\infty} \left| y(t) - y_d(t) \right| = 0 \tag{5.5}$$

This scenario is equivalent to considering a virtual target that follows a predefined path, which in some literature is called path-tracking. Thus, the problem could be solved using target tracking guidance laws. Differentiating $y_d(t)$ once will reveal the desired velocities, and a second differentiation will reveal the desired accelerations. This means that information about the desired state, and the differentiated states are available for the controller.

5.4 Waypoint Representation

Another important thing for the navigation system is that it has to know the point where the vehicle has to move to next to make sure that the orientation is correct. When the vehicle moves to a point, it will normally move straight forward, but in the case of many points a route is necessary. In this case waypoints are used. Fig. 5.2 illustrates the block diagram of how the waypoint representation is included in the process of controlling and navigating a vehicle.

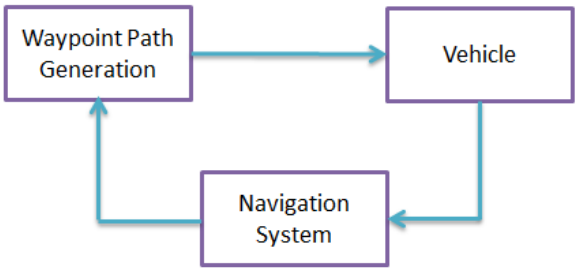

Fig. 5.2 Waypoint representation.

Way-points are used for specifying the route of a vehicle. The way-points are defined using Cartesian coordinates:

$$(x_k, y_k, z_k) \;\; for \;\; i = 1,...,n \tag{5.6}$$

The collection of waypoints is called the database and it consists of:

$$wpt.pos = \{(x_0, y_0, z_0), (x_1, y_1, z_1), ..., (x_n, y_n, z_n)\} \tag{5.7}$$

Because it is an underwater vehicle three coordinates are necessary. Additional waypoint properties can be added. These properties could be speed, heading etc. i.e.:

$$wpt.speed = \{U_0, U_1, ..., U_n\} \tag{5.8}$$

$$wpt.heading = \{\psi_0, \psi_1, ..., \psi_n\} \tag{5.9}$$

This means that the vehicle is passing through waypoint 1 at speed U_1 and with the heading ψ_1. The waypoint database is usually designed using many different criteria, which normally is based on:

- Mission
- Environmental data
- Geographical data
- Obstacles

- Collision avoidance
- Feasibility

The environmental data covers information of wind, waves and sea currents. The information can be used for optimal routing of the vehicle to consume the least amount of energy. Additionally it can be used to avoid really bad weather for safety reasons. It can also be possible to continuously update these if they are varying over time.

The geographical data is information about islands, shallow waters etc. The obstacles are all the constructions, floating constructions and other obstacles. All of these obviously have to be avoided.

The mission is the journey and the vehicle is on from the starting point (x_0, y_0, z_0) to the terminal point (x_n, y_n, z_n) via the way-points (x_i, y_i, z_i).

5.5 Path Following

Consider a straight line between two way-points $p_k^n = [x_k, y_k]^T$ and $p_{k+1}^n = [x_{k+1}, y_{k+1}]^T$, and define a path-fixed reference frame with a rotation angle.

$$\alpha_k = \arctan 2(y_{k+1} - y_k, x_{k+1} - x_k) \in S \tag{5.10}$$

The coordinates of the vehicle in the path-fixed reference frame is $\varepsilon(t) = [s(t), e(t)]^T \in R^2$ where.

$$s(t) = along - track\ error$$

$$e(t) = cross - track\ error$$

If the objective of the path following is considered as primarily a spatial constraint, then the path following problem is solved by defining the control objective:

$$\lim_{t \to \infty} e(t) = 0 \tag{5.11}$$

5.6 Line of Sight (LOS) Waypoint Guidance

Guidance is defined by Shneydor [60] as “The process for guiding the path of an object towards a given point, which in general may be moving”. A commonly used method for path-following is the Line of Sight (LOS) method. In this case, the guidance system is composed of a speed and LOS guidance law, where the LOS law computes a heading reference and the speed law computes a velocity reference.

These can be combined in different ways to achieve different motion control objectives.

Line of Sight is a three-point guidance scheme [83] since it is based on three points: A reference point (normally stationary, for instance p_k), the position of the marine vehicle (p(t)) and the desired position. LOS can be used to track a moving target, in which case the desired position is time-varying ($p_t(t)$), or to track a certain path, in which case the goal is the next waypoint (p_{k+1}). The focus for this dissertation is path-following, so LOS as target tracking is disregarded from this point on. Fig. 5.3 illustrates the LOS concept for a surface vehicle (this is simpler than an underwater vehicle since a surface vehicle is limited to a plane). The desired path is the straight line in light blue between p_k and p_{k+1}, and the vehicle is at position p(t), marked in red. In the NED reference frame the x-axis points north and the y-axis points east. However, the path can be specified in a path-fixed reference frame with origin in p_k and x-axis pointing toward p_{k+1}. This reference frame is illustrated in dark blue.

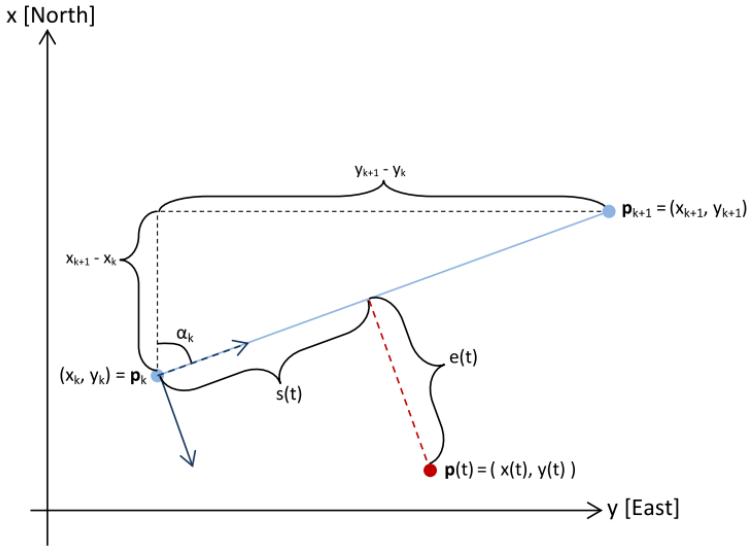

Fig. 5.3 Illustration of LOS guidance for surface vessels.

The vehicle is in position p(t) and should navigate towards and converge to the path given as the straight line between p_k and p_{k+1}. To simplify the calculations, the NED reference system is translated so the origin is in p_k and rotated so the x-axis points toward p_{k+1}. The position of the vehicle in this reference frame is given as $\varepsilon(t) = [s(t), e(t)]^T$

The path fixed coordinate system is defined by rotating the NED coordinate system α_k degrees about the z-axis and then translating the rotated coordinate system so the origin is placed in p_k . As can be seen from Fig.5.3, α_k is defined as:

$$\alpha_k = \arctan\left(\frac{y_{k+1} - y_k}{x_{k+1} - x_k}\right) \tag{5.12}$$

The transformation from NED to the path-fixed frame is then given as

$$\varepsilon(t) = \begin{bmatrix} s(t) \\ e(t) \end{bmatrix} = \left[R_{z,\alpha_k}(\alpha_k)\right]^T \left(p(t) - p_k^n\right) \tag{5.13}$$

Where

$$R_{z,\alpha_k}(\alpha_k) = \begin{bmatrix} \cos(\alpha_k) & -\sin(\alpha_k) \\ \sin(\alpha_k) & \cos(\alpha_k) \end{bmatrix} \tag{5.14}$$

As shown in Fig. 5.3, s(t) is the along-track distance and e(t) is the cross-track error. The control objective is to make the vehicle converge to the straight line and follow it. Mathematically, this corresponds to e(t) becoming 0, so the control objective is given as:

$$\lim_{t\to\infty} e(t) = 0 \tag{5.15}$$

There are two approaches to achieve this: Enclosure-based and look-ahead-based steering.

5.6.1 Enclosure-Based Steering

In enclosure-based steering a virtual circle with radius R and center in p(t) is considered as shown in Fig. 5.4. The circle will intersect the straight line at two points (provided the radius is large enough). The point p_{los} marked in green is the intersection point closest to the desired direction of travel (towards p_{k+1}).

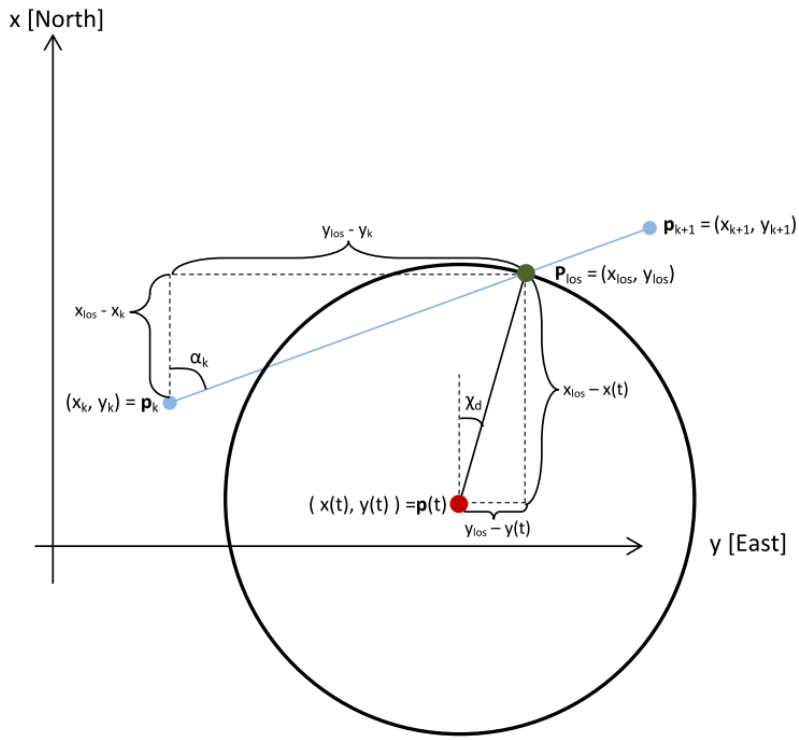

Fig. 5.4 Illustration of enclosure-based LOS steering.

The guidance law uses p_{los} to calculate the desired course angle $\mathrm{X}_d(t)$. As such, it is necessary to compute x_{los} and y_{los}. By geometric considerations, p_{los} can be calculated by solving the equation set below:

$$\left[x_{los} - x(t)\right]^2 + \left[y_{los} - y(t)\right]^2 = R^2 \tag{5.16}$$

$$\tan(\alpha_k) = \frac{y_{los} - y_k}{x_{los} - x_k} \tag{5.17}$$

Once p_{los} is known, the desired course angle can be decided using Eq. (5.18).

$$\tan(\mathrm{X}_d(t)) = \frac{y_{los} - y_k}{x_{los} - x_k} \tag{5.18}$$

5.6.2 Look-ahead Based Steering

This method of LOS is computationally easier than enclosure-based guidance. Rather than calculating a point p_{los}, it uses a design parameter $\Delta > 0$ referred to as the look-ahead distance. In general, Δ may vary as a function of time, e or other parameters. However, it is often chosen to be constant.

In this approach of LOS, the desired course angle is the sum of two angles:

$$X_d(e) = \alpha_k + X_r(e) \tag{5.19}$$

Where, α_k is defined in Eq. (5.12), and $X_r(e)$ is the path relative angle illustrated in Fig. 5.5.

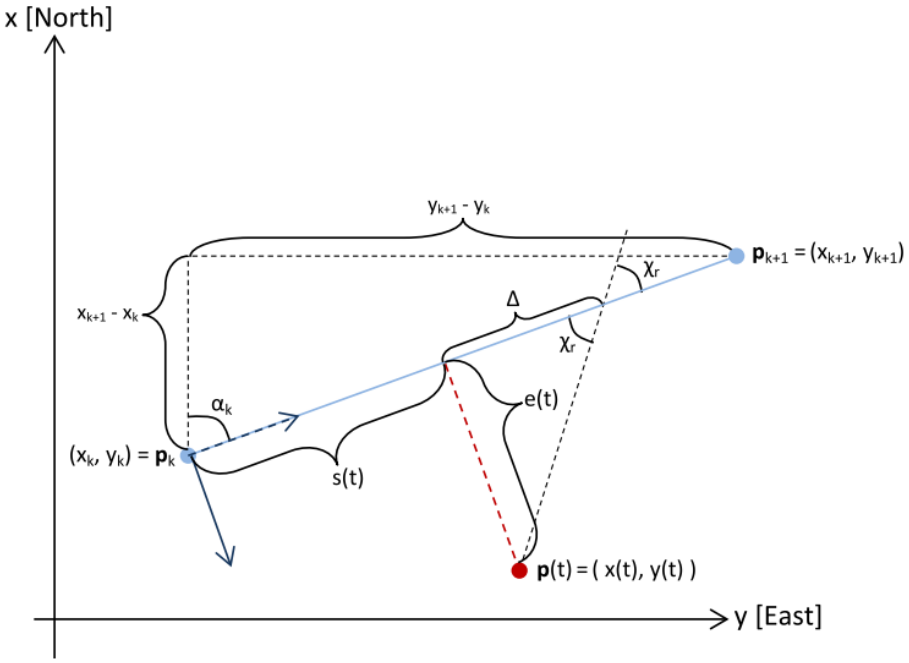

Fig. 5.5 Illustration of look-ahead-based LOS steering.

This angle depends on the cross-track error e and the look-ahead distance $\Delta > 0$ and is defined in equation.

$$X_r(e) = \arctan\left(-\frac{e}{\Delta}\right) \tag{5.20}$$

5.6.3 LOS Control

By using the task classification introduced by [79], the problem statement is established with the following two task objectives:

LOS Geometric Task: Force the ship position p to converge to a desired path by forcing the heading angle ψ to converge to the LOS angle ψ_{los} given by:

$$\psi_{los} = a\tan 2(y_{los} - y, x_{los} - x) \tag{5.21}$$

That is:

$$\lim_{t\to\infty}\left|\psi(t)-\psi_{los}(t)\right|=0 \tag{5.22}$$

where the four quadrant inverse target function ensures that:

$$\psi_{los}\in\left\langle -\pi,\pi\right\rangle \tag{5.23}$$

The LOS position $p_{los}=\left[x_{los},y_{los}\right]^T$ is the point on the path which the ship is supposed to point at.

LOS Dynamic Task: Force the surge speed u of the vehicle to converge to a desired surge speed u_d , that is:

$$\lim_{t\to\infty}\left|u(t)-u_d(t)\right|=0 \tag{5.24}$$

The first task is to reach and follow a desired path by utilizing a LOS projection algorithm. The basis for the LOS guidance and its implications towards positional convergence is treated above. The second task is used to satisfy a dynamic specification. The prescribed speed is given along the body-fixed x-axis of the ship, and will be identical to the path speed once the ship has converged to the path. Thus, the desired speed profile along the path can be assigned dynamically.

5.7 Cubic Polynomial for Path-Following

A simple way of doing it is to use circles and straight lines to connect the way-points. The disadvantage of this method is the vehicle has to follow a new line a jump in the yaw angle occurs. Therefore another method is use. This method generated a path using splines. Every waypoint also has to be feasible, meaning it has to be possible for the vehicle to manoeuver to the next waypoint without exceeding the limits in speed, turning rate etc.

Another way to make a path in this dissertation is to use the spline interpolation that creates a smoother path for vehicle. A spline consists of polynomial interpolation and is often used because it is more numeric stable then the fully polynomial interpolation in terms of oscillations between the way-points [84]. The cubic polynomials are given as [63]:

$$\begin{aligned} x_d(\theta)&=a_3\theta^3+a_2\theta^2+a_1\theta+a_0\\ y_d(\theta)&=b_3\theta^3+b_2\theta^2+b_1\theta+b_0\\ z_d(\theta)&=c_3\theta^3+c_2\theta^2+c_1\theta+c_0 \end{aligned} \tag{5.25}$$

Where

- $\left(x_d(\theta),y_d(\theta),z_d(\theta)\right)$ is the position of the vehicle.

- θ is the path variable, $\dot{\theta} = f(\theta, t)$
- a, b and c are the coefficients.

The algorithm for a cubic spline is given in the following.

If the path of the vehicle passes through way-point (x_{k-1}, y_{k-1}) and (x_k, y_k) it has to satisfy:

$$\begin{aligned} &x_d(\theta_{k-1}) = x_{k-1},\ x_d(\theta_k) = x_k \\ &y_d(\theta_{k-1}) = y_{k-1},\ y_d(\theta_k) = y_k \\ &z_d(\theta_{k-1}) = z_{k-1},\ z_d(\theta_k) = z_k \end{aligned} \tag{5.26}$$

Where $k = 1 \ldots n$. The boundary conditions for a cubic spline have to be the same before and after the way-point:

$$\begin{aligned} &x'_d(\theta_0) = x'_0,\ x'_d(\theta_n) = x'_n \\ &y'_d(\theta_0) = y'_0,\ y'_d(\theta_n) = y'_n \\ &z'_d(\theta_0) = z'_0,\ z'_d(\theta_n) = z'_n \end{aligned} \tag{5.27}$$

The same follows for the second derivative.

The parameters of the polynomials for n-waypoints are given in a vector:

$$x = \left[a_k^T, \ldots, a_{n-1}^T\right]^T \tag{5.28}$$

From this a linear form of the cubic interpolation can be expressed as:

$$y = A(\theta_{k-1}, \ldots, \theta_k)\, x, \qquad k = 1, 2 \ldots n \tag{5.29}$$

Where, A consists of the polynomial variables and x is the polynomial parameters.

$$y = \left[x_{start}, x_0, x_1, x_1, 0, 0, x_2, x_2, 0, 0 \ldots, x_n, x_{final}\right]^T \tag{5.30}$$

Where, x is the position in the x along the x-axis. Y and z are determined in the same way with respect to their polynomial coefficients.

The conditions for the endpoints are defined by constrains for the velocity and the acceleration:

$$x_{start} \in \left\{x'_0, x''_0\right\}, \quad x_{final} \in \left\{x'_n, x''_n\right\} \tag{5.31}$$

And, A is given as a matrix:

$$A=\begin{bmatrix} C_{start} & 0_{1\times4} & 0_{1\times4} & \dots & 0_{1\times4} \\ p(\theta_0) & 0_{1\times4} & 0_{1\times4} & \dots & 0_{1\times4} \\ p(\theta_1) & 0_{1\times4} & 0_{1\times4} & \dots & 0_{1\times4} \\ 0 & p(\theta_1) & 0_{1\times4} & \dots & 0_{1\times4} \\ -\upsilon(\theta_1) & \upsilon(\theta_1) & 0_{1\times4} & \dots & 0_{1\times4} \\ -a(\theta_1) & a(\theta_1) & 0_{1\times4} & \dots & 0_{1\times4} \\ 0_{1\times4} & p(\theta_2) & 0_{1\times4} & \dots & 0_{1\times4} \\ 0_{1\times4} & 0_{1\times4} & p(\theta_2) & \dots & 0_{1\times4} \\ 0_{1\times4} & -\upsilon(\theta_2) & \upsilon(\theta_2) & \dots & 0_{1\times4} \\ 0_{1\times4} & -a(\theta_2) & a(\theta_2) & \dots & 0_{1\times4} \\ \dots & \dots & \dots & \dots & \dots \\ 0_{1\times4} & 0_{1\times4} & 0_{1\times4} & \dots & p(\theta_n) \\ 0_{1\times4} & 0_{1\times4} & 0_{1\times4} & \dots & C_{final} \end{bmatrix} \tag{5.32}$$

Where,

$$\begin{aligned} p(\theta_k) &= \left[\theta_k^3, \theta_k^2, \theta_k, 1\right] \\ \upsilon(\theta_k) &= p^{'}(\theta_k) = \left[3\theta_k^2, 2\theta_k, 1, 0\right] \\ a(\theta_k) &= p^{''}(\theta_k) = \left[6\theta_k, 2, 0, 0\right] \end{aligned} \tag{5.33}$$

To determine the polynomials the parameters can be determined from:

$$x = A^{-1}y \tag{5.34}$$

Coefficient *b* and *c* are found in the same way.

Chapter 6: Control Algorithm Design and Analysis

A role of a control system is to generate the corrective actuator set-points for regulating the error between the desired and current state of the vehicle. This is normally done in a closed-loop manner. The current state of the vehicle is measured and fed back to the control system to compare with the reference state that is typically provided by the guidance system. The error signal is computed, and then actuator demands are generated accordingly based on the chosen control technique. In order to systematically handle such a challenge on the control performance and power, the control system is split into two cascade modules which are control law and control allocation, see Fig. 6.1.The control law is responsible for determining a generalized force for each degree of freedom that is necessary for achieving the desired response. On the other hand, the control allocation helps to distribute the generalized forces to the available actuators in such a way that the overall system consumes the least power. These two parts of the control system are discussed below.

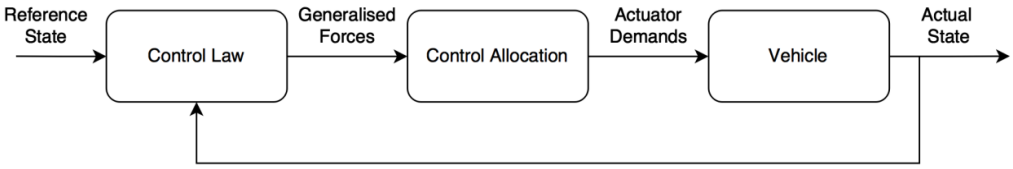

Fig. 6.1 A control system that consists of control law and control allocation modules.

The marine vehicle dynamics can be described by the 3DOF or 6DOF equations of motion with respect to a body-fixed frame. Such a dynamics model is highly nonlinear and involves multiple inputs and multiple outputs (MIMO). There does not appear to be a preferred type of control techniques. The more advanced control systems can serve a better performance at the expense of implementation complexity. On the other hand, the simpler controllers require less computing effort and are thus applicable to vehicles with low-power computers. In this work, only PID, and SMC are discussed in details.

6.1 Proportional Integral Differential (PID) Controller

6.1.1 General Theory

In this dissertation two different control systems will be designed. The first one is a regular Proportional-Integral-Derivative (PID) controller. Fig. 6.2 shows a block diagram of a regular PID controller. PID is the most widely used controller in

the industry because it is easy to implement and maintain. The controller is linear and is here applied to a highly nonlinear system, but it will work nonetheless.

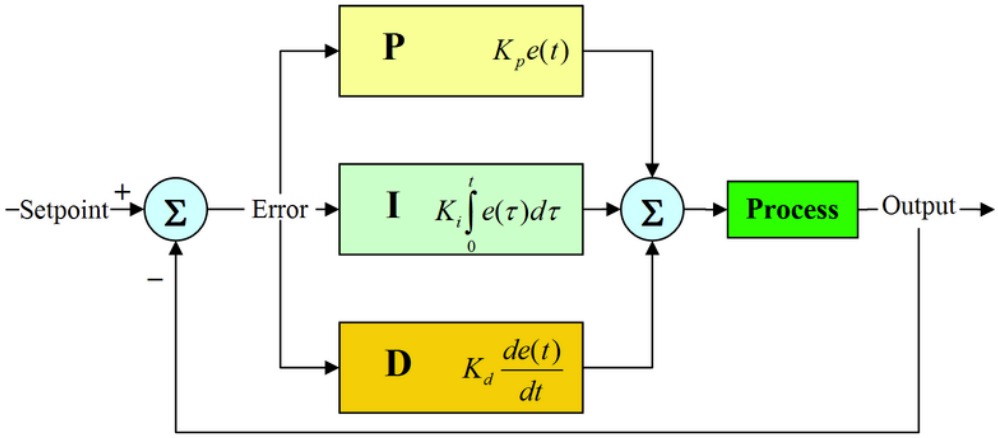

Fig. 6.2 A block diagram of a PID controller.

The aim of a PID controller is to make the error of the signal, the difference between wanted signal and actual signal, as small as possible, i.e. go to zero, by making control signals to the process:

$$\lim_{t\to\infty} e = \lim_{t\to\infty}\left(x_d - x\right) \to 0 \tag{6.1}$$

This can be done with four different controllers as:

- Proportional (P) controller.
- Proportional-Integral (PI) controller.
- Proportional-Derivative (PD) controller.
- Proportional-Integral-Derivative (PID) controller.

All these proposed controllers can be used, based on what kind of behavior that is wanted.

Mathematically, a PID controller can be described as:

$$\tau = K_p e(t) + K_i \int_0^t e(t)dt + K_d \frac{d}{dt} e(t) \tag{6.2}$$

Where, K_p, K_i and K_d represent proportional, integral and derivative gains respectively. By setting one or two of these to zero, you get a P, PI or PD controller. τ is the control signal, which will be sent to the process.

The proportional term gives an output that is proportional to the error. Too high proportional gain K_p can give an unstable process. The integral term K_i is proportional to both the duration of the error and the magnitude of it. The integral term deals with steady-state error by accelerate the movement of the process towards set-point. It can contribute to an overshoot because it responds to accumulated error from the past which can be solved by adding the derivative term. The derivative term K_d slows down the rate of change of the control signal and makes the overshoot smaller. The combined controller-process stability is improved by the derivative term, but it could make the process unstable because it is sensitive to noise in the error signal [85]. By changing the weights or gains on each of the P, I and D parameters, the controller can be fine tuned for specific requirements. Note that the use of the PID algorithm for control does not guarantee optimal control of the system or system stability.

6.1.2 Stability of General PID Controller

Stability of a PID controller is maintained by tuning K_p, K_i and K_d gains properly. They are to be tuned such that the error converges to zero. To find this values for K_p, K_i and K_d, test the control system with the process it is supposed to control, but without the guidance system, and have a constant desired signal. When the error converges to zero within a reasonable time and without too high overshoot and oscillations, the controller is stable. Fig. 6.3 shows different stabilities of PID.

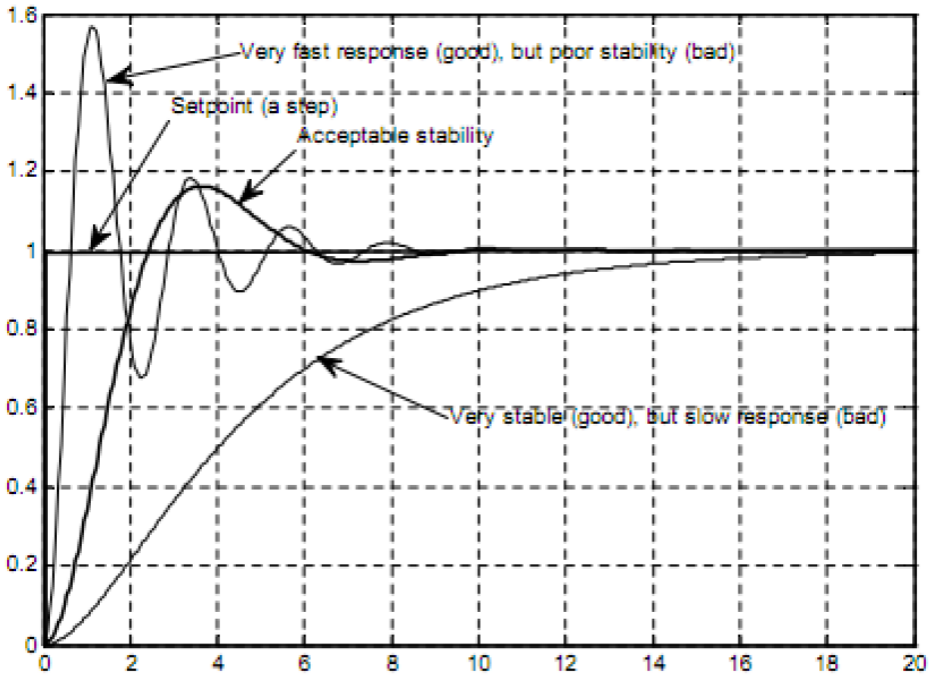

Fig. 6.3 Stability of PID controller [86].

The three different gains within the PID controller all have their own influence. Enlarging the K_p gain will result in a faster response of the controller, although an excessively larger chosen proportional term will lead to instability and oscillation. Enlarging the K_i gain will imply a quicker elimination of steady state errors but the drawback is a larger overshoot. A larger K_d gain will decrease the overshoot but slows down the response of the system and causes signal noise amplification in the differentiation of the error which may lead to instability. The effect of increasing gains is given in Table 6.1 and can also be found in [87].

Table 6.1. Effect of increasing PID control gains [87].

Gains	Rise Time	Overshoot	Settling Time	Steady State Error
Increase K_p	Decrease	Increase	Small Change	Decrease
Increase K_i	Decrease	Increase	Increase	Eliminate
Increase K_d	Small Decrease	Decrease	Decrease	None

Output from the controller exhibits four major measurable characteristics, rise time, overshoot, settling time and steady-state error. In Table 6.1, the rise time is the time required for the system response to rise from 10% to 90% of the final steady state value of the desired response. The overshoot is the maximum peak value of the response curve measured from the desired response of the system. The settling time is the time that is required for the response of the system to reach and stay within a specified error band which is usually chosen symmetrical about the final value. The steady state error is the error that exists as time goes to infinity, when the response reaches a steady state [88].

6.1.3 PID Tuning

"Tuning" a control loop is the process of adjustment of its control parameters to the optimum values for the desired control response. The optimum behavior on a process change or set point change varies depending on the application. Some processes must not allow an overshoot of the process variable from the set point. Other processes must minimize the energy expended in reaching a new set point. Generally stability of response is required and the process must not oscillate for any combination of process conditions and set points. Tuning of loops is made more complicated by the response time of the process; it may take minutes or hours for a set point change to produce a stable effect. Some processes have a degree of non-linearity and so parameters that work well at full-load conditions do not work when the process is starting up from no-load. Careful tuning is required to achieve fast response and stability. The gains, K_p, K_i, K_d was tuned manually. There are different methods for tuning a PID controller as shown in Table 6.2, but if a range is known, it is easy to tune them manually by simulating different cases and find what values that will give a satisfying behavior.

Table 6.2. PID tuning

Method	Advantages	Disadvantages
Manual Tuning	*No math required. Online method*	*Requires experienced personnel*
Ziegler-Nichols	*Proven method. Online method*	*Process upset, some trail-and-error, very aggressive tuning.*
Software tools	*Consistent tuning. Online or offline method. May include*	*Some cost and training involved*

	valve and sensor analysis.

6.1.3.1 Manual Tuning

Table 6.3 shows the effects of increasing the control gains. If the system must remain online, one tuning method is to first set K_i and K_d values to zero. Increase K_p until the output of the loop oscillates, then K_p should set to approximately half of that value for a "quarter amplitude decay" type response. Then increase K_i until any offset is corrected in sufficient time for the process. However, too much K_i will cause an instability. Finally, increase K_d if required, until the loop is acceptably quick to reach its reference after a load disturbance. However, too much K_d will cause excessive response and overshoot. A fast PID loop tuning usually overshoots slightly to reach the set-point more quickly; however, some systems can't accept overshoot, in which case an over-damped closed-loop systems is required, which will require a K_p setting significantly less than half that of the K_p setting causing oscillation.

Table 6.3. Effects of increasing a parameter independently.

Parameter	Rise time	Overshoot	Settling time	Steady-state error	Stability
K_p	*Decrease*	*Increase*	*Small change*	*Decrease*	*Degrade*
K_i	*Decrease*	*Increase*	*Increase*	*Decrease*	*Degrade*
K_d	*Minor Decrease*	*Minor Decrease*	*Minor Decrease*	*No effect*	*Improve if* K_d *small*

6.1.3.2 Ziegler-Nichols Method

As in the method above, K_i and K_d gains are first set to zero. The K_p gain is increased until it reaches the ultimate gain, K_u, at which the output of the loop starts to oscillate. The K_u and the oscillation period P_u are used to set the gains as shown Table 6.4.

Table 6.4. Ziegler-Nichols method

Control Type	K_p	K_i	K_d
P	$0.5\,K_u$		
PI	$0.45\,K_u$	$1.2\,K_p\ /\ P_u$	
PID	$0.6\,K_u$	$2\,K_p\ /\ P_u$	$K_p\,P_u\ /8$

6.1.3.3 PID Tuning Software

Most modern industrial facilities no longer loop using the manual calculation methods shown above. Instead, PID tuning and loop optimization software are used to ensure consistent results. The software will gather the data, develop process models, and suggest optimal tuning. Some software packages can even develop tuning by gathering data from reference changes. Advances in automated PID loop tuning software also deliver algorithms for tuning PID loops in a dynamic or Non-Steady State (NSS) scenario. The software will model the dynamics of a process, through a disturbance, and calculate PID control parameter in response.

In this dissertation, PID gains are obtained from auto-tuning options of MATLAB PID block. These values are used as initial guesses for MATLAB Response Optimization Toolbox. Final gain values for PID controller are found by the toolbox.

6.1.4 Nonlinear PID for Marine Vehicles

By calculating the difference between the desired and estimated state, the controller typically calculates the forces and moments needed to minimize the error. These desired forces and moments are the sent to the control allocation. The controller that is implemented on the ROV control system is a nonlinear PID. The nonlinear PID control is found in [60], and is used due to being robust and can easily be tuned [89]. The control law is given for each controlled degree of freedom of the form as:

$$\tau_{PID} = -J^T(\eta)\left(K_p\tilde{\eta} + K_d J(\eta)\nu + K_i \int_0^t \tilde{\eta}(\tau)d\tau \right) \tag{6.3}$$

Where $\tilde{\eta} = \eta - \eta_d$ and $\dot{\tilde{\eta}} = \nu - \nu_d$ are the position and velocity tracking error vectors, respectively, in body coordinates, and K_p, K_i, and $K_d \in R^{6\times 6}$ are diagonal gain matrices, and τ_{PID} is the vector of net forces and moments commanded to the vehicle thruster system.

6.1.5 Nonlinear PD for Marine Vehicles

By setting K_i to zero, we get a PD controller, the basic PD controller for a single-degree-of-freedom takes the form:

$$\tau_{PD} = -J^T(\eta)\left(K_p\tilde{\eta} + K_d J(\eta)\nu\right),\ K_p, K_d > 0 \tag{6.4}$$

Where K_p and K_d are scalar error feedback gains. The state error coordinates are defined as:

$$\begin{aligned} \tilde{\eta}(t) &= \eta_d(t) - \eta(t), \\ \tilde{\nu}(t) &= \nu_d(t) - \nu(t), \\ \dot{\tilde{\nu}}(t) &= \dot{\nu}_d(t) - \dot{\nu}(t), \end{aligned} \tag{6.5}$$

Where $\dot{\tilde{\nu}}(t)$, $\tilde{\nu}(t)$, and $\tilde{\eta}(t)$ are the desired acceleration, velocity, and position. Note that $\tilde{\nu}(t) = \dfrac{d(\tilde{\eta}(t))}{dt}$.

6.1.6 Stability of Designed PD Controller

The control objective is to ensure that the endpoint of the vehicle is maintained at the same position with respect to the target. This case is a regulation problem since the target point fixed and not moving hence, the control law is designed as a regulation problem. The control objective is stated as follows:

$$z \to z_d, \quad \nu \to \nu_d \quad as \quad t \to \infty \tag{6.6}$$

where $z = \begin{bmatrix} x_t & y_t & z_t & \phi_t & \theta_t & \psi_t \end{bmatrix}^T$, $\nu = \begin{bmatrix} u & v & w & p & q & r \end{bmatrix}^T$ and z_d and ν_d are the desired states of z and v, respectively. The vehicle must be maintained in its position, hence z_d = constant and $\nu_d = 0$. The orientations are properly determined according to the circumstances.

Our vehicle's dynamic model (Eq. (4.96)) is a nonlinear system, and hence, we use the Lyapunov function for the stability analysis. The Lyapunov function candidate for the system is as follows:

$$V = \frac{1}{2}\hat{\nu}^T M\hat{\nu} + \frac{1}{2}e^T K_p e \tag{6.7}$$

Eq. (6.7) consists of kinetic energy and the potential energy. K_p is a positive definite matrix, and $e = z_d - \hat{z}$ is the tracking error vector. For a rigid body, the

mass matrix is strictly positive M > 0. Differentiating Eq. (6.7) with respect to time yields:

$$\begin{aligned}\dot{V} &= \hat{v}^T M\dot{\hat{v}} + e^T K_P \dot{e} \\ &= \hat{v}^T M\left\{M^{-1}\left(\tau - C(\hat{v})\hat{v} - G(\eta) - D(\hat{v})\hat{v}\right)\right\} + e^T K_P J\hat{v} \\ &= \hat{v}^T\left\{\tau - C(\hat{v})\hat{v} - G(\eta) - D(\hat{v})\hat{v} - J^T K_P e\right\}\end{aligned} \tag{6.8}$$

We choose the controller as follows:

$$\tau = J^T K_P e - K_D\hat{v} + C(\hat{v})\hat{v} + G(\eta) \tag{6.9}$$

$K_P e$ is defined in the task space and $K_D\hat{v}$ is defined in the configuration space. Substituting Eq. (6.9) into Eq. (6.8) yields:

$$\dot{V} = -\hat{v}^T\left\{V(\hat{v}) + K_D\right\}\hat{v} \le 0 \tag{6.10}$$

where K_D is a positive definite matrix. $\hat{v}^T V(\hat{v})\hat{v}$ for all $\hat{v}$ due to its skew-symmetric property. We now introduce the LaSalle's invariance theorem since Eq. (6.10) is negative semi-definite.

Let S be the set of all points where $\dot{V} = 0$ as follows:

$$S = \left\{x \in R \middle| \dot{V} = 0\right\} \tag{6.11}$$

The set S is satisfied by:

$$S = \left\{x \in R \middle| \hat{v} = 0\right\} \tag{6.12}$$

If v(t) = 0, then $M\dot{v} = J^T K_P e$ and $\dot{v} \neq 0$ as long as $e \neq 0$. This implies that no solution can stay identically in S other than e = 0. Hence, the equilibrium point (e, v) = (0, 0) is globally asymptotically stable.

6.2 Sliding Mode Controller

A robust nonlinear design technique for controlling complex nonlinear systems is the sliding-mode control. This technique has been studied since the early sixties by the name variable system structure (VSS). The name variable structure system stems from the fact that the state-feedback control law is not a continuous function of time. Instead, the controller can switch between continuous structures, depending on the current position in the state space. The control structure of sliding-mode control is designed such that the trajectories will move towards a sliding surface or manifold. It is important that the trajectory converges to this surface in finite time. As it reaches this manifold, the dynamics is ruled by a new control structure and the trajectory will slide along this sliding surface. This means

that the closed-loop response becomes insensitive to disturbances and other uncertainties. The method is therefore known for its robustness when it comes to modeling uncertainties, system parameters variation, external disturbances. One negative aspect of sliding-mode is that digital implementation of the controller can lead to a phenomenon called chattering, and also possible instability with large gains. Chattering occurs due to the limitations in sampling interval of switching devices. There are ways to reduce, or possibly remove, this phenomenon. Some of these will be presented in this section.

6.2.1 Tracking Error and Sliding Surface

The tracking error is defined as:

$$e = \eta - \eta_d \tag{6.13}$$

where η_d is the desired position.

We define a scalar measure of tracking error:

$$s = \dot{e} + \lambda e \tag{6.14}$$

where e is the tracking error, and $\lambda > 0$ is the control bandwidth.

Suppose we can design a control law that constrains the motion of the system to the manifold (or surface).

$$s = \dot{e} + \lambda e = 0 \tag{6.15}$$

This surface is called sliding surface.

On this surface, the motion is governed by:

$$\dot{e} = -\lambda e \tag{6.16}$$

The solution to this equation is:

$$e(t) = \exp(-\lambda(t - t_0))e(t_0) \tag{6.17}$$

Choosing $\lambda > 0$ guarantees that η tends to zero as t tends to infinity and the rate of convergence can be controlled by choice of λ. The error trajectory actually will reach the time-varying sliding surface in finite time for any initial condition $e(t_0)$ and then slide along the sliding surface towards $e(t) = 0$ exponentially. The motion of the system on the sliding surface $s = 0$ is independent of the original system. The sliding surface is depicted in Fig. 6.4. Once the system gets on the sliding surface, it cannot leave it.

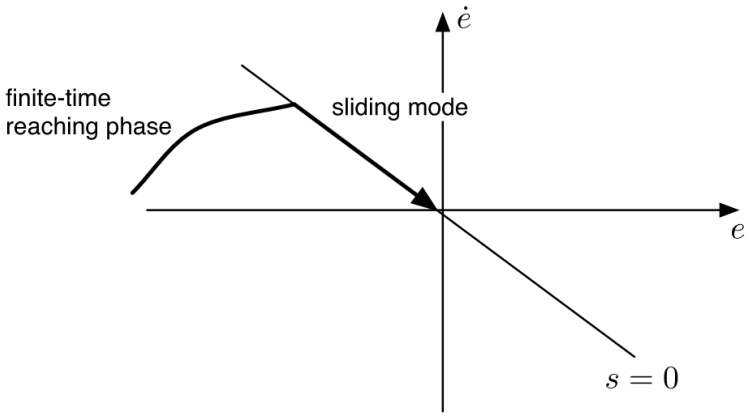

Fig. 6.4 Graphical interpretation of sliding surface.

Hence, the control objective is reduced to finding a nonlinear control law to ensure that:

$$\lim_{t\to\infty} s(t) = 0 \tag{6.18}$$

6.2.2 Chattering Situation

Because of the imperfections in switching devices and delays, sliding mode control suffers from chattering. In Fig. 6.5, the system trajectory starts off the sliding surface s = 0. It first hits the manifold at some point *a*. In ideal sliding mode control, the trajectory should start sliding on the manifold from point *a*. In reality, there will be a delay between the time the sign of *s* changes and the time the control switches. During this delay period, the trajectory crosses the manifold. When the control switches, the trajectory reverses its direction and heads again toward the manifold. Once again it crosses the manifold, and repetition of this process creates the "zig-zag" motion known as chattering. See Fig. 6.5.

Chattering results are in low control accuracy, high heat losses in electrical power circuits, and high wear of moving mechanical parts. It may also excite un-modeled high-frequency dynamics, which degrades the performance of the system and may even lead to instability.

Practically, for the controller to perform properly, elimination of chattering is desirable. One method to eliminate chattering is to replace the *sgn(·)* function in the control law with a saturation function *sat(·)* to smooth out the discontinuity inside a boundary layer [90]:

$$sat(\frac{s}{\phi}) = \begin{cases} \text{sgn}(s) & if \ \left|\frac{s}{\phi}\right| > 1 \\ \frac{s}{\phi} & if \ otherwise \end{cases} \tag{6.19}$$

where ϕ is the boundary layer thickness.

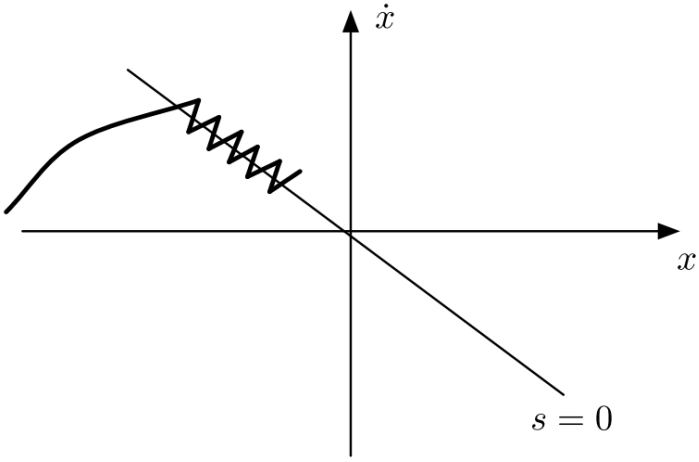

Fig. 6.5 Chattering as a result of imperfect control switching.

For better accuracy, we need to choose ϕ as small as possible, but too small a value of ϕ will induce chattering in the presence of time delays or un-modeled fast dynamics.

6.2.3 Control Law and Stability

The dynamic equations for the whole system expressed in Eq. (4.51) have some properties as follows.

- **Property 1:** The inertia matrix *M(q)* of the whole system is symmetric and positive definite: $M = M^T > 0$

  This means the all eigenvalues of the matrix M are greater than zero: $0 < \lambda_{\min}(M) \le \|M\| \le \lambda_{\max}(M)$

- **Property 2:** $\dot{M} - 2\dot{C}$ is skew-symmetric: $x^T\left[\dot{M} - 2\dot{C}\right]x = 0$

- **Property 3:** The matrix $D(q,\zeta)$ is positive definite : D>0

- **Property 4:** Assume that the model uncertainties are bounded by some known functions. ^ denote the estimated system matrices and ~ represent the estimation error matrices.

$$\left\|\tilde{M}_\eta\right\| = \left\|M_\eta - \hat{M}_\eta\right\| \le \Delta M_\eta < \infty \quad \left\|\tilde{C}_\eta\right\| = \left\|C_\eta - \hat{C}_\eta\right\| \le \Delta C_\eta < \infty$$

$$\left\|\tilde{D}_\eta\right\| = \left\|D_\eta - \hat{D}_\eta\right\| \le \Delta D_\eta < \infty \quad \left\|\tilde{G}_\eta\right\| = \left\|G_\eta - \hat{G}_\mu\right\| \le \Delta G_\eta < \infty$$

$$\left\|\tilde{\tau}_{cab}\right\| = \left\|\tau_{cab} - \hat{\tau}_{cab}\right\| < \bar{\tau}_{cab}\ ,\ \left\|\tilde{\tau}_{dis}\right\| = \left\|\tau_{dis} - \hat{\tau}_{dis}\right\| < \bar{\tau}_{dis}$$

In the 6DOF sliding controller, the tracking dynamic variable s of the SISO sliding control is replaced by 6-element vector s which is defined as:

$$s = \dot{e} + \Lambda e,\ \Lambda > 0 \tag{6.20}$$

Where, an error vector *e(t)* of the vehicle posture and the sliding manifold *s(t)* are defined in Eq. (6.21).

$$e(t) = \eta_d - \eta \tag{6.21}$$

Differentiating with respect to time, Eq. (6.21) becomes:

$$e(t) = \dot{\eta}_d - \dot{\eta} \tag{6.22}$$

In which, the subscript *d* means the desired value, and Λ is a positive definite gain matrix.

To ensure that the system converges to the sliding manifold s = 0, we use the following Lyapunov function candidate:

$$V = \frac{1}{2} s^T M_\eta s > 0 \tag{6.23}$$

The proposed function is positive definite by the property 1. Differentiating *V* with respect to time, Eq. (6.24) can be obtained as follows:

$$\dot{V} = \frac{1}{2} s^T \dot{M}_\eta s + s^T M_\eta \dot{s} \tag{6.24}$$

From the time-varying differential equation of the sliding manifold *s(t)* and the dynamic equations of vehicle expressed in Eq. (4.51), Eq.(6.24) can be rewritten as Eq. (6.25).

$$\dot{V} = \frac{1}{2} s^T \dot{M}_\eta s + s^T M_\eta \left[M_\eta^{-1} \left\{ \left(C_\eta + D_\eta \right) \eta + G_\eta - \tau - \tau_{cable} - \tau_{dis} \right\} + \dot{\eta}_d + \Lambda \dot{e} \right] \tag{6.25}$$

Eq. (6.26) is also obtained by taking into account the property 2 and Eq. (6.21).

$$\dot{V} = -s^T D_\eta s + s^T \left[M_\eta \left(\dot{\eta}_d + \Lambda \dot{e} \right) + \left(C_\eta + D_\eta \right) \left(\eta_d + \Lambda e \right) + G_\eta - \tau - \tau_{cable} - \tau_{dis} \right] \tag{6.26}$$

The sliding mode control law can be chosen as shown in Eq. (6.27) in order to follow the desired trajectories of the vehicle.

$$\tau = \hat{M}_\eta\left(\dot{\eta}_d + \Lambda\dot{e}\right) + \left(\hat{C}_\eta + \hat{D}_\eta\right)\left(\eta_d + \Lambda e\right) + \hat{G}_\eta - \hat{\tau}_{cable} - \hat{\tau}_{dis} + Ksign(s) \tag{6.27}$$

where K are positive definite matrix of gain and *sgn(s)* is a sign function as:

$$sign(s) = \begin{cases} 1 & if\ \ s > 0 \\ 0 & if\ \ s = 0 \\ -1 & otherwise \end{cases} \tag{6.28}$$

The designed control law represented in Eq. (6.27) is substituted into the Eq. (6.26), which yields the closed-loop equation, as follows:

$$\begin{aligned} \dot{V} = & -s^T D_\eta s - s^T K\,\mathrm{sgn}(s) + s^T\Big[\tilde{M}_\eta\left(\dot{\eta}_d + \Lambda\dot{e}\right) + \left(\tilde{C}_\eta + \tilde{D}_\eta\right)\left(\eta_d + \Lambda e\right) \\ & + \tilde{G}_\eta - \hat{\tau}_{cable} - \hat{\tau}_{dis}\Big] \end{aligned} \tag{6.29}$$

In view of properties 1, 3 and the positive definiteness of gain matrices K_1 and K_2, the function $\dot{V}$ can be upper bounded as shown in Eq. (6.30).

$$\begin{aligned} \dot{V} = & -\lambda_{\min} D_\eta \|s\|^2 - \lambda_{\min}(K)\|s\| + \Big\| s^T\Big[\tilde{M}_\eta\left(\dot{\eta}_d + \Lambda\dot{e}\right) + \left(\tilde{C}_\eta + \tilde{D}_\eta\right)\left(\eta_d + \Lambda e\right) \\ & + \tilde{G}_\eta - \hat{\tau}_{cable} - \hat{\tau}_{dis}\Big]\Big\| \end{aligned} \tag{6.30}$$

By property 4 and a triangle inequality condition, the inequality can be rewritten as follows.

$$\begin{aligned} \dot{V} \le & -\lambda_{\min}\left(D_\eta\right)\|s\|^2 - \lambda_{\min}(K)\|s\| + \Big(\|\tilde{M}_\eta\|\|\dot{\eta}_d + \Lambda\dot{e}\| + \left(\|\tilde{C}_\eta\| + \|\tilde{D}_\eta\|\right)\|\eta_d + \Lambda e\| \\ & + \|\tilde{G}_\eta\| + \|\tilde{\tau}_{cable}\| + \|\tilde{\tau}_{dis}\|\Big)\|s\| \end{aligned} \tag{6.31}$$

$$\begin{aligned} \dot{V} \le & -\lambda_{\min}\left(D_\eta\right)\|s\|^2 - \lambda_{\min}(K)\|s\| + \Big(\Delta M_\eta\|\dot{\eta}_d + \Lambda\dot{e}\| + \left(\Delta C_\eta + \Delta D_\eta\right)\|\eta_d + \Lambda e\| \\ & + \Delta G_\eta + \Delta\tau_{cable} + \Delta\tau_{dis}\Big)\|s\| \end{aligned} \tag{6.32}$$

where $\lambda_{\min}$ means the smallest eigenvalue of the corresponding matrix.

By choosing K such that:

$$\lambda_{\min}(K) \ge \Delta M_\eta\|\dot{\eta}_d + \Lambda\dot{e}\| + \left(\Delta C_\eta + \Delta D_\eta\right)\|\eta_d + \Lambda e\| + \Delta G_\eta + \Delta\tau_{cable} + \Delta\tau_{dis} \tag{6.33}$$

The time derivative of the positive definite function V is negative definite and thus the sliding manifold *s(t)* tends to zero asymptotically. Thus, the designed sliding mode controller satisfies the stability against any uncertainty for the vehicle.

As customary in sliding mode control, we will use a saturation function sat(s) instead of the sign function sign(s) in Eq. (6.27). This is to avoid chattering which is caused by the discontinuity of the sign function. The sat function can be defined as Eq. (6.19). And, the parameter ϕ can be tuned sufficiently low. The asymptotic

convergence to s = 0 is then only assured for $\phi = 0$ (where sat(s) = sign(s)). For a non-zero ϕ, however, s can only be ultimate bounded, where the bound on s can be reduced by decreasing ϕ. Thus, for practical use, s can get sufficiently close to zero by tuning ϕ sufficiently low.

Finally, the sliding mode control law in Eq. (6.27) becomes:

$$\tau = \hat{M}_\eta(\dot{\eta}_d + \Lambda\dot{e}) + \left(\hat{C}_\eta + \hat{D}_\eta\right)(\eta_d + \Lambda e) + \hat{G}_\eta - \hat{\tau}_{cable} - \hat{\tau}_{dis} + Ksat(s) \tag{6.34}$$

6.3 Allocation Control

For marine crafts in n DOF it is necessary to distribute the generalized control forces $\tau \in R^n$ to the actuators in terms of control inputs $u \in R^r$ as shown in Fig. 6.6. If r > n this is an over-actuated control problem, while r < n is referred to as an under-actuated control problem.

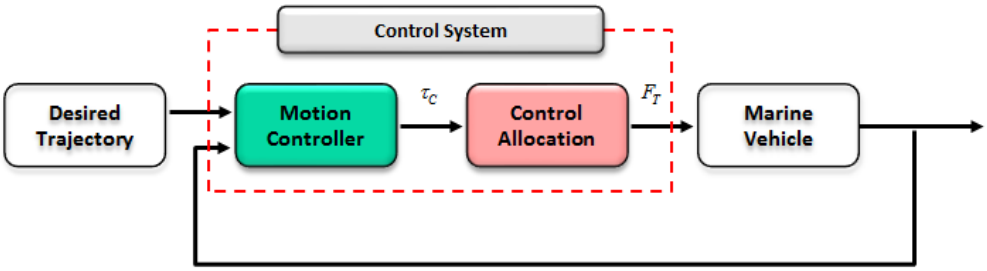

Fig. 6.6 Block diagram showing the control allocation block in a feedback control system.

Autonomous underwater vehicles tend to involve over-actuated designs in which multiple actuators can affect to the same degree of freedom. These over-actuated designs allow the AUVs to perform a wider range of missions, ranging from typical flight-style exploration tasks to hover-style detailed inspection tasks. However, the over-actuated configuration makes the AUV control a challenging problem because there are a number of ways to operate available actuators to achieve the same desired response but at a different amount of energy spent on the actuators. The control allocation technique is used for distributing the forces required by the control law onto the available set of actuators in the most effective and energy efficient way. Control allocation problems for underwater vehicles can be formulated as optimization problems, where the objective typically is to produce the specified generalized forces while minimizing the use of control effort (or

power) subject to actuator rate and position constraints, power constraints as well as other operational constraints.

For the control allocation problem two sorts of requirements have to be met. First the total delivered forces and moments have to equal the desired ones, and secondly limits may be imposed on the provided power and orientation angle of the thrusters. In practice, for control allocation Lagrange multiplier methods are frequently used. In order to allocate the control, first the allocation problem is solved neglecting the limits on the provided power. After the optimal configuration for this relaxed problem is obtained it is checked if all limits are satisfied. If not, one of the actuators for which the bounds are exceeded is scaled back to its limit and held constant. Then again the allocation problem is solved with the saturated thruster fixed, and the procedure is repeated until a feasible configuration is found.

The control allocation techniques may broadly be categorized into three main schemes: Lagrange multipliers, input scaling, and quadratic programming (QP) method. These three schemes are discussed below.

6.3.1 Linear Quadratic Unconstrained Control Allocation Using Lagrange Multipliers

Most thrust allocation algorithms assume a linear model as follows:

$$\tau = Tu \tag{6.35}$$

In Eq. (6.35), T is no longer a function of α. This result implies that the propulsion system of the vessel is composed of only non-rotatable thrusters. In most thrust allocation problems, the matrix T is not a square matrix. In most cases, T has full row rank and/ or a non-trivial null space. This result implies there is an infinite number of control vectors u that satisfies Eq. (6.35). A common method of compensating for actuator redundancy is to use the Moore-Penrose pseudo-inverse, within the framework of minimizing a least-square cost function. Now, we can formulate a cost function as follows:

$$\begin{aligned} &u^* = \arg\min\left(u^T W u\right) \\ &\textit{subject to } \tau_d = Bu \end{aligned} \tag{6.36}$$

The objective function $u^T W u$ is representative of the total energy or control effort, where W is a positive definite matrix weighting the actuator cost. Thus, the control allocation seeks the solution that implements the desired generalized force τ_d whilst minimizing the control effort.

Considering the quadratic energy function:

$$J = \frac{1}{2} u^T W u \tag{6.37}$$

which can be minimized subject to

$$\tau - Bu = 0 \tag{6.38}$$

Considering the Lagrangian:

$$L(u, \lambda) = \frac{1}{2} u^T W u + \lambda^T (\tau - Bu) \tag{6.39}$$

Where λ denotes the Lagrange multiplier, W is the selected positive weighting matrix. By differentiating Lagrangian L with respect to u yields:

$$\frac{\partial L}{\partial u} = Wu - B^T \lambda = 0 \tag{6.40}$$

Since $\tau = Bu$, then Eq. (6.40) can be rewritten as:

$$\tau = BW^{-1}B^T \lambda \tag{6.41}$$

Assuming that $BW^{-1}B^T$ is non-singular, then the optimal solution for the Lagrange multiplication can be found as:

$$\lambda = \left(BW^{-1}B^T\right)^{-1} \tau \tag{6.42}$$

Suggest that u can be calculated as $u = B_W^{\dagger} \tau$ by substituting Eq. (6.42) into Eq. (6.41) the generalized inverse $B_W^{\dagger}$ can be calculated as:

$$B_W^{\dagger} = W^{-1}B^T \left(BW^1B^T\right)^{-1} \tag{6.43}$$

Since state space dimension of the designed AUV can be reduced by removing sway and roll dynamics, then B matrix can be reduced as well, resulting the number thruster equal to the number of state which and makes B matrix become a square matrix. If all inputs are equally weighted as $W=I$, thus generalized inverse $B_W^{\dagger}$ in Eq. (6.43) can be simplified as:

$$B^{\dagger} = B^T \left(BB^T\right)^{-1} \tag{6.44}$$

Using Eq. (6.44), since the B matrix is square then $B^{\dagger}$ is simply equal to B^{-1}, thus u can be calculated as:

$$u = B^{-1}\tau \tag{6.45}$$

Note that since B depends only on the location of the actuators on the vehicle, the right inverse $B^{\dagger}$ can be pre-computed.

The optimization problem in Eq. (6.36) does not take into account the fact that the vector u must belong to a constraint set due to the maximum force that the various actuators can produce. Adding this constraint to Eq. (6.36) requires on-line numerical optimization, and the solution Eq. (6.43) is no longer the optimal solution.

Constrained numerical optimization brings out time feasibility issues since the optimization algorithm must always provide a feasible solution within the required sampling period [91, 92]. An alternative to this approach is to constrain the desired generalized force τ_d such that the constraints on u are always satisfied [93]. By doing so, the force controller is also informed about reaching constraints, which prevents performance degradation due to the combination actuator saturation and integral action. This control method is described in the next section.

6.3.2 Thruster Allocation with a Constrained Linear Model

To address the saturation issue, inequality constraints are added to the optimization problem. In this case, thrust allocation methods based on the generalized inverse cannot guarantee feasibility. In the past several decades, various approaches to the use of inequality constraints have been proposed. The following methods can provide better solutions than simply saturating the thrust forces.

6.3.2.1 Constrained Control via Input Scaling

Some of the constrained thrust allocation methods meet constraints by scaling the result of the unconstrained optimal thrust allocation such that the resulting solution is projected onto the boundary of the set of attainable generalized forces as shown in Fig.6.7.

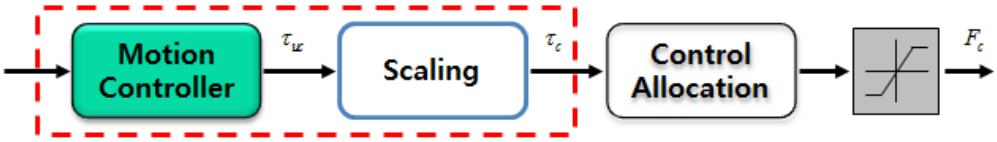

Fig. 6.7 Block diagram showing the constrained control allocation block using input scaling.

The first step of the direct allocation method is to solve the unconstrained thrust allocation problem using the pseudo-inverse method. If the result satisfies the constraints, no further steps are needed; otherwise, the method will find α using the following formulation:

$$\begin{aligned} &\max_{\alpha} \ \alpha \\ &subject\ to \\ &Bu = \alpha T \\ &\alpha T \in A \end{aligned} \tag{6.46}$$

Where α is a scalar between 0 and 1, and A is a polyhedral set that can be realized by the propulsion system of the vehicle.

In order to constrain τ_d we need to construct a set such that:

$$\tau_d \in \mathrm{T} \Leftrightarrow u \in U \tag{6.47}$$

One way of enforcing these constraints is by computing an unconstrained control τ_{uc} and then scaling it down if it is outside the constraint set, that is:

$$\tau_d = \begin{cases} \tau_{uc} & if\ \ \tau_{uc} \in T \\ \alpha\tau_{uc} & if\ \ \tau_{uc} \notin T, \alpha < 1 : \alpha\tau_{uc} \in \partial T \end{cases} \tag{6.48}$$

By scaling the vector τ_{uc}, we preserve its direction. In order to implement Eq. (6.48) we need to compute τ_{uc} and then obtain α.

The explicit computation of the set T is not always easy. To simplify this computation we can consider an approximating polyhedron subset $U^* \subseteq U$ of the actuator force components [94]:

$$U^* = \{u : L < u < U\} \tag{6.49}$$

Or alternatively,

$$U^* = \{u : Fu < f\},\ F = \begin{bmatrix} I \\ -I \end{bmatrix},\ f = \begin{bmatrix} U \\ -L \end{bmatrix} \tag{6.50}$$

Using the set U^*, the following algorithm determines the scaling factor [93]:

- Compute the unconstrained control, and evaluate $f_{uc} = FB^{\dagger}\tau_{uc}$,
- Set α = 1,
- If $f_{uc}(i) = f(i)$ and $\frac{f(i)}{f_{uc}(i)} < \alpha$ then, re-set $\alpha = \frac{f(i)}{f_{uc}(i)}$. Do this for all the components i = 1, ..., 4N.

Once the scaling factor is computed the control can be implemented as:

$$\tau_d = \alpha\tau_{uc} \tag{6.51}$$

6.3.2.2 Constrained Control via Quadratic Programming

Quadratic programming is a powerful approach to thrust allocation. We can formulate the thrust allocation problem as follows:

$$\begin{aligned} &\min_{u} \; u^T W u \\ &subject\ to \\ &\tau = Tu \\ &Au \le b \end{aligned} \tag{6.52}$$

Eq. (6.52) is the simplest quadratic programming (QP) formulation of the power-minimizing thrust allocation problem. This problem can be solved using a QP solver. The advantage of using QP is that we can simultaneously minimize power consumption and meet the thrust constraint. The only thing we must do is model the thrust constraint.

An explicit solution approach for parametric quadratic programming has been developed by Tøndel et al. [95] while applications to marine vessels are presented by Johansen et al. [96]. In this work the constrained optimization problem is formulated as:

$$\begin{aligned} &\min_{f,s,\bar{f}} \left\{ J = f^T W f + s^T Q s + \beta \bar{f} \right\} \\ &\quad subject\ to: \\ &\quad Tf = \tau + s \\ &\quad f_{min} \le f \le f_{\max} \\ &\quad -\bar{f} \le f_1, f_2, \ldots f_r \le \bar{f} \end{aligned} \tag{6.53}$$

where $s \in R^n$ is a vector of slack variables and forces:

$$f = \left[f_1, f_2, \ldots f_r \right]^T \in R^r \tag{6.54}$$

The first term of the criterion corresponds to the LS criterion Eq. (6.39), while the third term is introduced to minimize the largest force $\bar{f} = \max_i |f_i|$ among the actuators. The constant $\beta \ge 0$ controls the relative weighting of the two criteria. This formulation ensures that the constraints $f_i^{\min} \le f_i \le f_i^{\max}$ (i=1,…,r) are satisfied, if necessary by allowing the resulting generalized force Tf to deviate from its specification τ. To achieve accurate generalized force, the slack variable should be close to zero. This is obtained by choosing the weighting matrix $Q \gg W > 0$. Moreover, saturation and other constraints are handled in an optimal manner by minimizing the combined criterion Eq. (6.53). Let:

$$p = \left[\tau^T, f_{\min}^T, f_{\max}^T, \beta \right]^T \in R^{n+2r+1} \tag{6.55}$$

Denote the parameter vector and,

$$z = \left[f^T, s^T, \bar{f} \right]^T \in R^{n+r+1} \tag{6.56}$$

Hence, it is straightforward to see that the optimization problem Eq. (6.53) can be reformulated as a QP problem:

$$\begin{aligned} &\min_z \left\{ J = z^T \Phi z + z^T R p \right\} \\ &\quad subject\ to: \\ &\quad A_1 z = C_1 p \\ &\quad A_2 z \le C_2 p \end{aligned} \tag{6.57}$$

Where

$$\Phi = \begin{bmatrix} W & 0_{r\times n} & 0_{r\times 1} \\ 0_{n\times r} & Q & 0_{n\times 1} \\ 0_{1\times r} & 0_{1\times n} & 0 \end{bmatrix} \tag{6.58}$$

$$R = \begin{bmatrix} 0_{(r+n+1)\times(n+2r)} & \begin{bmatrix} 0_{(r+n)\times 1} \\ 1 \end{bmatrix} \end{bmatrix} \tag{6.59}$$

$$A_1 = \begin{bmatrix} T & -I_{n\times n} & 0_{n\times 1} \end{bmatrix} \tag{6.60}$$

$$A_2 = \begin{bmatrix} -I_{r\times r} & 0_{r\times n} & 0_{r\times 1} \\ I_{r\times r} & 0_{r\times n} & 0_{r\times 1} \\ I_{r\times r} & 0_{r\times n} & \begin{bmatrix} 1 \\ 1 \\ . \\ 1 \end{bmatrix} \\ I_{r\times r} & 0_{r\times n} & -\begin{bmatrix} 1 \\ 1 \\ . \\ 1 \end{bmatrix} \end{bmatrix} \tag{6.61}$$

$$C_1 = \begin{bmatrix} I_{n\times n} & 0_{n\times(2r+1)} \end{bmatrix} \tag{6.62}$$

$$C_2 = \begin{bmatrix} 0_{r\times n} & -I_{r\times r} & 0_{r\times r} & 0_{r\times 1} \\ 0_{r\times n} & 0_{r\times r} & I_{r\times r} & 0_{r\times 1} \\ 0_{r\times n} & 0_{r\times r} & 0_{r\times r} & 0_{r\times 1} \\ 0_{r\times n} & 0_{r\times r} & 0_{r\times r} & 0_{r\times 1} \end{bmatrix} \tag{6.63}$$

Since W >0 and Q >0 this is a convex quadratic program in z parameterized by p. Convexity guarantees that a global solution can be found. The optimal solution is $z^*(p)$ a continuous piecewise linear function $z^*(p)$ defined on any subset,

$$p_{\min} \le p \le p_{\max} \tag{6.64}$$

of the parameter space.

6.4 Simulation Results and Discussion

This chapter reviews techniques required for a vehicle to transit from a start location to a prescribed destination automatically. According to [60], the autonomous system for vehicles may be classified into four interconnected modules. They are guidance, navigation, control and path planning. This classification applies to the vehicles moving underwater, on the surface or in space. The system for the vehicle to navigate between the two locations is denoted as the navigation system, which consists of four interconnected modules: guidance, localisation, control and path planning. A definition of each module is given below.

Guidance: a module that guides an vehicle to move along a predefined path. It regularly determines a reference point for the vehicle to track based on a given path and a current vehicle's state in that instant.

Localisation: a technique to realise a current state of the vehicle, including position, orientation and velocities. The vehicle's state may be measured directly using suitable sensors, or estimated by using observers when a direct measurement is impractical.

Control: a module that generates actions to satisfy a control objective, and is subjected to constraints. A control objective is, for example, regulating a heading error. Constraints are, for example, limits on actuator setpoints or vehicle's dynamics.

Path planning: a process of finding the best valid path leading from a start location to a goal location. The suggested path must take into consideration the dynamic and geometrical constraints of the vehicle, e.g., the path does not collide with obstacles and is possible for the vehicle to manoeuvre along. The quality of

path will have a direct impact on the performance of the guidance and control modules.

The navigation system works in the following way. First, the path planning module executes a valid path that leads towards a goal location. Typically, the desired path is described as waypoints, which is a sequence of points in space. The desired path together with the current vehicle state is fed to the guidance module, and a temporary reference location for the vehicle to track is determined accordingly. An error between the current location and the reference location is computed. This error is taken as an input to the control module for generating actuator demands to regulate the error. The localisation module regularly updates the current state of the vehicle. This navigation system is illustrated in Fig. 6.8.

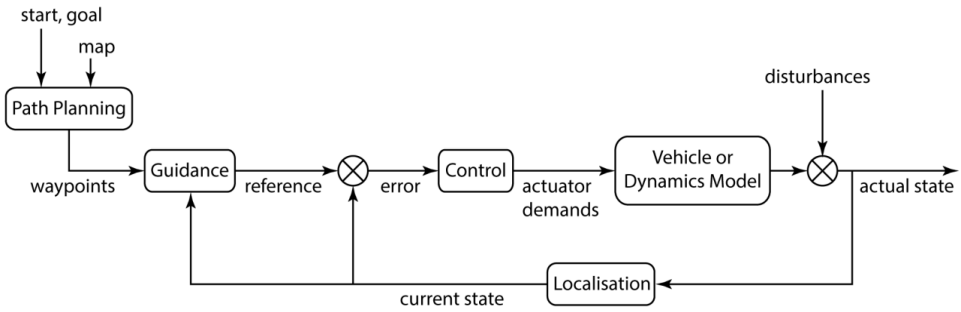

Fig. 6.8 A navigation system that consists of four interconnected modules.

Typically, determining current vehicle position is a huge challenge for a GPS-denied environment as in the case for underwater operation. Thus, the localisation module will not be covered in this research, and the vehicle state is assumed to be available always.

Two different levels of guidance strategies are discussed. Main attention is paid to a line-of-sight (LOS) path following scheme where the vehicle is considered to have a fixed visibility range and cubic polynomial method. An interception between the visibility range and the path is taken as a moving target in which the vehicle must follow in order to navigate along the path. A control system is used to make the vehicle moves regarding the guidance law. This control system consists of two cascade blocks which are control law, control allocation. The control law responsible for generating sufficient amount of forces required to fulfil the demands given by the guidance system. This control law can be based on a proportional- integral-derivative (PID) technique as well as nonlinear control techniques such as a sliding mode control (SMC). On the other hand, the control allocation module is responsible for distributing the generalised forces given by the

control law onto the available actuators with a minimum total energy spent on the actuators.

6.4.1 Berthing (parking) Control of USV

In this section, a berthing control of USV was performed by using the classical PD controller. The detail algorithm of the berthing control of USV is shown in Fig 6.9 while the Matlab and Simulink diagram is shown in Fig. 6.10. For more details, the simulations have been performed for two cases of control of USV yaw angle for navigations and berthing, which generated two trajectories of USV as shown in Fig. 6.11. The first case we set up condition of USV moving from star point A (x = 2000 m, y =1000 m, yaw angle = 50 degrees) to goal point B (0 m, 0 m, -180 degrees). For the other case, we set up condition of USV moving from star point A (x = 2000 m, y =1000 m, yaw angle = -50 degrees) to goal point B (0 m, 0 m, -180 degrees). For both cases the initial velocities of USV are $v_x = 3$ *(m/s)*, $v_y = 0$ *(m/s)* and $v_z = 0$ *(m/s)*, respectively. The simulation period is 2000 seconds with starting time of 0 second, and finishing time of 2000 seconds with time step 0.01 second for first case. And simulation time is 1200 seconds with time step 0.01 second for second case. Fig. 6.11 (a) shows USV trajectories in both cases, and Fig. 6.11 (b) shows the control input of USV of revolution of the thruster and the rudder angle. In more detail, we can see the yaw angle of USV as well as the position and velocity of USV as shown in Fig. 6.12, respectively. From these results, we can obviously realize that the USV reached the goal point B (0 m, 0 m, -180 degrees) faster than the second case such as it took 2000 seconds for second case but only 1200 seconds for first case. Also, the trajectory of second case more and more complicated than first case as well as velocity and rudder angle of USV when we compare both cases. Generally speaking, in order to USV reach the goal point effectively, we have to define the optimal yaw angle of USV as well as carefully control its rudder angle.

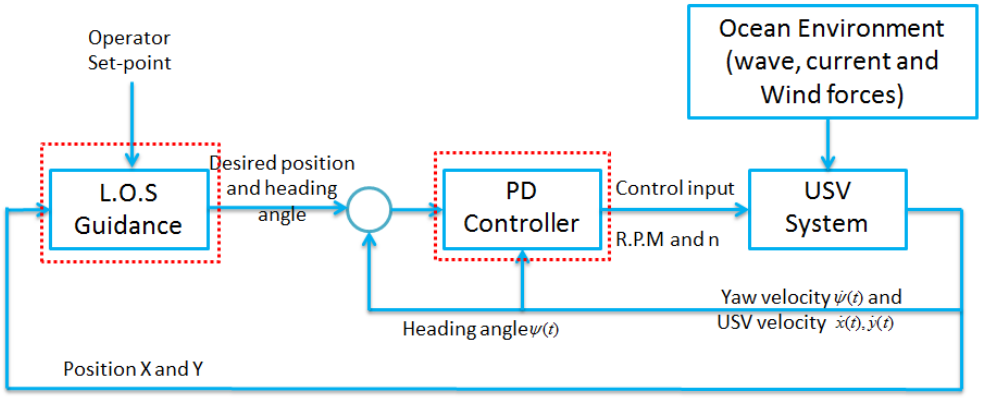

Fig. 6.9 A block diagram of a PD controller.

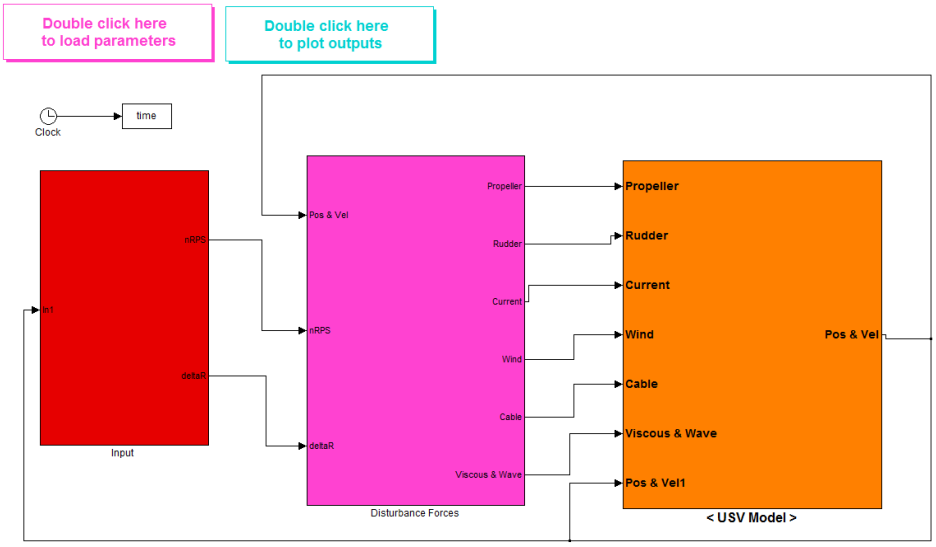

Fig. 6.10 Computer program.

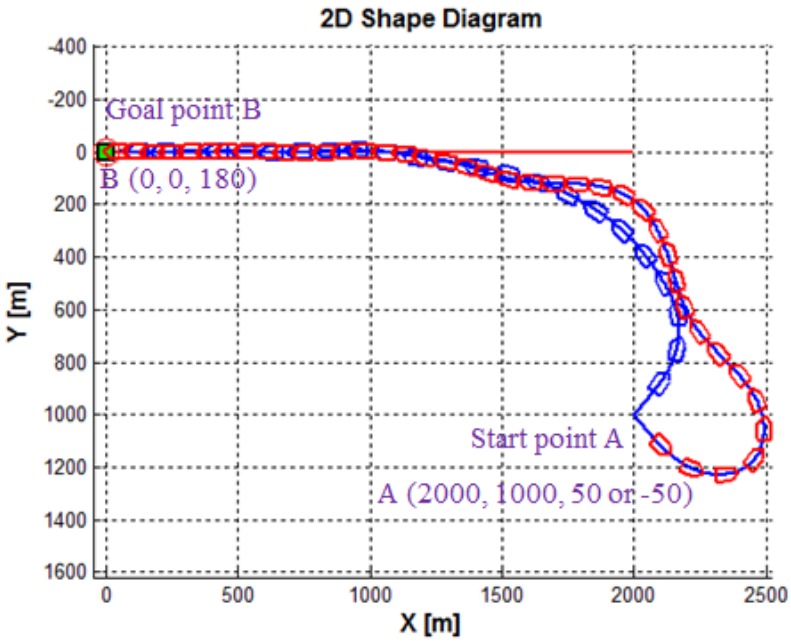

(a) Trajectories

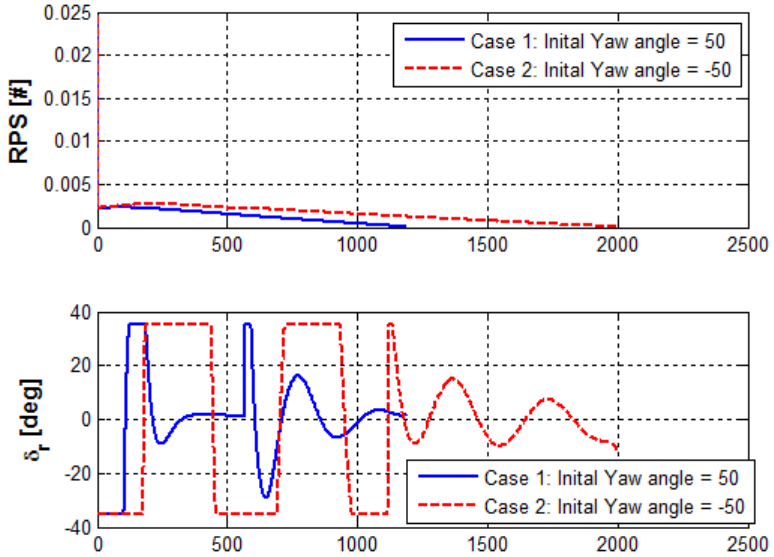

(b) The control inputs

Fig. 6.11 USV trajectories and control inputs in both cases.

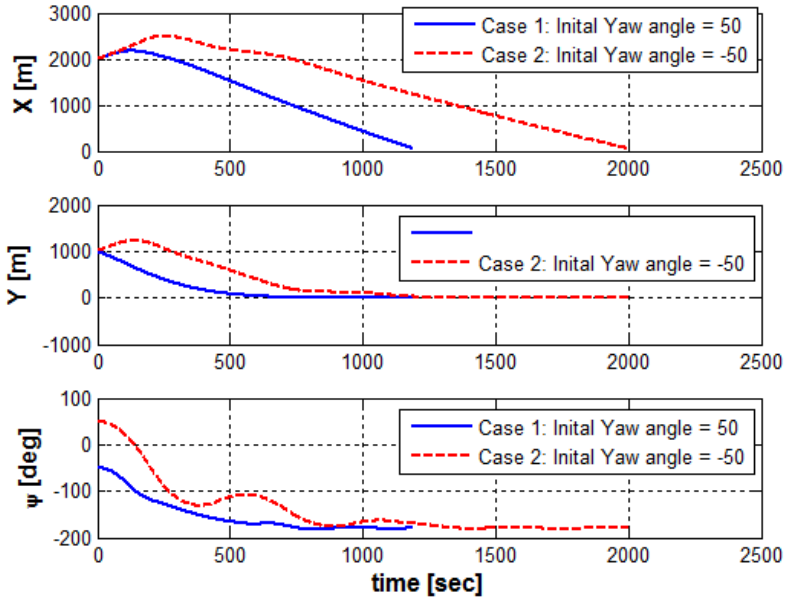

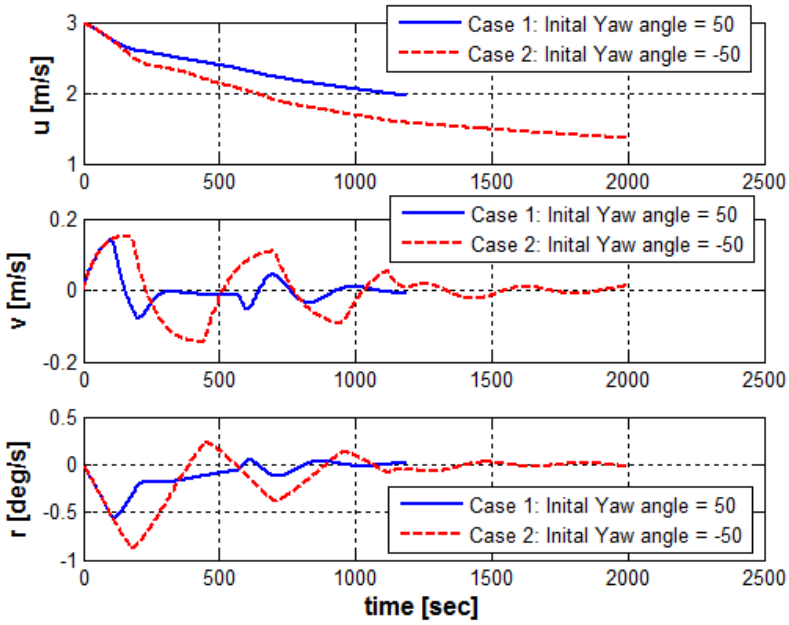

Fig. 6.12 USV dynamic behaviors in both cases.

6.4.2 Motion Control of UV

In this section, we present numerical simulations that both verify and illustrate the performance of the proposed control system. We consider a model of an open-frame underwater vehicle-like the one shown in Fig. 4.6. This vehicle has four horizontal thrusters are used to generate autonomous navigation, and the three vertical thrusters are designed for heaving, pitching, and rolling motion. Further details of the vehicle model are given in Section 4.12.

MATLAB/Simulink has been used to design the control system used in simulations. Simulink is a well-known graphical programming environment by MathWorks for modeling, simulating and analyzing dynamical systems. Simulink is tightly linked with the programming language MATLAB, which can be used to script Simulink. The maneuverability of the underwater vehicle was assessed by using computer simulation. The following maneuvers were performed:

- Dynamic positioning of AUV in 6DOF.
- Waypoints tracking control of AUV.

In order to perform the mentioned maneuvers, both control systems of the underwater vehicle PD and SMC were established. The SMC controller is nonlinear and more robust than the PID. To investigate the effect of parameter

uncertainties on the sliding mode control performance, the model parameters used in the control section were individually varied between ± 30% of the estimated values used in the simulation section. Also, the ocean current effect on the AUV was studied and generated by the first Gauss-Markov process expressed in 2D current models, and the average velocity of current is 0.5 m/s (about 1 knot) or more. Moreover, the constrained thrust allocation is considered, which are set to $u_{\max,i} = 100N$ and $u_{\min,i} = -100N$ for all individual thrusters.

First, we have considered the design of a positioning controller in conjunction with control allocation for over-actuated marine vehicles. The proposed design is based on PD controller together with a control allocation mapping. Next, trajectory tracking control of AUV was developed and implemented by using two kinds of controllers PID and SMC controllers.

6.4.2.1 Dynamic Position of UV in 6DOF

A vehicle in sea is subjected to various forces and moments due to waves, wind, sea currents, propulsion system, and un-modeled disturbances due to the environmental effects and the propulsion system. In practice, a floating vehicle cannot maintain a completely static position at sea. Therefore, for practical reasons, DP control means maintaining the desired position and heading within limits that reflect the environmental effects and the system capability. Using active thrusters, DP control systems automatically maintain the position and heading of floating structures subjected to environmental disturbances. DP systems are generally composed of a controller and a thrust allocator. Most DP controlled vehicles are over-actuated and the allocator decides how to distribute the thrust forces to each actuator device based on mechanical or operational constraints. The use of control allocation allows the control design to be focused on the generalized forces related to the degrees of freedom of concern rather than on actuator forces. In the proposed control system, we map the constraint set of actuator forces due to the limited authority of the actuators into a constraint set for the generalized forces.

The block diagram of this simulation is shown in Fig. 6.13. There are six PD controllers run in the system. The main simulation parameters are shown in Table 6.5. This study presents both constrained and unconstrained optimization problems to solve the allocation problem as follow:

- **Case 1: Unconstrained Thrust Allocation**

In case 1, the thrust allocation is considered unconstrained. This is done by setting a virtual constraint on the individual thruster forces u_i which is high enough that the saturation limit should never be reached. In the simulations performed in

case 1, the constraints are set to $u_{\max,i} = 1000N$ and $u_{\min,i} = -1000N$. Simulations are performed for both planar and three-dimensional motion using standard damped inverse, least square method for thrust allocation.

- **Case 2: Constrained Thrust Allocation**

In case 2, constrained thrust allocation is considered. The constraints implemented are thruster saturation limits, which are set to $u_{\max,i} = 100N$ and $u_{\min,i} = -100N$ for all individual thrusters. This makes the simulations more equal to real-life conditions as all physical thrusters have saturation limits. Simulations are performed for both planar and three-dimensional motion using quadratic programming algorithm for thrust allocation.

Figs. 6.14 and 6.16 show two DP capability plots for an AUV containing seven thrusters. Because the AUV is over-actuated system has seven thrusters, the Lagrange multiplier method and the Quadratic Programming methods can be compared for the AUV. Also, Fig. 6.15 shows the velocity and direction of the current during the simulation. As shown in Fig. 6.15, the velocity of the current and the angle of attack of the current would be changed every five seconds time.

It can be clearly seen from Figs. 6.16-6.18 that the Lagrange multiplier method results in less DP capability for this AUV, where the QP thrust allocator is still able to find solutions for some more extreme conditions. This is not very surprising, because the Lagrange multiplier method cannot generate optimal solutions. It actually solves the problem for thrusters with unlimited thrust capabilities and then saturation handling takes into account the thrust regions. Generally speaking, it was concluded that QP gave the best results. This motivates us further to formulate the thrust allocation problem as a QP-problem. Furthermore, Fig. 3.4 (a) and Fig. 3.4 (b) show the position and orientation angle of the AUV with time. As shown in these results, the AUV rotates its heading angle against the environmental disturbance. Occasionally, this operation is performed manually by changing the heading set point using the information obtained from the current estimation, and thrust utilization of the DP system. In order to keep track of the desired direction while keeping the initial position, the control input obtained through the PD controller is shown in Figs. 6.17 and 6.18 for both cases LS and QP methods. The thrust generated by the seven thrusters is obtained through an allocation control algorithm which is designed to optimize the energy consumed. As can be seen from the results, it can be seen that the thrust generated in each propeller is operated within the limit value ± 100N of the predetermined thrust.

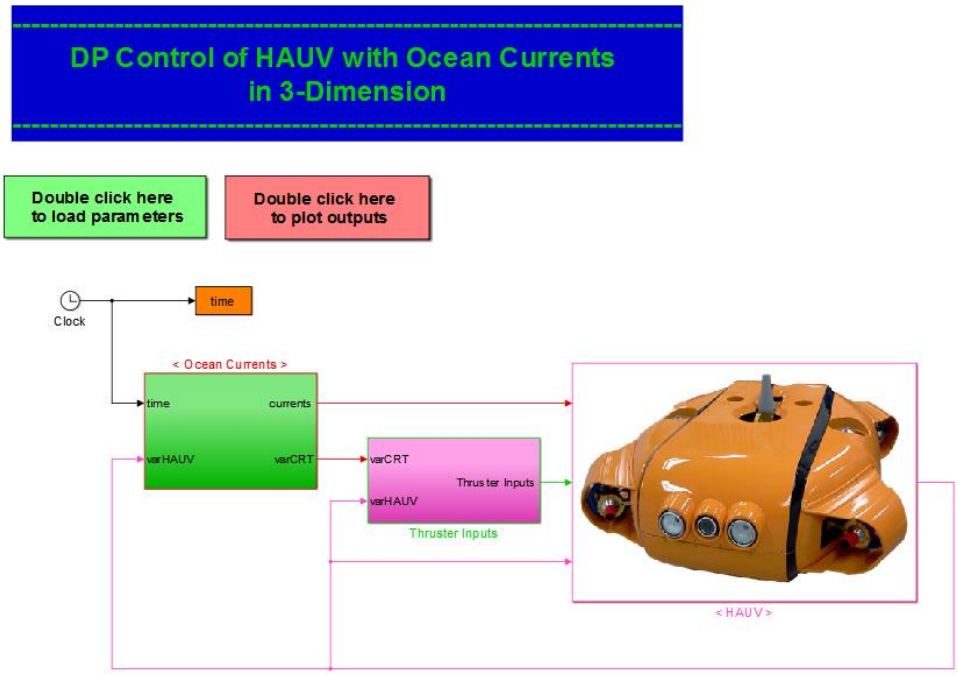

Fig. 6.13 Simulation program for DP control of AUV.

Table 6.5. Parameters for DP control of AUV without cable effects

Time for simulation	
Simulation time	*20 seconds*
Sampling time	*0.01*
Position initial values	
$[X \quad Y \quad Z \quad \phi \quad \theta \quad \psi] = [60 \quad 0 \quad 60 \quad 0 \quad 0 \quad 0]$	
Velocity initial values	
$[u \quad v \quad w \quad p \quad q \quad r] = [0.3 \quad 0 \quad 0 \quad 0 \quad 0 \quad 0]$	
Desired trajectory	
$[X_d \quad Y_d \quad Z_d \quad \phi_d \quad \theta_d \quad \psi_d] = [63 \quad 2 \quad 65 \quad 0 \quad 0 \quad LOS]$	
Current parameters (3D)	
Average speed	*1.2 m/s*
Angle of attack	*10 degrees*

Heading angle of current	*60 degrees*
PD Controller	
$[X \quad Y \quad Z]$	$[K_p \quad K_I \quad K_d] = [500 \quad 0 \quad 500]$
$[\phi \quad \theta \quad \psi]$	$[K_p \quad K_I \quad K_d] = [200 \quad 0 \quad 200]$

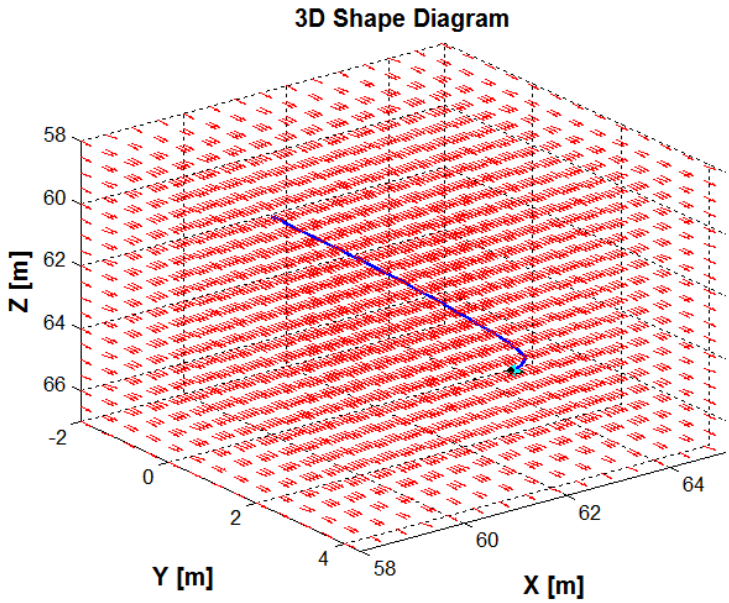

(a) Least Square Method (LSM)

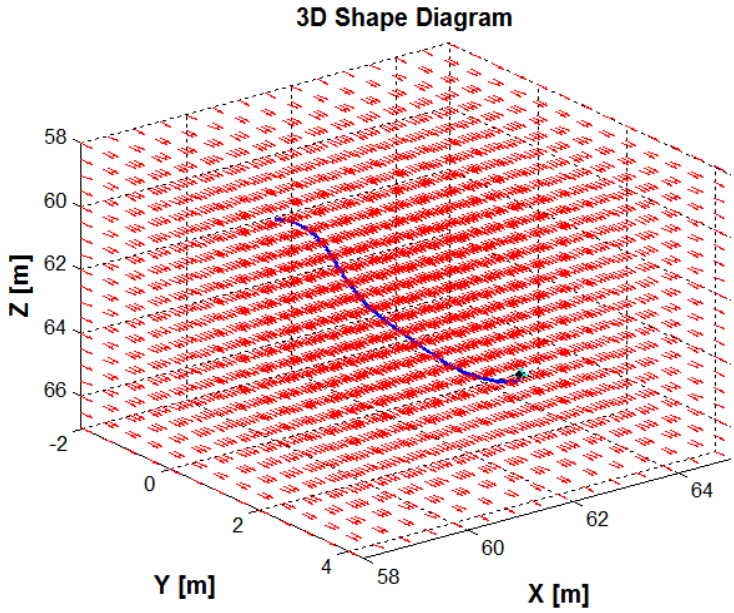

(b) Quadratic Program (QP)

Fig. 6.14 3D trajectories of AUV using least square method and quadratic program.

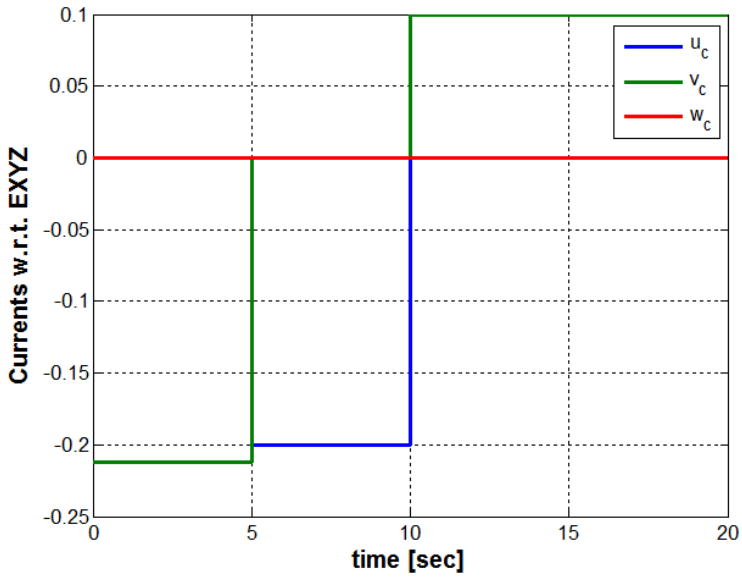

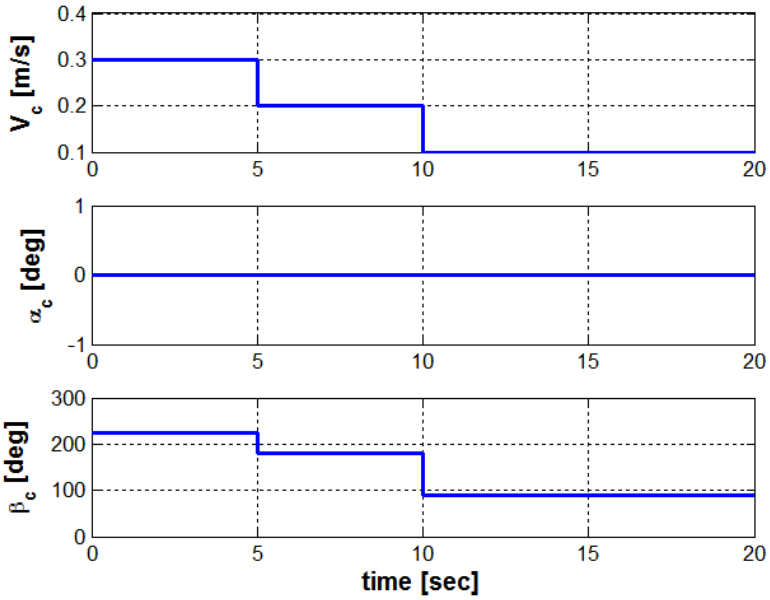

Fig. 6.15 Current forms.

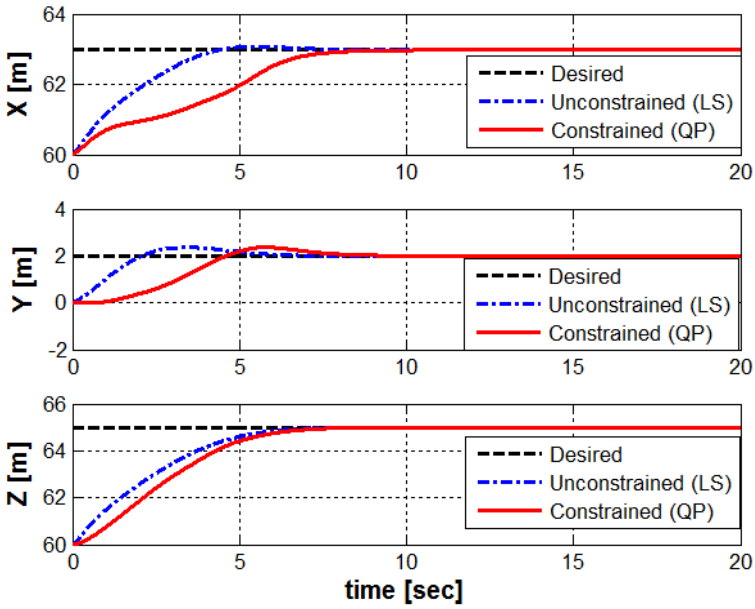

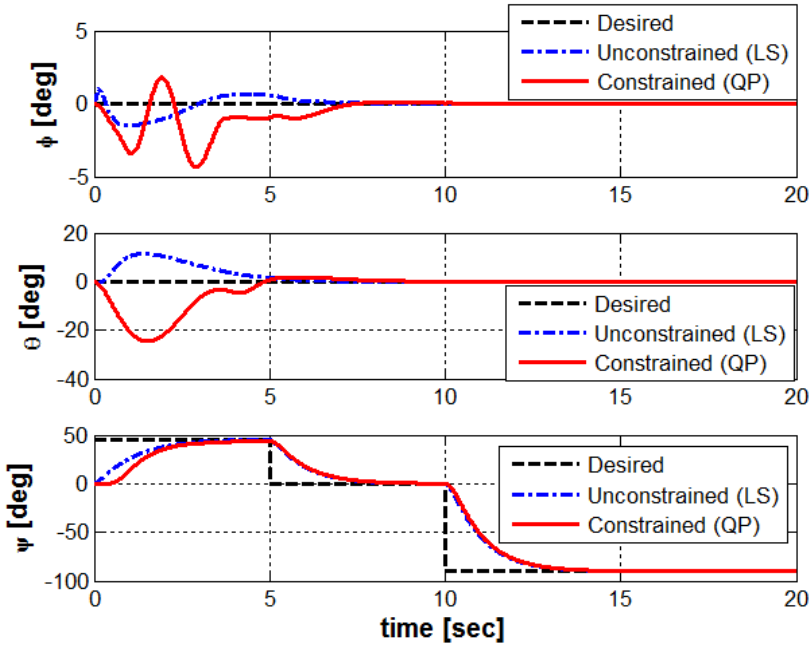

Fig. 6.16 AUV dynamic behaviors in both cases.

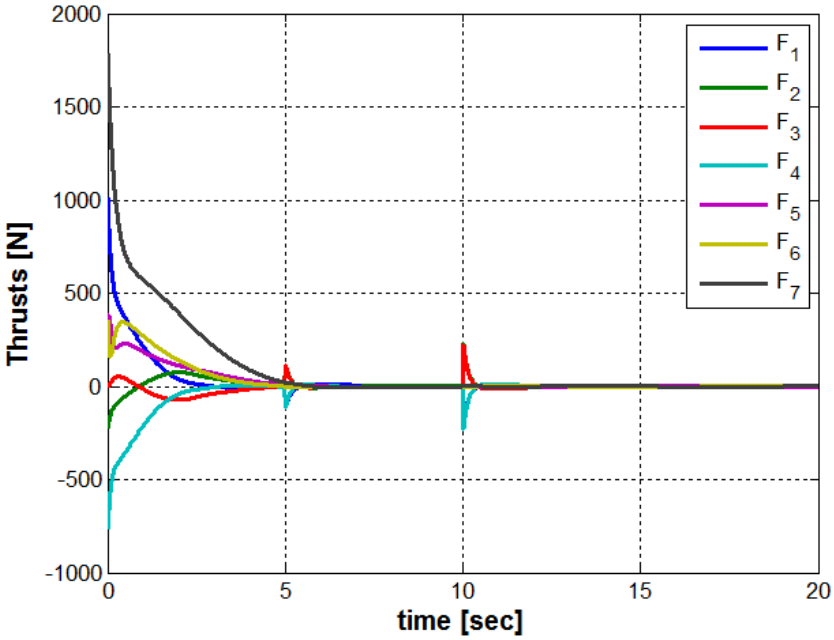

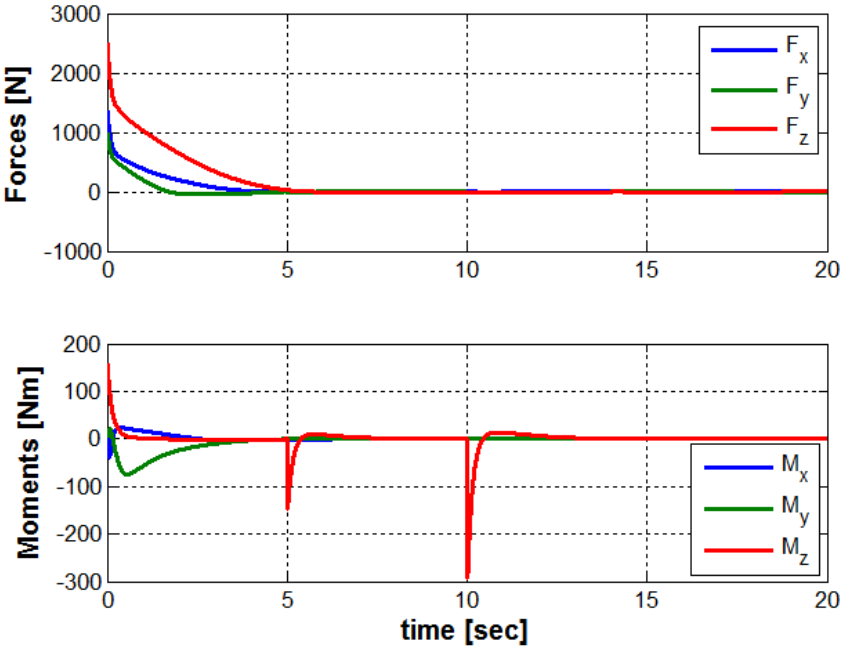

Fig. 6.17 Control inputs using least square method.

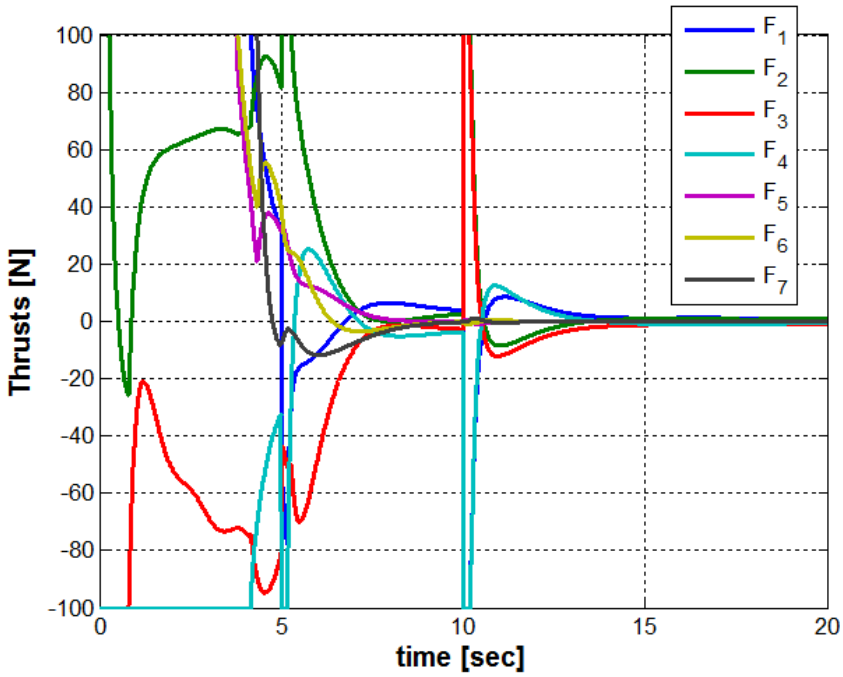

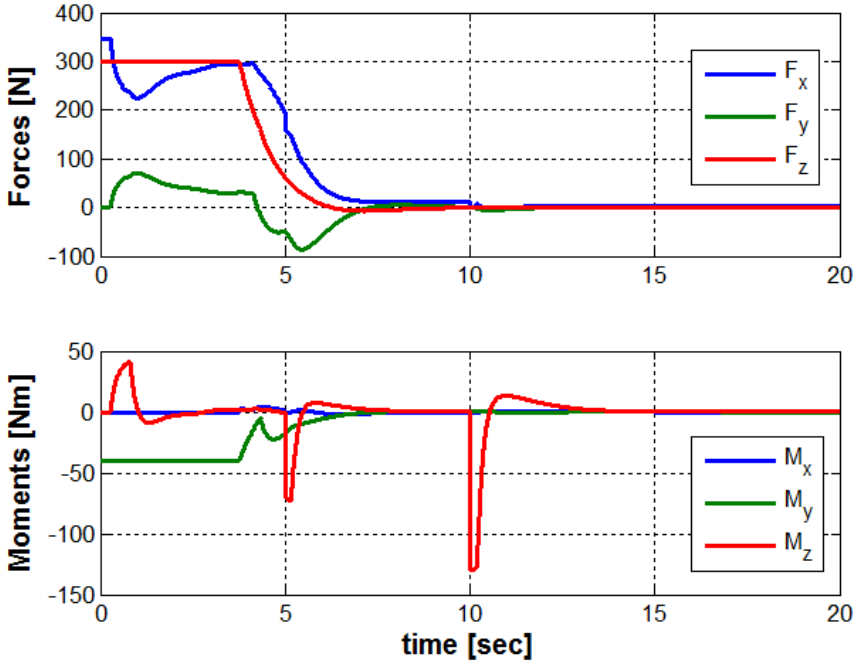

Fig. 6.18 Control inputs using quadratic program method.

6.4.2.2 Waypoints Tracking Controller of UV

Next, we set the trajectory for the AUV to move from the initial position to the predefined target position and performed the simulation to follow the desired trajectory while overcoming the model uncertainty and current effects. The trajectory of the position and orientation angle of AUV from the initial position to the target position was generated using a cubic polynomial. An interesting alternative is a Cubic polynomial which passes through all the waypoints, and it is possible to assign the derivative values at the control points and also obtain local control over the path. In this section, a series of mission plans are designed, consisting of a set of predefined waypoints. Trajectory tracking control was developed and implemented to enable autonomous orientation control of the vehicle while traversing the waypoints by using 2 kinds of PID and SMC controllers. The simulation program for waypoints tracking of AUV is shown in Fig. 6.19.

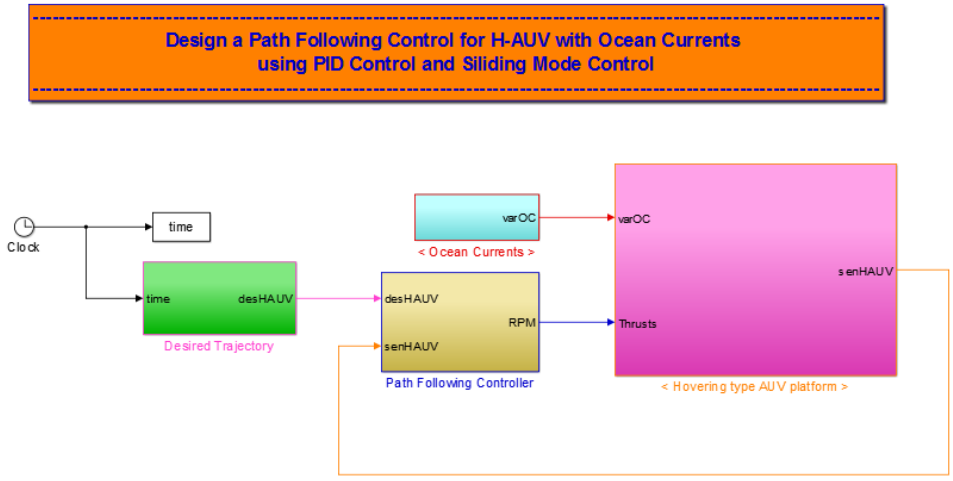

Fig. 6.19 Simulation program for waypoints tracking of AUV.

a) Four Waypoints (3D)

In this chapter, we will propose an autopilot design for the AUV considering the current effects. The autopilot will consist of a guidance system using cubic polynomial and two different controllers PD and SMC which will be tested against each other. The guidance system will make a path for the AUV to follow based on the waypoints given. The control system has been implemented first with SMC control, then with PD.

The first desired trajectory was a 3-D trajectory with 4 waypoints as: WP1 (55,0,55,0,0,0), WP2 (60,-4,58,0,0,-30), WP3 (67,-2,61,0,0,-90), and WP4 (62,2,64,0,0,0). We adjust the depth of the waypoints along the tracks to illustrate the vehicle's ability to follow a more complex path than simply a planar survey. An example of where this may be useful is if the vehicle needs to follow the contours of the ocean floor.

As shown in Fig. 6.21, the current effects are applied to the AUV at a reference speed of 0.5 m/s (about 1 knot) and its orientation w.r.t. the inertial frame is 60°. Likewise, the model uncertainty is assumed to set at random within the range of ± 30%. In order to maintain stability underwater vehicle due to the characteristics of the AUV, the roll angle and the pitch angle of AUV are set to 0° during the simulation, and the target heading angle of AUV is defined as the interval -30°, -90° and 0°, respectively. The parameters for 4 waypoints of AUV are shown more detail in Table 6.6.

Table 6.6. Parameters for 4 waypoints of AUV without cable effects

Time for simulation	
Simulation time	*30 seconds*
Sampling time	*0.01*
Position initial values	
$\begin{bmatrix} X & Y & Z & \phi & \theta & \psi \end{bmatrix} = \begin{bmatrix} 52 & -2 & 55 & 10 & 10 & 30 \end{bmatrix}$	
Velocity initial values	
$\begin{bmatrix} u & v & w & p & q & r \end{bmatrix} = \begin{bmatrix} 0 & 0 & 0 & 0 & 0 & 0 \end{bmatrix}$	
Waypoints	
Waypoint 1	$\begin{pmatrix} x & y & z & \phi & \theta & \psi \end{pmatrix} = \begin{pmatrix} 55 & 0 & 55 & 0 & 0 & 0 \end{pmatrix}$
Waypoint 2	$\begin{pmatrix} x & y & z & \phi & \theta & \psi \end{pmatrix} = \begin{pmatrix} 60 & -4 & 58 & 0 & 0 & -30 \end{pmatrix}$
Waypoint 3	$\begin{pmatrix} x & y & z & \phi & \theta & \psi \end{pmatrix} = \begin{pmatrix} 67 & -2 & 61 & 0 & 0 & -90 \end{pmatrix}$
Waypoint 4	$\begin{pmatrix} x & y & z & \phi & \theta & \psi \end{pmatrix} = \begin{pmatrix} 62 & 2 & 64 & 0 & 0 & 0 \end{pmatrix}$
Current parameters (3D)	
Average speed	*0.5 m/s*
Angle of attack	*10 degrees*
Heading angle of current	*60 degrees*
PD Controller	
K_p	$K_p = \begin{pmatrix} K_x & K_y & K_z & K_\phi & K_\theta & K_\psi \end{pmatrix} = \begin{pmatrix} 700 & 700 & 700 & 700 & 700 & 700 \end{pmatrix}$
K_d	$K_d = \begin{pmatrix} K_x & K_y & K_z & K_\phi & K_\theta & K_\psi \end{pmatrix} = \begin{pmatrix} 100 & 100 & 100 & 100 & 100 & 100 \end{pmatrix}$
SMC Controller	
Λ	$\Lambda = \begin{pmatrix} \Lambda_x & \Lambda_y & \Lambda_z & \Lambda_\phi & \Lambda_\theta & \Lambda_\psi \end{pmatrix} = \begin{pmatrix} 10 & 10 & 10 & 40 & 40 & 10 \end{pmatrix}$
K	$K = \begin{pmatrix} K_x & K_y & K_z & K_\phi & K_\theta & K_\psi \end{pmatrix} = \begin{pmatrix} 0.5 & 0.5 & 0.5 & 2.5 & 2.5 & 0.5 \end{pmatrix}$

➢ **SMC Controller**

In first simulation, a robust SMC controller is designed to enable autonomous orientation control of the vehicle while traversing the waypoints. Fig. 6.20 shows the trajectory of the AUV moving in 3D. From Fig. 6.20, it can be seen that the AUV applied the SMC controller could track the desired 3-D trajectory well, and it reached all waypoints. The waypoints are used to define the desired path and direction of movement along the path, so the controller will not try to directly reach the waypoints. Because of this, the first waypoint is never reached. Fig. 6.24 shows the position and orientation angle of the AUV with time. As shown in Fig. 6.24, the AUV converges to the target trajectory of the AUV after approx. 4 seconds, even though there is an error in the initial position and heading angle. In order to follow the target trajectory, the control input obtained through the sliding mode motion controller and the thrust distributed to each propeller by the control allocation algorithm are shown in Fig. 6.22. Looking at the individual thruster actuation in Fig. 6.22, it is also easy to see that the thruster allocation system tries to optimize the thruster actuation. In addition, the thrust of each thruster satisfies the desired performance within the limit value ± 100N.

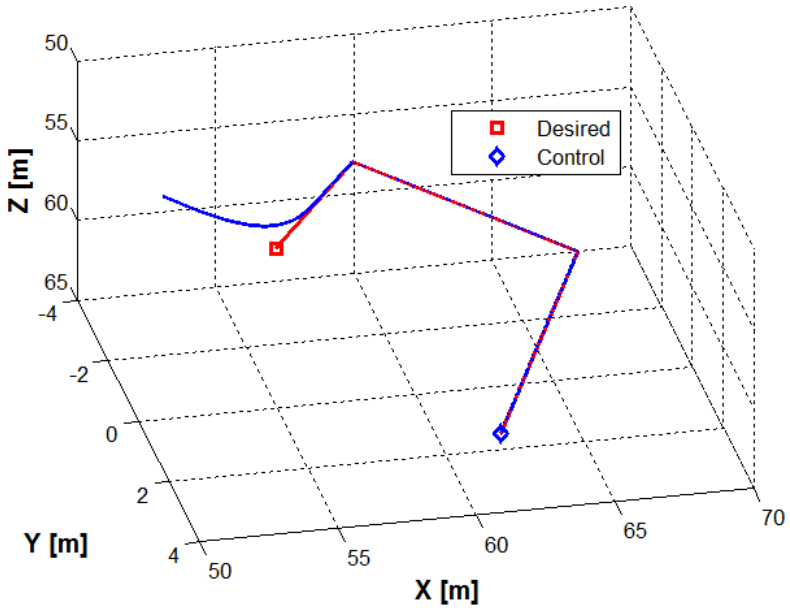

Fig. 6.20 3D trajectories of AUV using SMC controller.

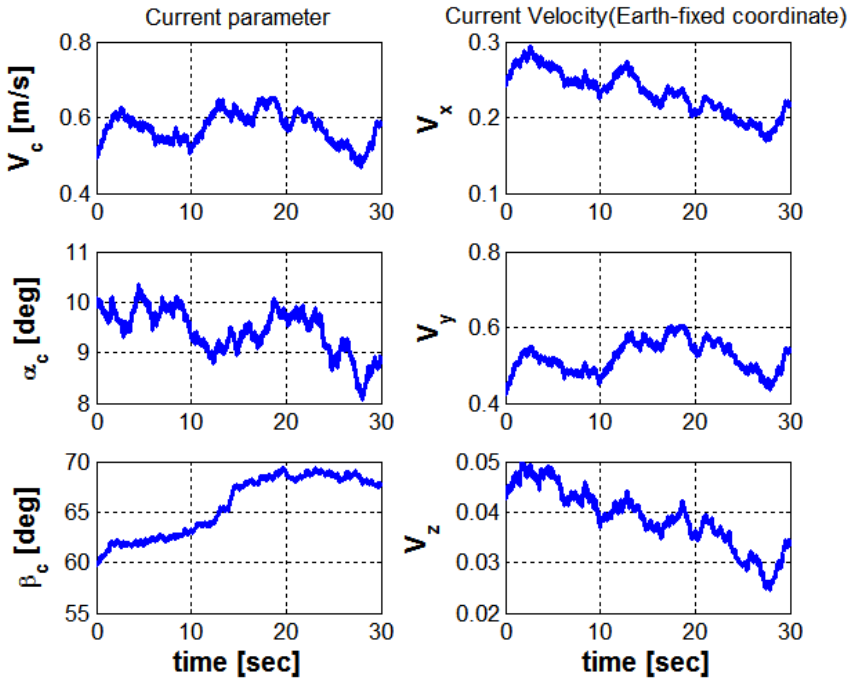

Fig. 6.21 Current forms.

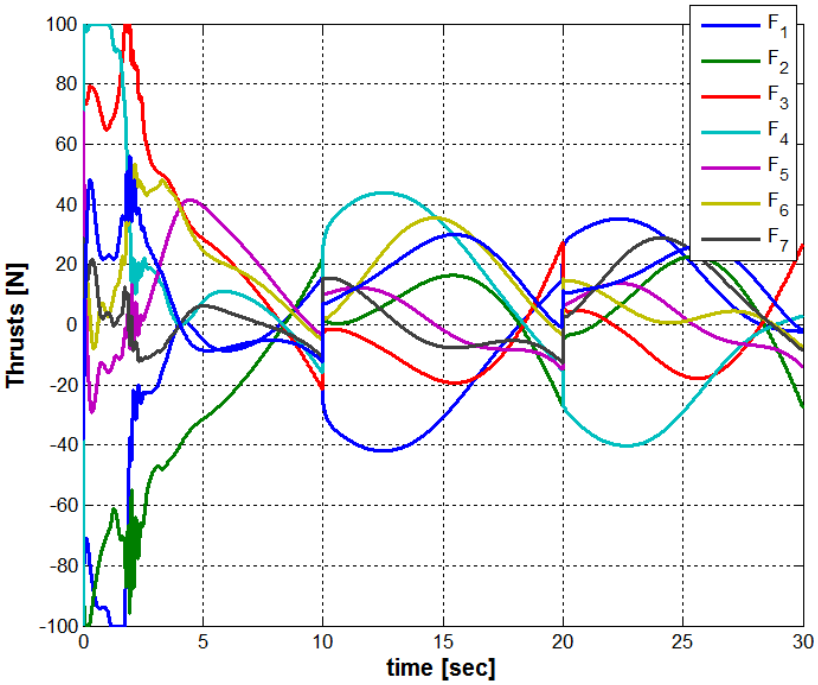

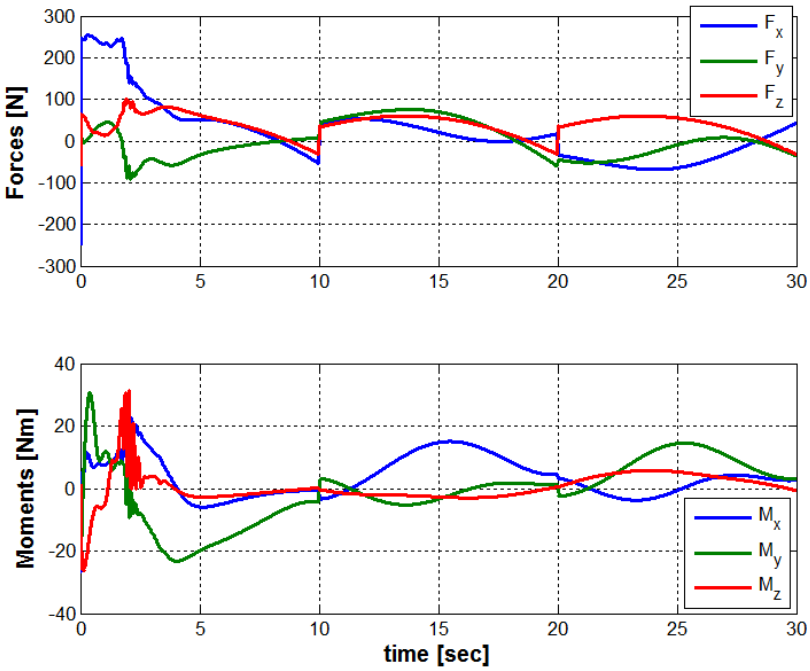

Fig. 6.22 Control inputs using SMC controller.

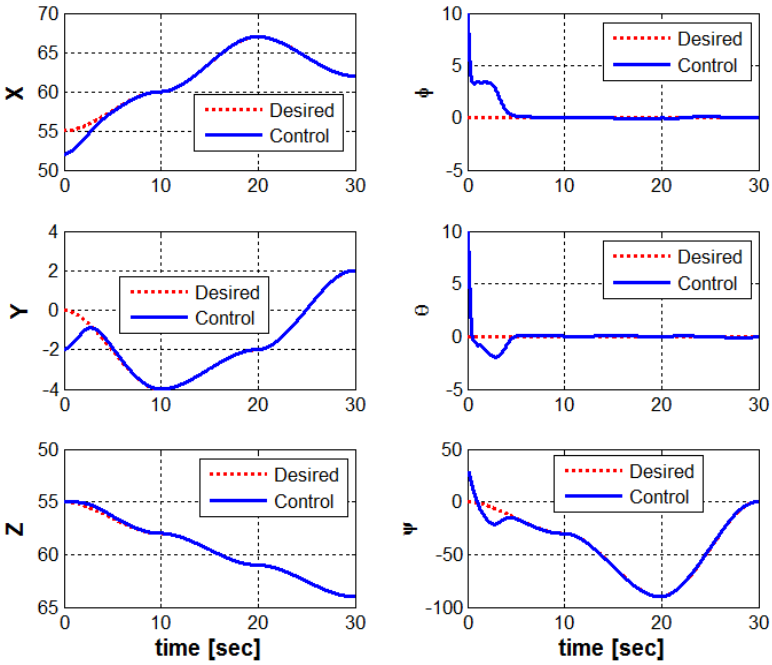

Fig. 6.23 Positions and orientation angles of AUV using SMC controller.

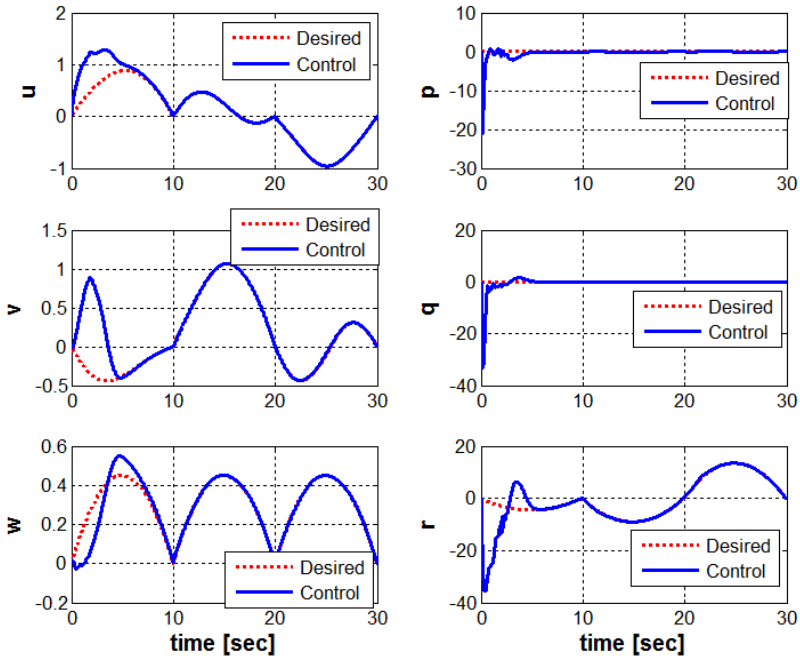

Fig. 6.24 Velocities of AUV using SMC controller.

- **PD Controller**

In the second simulation, the ocean current and the model uncertainties are the same as the previous experiments, but in this case, PD controller is sued to control the AUV position and orientation angles. The PD controller applied here has a limitation in controlling AUV due to the effects of currents. The simulation results are shown in Fig. 6.25-6.28. Fig. 6.25 shows the trajectory of the AUV using PD controller. It can be seen that the AUV cannot follow the target trajectory, and the unsteady behavior is shown as well as the position of the AUV. As a result, since the AUV could not follow the target trajectory, the control input and the thrust of each propeller repeatedly reach the limit value as shown in Fig. 6.26.

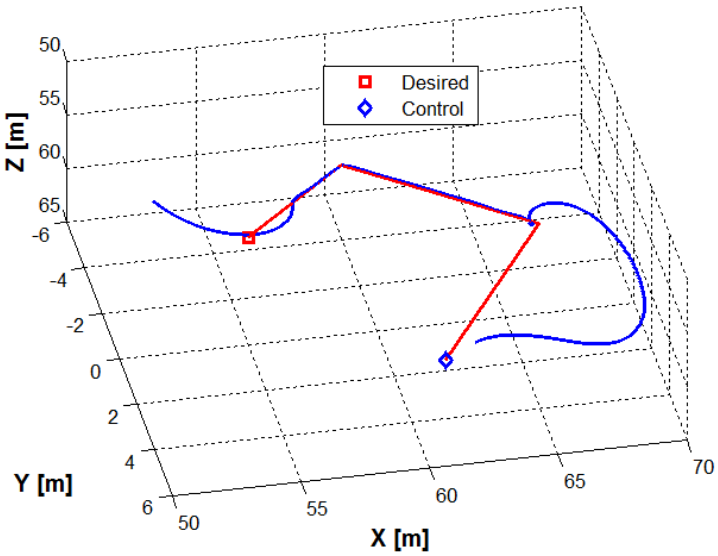

Fig. 6.25 3D trajectories of AUV using PD controller.

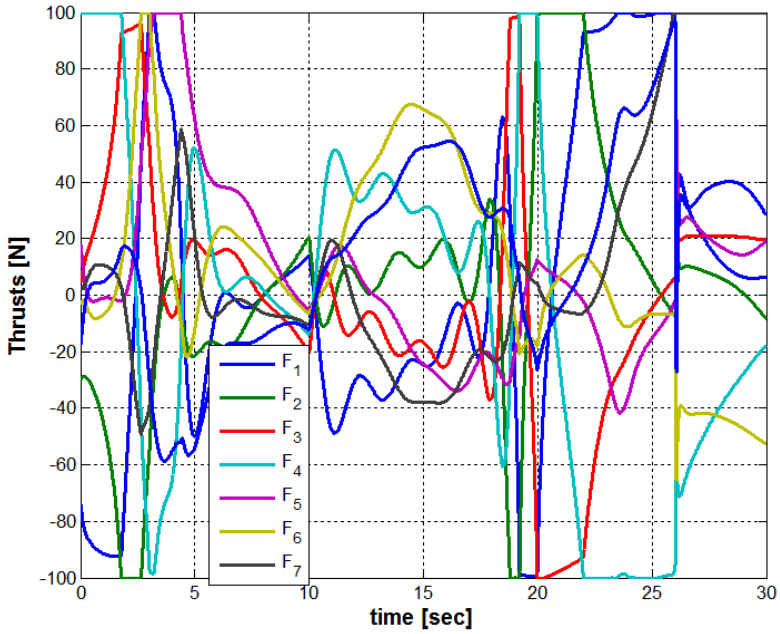

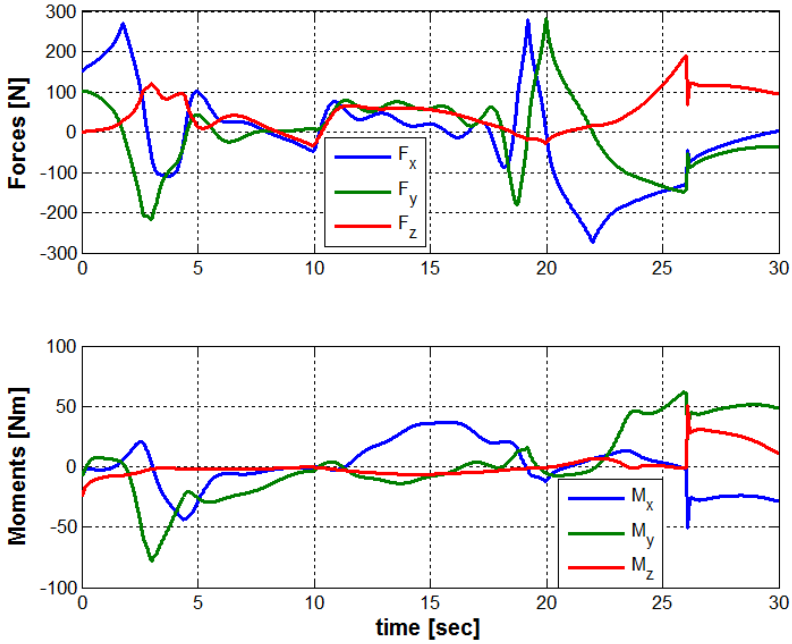

Fig. 6.26 Control inputs using PD controller.

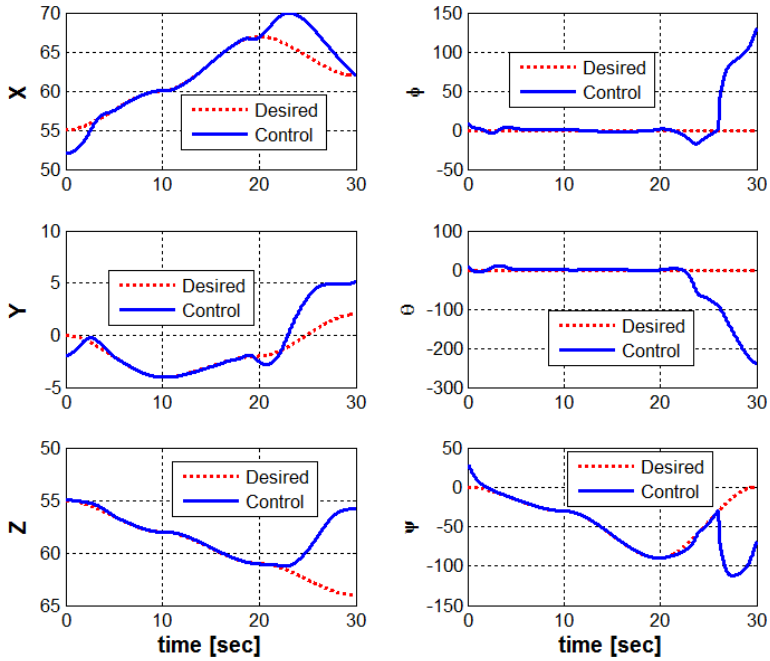

Fig. 6.27 Positions and orientation angles of AUV using PD controller.

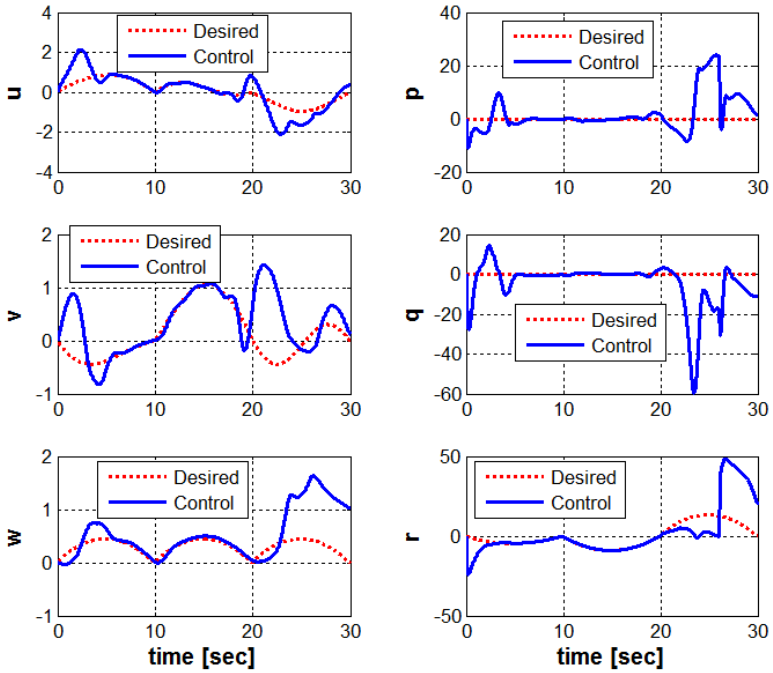

Fig. 6.28 Velocities of AUV using PD controller.

➢ **Combined Between PD Controller and SMC**

Fig. 6.29-6.30 show the comparison of the vehicle trajectories. The red dotted line denotes the desired trajectory of AUV passing though the waypoints, the green solid line denotes the actual trajectory of AUV using the PD controller, and the blue dotted line denotes the actual trajectory of AUV using the SMC controller. From the results, it is seen that the SMC controlled the AUV converges faster to the desired position than the PD controller. Also, the AUV controlled by the SMC scheme is seen to follow the reference trajectory well, converging fairly fast to the desired position.

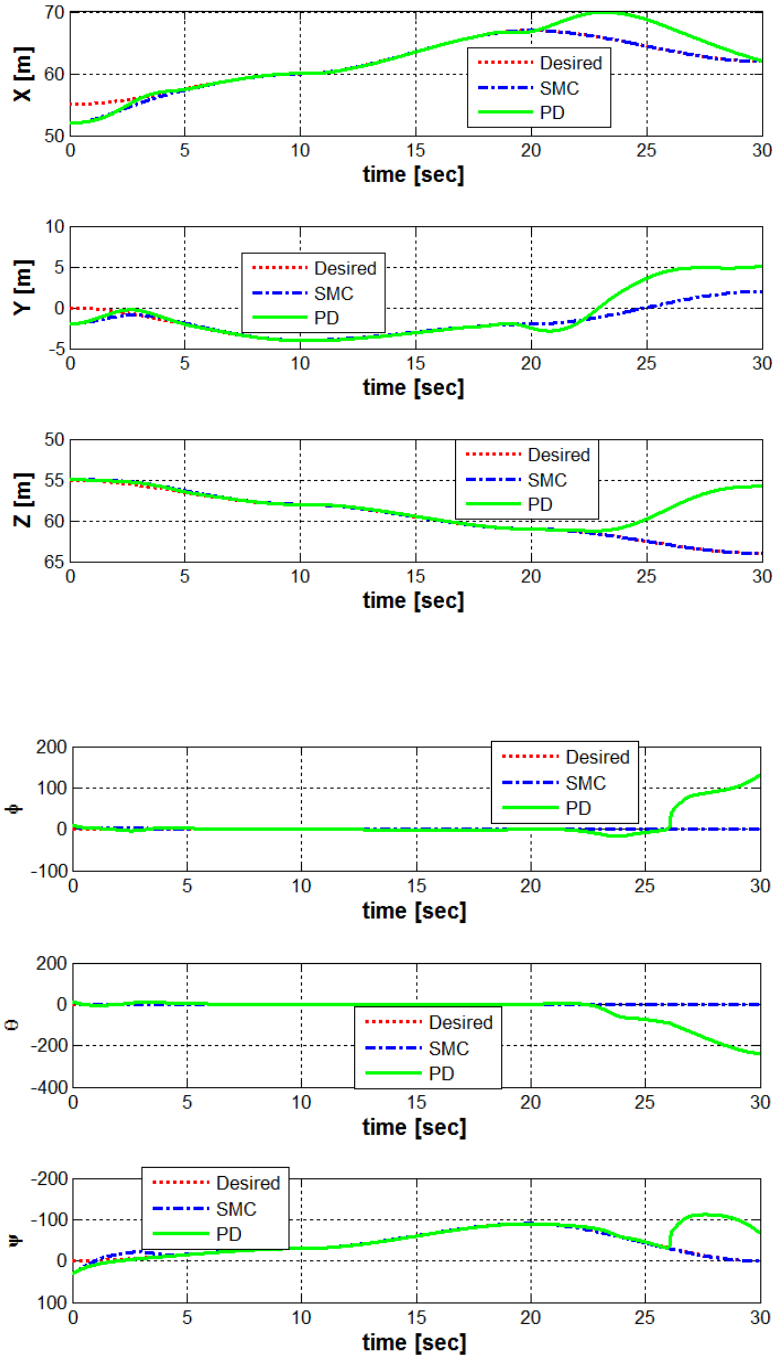

Fig. 6.29 Positions and orientation angles of AUV in both cases: PD and SMC controllers.

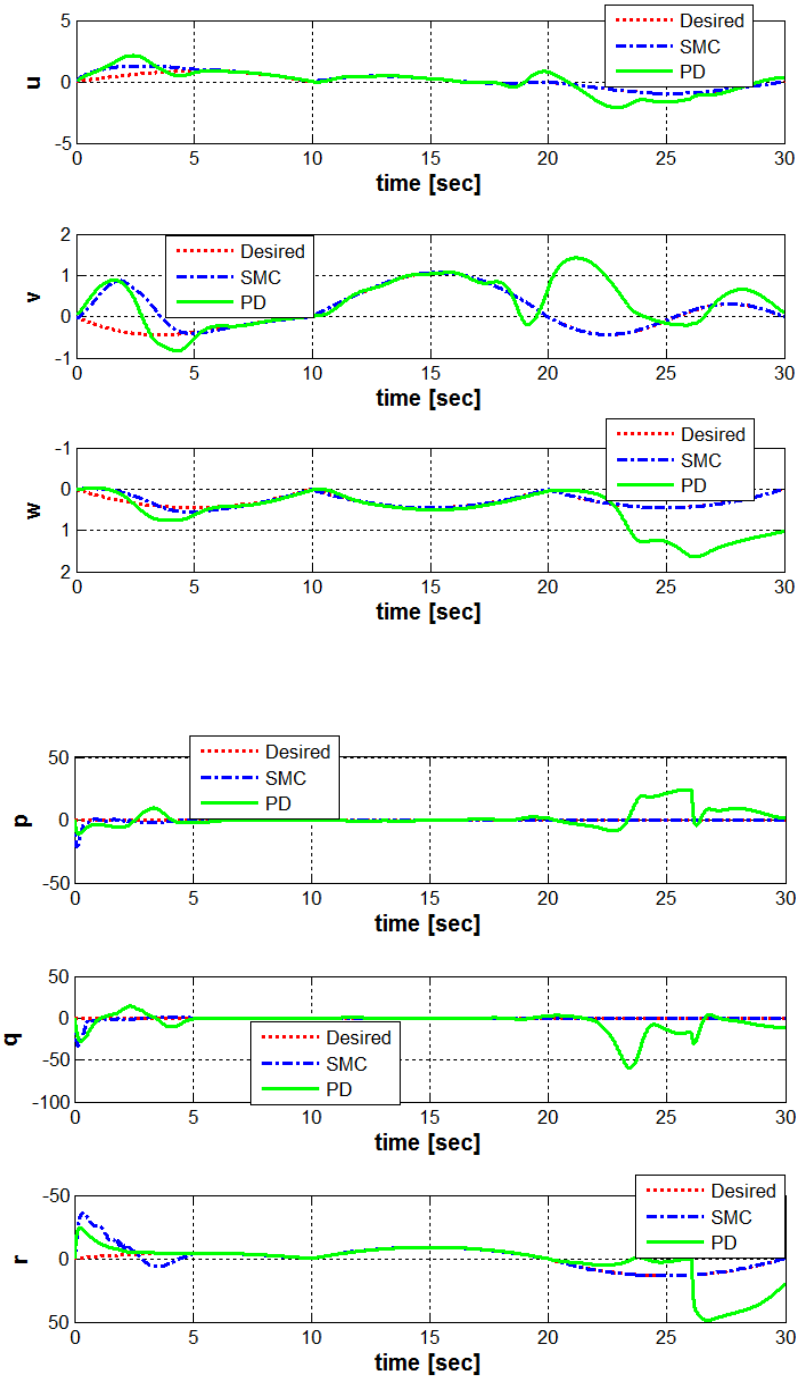

Fig. 6.30 Velocities of AUV in both cases: PD and SMC controllers.

b) Five Waypoints

The second desired trajectory was a 2-D horizontal trajectory at a depth of 60 meters. The five desired waypoints are WP1 (60,0,60,0,0,0), WP2 (63,0,60,0,0,-30), WP3 (66,3,60,0,0,-90), WP4 (66,6,60,0,0,0), and WP5 (63,9,60,0,0,0). The starting point WP1 (60,0,60,0,0,0) at time t_0=0 and stopping time t_f =40s at WP5 (63,9,60,0,0,0). The model uncertainty was applied in the same way as in the previous simulation, assuming that a 3-dimensional current model with an average speed of 0.5m/s, an attack angle of current 60° acting on the AUV as shown in Fig. 6.32. Similarly to the previous simulation, in order to maintain stability underwater vehicle due to the characteristics of the AUV, the roll angle and the pitch angle of AUV are also set to 0° during the simulation, and the target heading angle of AUV is defined as the interval -30°, -90°, 0° and 0°, respectively. The main parameters for 5 waypoints control of AUV are shown in Table 6.7. In order to verify whether the underwater vehicle using PD and SMC is capable of tracking the desired trajectory, simulations for both controllers were presented as below.

Table 6.7. Parameters for 5 waypoints of AUV without cable effects

Time for simulation	
Simulation time	*40 seconds*
Sampling time	*0.01*
Position initial values	
$[X \quad Y \quad Z \quad \phi \quad \theta \quad \psi] = [58 \quad -2 \quad 57 \quad 10 \quad 10 \quad 30]$	
Velocity initial values	
$[u \quad v \quad w \quad p \quad q \quad r] = [0 \quad 0 \quad 0 \quad 0 \quad 0 \quad 0]$	
Waypoints	
Waypoint 1	$(x \quad y \quad z \quad \phi \quad \theta \quad \psi) = (60 \quad 0 \quad 60 \quad 0 \quad 0 \quad 0)$
Waypoint 2	$(x \quad y \quad z \quad \phi \quad \theta \quad \psi) = (63 \quad 0 \quad 60 \quad 0 \quad 0 \quad -30)$
Waypoint 3	$(x \quad y \quad z \quad \phi \quad \theta \quad \psi) = (66 \quad 3 \quad 60 \quad 0 \quad 0 \quad -90)$
Waypoint 4	$(x \quad y \quad z \quad \phi \quad \theta \quad \psi) = (66 \quad 6 \quad 60 \quad 0 \quad 0 \quad 0)$
Waypoint 5	$(x \quad y \quad z \quad \phi \quad \theta \quad \psi) = (63 \quad 9 \quad 60 \quad 0 \quad 0 \quad 0)$
Current parameters (3D)	

Average speed	*0.5 m/s*
Angle of attack	*10 degrees*
Heading angle of current	*60 degrees*
PD Controller	
K_p	$K=\begin{pmatrix}K_x & K_y & K_z & K_\phi & K_\theta & K_\psi\end{pmatrix}$ $=\begin{pmatrix}700 & 700 & 700 & 700 & 700 & 700\end{pmatrix}$
K_d	$K=\begin{pmatrix}K_x & K_y & K_z & K_\phi & K_\theta & K_\psi\end{pmatrix}$ $=\begin{pmatrix}50 & 50 & 50 & 50 & 50 & 50\end{pmatrix}$
SMC Controller	
Λ	$\Lambda=\begin{pmatrix}\Lambda_x & \Lambda_y & \Lambda_z & \Lambda_\phi & \Lambda_\theta & \Lambda_\psi\end{pmatrix}$ $=\begin{pmatrix}8 & 8 & 8 & 40 & 40 & 8\end{pmatrix}$
K	$K=\begin{pmatrix}K_x & K_y & K_z & K_\phi & K_\theta & K_\psi\end{pmatrix}$ $=\begin{pmatrix}0.5 & 0.5 & 0.5 & 2.5 & 2.5 & 0.5\end{pmatrix}$

- **SMC Controller**

Firstly, SMC control is applied for the AUV path tracking control. This method decouples the stabilizing control and guidance control. First, attitude controller is designed to stabilize the system and then velocity and position controller are designed to follow the path. The simulated results are shown in Figs. 6.31-6.35, where it is seen that the actual trajectory tracked the desired trajectory and reached every waypoint.

Fig. 6.31 shows the trajectory of the AUV moving in 3D. In the early stage, the heading angle of AUV is 30° and the initial position of AUV is (58, -2, 57, 10, 10) in the horizontal plane. Until 10 seconds, the AUV aimed at the heading angle of -30° while reaching the first target position (63, 0, 60, 0, 0). After that, the AUV moved to the second target position (66, 3, 60, 0, 0) by 20 seconds, and the heading angle was changed to -90°. Then, the AUV kept moving to the next target position (66, 6, 60, 0, 0) by 30 seconds, and the heading angle at that point was 0°. Thereafter, simulations were performed to last target position and orientation angle at that time were also 0° for 10 seconds. Figs. 6.34 and 6.35 show the position and orientation angle and velocities of the AUV with time, respectively. As shown in Fig. 6.34, the AUV converges to the target trajectory of the AUV after approx. 7

seconds, even though there is an error in the initial position and heading angle. The control input of the sliding mode controller and thrusts distributed to the seven thrusters are shown in Fig. 6.33.

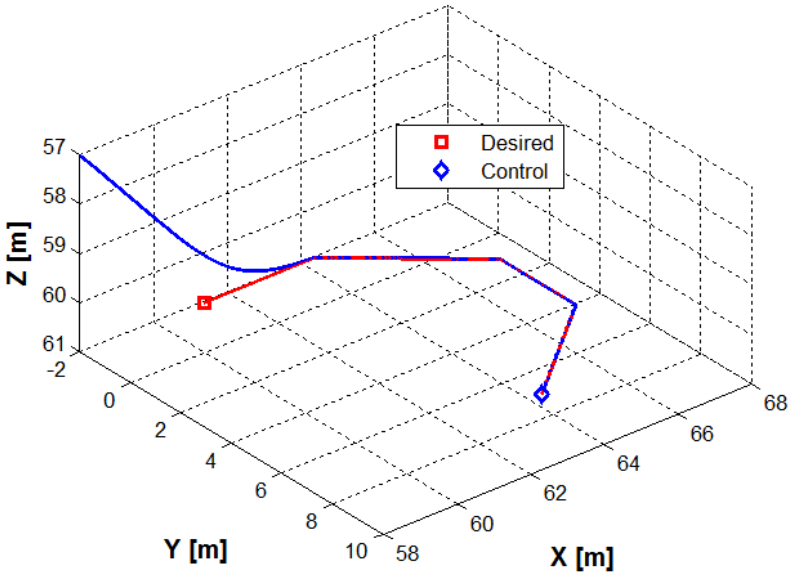

Fig. 6.31 3D trajectories of AUV using SMC controller.

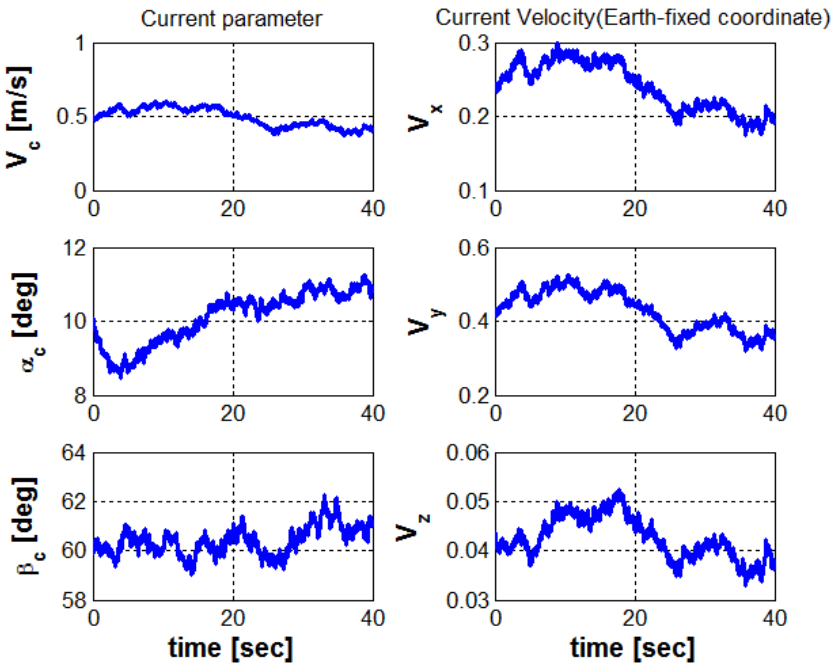

Fig. 6.32 Current forms.

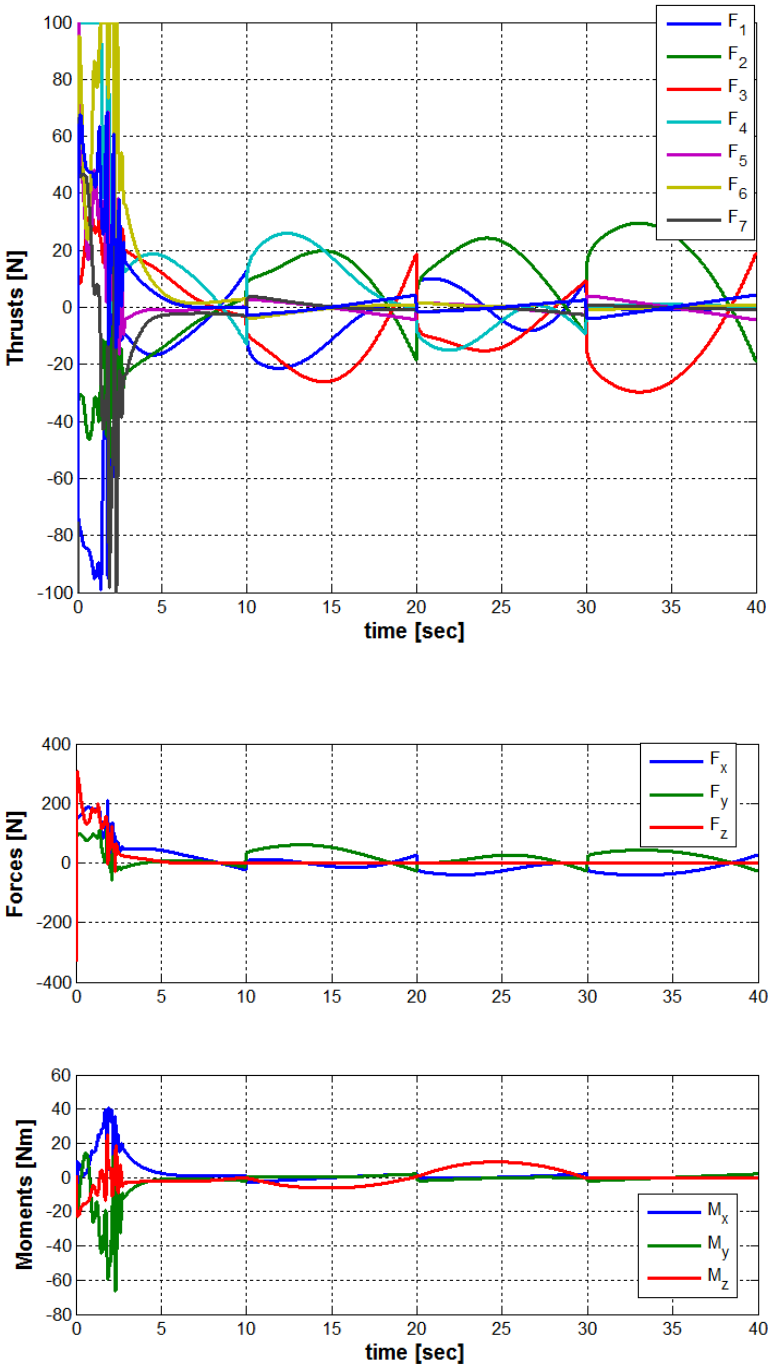

Fig. 6.33 Control inputs using SMC controller.

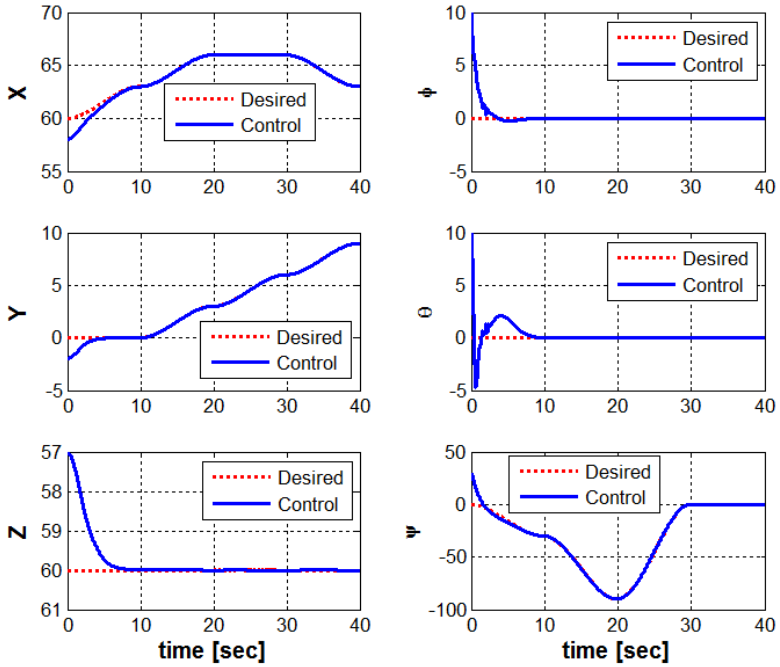

Fig. 6.34 Positions and orientation angles of AUV using SMC controller.

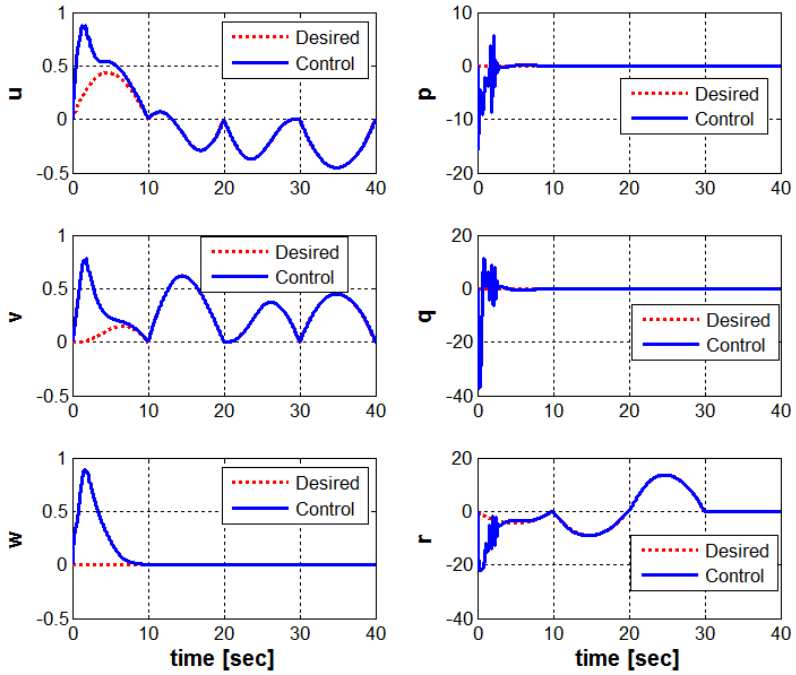

Fig. 6.35 Velocities of AUV using SMC controller.

➢ **PD Controller**

In order to compare performance with sliding mode control, the PD controller has been made by running a simulation with the same path and conditions as before, and comparing the results with the first simulation. Figs. 6.35 and 6.39 show the trajectory of the AUV using PD controller and the positions and velocities of AUV, respectively. From these results, it can be seen that the AUV drifts without control due to strong current effects. Therefore, it can be seen that robust control performance could not be guaranteed through the PD controller. Moreover, Fig. 6.37 is the control input of the PD controller for waypoint control, and the thrust of each thruster through the control allocation algorithm.

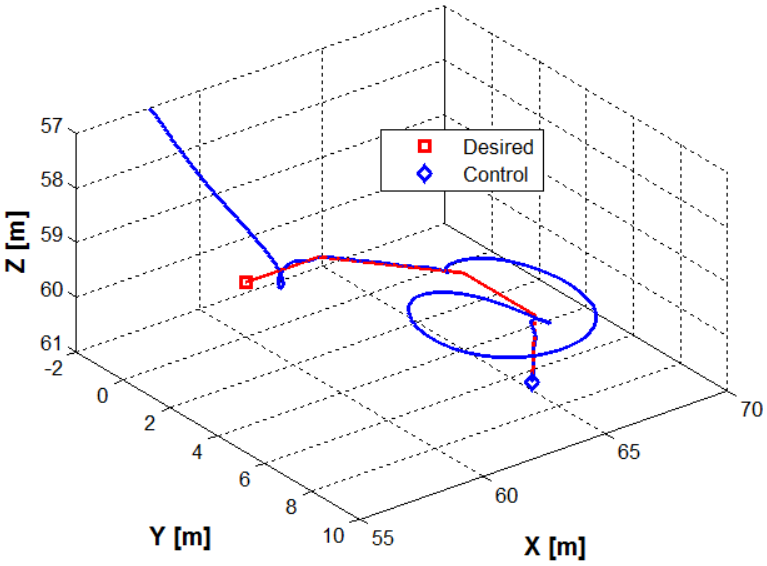

Fig. 6.36 3D trajectories of AUV using PD controller.

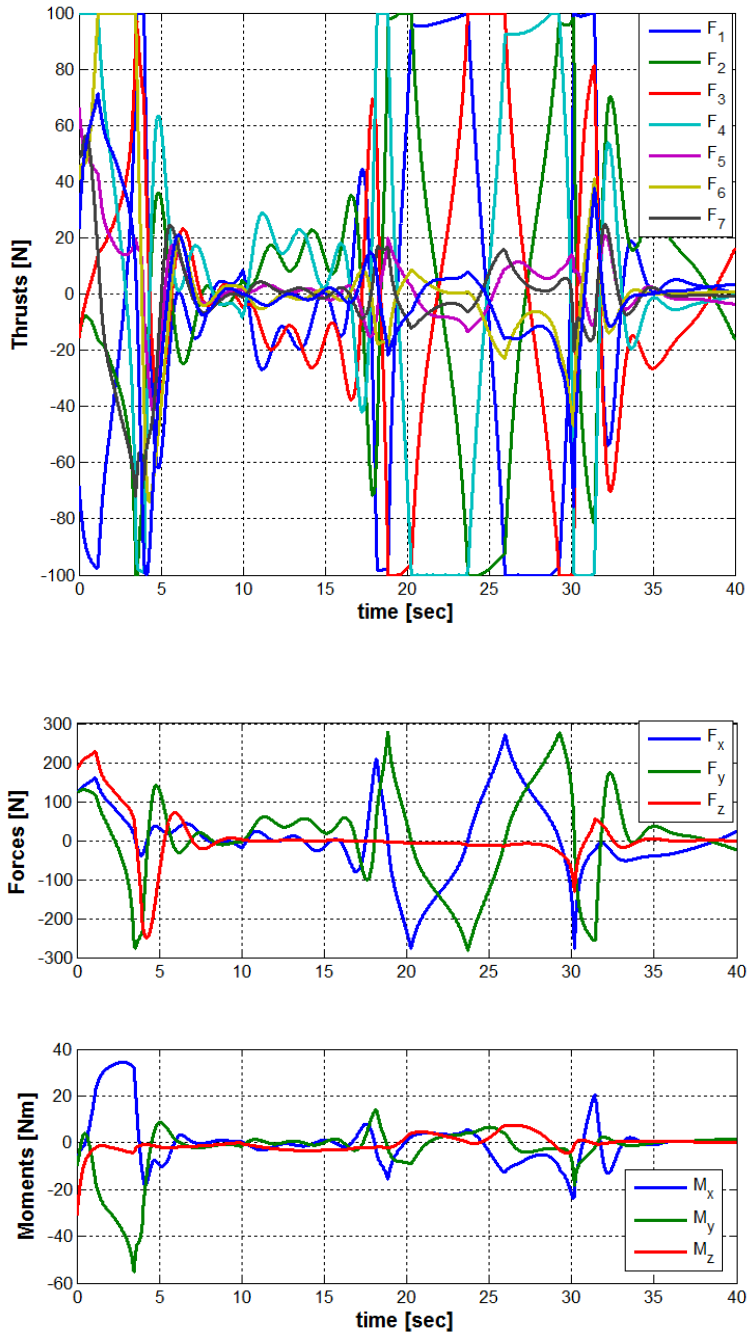

Fig. 6.37 Control inputs using PD controller.

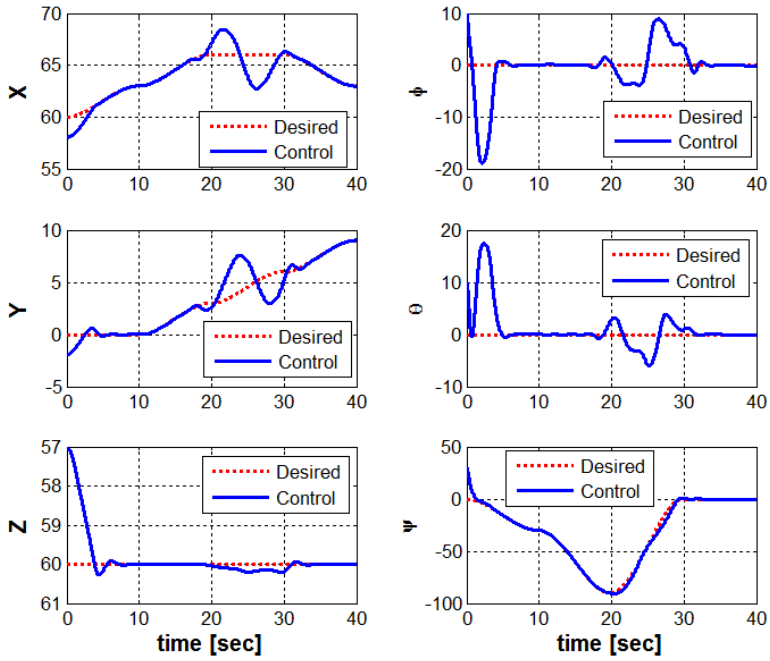

Fig. 6.38 Positions and orientation angles of AUV using PD controller.

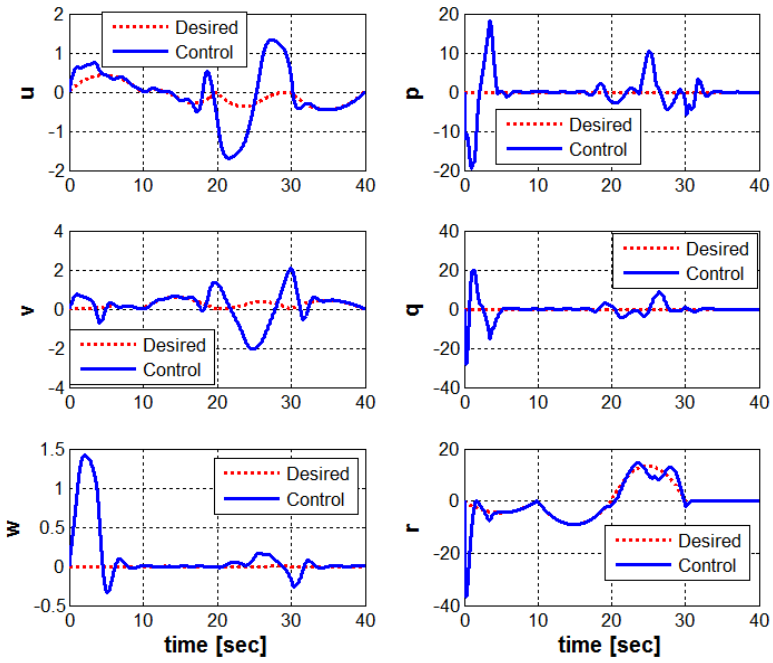

Fig. 6.39 Velocities of AUV using PD controller.

➢ **Combined Between PD Controller and SMC**

Figs. 6.40-6.41 show the comparison of the vehicle trajectories where the green solid line signifies that the AUV is controlled by PD scheme, while the blue dotted line signifies SCM controller. When comparing the PD scheme to the proposed SMC scheme, the differences in performance of AUV are obvious; the SMC performance is more consistent and does not degrade as the speed increases. This suggests robustness of the SMC scheme over the environmental disturbances and parameter uncertainties.

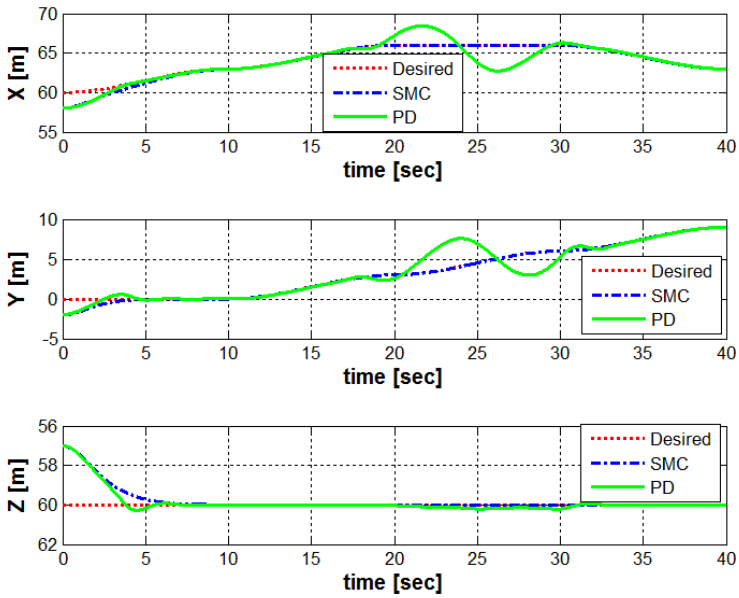

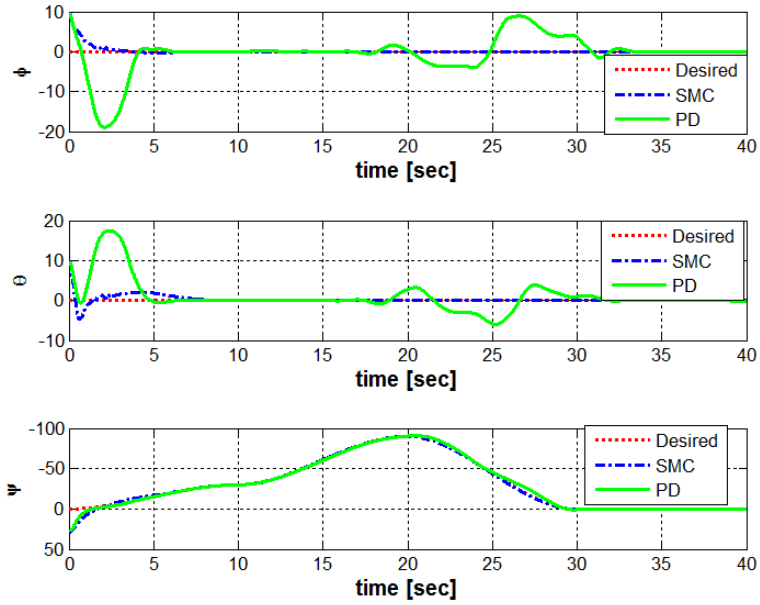

Fig. 6.40 Positions and orientation angles of AUV in both cases: PD and SMC controllers.

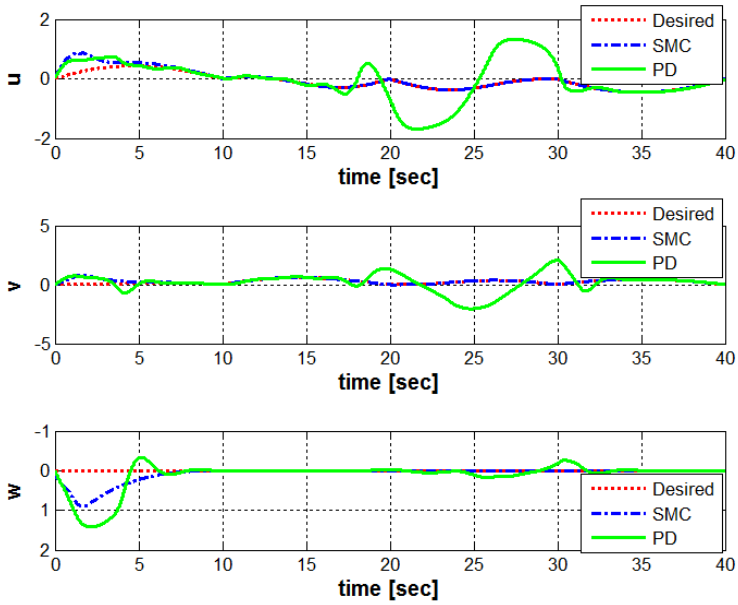

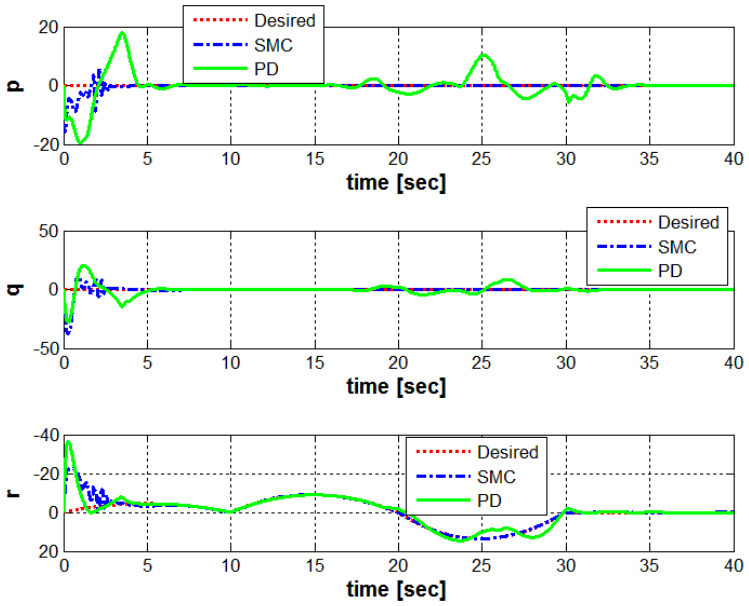

Fig. 6.41 Velocities of AUV in both cases: PD and SMC controllers.

Chapter 7: Obstacle Avoidance and Path Planning for Vehicle Using Rapidly-Exploring Random Trees Algorithm

Navigation of system with an obstacle avoidance process is one of the most important abilities and behaviors of such marine vehicles. In some conditions, navigation and guidance of AUVs are more difficult than land vehicles and air ones, because there are some environment subsurface restrictions. Many path planning techniques for autonomous vehicles have been discussed in the literature. Among them, much of work on search algorithms [97-101] provide the computationally efficient way in discrete state spaces. However, the resulting paths by such algorithms do not tend to be smooth (piecewise linear) and hence, do not satisfy kinematic feasibility of the vehicle. Moreover, most path planning techniques introduced to date are based firmly on deterministic methods and graph searches. Unfortunately, due to their sample space discretization issues, the generated trajectories need extra smoothing and interpolation. Notwithstanding this, the system dynamics are also neglected to avoid state-explosion effect. Collectively, these factors ensue a very conservative system performance. Randomization methods are becoming popular as they are inherently more robust to the state explosion effect. To pass through this problem, it is necessary to use a planner which can explore the whole configuration space. This kind of planners is the purpose of the number of research works [102–104]. We chose to study the efficiency of an RRT planner [102] in exploring the uncertain-configuration space.

The RRT structure and algorithm is designed to efficiently and quickly explore high-dimensional spaces that are not necessarily convex [105, 106]. The main advantage of the RRT, aside from its computational efficiency, is its ability to quickly find a feasible solution between complex obstacle configurations. Its main disadvantage is that the solution may be far from optimal. Despite this, however, the RRT algorithm is well suited for use in motion planning since it inherently accounts for the differential constraints arising from vehicle dynamics as well as the spatial constraints due to the presence of obstacles in the environment.

7.1 Path Planning and Guidance: Two Interrelated Problems

An autonomous vehicle is one that possesses self-governing characteristics which, ideally, allow it to perform pre-specified tasks without human intervention. These characteristics are associated with the vehicle's (or, more generally, system's) available information regarding its position and surroundings, and also

the vehicle's ability to use its actuators so as to accomplish a mission. In the context of this dissertation, the following four terms summarize the aforementioned properties: a) path planning, b) guidance, c) navigation, and d) control.

Path planning (or Module 1) refers to the system responsible for designing paths to be assigned to the vehicle in order to accomplish its mission. These paths must satisfy several desired properties related to both the vehicle's constraints and the morphology of the environment in which the vehicle navigates. In other words, this module must ensure that the generated path takes into account the dynamic constraints of the vehicle (such as maximum curvature and velocity) while keeping the vehicle at a safe distance from obstacles at all times. Naturally, this process includes two main steps:

1. The determination of a set of points on the map, namely, the waypoints.
2. The generation of a path based on the waypoints.

In practice, both steps should be implemented with the problem constraints in mind. In the robotics literature, the term "motion planning" is used, see for instance [107-110]. However, motion planning often includes both the design of a suitable path and the actions that should be taken by the robot in order to accomplish the mission. For that reason, we will use the terms "path planning" for the two steps above.

Guidance (or Module 2) is the action or the system that continuously computes the reference (desired) position, velocity and acceleration of a marine craft to be used by the motion control system. These data are usually provided to the human operator and the navigation system. The basic components of a guidance system are motion sensors, external data such as weather data (wind speed and direction, wave height and slope, current speed and direction) and a computer. The computer collects and processes the information, and then feeds the results to the motion control system. In many cases, advanced optimization techniques are used to compute the optimal trajectory or path for the marine craft to follow. This might include sophisticated features such as fuel optimization, minimum time navigation, weather routing, collision avoidance, formation control and synchronization.

Navigation (or Module 3) is the science of directing a craft by determining its position/attitude, course and distance traveled. In some cases velocity and acceleration are determined as well. This is usually done by using a global navigation satellite system (GNSS) combined with motion sensors such as accelerometers and gyros. The most advanced navigation system for marine applications is the inertial navigation system (INS).

Control (or Module 4) or more specifically motion control, is the action of determining the necessary control forces and moments to be provided by the craft in order to satisfy a certain control objective. The desired control objective is usually seen in conjunction with the guidance system. Examples of control objectives are minimum energy, set-point regulation, trajectory-tracking, path-following and maneuvering control. Constructing the control algorithm involves the design of feedback and feed-forward control laws. The outputs from the navigation system, position, velocity and acceleration are used for feedback control while feed-forward control is implemented using signals available in the guidance system and other external sensors.

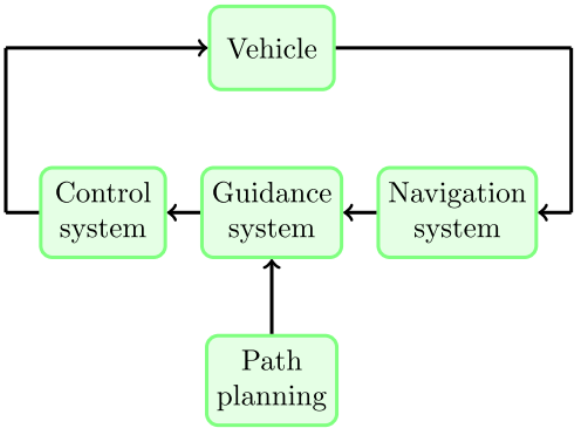

Fig. 7.1 Interaction among the 4 main modules.

According to the definitions above, we may say that the four modules act repeatedly in the following order (see also Fig. 7.1):

- ***Module 1:*** The path-planning algorithm generates a path which (if followed without deviations) is guaranteed to be safe and feasible. In the case where the mission involves temporal assignments, this module specifies where on the path the vehicle should be at any time instant.
- ***Module 3:*** The navigation system uses the vehicle's sensors in order to determine the vehicle's position, velocity, and attitude.
- ***Module 2:*** Depending on where the vehicle should be (Module 1) and where it actually is (Module 3), the guidance system determines the reference trajectories to be fed to the control system (Module 4) in order to minimize the error.
- ***Module 4:*** Based on the reference trajectories generated by Module 2, the control system calculates the necessary forces that each one of the actuators must produce.

In this dissertation, we are concerned almost exclusively with the first and second modules, namely, path planning and guidance. From an autonomy point of view, these two modules are of great interest because path planning is related to what we want to achieve (by defining spatial and temporal constraints), and guidance dictates how we should act in order to achieve it (by generating appropriate reference trajectories).

7.2 RRT Algorithm for Exploration

The RRT algorithm incrementally builds a tree from the starting point to the goal point by adding a new vertex to randomly selected points. A good trait of RRT is that the tree grows towards unvisited regions of the space and never regresses into already explored areas which results in a rapid exploration of the space [111].

The primary factors affecting RRT performance are the number of random points generated, segment length used for tree extension, probability distribution used for random point generation, and the number of trees used. RRT is typically initialized with one node (starting point) and no edges. Fig. 7.2 shows a simple RRT, and the basic steps involved in its development. The main concept behind RRT is to bias the growth of the tree towards the largest unexplored regions of space. By uniformly picking a random point and finding the nearest point on the RRT to extend, the search is biased towards splitting the largest Voronoi region for all the existing vertices on the tree. Note that the probability that a vertex is selected for extension (and hence its Voronoi region split) is proportional to the area of its Voronoi region.

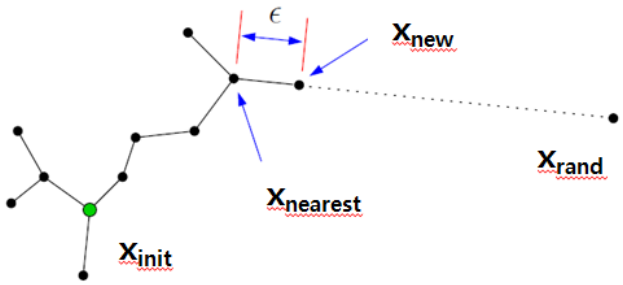

Fig. 7.2 RRT expansion.

Algorithm 1 shows the RRT algorithm which runs K iterations. RRT algorithm operates as follows: First RRT draws a state (x_{state}) and then decides a node to extend among the existing trees (x_{node}) and finally adds a new node (x_{new}) by connecting the selected node x_{node} with the random state x_{rand} in terms of distance metric. There are three functions within RRT algorithm: drawing a state (line 4),

choosing a node to extend (line 5), and finally extending the selected node (line 6). The performance of RRT depends on these three functions.

Algorithm 1 RRT Algorithm

1: **START_RRT1** (x_{init})

2: T .init (x_{init})

3: **for** 1 to K **do**

4: $x_{state} \leftarrow$ **DrawState** ()

5: $x_{node} \leftarrow$ **NodeSelection** (T, x_{state})

6: $x_{new} \leftarrow$ **NodeExtension** (T, x_{state}, x_{node})

7: **end for**

7.2.1 Random Node Selection

The first function of RRT is **DrawState** which selects a state. Traditional RRT chooses a state randomly within an allowable set of states. The sampling strategy greatly affects the performance of the planner. This function will be described in detail in Section 7.3.

After drawing a state, **NodeSelection** function is applied to decide the node to extend. One possible way is to choose a node randomly among existing trees and then extend for fixed distance d toward x_{state} using **NodeExtension** function.

Fig. 7.3 shows the tree expansion result of the random node selection algorithm. The environment size is 100m × 100m, and the starting point is (50m, 50m). The RRT planner starts on growing trees at stating point within the environment. It is interesting to observe that trees do not grow much from the starting point even after 2000 iterations and are aggregated in the starting point. From this result, it can be seen that random node selection is not a good approach to the problem.

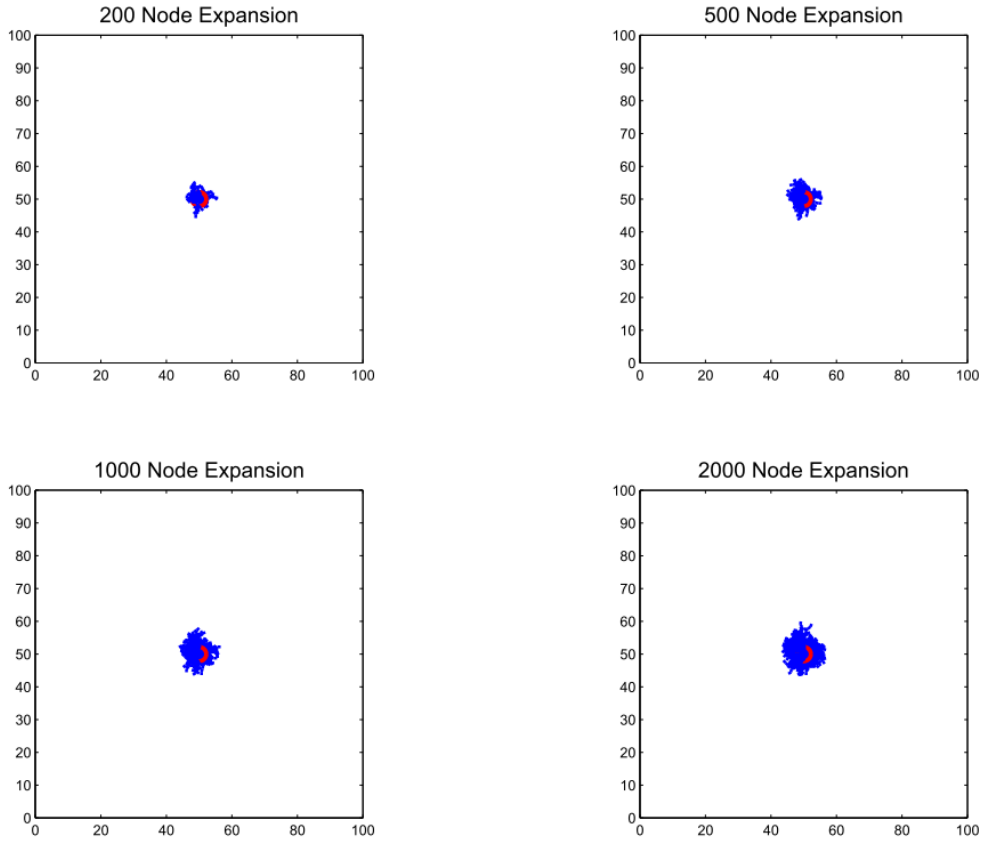

Fig. 7.3 Random node selection RRT algorithm.

7.2.2 Nearest Neighbor Node Selection

Instead of choosing random node among the existing tree, the nearest neighbor from the random point is chosen as a node for expansion. This change results in a totally different behavior of tree expansion. Whereas trees are strongly warped to already explored areas in the random node selection case, trees grow rapidly to unexplored regions in the nearest neighbor node selection case. This comes from the Voronoi regions in RRT nodes. Larger Voronoi regions exist on the border of the tree. Therefore, the nearest neighbor node selection makes vertices with large Voronoi regions be selected for expansion [112].

Fig. 7.4 shows the tree expansion result of the nearest neighbor node selection algorithm. Initially, the RRT tree rapidly grows to the diagonal direction from the center and then it incrementally splits Voronoi regions of the visited region into smaller Voronoi ones. After 2000 iterations, the RRT tree covers most of the area while not regressing to the already explored area.

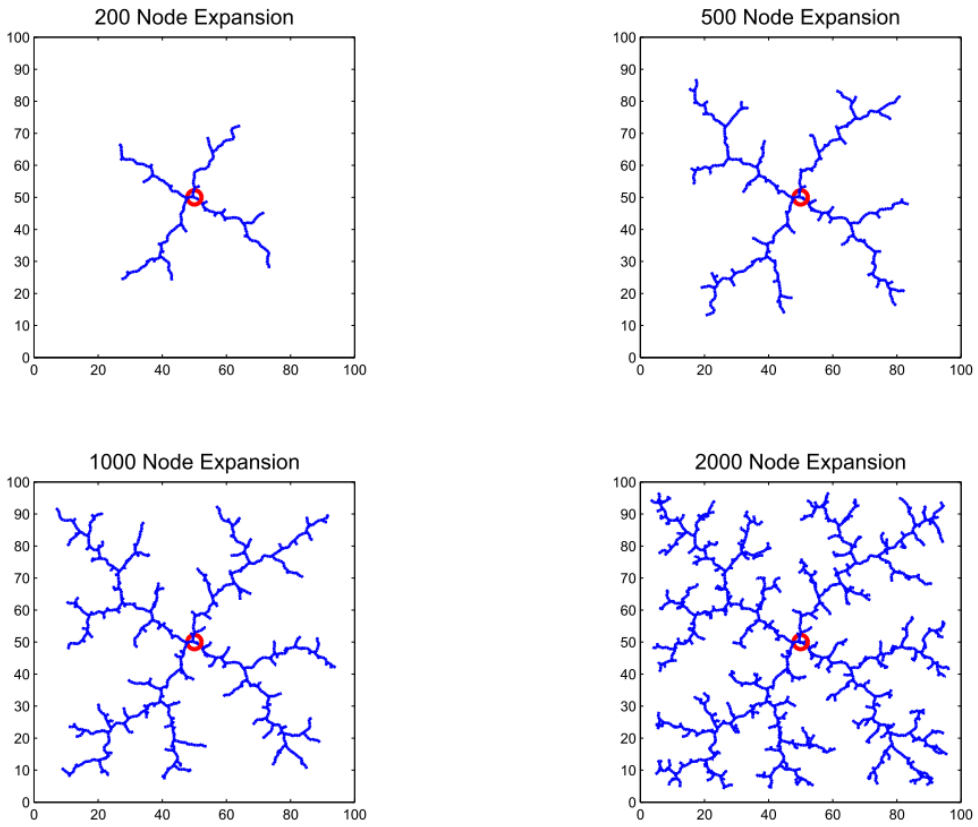

Fig. 7.4 Nearest neighbor node selection RRT algorithm.

7.2.3 RRT Exploration with Obstacles

The main advantage in RRT is that it makes trees grow quickly to unexplored areas. This property can also be applied to a cluttered environment with obstacles. In this case, the collision function is applied before adding a new node as a new tree. If there is no collision between the existing tree and the candidate point, this new point is added to the tree.

Algorithm 2 RRT Exploration Algorithm in Cluttered Environment

1: **START_RRT2** (x_{init})

2: T .init (x_{init})

3: **for** 1 to K **do**

4: $x_{rand} \leftarrow$ **RandomState** ()

5: $x_{near} \leftarrow$ **NearestNeighbor** (T, x_{rand})

6: $x_{new} \leftarrow$ **Extend** $(\mathrm{T}, x_{rand}, x_{near})$

7: **if Collision**(x_{rand}, x_{near}) == No **then**

8: $\mathrm{T}.add(x_{new})$

9: **end if**

10: **end for**

Algorithm 2 shows the RRT exploration algorithm in a cluttered environment. The algorithm operates as follows. First, a position x_{rand} is chosen at random from within the workspace, and this point is compared with existing tree nodes to find the closest point in the tree, x_{near}. A line is drawn connecting x_{near} to x_{rand}, and a new point x_{new} is generated along this ray at a fixed distance d from x_{near}. If there is no collision on the interval between x_{near} and x_{new}, the latter is added to the tree. This process is repeated until the K_{th} iteration.

Fig. 7.5 shows the tree expansion result of the RRT exploration algorithm in a cluttered environment case. With the similar fashion of the free space, the trees grow quickly in the diagonal direction from the center although tree growth is frequently blocked by obstacles. After 2000 iterations, the RRT tree covers most of the unoccupied areas of the environment.

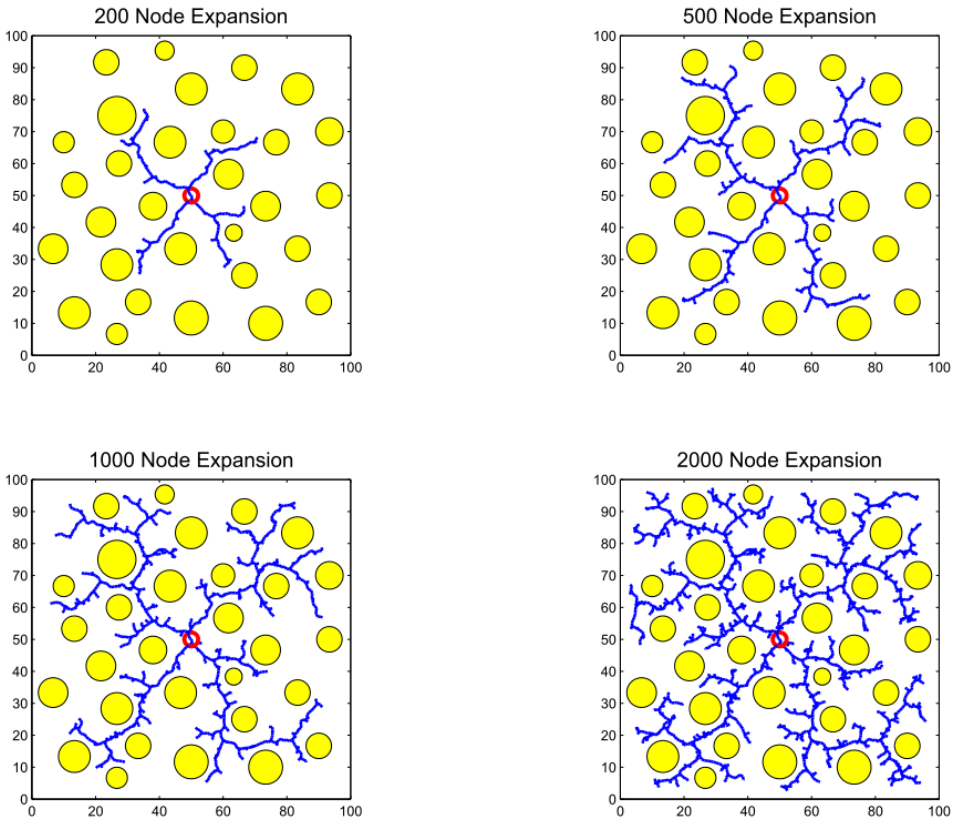

Fig. 7.5 RRT exploration in a cluttered environment.

From this result, it can be seen that RRT can preserve the rapidly growing property towards unvisited area even though the environment is occupied with obstacles.

7.3 RRT Algorithm for Navigation of AUV

Navigation is the problem of finding a collision free motion for the robot system from one configuration to another [113]. Therefore, the difference between exploration and navigation is the existence of goal configuration. The goal of the exploration is to cover the entire environment but that of navigation is not to explore the entire space but to find a path between two configurations. Due to this property, the RRT algorithm for exploration needs to be modified to improve the performance so as to find a path in the navigation mission.

7.3.1 Basic RRT Algorithm

Algorithm 3 shows the basic RRT algorithm for navigation. The operation of RRT Algorithm for Navigation is the same as RRT Algorithm for Exploration except for line 10-12 in algorithm 3. The RRT Algorithm for Exploration repeats the tree growing process during the specified K iterations whereas RRT Algorithm

for Navigation continues the process until any of the existing trees reach the goal point within the specified limit $d_{\lim}$.

Algorithm 3 Basic RRT Algorithm

START_RRT3 (x_{init})

  T .init (x_{init})

while Distance (x_{goal}, x_{new}) $> d_{\lim}$ **do**

  $x_{rand} \leftarrow$ **RandomState** ()

  $x_{near} \leftarrow$ **NearestNeighbor** (T, x_{rand})

  $x_{new} \leftarrow$ **Extend** (T, x_{rand}, x_{near})

  if Collision(x_{rand}, x_{near}) == No **then**

    T.$add(x_{new})$

  end if

  if Distance (x_{goal}, x_{new}) $\leq d_{\lim}$ **then**

    Return T

  end if

end while

Fig. 7.6 shows the basic RRT path planning results which apply basic RRT. The green lines denote all RRT trees and the red lines denote the generated path. The starting point is (0, 0) and the goal point is (290, 290). In Fig. 7.6 (a), RRT can find the collision free path quickly without exploring the whole space but this is not often the case. RRT tries to explore the whole space as shown in Fig. 7.6 (b) for the most part. This comes from the fact that the basic RRT algorithm always selects the candidate point randomly which makes the tree growth uniform. It is not an efficient way to wander the whole space as the primary goal of navigation is to find a feasible path between start and goal configurations.

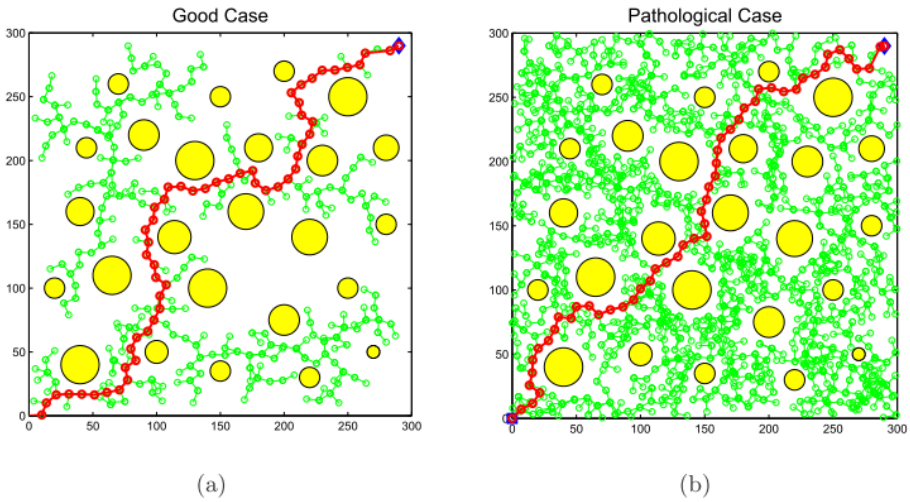

Fig. 7.6 Basic RRT planning results. (a) Good case. (b) Pathological case.

7.3.2 Biased-Greedy RRT Algorithm

Biased RRT can make the tree grow toward the goal location and the efficiency will be enhanced by combining the biased and greedy RRT. Algorithm 4 shows this biased-greedy RRT algorithm. RRT planner chooses a state using a biased sampling strategy and then grows trees as many times as possible before a collision is detected. Fig. 7.7 shows the result of the biased-greedy RRT planning method.

Algorithm 4 Biased-Greedy RRT Algorithm

1: **START _RRT4** (x_{init})

2: T .init (x_{init})

3: **while Distance** (x_{goal}, x_{new}) $> d_{\lim}$ **do**

4: $x_{rand} \leftarrow$ **BiasedState** ()

5: $x_{near} \leftarrow$ **NearestNeighbor** (T, x_{rand})

6: $x_{new} \leftarrow$ **GreedyExtend** (T, x_{rand}, x_{near})

7: **if Collision**(x_{rand}, x_{near}) == No **then**

8: T.$add(x_{new})$

9: **end if**

10: **if Distance** $(x_{goal}, x_{new}) \le d_{\lim}$ **then**

11: Return T

12: **end if**

13: **end while**

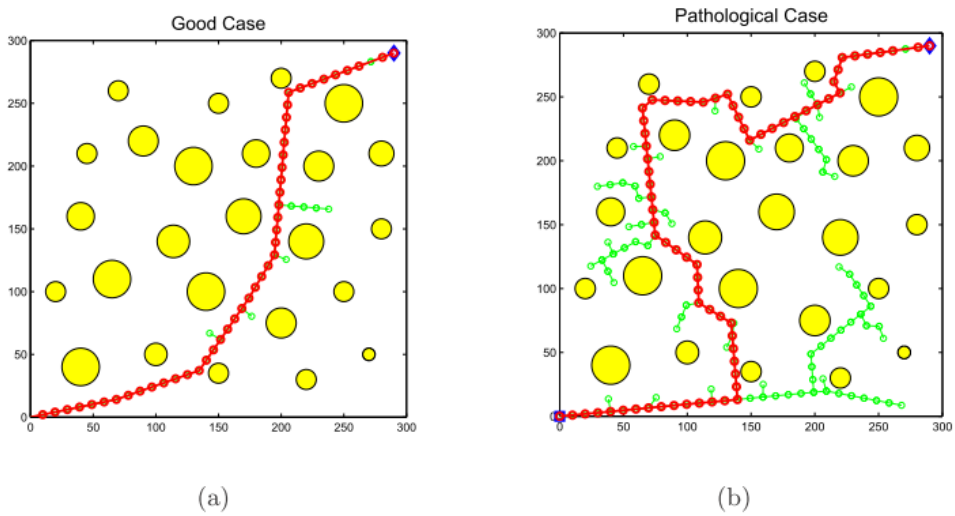

Fig. 7.7 Biased-greedy RRT planning results. (a) Good case. (b) Pathological case.

7.3.3 Synchronized Biased-Greedy RRT Algorithm

The biased-greedy RRT algorithm shows better performance in terms of the computational time. However, this algorithm has the advantages and disadvantages of the combined biased RRT and the greedy RRT algorithms. The advantages of the biased RRT and greedy RRT are that it grows trees towards the goal location and it makes trees traverse the environment in a single iteration respectively. The disadvantage of the biased RRT algorithm is that it requires frequent use of the nearest neighbor function as extensions occur only once though potential direction is selected and the greedy RRT frequently explores unnecessary areas as it extends trees regardless of goodness in that direction. A synchronized biased-greedy RRT algorithm is proposed to improve the path planning performance which has only the good properties of both methods.

The synchronized biased-greedy RRT executes a greedy extension where the goal location is selected as a target point and extends just one time otherwise. Algorithm 5 shows the synchronized biased-greedy RRT algorithm.

Algorithm 5 Synchronized Biased-Greedy RRT Algorithm

START_RRT5 (x_{init})
  T .init (x_{init})
while Distance (x_{goal}, x_{new}) $> d_{\lim}$ **do**
  $x_{rand} \leftarrow$ **BiasedState** ()
  $x_{near} \leftarrow$ **NearestNeighbor** (T, x_{rand})
  $x_{new} \leftarrow$ **SyncGreedyExtend** (T, x_{rand}, x_{near})
  if Collision(x_{rand}, x_{near}) == No **then**
    T.$add(x_{new})$
  end if
  if Distance (x_{goal}, x_{new}) $\leq d_{\lim}$ **then**
    Return T
  end if
end while

The synchronized biased-greedy RRT can be interpreted as a gradient descent search with a p probability and a uniform exploration with $1 - p$ probability. This approach will not get trapped in a local minima due to the $1 - p$ probability of random exploration and will find the shortest path with p probability due to the greedy extension. With this synchronized combination of the biasness and greediness, the method is effective in reducing the computational time in comparison with biased RRT. In addition, it generates a more optimal path compared to greedy RRT.

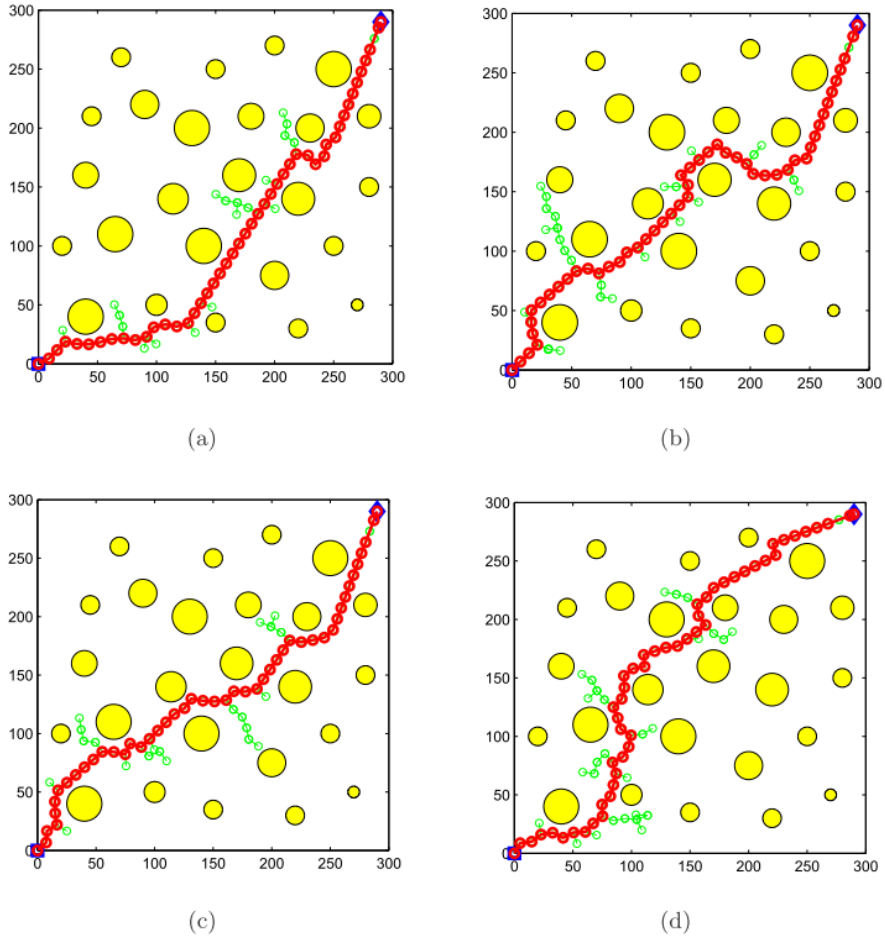

Fig. 7.8 Synchronized biased-greedy RRT planning results.

Fig. 7.8 shows several planning results of a synchronized biased-greedy RRT algorithm. There are two long greedy extensions in Fig. 7.8(a) case which can quickly extend trees toward the goal location. The resulting path is shorter and takes less time to generate compared to previous methods. There are a significant number of obstacle blockages in other cases but it can easily get away from the local minima and find the shortest path quickly without exploring unnecessary areas. From Fig. 7.8 it can be seen that the greedy extension is stopped when a collision is detected but it can easily find the collision free path in that regions by uniformly searching the free space with $1 - p$ probability. After escaping from an obstacle, it tries again to extend the tree in the direction of the gradient descent to the goal with p probability.

7.4 Path Pruning

Even though RRT is an effective and computationally efficient tool for complex online motion planning, the solution is far from optimal due to its random exploration of the space. There are a lot of redundant nodes and wavy motions which simply increase the path length. In this Section, a simple yet an efficient method which is able to eliminate most extraneous and wavy nodes within a short time are described. Two algorithms are proposed for this path pruning.

7.4.1 Path Pruning Using LOS

The first path pruning method uses local information about the path. Let the pruned path be initially an empty set. First, define the begin node (BNode) and end node (ENode) for collision checking. Initially, the BNode is assigned to the first node of RRT path and the ENode is the second node of the RRT path. Then check the line between the BNode and the ENode for a collision, stopping when a collision is detected between them. If there is a collision, the previous node from this ENode is added to the pruned path and reassigned to the BNode and ENode. This process is repeated until a complete path is generated. Finally, the final path is obtained adding the first and the last RRT path to the pruned path.

Algorithm 6 shows the path pruning algorithm. This algorithm is called a line of sight (LOS) path pruning because the pruning process operates based on the visibility of the first collision free straight line from the current location.

Algorithm 6 LOS Path Pruning Algorithm

```
Initialize
    PrunedNode = [ ];
    i = 2;
    BNode = RRT_p(1);
    ENode = RRT_p(2);
    GNode = RRT_p(end);
while (ENode ≠ GNode) do
    if (Collision (BNode, ENode) == no) then
        i = i + 1;
        ENode = RRT_p(i);
```

```
    else
        BNode = RRT_p (i − 1);
        ENode = RRT_p (i);
        PrunedNode = [PrunedNode; BNode];
    end if
end while
FinalPath = [ RRT_p (1); PrunedNode; RRT_p (end)];
```

Fig. 7.9(b) shows the pruning result of the LOS path pruning algorithm applied to the initial RRT path in Fig. 7.9(a). The RRT path initially has 59 nodes between the start and goal point. However, this number reduces to only 5 after the redundant waypoints are pruned.

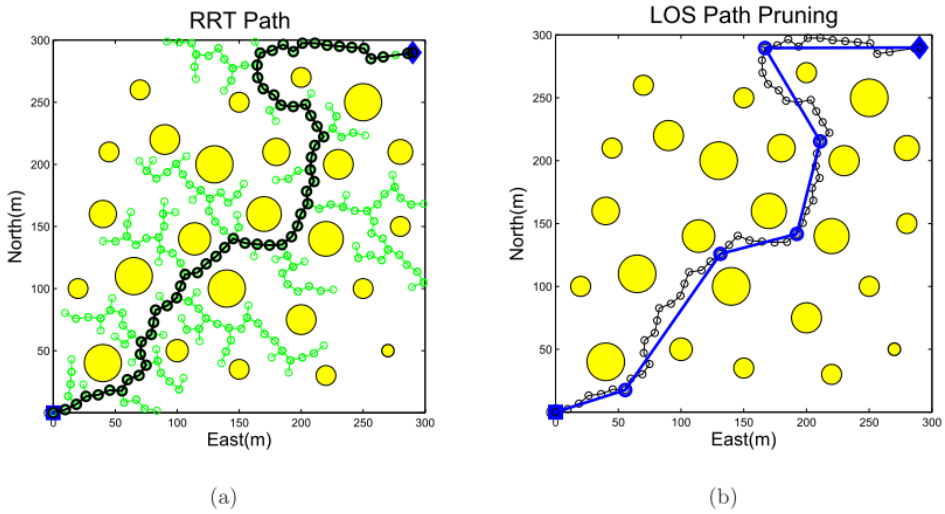

Fig. 7.9 Line of sight path pruning. (a) RRT path before pruning. (a) RRT path after pruning.

There are several benefits to this pruning algorithm. First, it reduces the path length by removing the wavy nodes. Second, path following is made easily since most of the path consists of straight lines. Finally, it is also beneficial to the vehicle actuators because a lot of jaggy motions are removed.

7.4.2 Global Path Pruning

As seen in the preceding Section, the LOS path pruning can efficiently remove the redundant waypoints in most cases. However, there still exist wavy motions due to short-sightedness of LOS. To provide better reasoning about the pruning

process, a modification is made to the LOS path pruning. The LOS algorithm starts the pruning process from the next point of BNode and stops the process when a collision is detected. Although there is a collision in the j_{th} node, there can be no collisions between BNode and the $j+1_{th}$ node. Based on this reasoning, the pruning process starts on the last node of the RRT path. It slightly increases the processing time but removes the myopic behavior of the LOS pruning. This method is called Global path pruning as it tries to prune the path considering the entire path nodes.

Algorithm 7 Global Path Pruning Algorithm

```
Initialize
    PrunedPath = [ ];
    N = size( RRT_p );
    i = N;
    LNode = RRT_p (N);
    BNode = RRT_p (1);
    ENode = RRT_p (N);
while (Collision (LNode, BNode) == yes) do
    if (Collision (LNode, BNode) == yes) then
        i = i - 1;
        ENode = RRT_p (i);
    else
        BNode = RRT_p (i);
        ENode = RRT_p (N);
        PrunedNode = [PrunedNode; BNode];
        i = N;
    end if
end while
FinalPath = [ RRT_p (1); PrunedPath; RRT_p (end)];
```

Algorithm 7 shows the global path pruning method. The only difference between the global pruning algorithm and the LOS is the assignment of ENode. Whenever a collision is detected, ENode is assigned as the last node of the RRT path in global path pruning. Whereas, it is assigned as the next of BNode in the LOS path pruning.

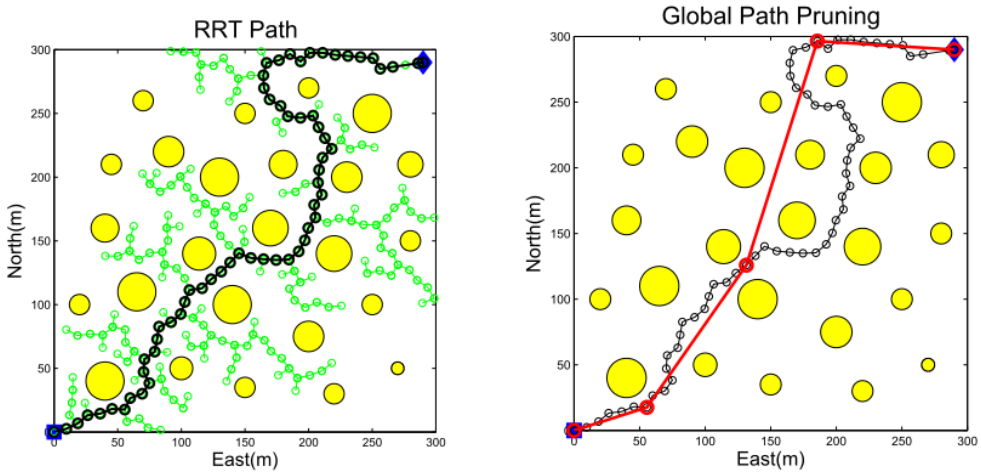

(a) (b)

Fig. 7.10 Global path pruning. (a) RRT path before pruning. (a) RRT path after pruning.

Fig. 7.10 shows the pruning result of the global path pruning which is the same path as seen in Fig. 7.10. After applying the global path pruning algorithm, nodes between the start and the goal point are reduced to 3 which is less than the LOS pruning case.

7.5 Summarize the Proposed RRT Algorithm

Fig. 7.11 shows the process of the proposed algorithm used in this chapter. In this chapter, RRT properties and several RRT path planning algorithms are described. Normal RRT is not an efficient way to find a path between start and goal configurations because the tree wanders the whole space. By selecting the goal point with some probability, the growth of RRT is biased towards the goal instead of exploring the whole space. A greedy variation of the algorithm reduce the planning time by extending trees successively along the ray connecting selected node and random points until a collision occurs. The efficiency of planning algorithm is further enhanced by combining the biased and greedy RRT. A new synchronized biased-greedy RRT is proposed which leverages the good properties of the biased and greedy RRT. This method can be interpreted as a gradient descent

search with a designated probability and uniform exploration with the other's probability. This approach will not get trapped in local minima due to its random exploration characteristic. In addition, the path output is less jaggy than other RRTs. With the synchronized combination of the biasness and greediness, this method can reduce the computational time compared to biased RRT as well as generate a more optimal path compared to greedy RRT. The RRT is a computationally efficient tool for complex online motion planning but the resulting path contains a lot of wavy redundant nodes. A pruning algorithm is proposed which is able to remove most of the extraneous nodes within a short time. After applying the pruning algorithm, the most path consists of straight lines and has less jaggy motion.

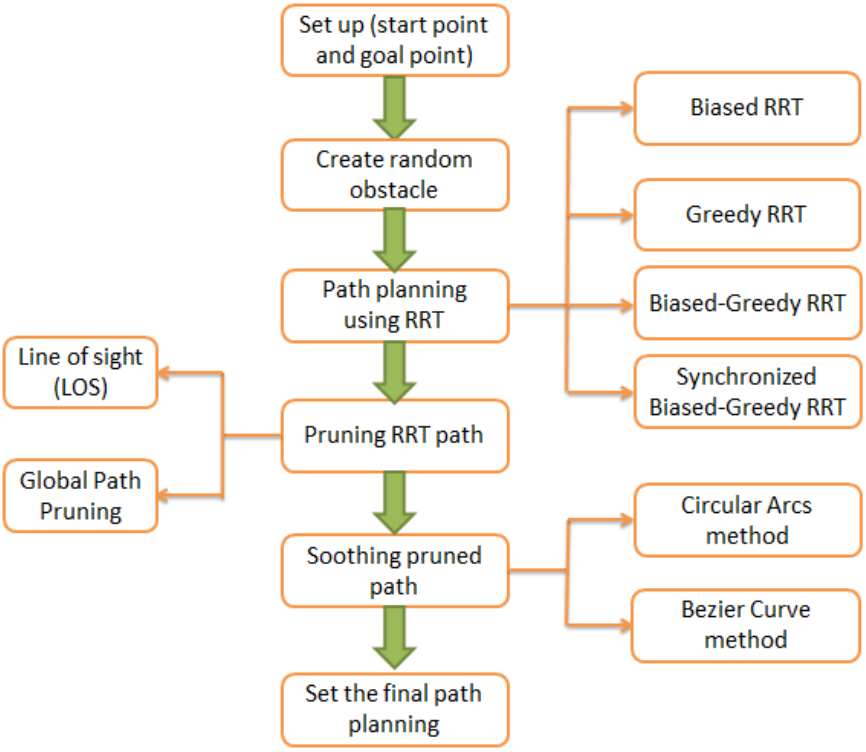

Fig. 7.11 RRT algorithm.

The steps of the RRT algorithm are summarized below:

Step 1: At each iteration, a new random point in the search space is chosen. The choice may either be generated by a pseudo-random number generator, or by a quasi-random selection process, such as the Halton sequence. The latter yields a more even distribution of random points throughout the search space, and this provides some speed advantages when used with RRT [114].

Step 2: The random point is examined against the current tree of reachable points, and the RRT vertex nearest the random point is selected. "Nearest" is

measured using a metric that will provide a point with the optimal obstacle-free trajectory towards the random point. The choice of optimality may be based on path distance, fuel consumption, total time, risk minimization, or other desired criteria.

Step 3: If no trajectory can be found, the random point is discarded. Otherwise, an edge of length ε is added along the feasible trajectory from the closest point to the random point.

Step 4: Then, a check is performed to see if the goal is reachable from the new node added to the tree. If it is, a feasible path has been found. If not, steps 1 through 4 are repeated until it is, or until a maximum number of steps have been taken.

Step 5: The RRT search may continue to run even after a solution has been found in order to find a potentially shorter or lower-cost path.

Many variations to these basic steps have been tested by researchers in many applications with varying success. The goal of these variations is generally to achieve some increase in performance, and aside from paths that may be far from optimal the RRT algorithm has a few other areas where this could happen. Since, in practice, the number of iterations (i.e. random points generated) cannot be very large, a solution may not be found within the window of iterations performed. Also, nearest neighbor searches are quite computationally expensive. One method suggested to work around the iterations limitation is to simply repeat the procedure, or perhaps backtrack and use a different starting point. As for the nearest neighbor searches, these could depend on the density/complexity of obstacles saving exhaustive searches for densely populated areas. There are numerous ideas for tuning and enhancing the basic RRT algorithm. However, the biggest performance increase has been achieved by using dual RRTs that is one tree expanding from the starting point and another from the end point.

7.6 Simulation for Path Following of AUV

Precision path tracking control is an important capability for operating a mission in a complex environment. Fig. 7.12 shows the PID or SMC path following control architecture. There are three blocks within the PID control architecture. The Path Generation block is responsible for the generation of the reference path. The Error Calculation block computes tracking errors between the reference path and the AUV. Finally, the PID or SMC control block generates a control action (u) to compensate tracking errors.

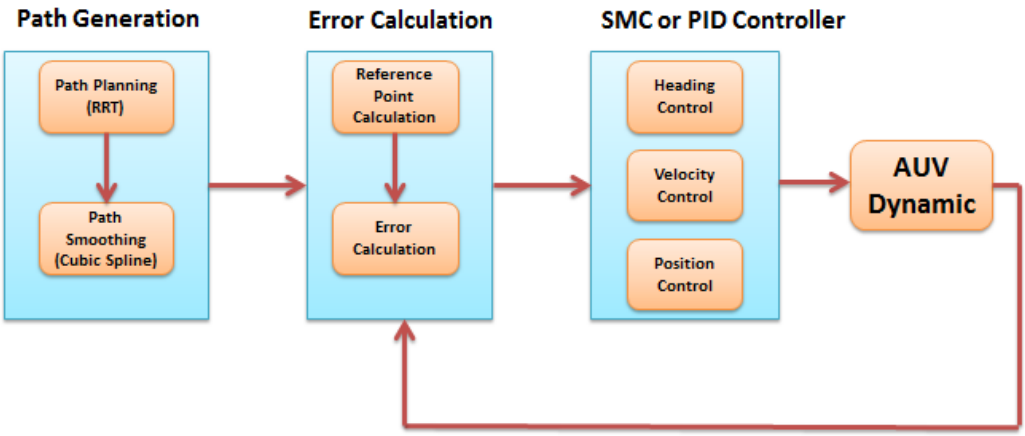

Fig. 7.12 A block diagram of path following controller of UV.

To illustrate our RRT algorithm efficiency in planning safe paths of an AUV in an uncertain-configuration space, we implemented our algorithm using Matlab software as shown in Fig. 7.13. Also, the parameters for path following of AUV are shown more detail in Table 7.1. In this simulation, we assume that the AUV moves with a certain speed and heading. The speed of AUV is constant and heading of the vehicle changes when it detects any obstacle. When an obstacle is detected, then by considering the detected obstacle specification, the proposed algorithm will guide the vehicle to avoid the obstacles. It is used to generate steering commands for the AUV to pass fixed obstacles safely without collision based on the distance to the obstacle, the angle between the AUV's line of sight to the obstacle and the connected line between AUV and the next waypoint. The system consists of a two-level construction. One level is the path planning, which generates a path for the vehicle to follow and the other guides the vehicle by avoiding the obstacles.

Table 7.1. Parameters for path following of AUV

Start Node	(0,0)
Goal Node	(500,500)
The length to extend from the nearest node to the direction of random node	10 m
The radius of the obstacle considering the safety of the submarine (1.5 times the radius of the obstacles)	1.5
The maximum number of the generated obstacles	50
The minimum number of the generated obstacles	30

The maximum radius of the generated obstacles	15
The minimum radius of the generated obstacles	5
Initial forward velocity	1 m/s
K_p ***(Heading controller)***	10
K_d ***(Heading controller)***	6
K_p ***(Depth controller)***	10
K_d ***(Depth controller)***	50
K_i ***(Depth controller)***	30

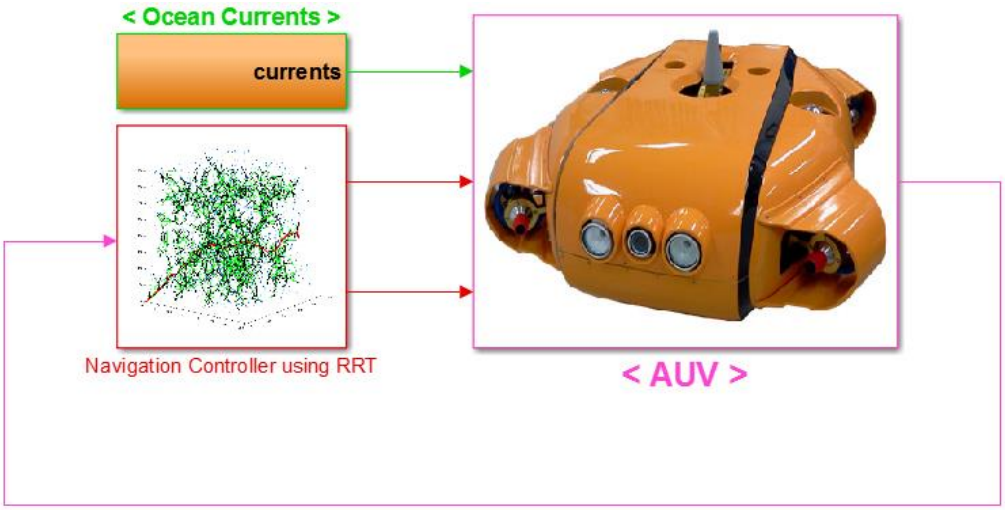

Fig. 7.13 Velocity and control inputs.

Fig. 7.14 shows the path planning of AUV and a network of obstacles. In Fig. 7.14(a) path of AUV is demonstrated while the vehicle travels toward to unknown fixed obstacle. The environment, based on the North-East-Down coordinate, is set to 500x500m in dimension. The simulations assume an ideal case where a priori information of the environment is provided. The simulations are run with 200 maximum nodes, 300 maximum iterations, terminating when either criterion is reached or if a solution is found. The start point is in (0, 0) and the target is situated in (500, 500). AUV starts its path from (0, 0) and continues to reach the target without any collision to the obstacles in its path. The RRT path is shown with blue color and the optimal RRT path with red as shown in Fig. 7.14 (b). The final

optimal path of AUV is selected as shown in Fig 7.14(c) because AUV can pass an obstacle in a shorter path in comparison with a blue one in Fig 7.14(b). Therefore, AUV can pass the obstacles faster without any collision. The simulation results also show the efficiency of the proposed method to avoid obstacles with least detour. As it is clear in Fig 7.14(d), AUV after starting its path and detecting the unknown fixed obstacles then turning to avoid a collision. Moreover, the dynamic behaviors of AUV during its path planning are shown detail in Fig. 7.15. Also, the configuration of control inputs needs to apply to force AUV to follow the desired optimal path as in Fig. 7.16.

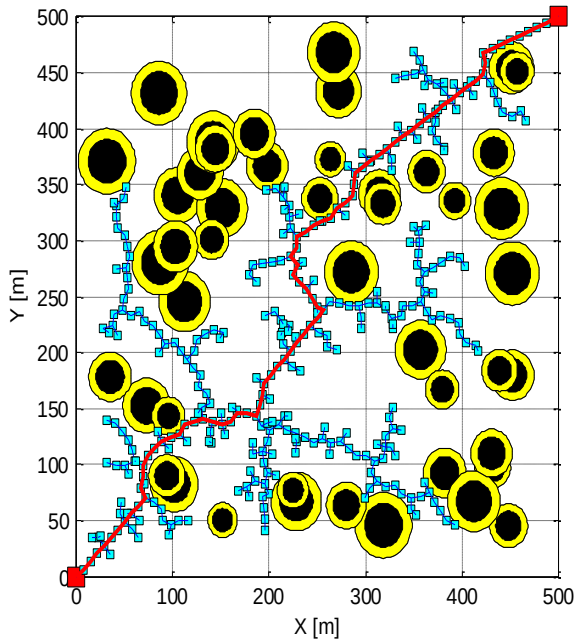

(a) Path Planning using RRT

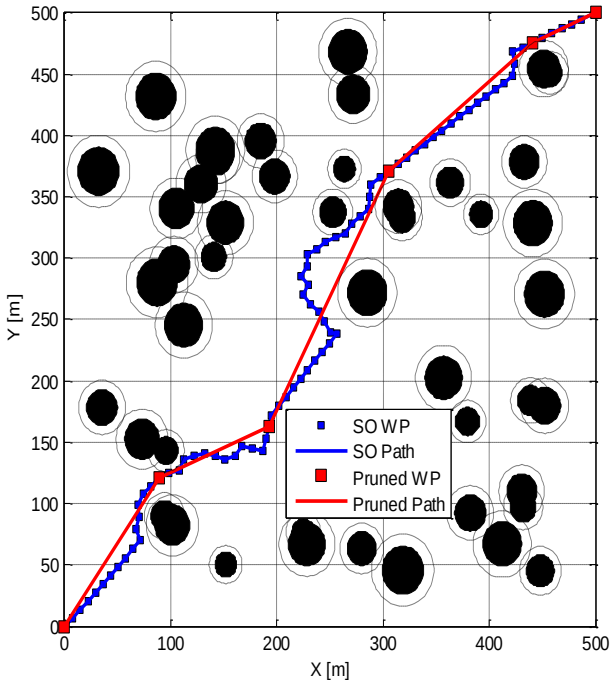

(b) Pruned Path

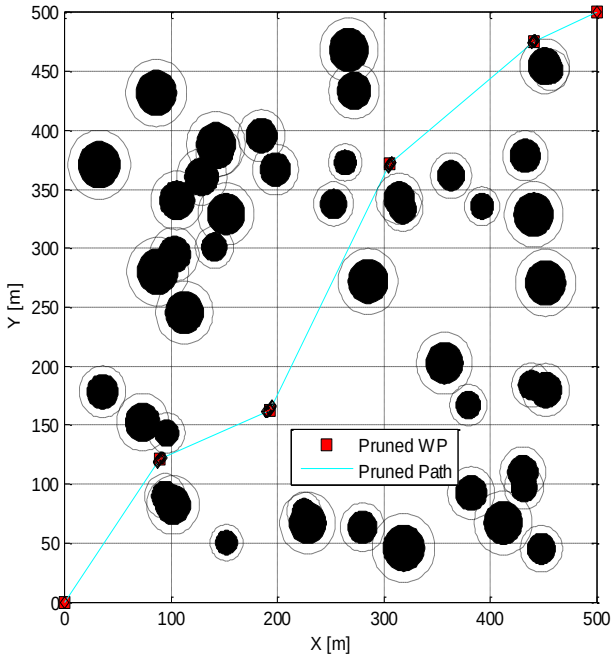

(c) Optimal path

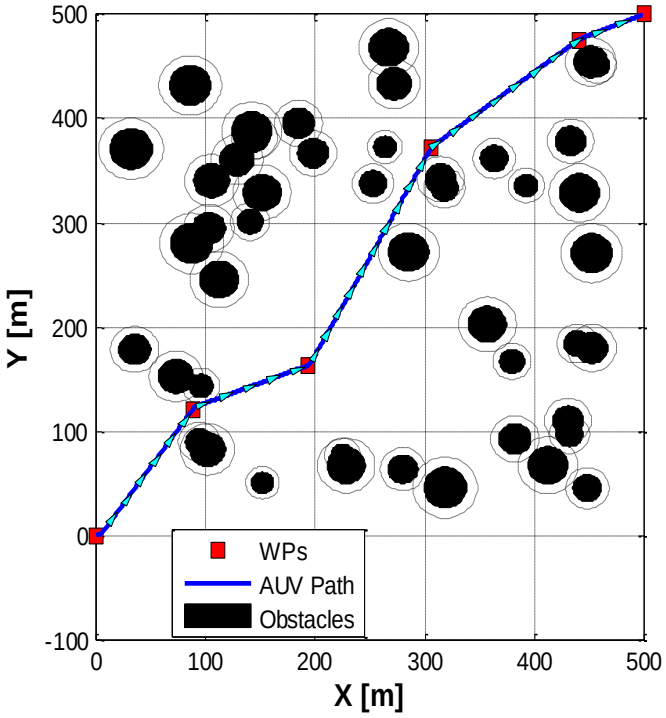

(d) Followed path

Fig. 7.14 Path planning of AUV and a network of obstacles.

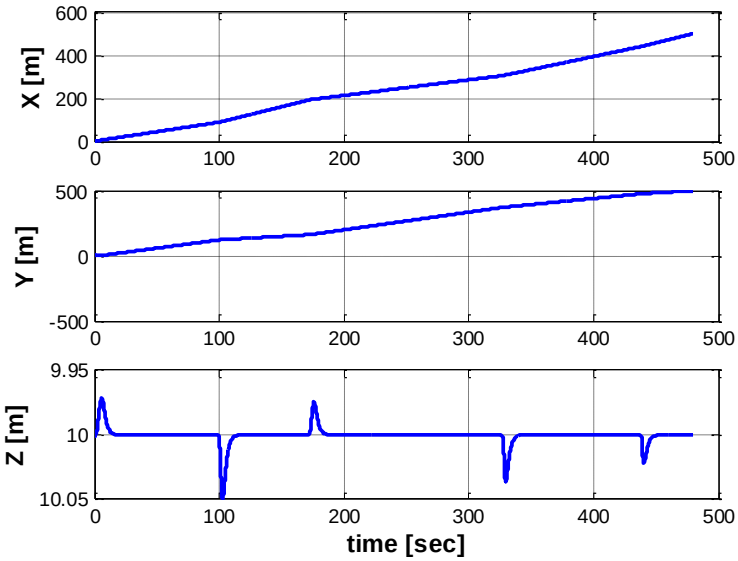

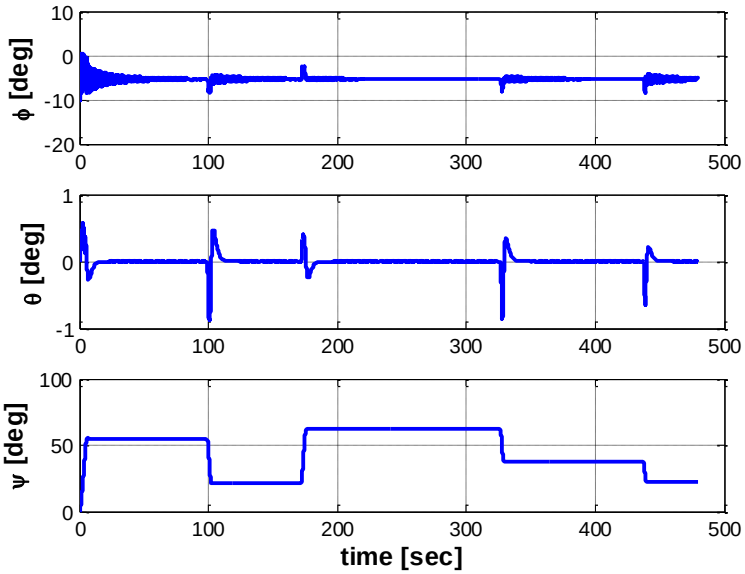
ϕ [deg]
θ [deg]
ψ [deg]
time [sec]

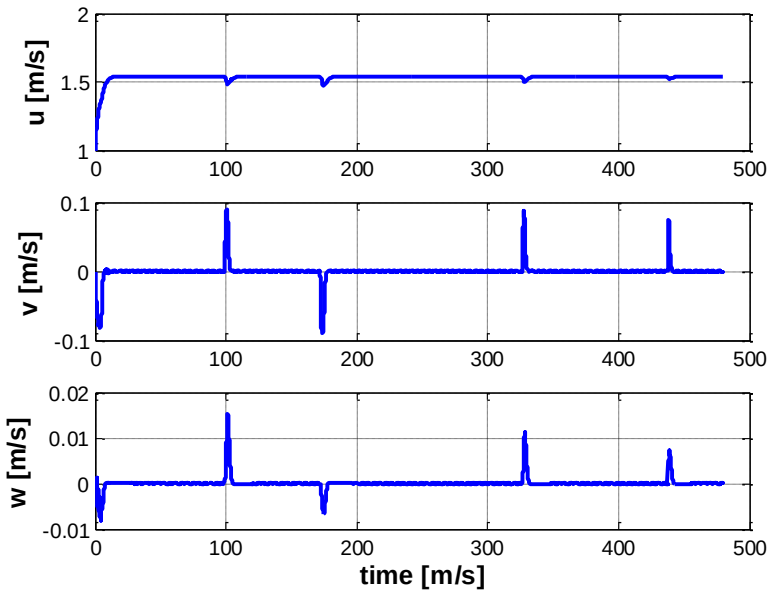
u [m/s]
v [m/s]
w [m/s]
time [m/s]

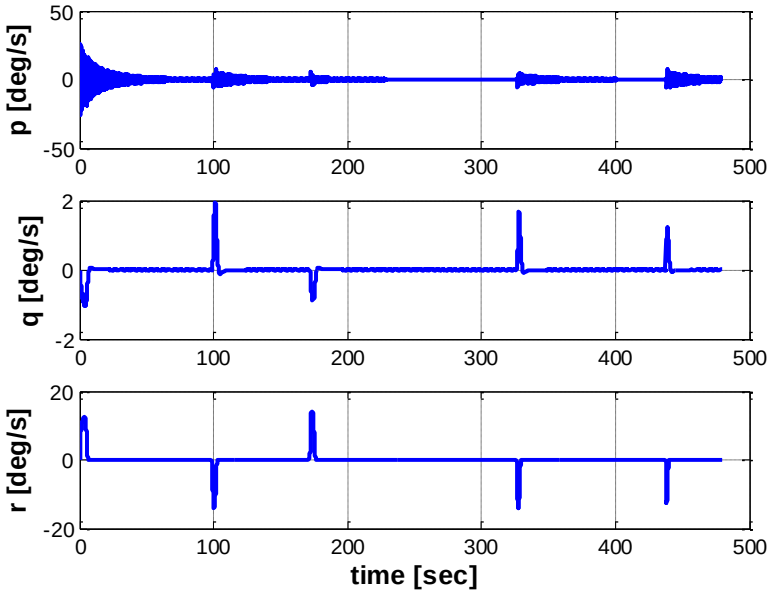

Fig. 7.15 Dynamic behaviors of AUV.

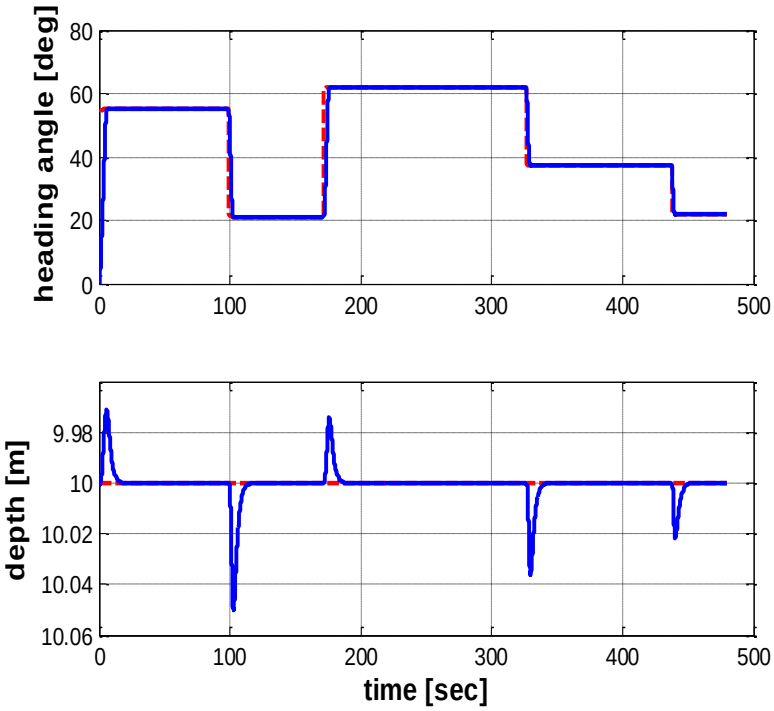

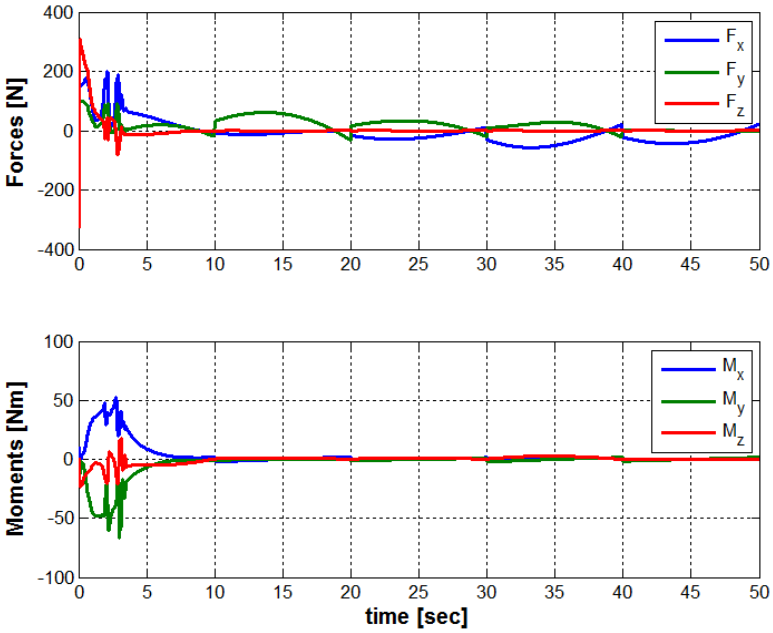

Fig. 7.16 Control input of AUV.

Chapter 8: Simulation of Complete USV-UC-UV Systems

As the nonlinear dynamic equations are difficult to be solved analytically, the numerical simulation method is adopted to simulate the motion of the AUV and cable system. Based on the simulation scheme introduced in this chapter, model-based motion simulation is further implemented in the later sections.

8.1 Simulation Procedure

In this dissertation, the model-based simulation process is proceeded as shown in Fig. 8.1. After the establishment of the respective dynamic equations of the coupled AUV and cable system, the dynamic equations are further discretized for numerical simulation. Thus, several iteration methods could be applied to solve the discretized equations.

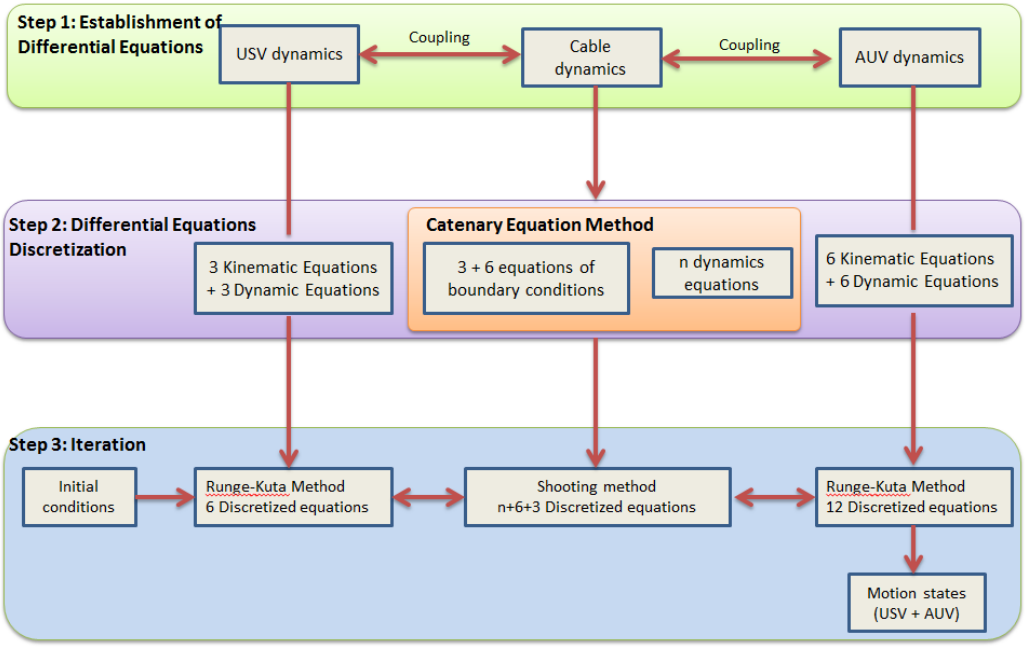

Fig. 8.1 The model-based simulation process.

As for the cable, the partial differential Eq. (3.40) under the boundary conditions Eqs. (3.45)-(3.46) can be solved numerically using the shooting method.

In this method, the cable is considered to be divided into n segments (or nodes) equally, so that shooting method could discretize the cable dynamics both over time (Δt) and cable length (Δs). Note that in our case, the length of the cable is fixed in a mission, when the AUV towing the cable moves forward in the water. In this case, the length of each segment of the cable is fixed in the finite difference method.

The above finite difference in Eq. (3.40) involves n cable nodes, and according to Eqs. (3.45)-(3.46), so there are n+6+3 cable node variables in total. Because the AUV is a rigid body, 12 motion states are used to describe its dynamics. While the USV is used 6 motion states to describe the dynamics. Thus, for the combined USV-cable-AUV system, there are in total 6+(n+6+3)+12 dynamic equations involved to solve the 6+(n+6+3)+12 motion states, which are:

$$Y = \left\{ y_{1:n+1}, \left(X, Y, Z, \phi, \theta, \psi, u, v, w, p, q, r \right) \right\}^T \tag{8.1}$$

The initial condition of the system (Y^0) should be provided for further calculation. Then, the previous iteration result (Y^k) will be used as the initial guess for the next iteration (Y^{k+1}).

In order to solve the nonlinear differential equations, different iteration methods are applied to the respective AUV and cable dynamic equations due to their different dynamic characteristics. Usually, the Runge-Kutta Method is well-known to solve the differential equations of AUV dynamics, while the shooting method is used to solve the partial differential equations of cable dynamics.

In this section, we analyze the behavior of the AUV under the influence of the UC, and implement a simulator using a model of the AUV. For the simulation, we use a Matlab-Simulink model. The model uses the Matlab-Simulink including three subsystems for the thruster modeling, the cable dynamic modeling, and the underwater dynamic of the vehicle modeling. Fig. 8.2 illustrates the blocks used in the Matlab-Simulink.

Table 8.1. Cable and sea parameters.

Properties	Units	Symbols	Values
Cable parameters			
Length of cable	*m*	L_c	*100*
Cable density	kg/m^3	ρ_c	*662.2*
Diameter of cable (m)	*m*	d_c	*0.025*
Axial stiffness (N)	*N*	*EA*	3×10^4
Position of first end point	*m*	P_{vessel}	*(0,0,0)*
Position of second end point	*m*	P_{ROV}	*(60,0,60)*
Guess for end force (we know this guess is wrong)	*N*	F_{end}	*(4,5, 100)*
Weight per length of cable	*kg/m*	w_c	*0.5*
Mesh frame of cable	*m*	*s*	*0:0.1:100*
Normal drag coefficient	-	C_n	*1.2*
Tangential drag coefficient	-	C_f	*0.062*
Tension rigidity	*N*	*T*	*Inextensible*
Environments parameters			
Sea state	-	-	*Calm sea*
Water current velocity	*m/s*	v_w	*0.1*
Seawater density	kg/m^3	ρ_w	*1000*

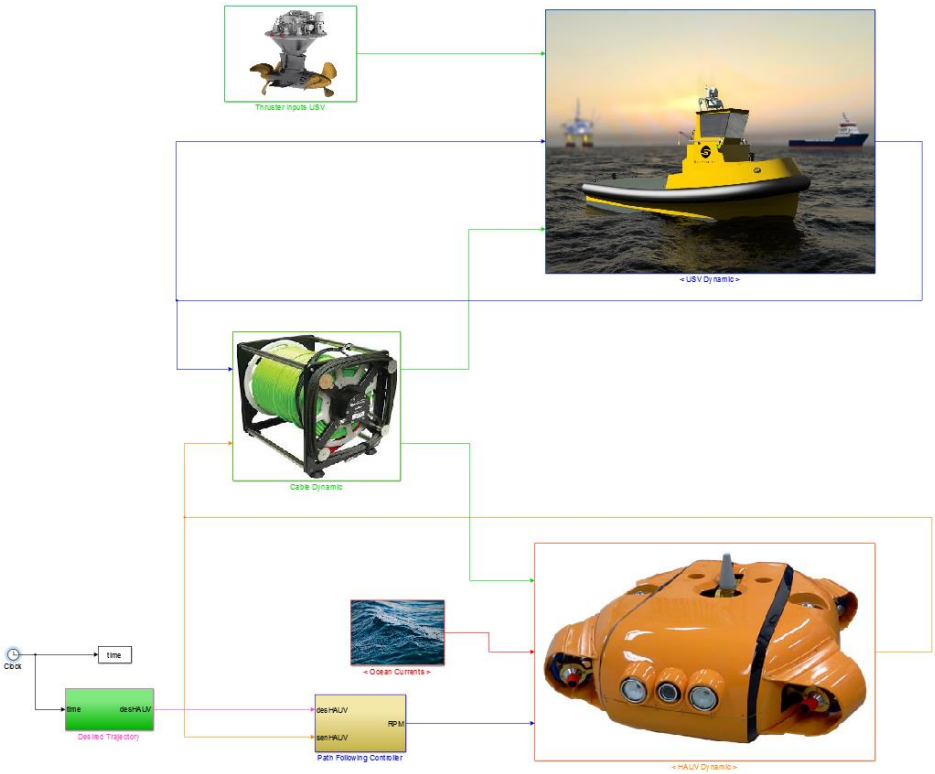

Fig. 8.2 Simulation program for the AUV with the UC.

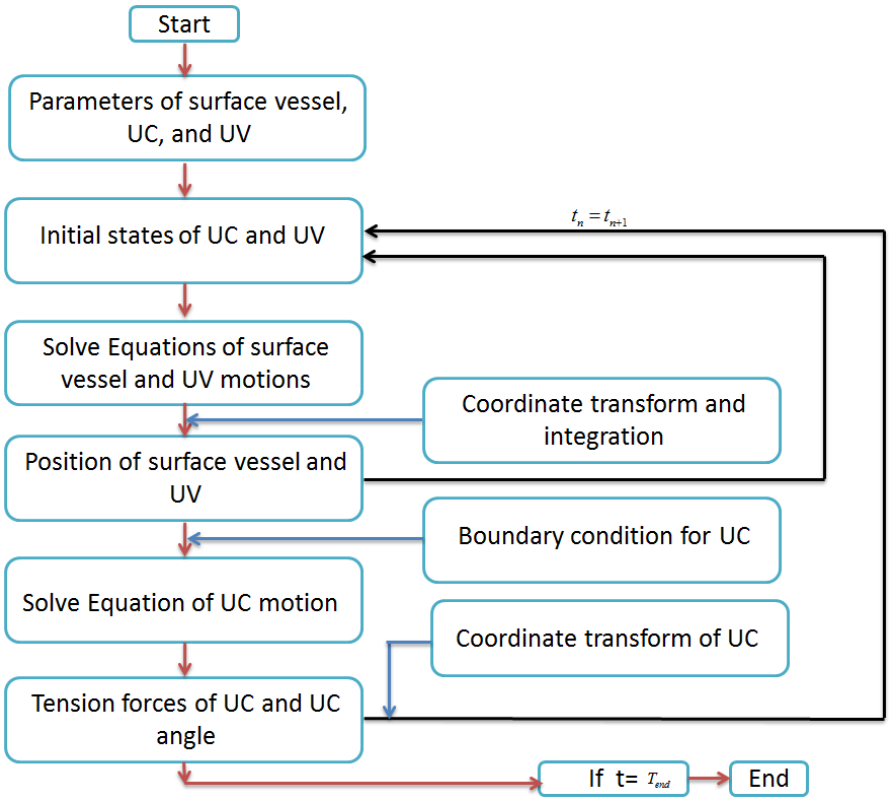

Fig. 8.3 Simulation procedure for complete system.

Fig. 8.3 illustrates the simulation procedure for complete system. The steps in the simulation procedure are as follows.

Step 1: Startup. Initialize the parameters of complete system including support vessel, the UC and the AUV.

- Set the time step Δt and stop time of the simulation.
- Parameters of support vessel: we assume that the support vessel always keeps at constant value of (0, 0, 0) m (see Section 3.6 and Eqs. (3.45) and (3.46)).
- Parameters of the UV: initial states of the AUV (such as: six state variables of the AUV and its initial position) need to be given.
- Parameters of the UC: initial data of the UC according to Table 8.1.

Step 2: Solve the equation of motion for the support vessel and the AUV.

- Calculate the force by means of Eqs. (4.97) - (4.102) and see Section 4.9.

- Coordinate transform for state variables of the AUV (see Section 2.2 and Eqs. (2.1) and (2.2)).

Step 3: Using the results of Step 2 as boundary conditions for the UC equation, solve the UC dynamics equation using the catenary equation (see Eq. (3. 40)) and shooting method (see Section 3.5).

- Position of support vessel always keeps at constant value of (0, 0, 0) m.
- Position of the UV is the function of time during simulation (see Section 3.6 and Eqs. (3.45) and (3.46)).
- Coordinate transform for state variables of the UC (see Section 2.2 and Eqs. (2.3)-(2.5)).

Step 4: Update state of vehicles and UC state.

Step 5: Iterate Steps 2-4 until the simulation termination time is reached.

8.2 Simulation Results and Discussion

8.2.1 Dynamic Behaviors of Complete USV (Stable)-Cable- AUV (Turning Motion)

Fig. 8.4 shows the thruster directions of the AUV during a turning motion.

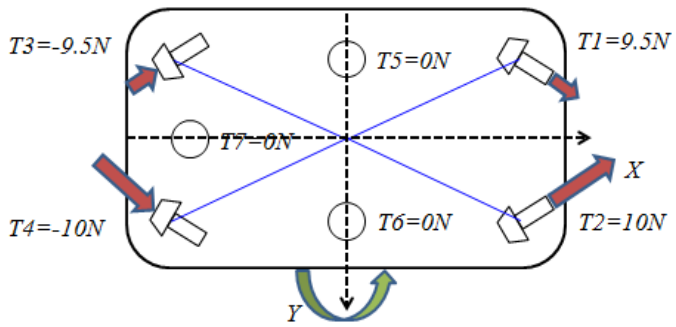

Fig. 8.4 Thruster directions of the AUV in the turning motion.

Let us consider the dynamical equation for each single-degree-of-freedom motion first. From Eqs. (4.97)-(4.102), we can simplify the dynamical equations of the turning motion as:

$$
\begin{cases}
\dot{u} = [(m - Y_{\dot{v}})vr + (X_u + X_{u|u|}|u|)u + F_x + F_{xcable}] / (m - X_{\dot{u}}) \\
\dot{v} = [(-m - X_{\dot{u}})ur + (Y_v + Y_{v|v|}|v|)v + F_{ycable}] / (m - Y_{\dot{v}}) \\
\dot{w} = F_{zcable} / (m - Z_{\dot{w}}) \\
\dot{p} = M_{xcable} / (I_x - K_{\dot{p}}) \\
\dot{q} = M_{ycable} / (I_y - M_{\dot{q}}) \\
\dot{r} = [uv(Y_{\dot{v}} - X_{\dot{u}}) + (N_r + N_{r|r|}|r|)r + M_z + M_{zcable}] / (I_z - N_{\dot{r}})
\end{cases}
\tag{2.16}
$$

Figs. 8.5(a) and (b) show the trajectory of the AUV doing the turning motion without the UC and with the UC, respectively. In order to simulate the turning motion, the counterclockwise rotating forces 10 N and 9.5 N are set for the thrusters T_2 and T_1, respectively, and -10 N and -9.5 N are set for the thrusters T_4 and T_3, respectively. We set the thrusters T_5, T_6, T_7 to 0N ($T_5=T_6=T_7=0\ N$) to achieve a pure turning motion, and the initial UV surge speed is 0.3 m/s. According to the application of all thrusters as shown in Fig. 8.4, both the force along x-axis and the moment along z-axis have different constant values, while the other variables remain zero during all simulation. The effect of the UC can be clearly seen in Figs. 8.7 and 8.8. We can also observe from Figs. 8.7 and 8.8 that the AUV initially moves surge, then moves rightward and finally moves backward. The results also reveal that the surge speed increases at the beginning and then decreases to a constant speed, and the sway speed increases from 0 m/s to a positive small constant speed. When the UC is considered in the turning motion, all motions are significantly affected, as shown in Figs. 8.7 and 8.8. With the UC effect, the depth, heave velocity, roll motion and pitch motion of the AUV vary with time.

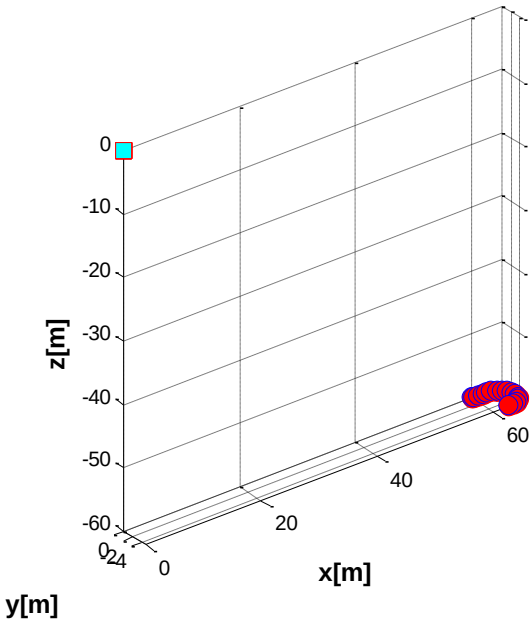

(a) Trajectory of the turning motion without the UC.

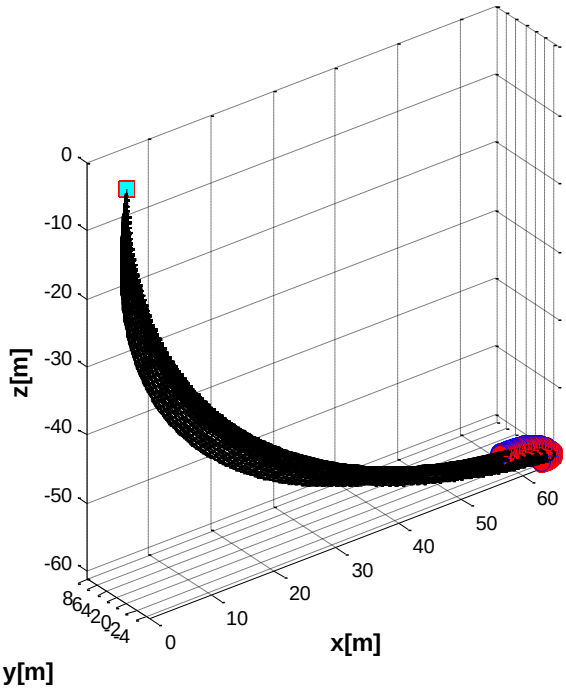

(b) Trajectory of the turning motion with the UC

Fig. 8.5 Trajectories of complete systems.

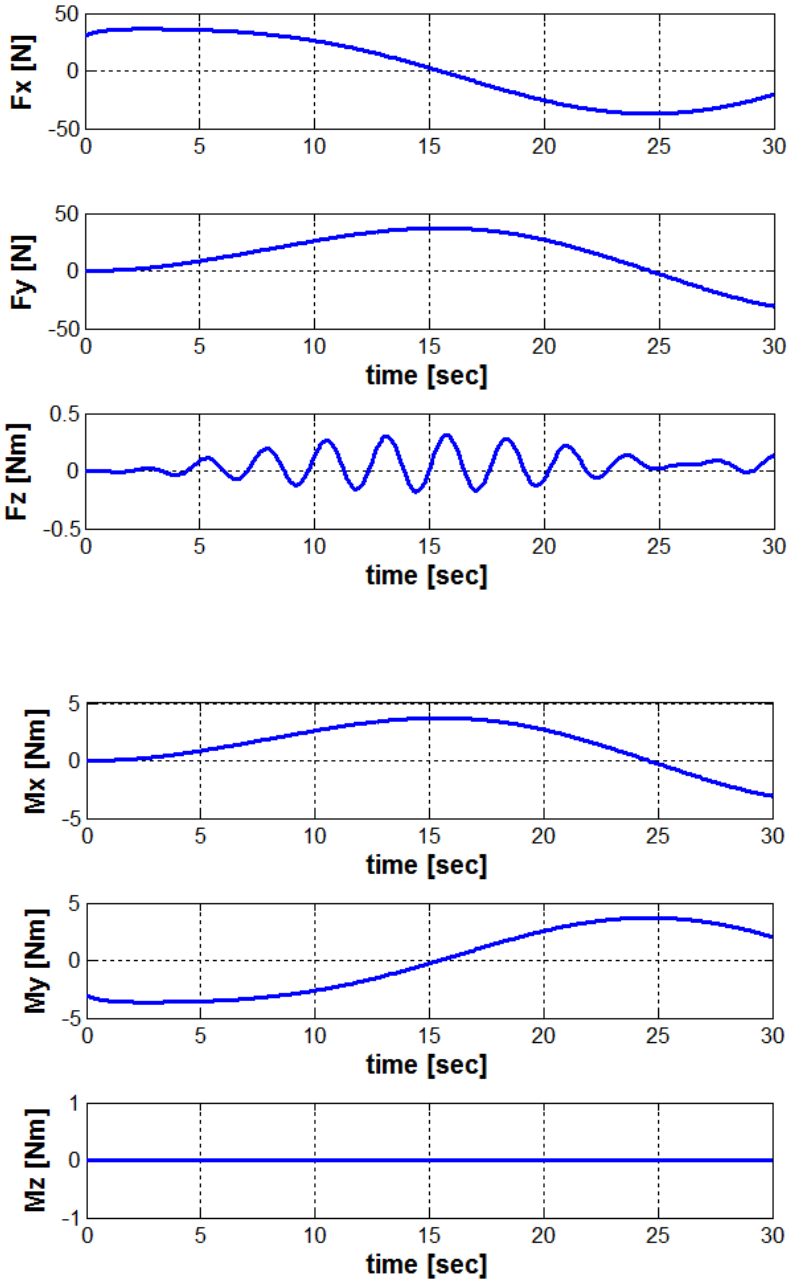

Fig. 8.6 Forces and moments of the UC on the AUV doing the sway motion w.r.t a vehicle-fixed coordinate.

The depth of the AUV decreases initially and then slightly increases to a constant value. Moreover, due to the attachment of the UC, the heave velocity

appears to be oscillatory due to the heave force F_{cz} generated from the UC effect, and the roll angle θ also oscillates regularly. The surge and sway motions are also slightly different from those without the UC. Besides, the pitch motion is also present because of the UC. The UC makes the pitch motion to increase positively initially and then decrease even to a negative value. However, the yaw motion is not affected by the UC in this case.

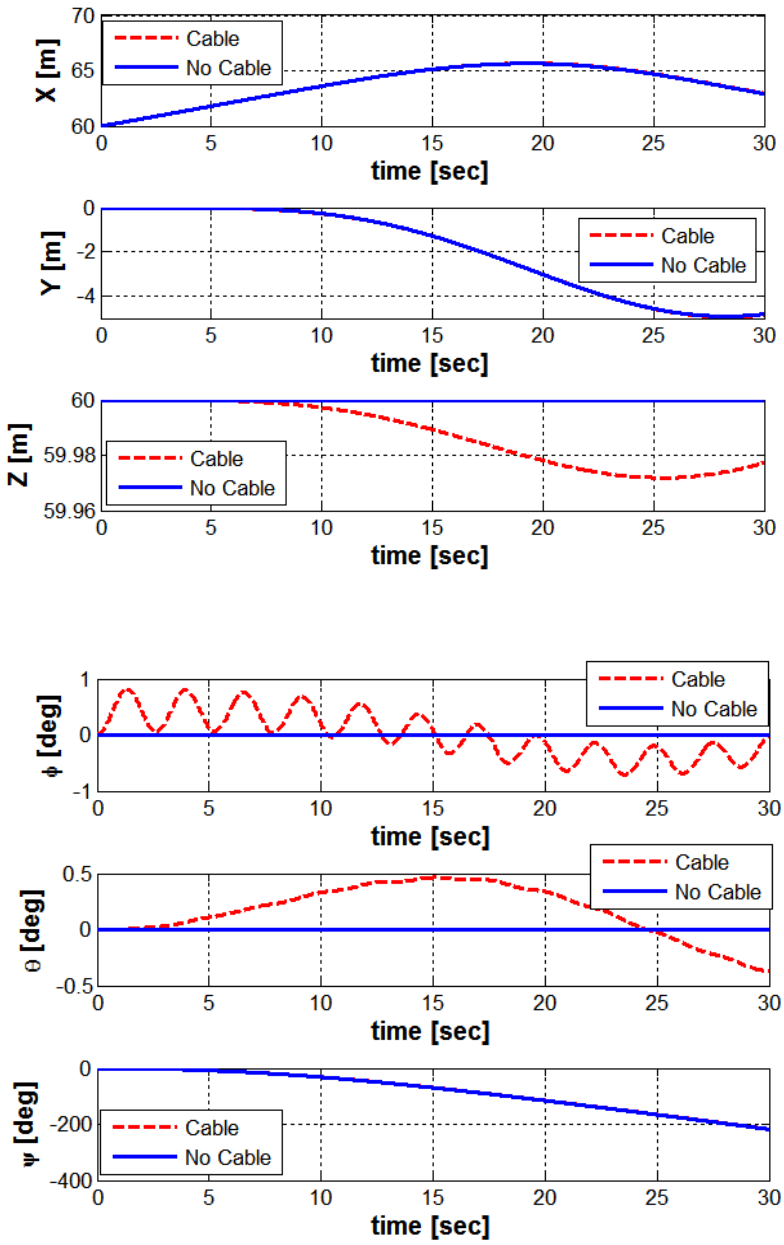

Fig. 8.7 Simulation results of position behaviors of AUV.

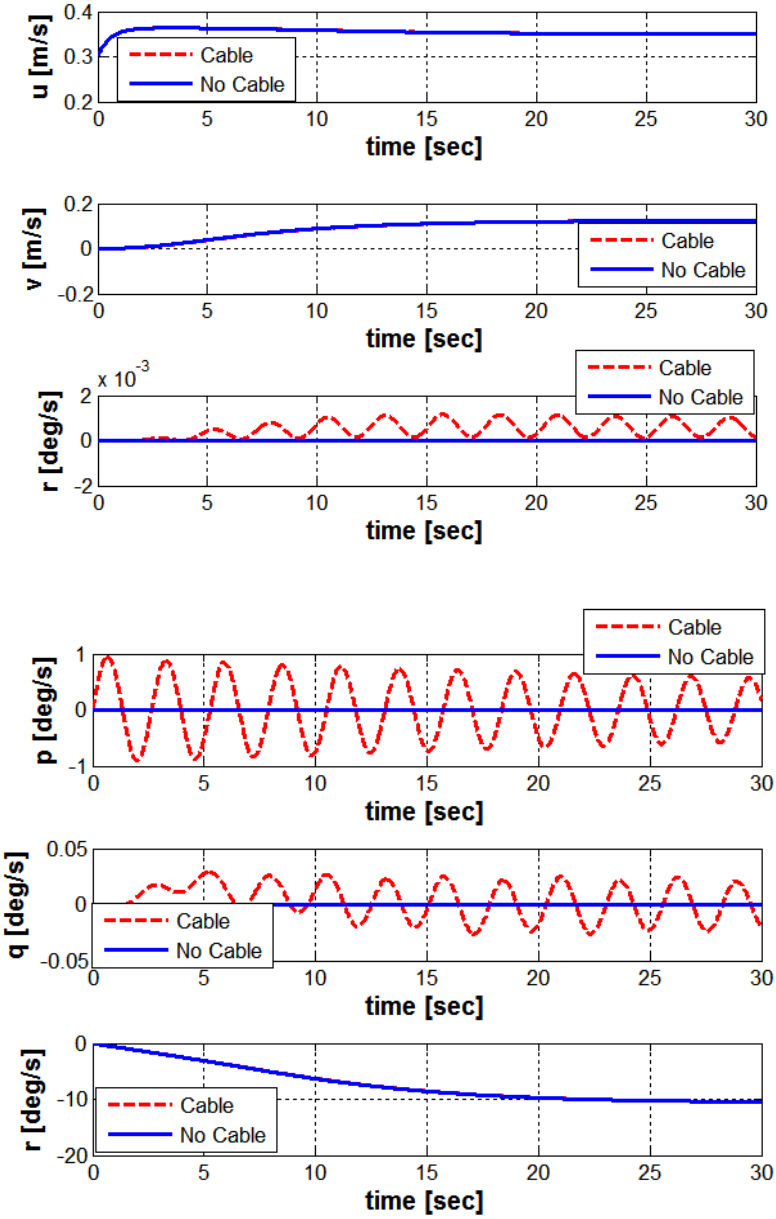

Fig. 8.8 Simulation results of velocity behaviors of AUV.

Fig. 8.6 shows that the force and moment of the UC including the current effect with respect to a vehicle-fixed coordinate for the reference. The results show that the oscillatory heave force F_{cz} and the roll moment M_{cx} cause the oscillatory heave velocity and roll motions, respectively. The results in Fig. 8.6 also reveal that the

surge force F_{xz} initially decreases and then increases. On the other hand, the sway force F_{cy} increases at the beginning and then decreases to a negative value after about halftime history.

8.2.2 Dynamic Behaviors of Complete USV (Forward motion)-Cable- AUV (Turning Motion)

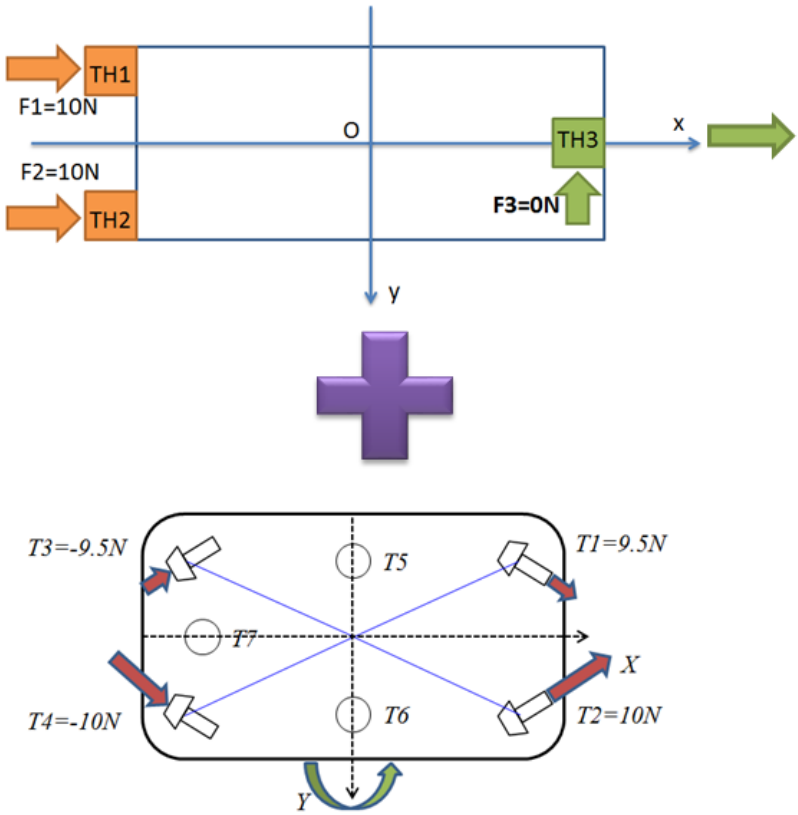

Fig. 8.9 Thruster directions of the USV and AUV.

In this section, we analyze the behavior of both USV and AUV under the influence of the UC, and implement a simulator using a complete USV-Cable-AUV system. Fig. 8.2 illustrates the blocks used in the Matlab-Simulink. The UC's parameters for simulation are shown in Table 8.1. Moreover, Fig. 8.9 shows the thruster directions of both AUV and USV during the motion. The detailed parameters of USV and AUV used in this study are given in [56] and [115], respectively.

A basic simulation using a 3-DOF USV connected to 6-DOF AUV by a UC to show the effects of the UC on both USV and AUV motions with different operations on the horizontal plane, i.e., USV is going straight in forward while AUV doing the turning motion was carried out and shown in Figs. 8.10-8.14. With time interval of 0.01 sec dynamic simulation was conducted for 30 sec. Using above proposed new model for the complete system, the trajectories of USV and AUV without the UC and with the UC are simulated as shown in Fig. 8.10. The USV moves in a straight line with a theoretical velocity of the sprocket V_{usv} = 0.25m/s, after about 25 sec the velocity increases to maximum values about 0.8 m/s. On the other hand, the AUV firstly moves in a straight line with a velocity of the sprocket V_{ROV} = 0.2 m/s, then turns right after about 2 sec with the maximum velocity about V_{max} = 0.35m/s. In the case of USV moving forward, the effect of the UC on the USV motion can be clearly seen by Figs. 8.11 and 8.12. The results show that the USV would be faster than without attaching the UC due to the surge force F_x arising out of the UC effect. In other words, for the AUV doing the turning motion, we can observe from Figs. 8.13 and 8.14 that the AUV initially moves surge, then moves rightward and finally moves backward. The results also reveal that the surge speed increases at the beginning and then decreases to a constant speed, and the sway speed increases from 0 m/s to a positive small constant speed. When the AUV is considered in the turning motion, all motions are significantly affected, as shown in Fig. 8.13. With the UC effect, the depth, heave velocity, roll motion, pitch motion and yaw motion of the AUV vary with time. The simulations conducted show that the UC can greatly influence the motions of the vehicle, especially on the AUV motions. Therefore, an accurate complete USV-Cable-AUV model is of great importance.

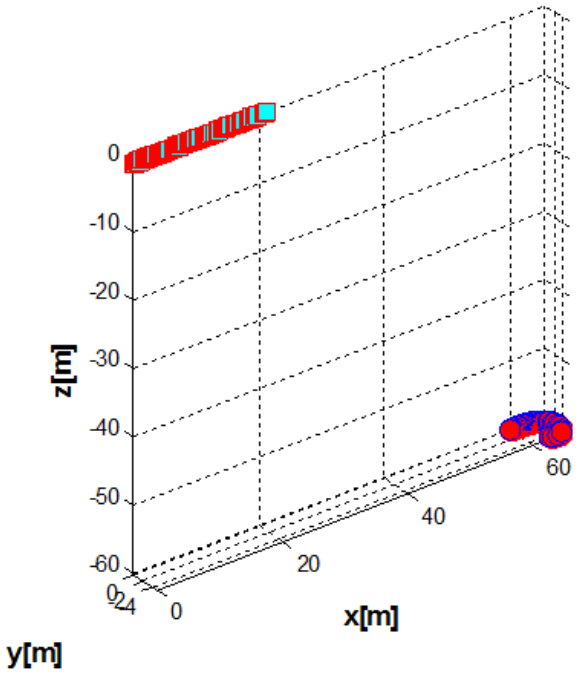

(a) Trajectory of UV

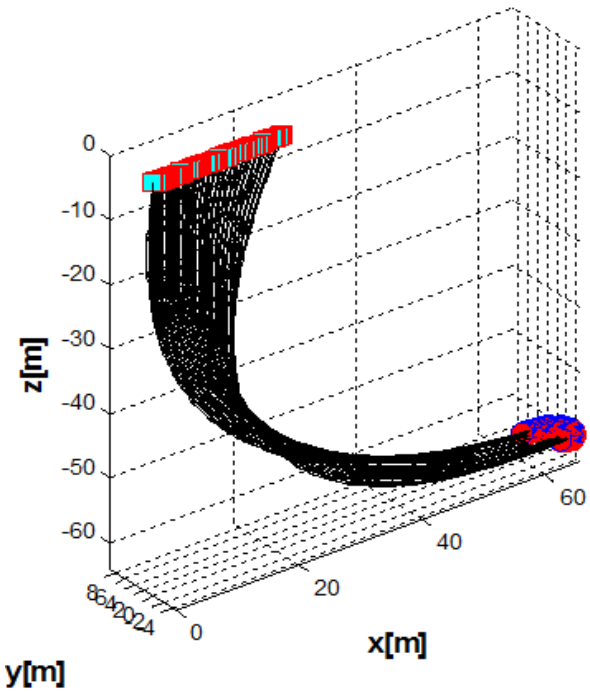

(b) Trajectory of UV

Fig. 8.10 Trajectories of complete systems.

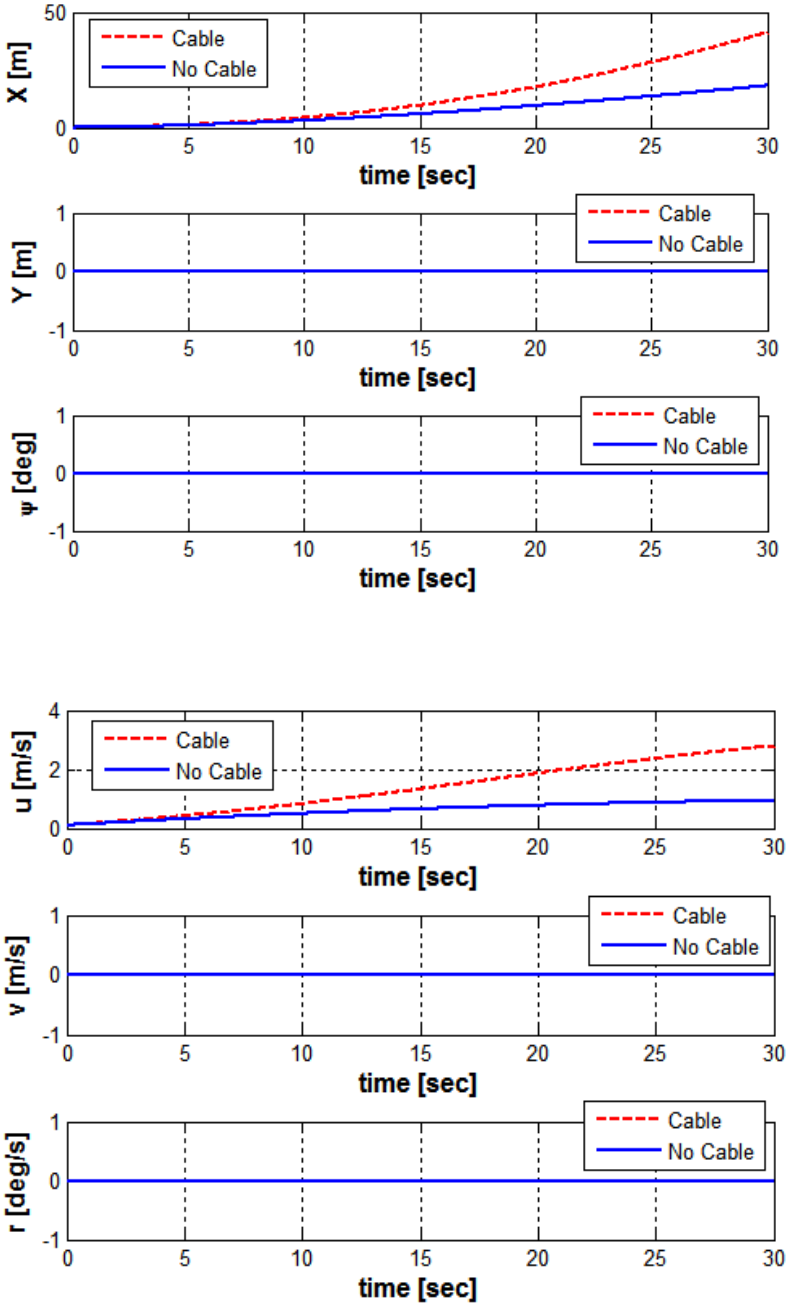

Fig. 8.11 Simulation results of dynamic behaviors of USV.

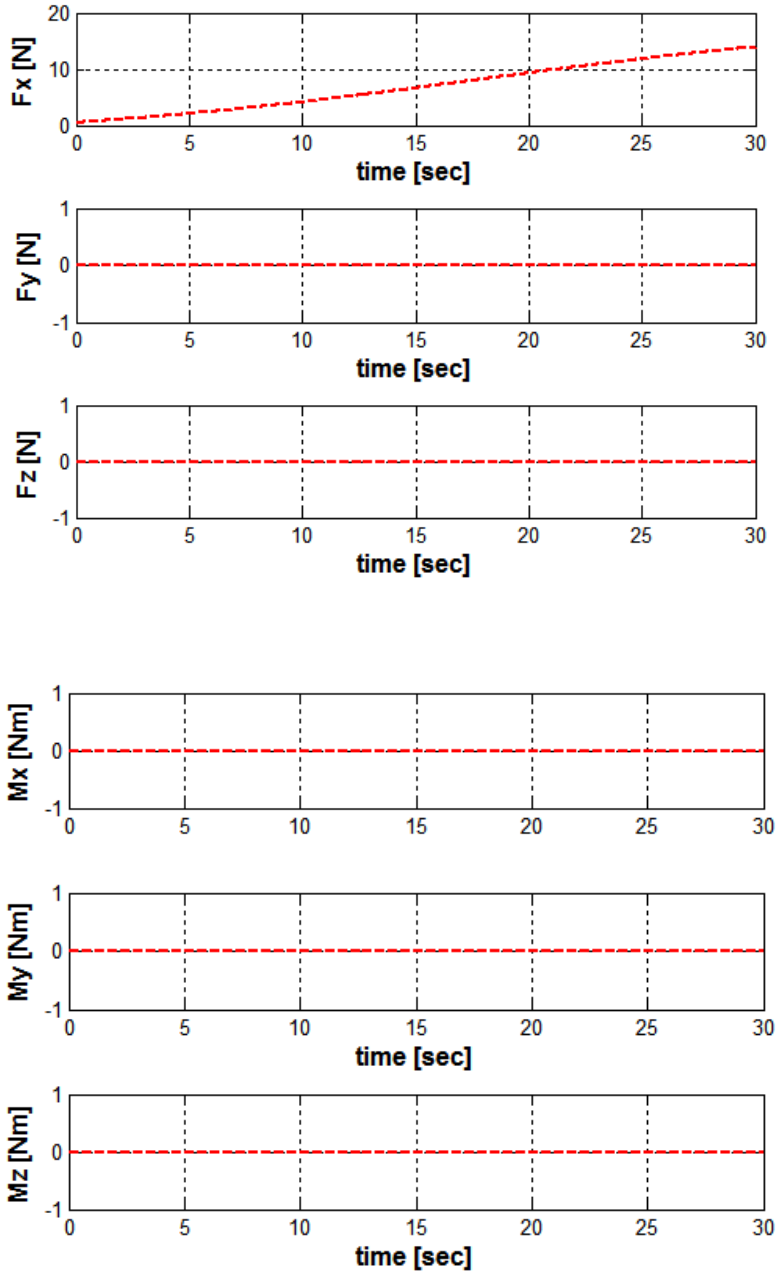

Fig. 8.12 Cable forces effecting to USV.

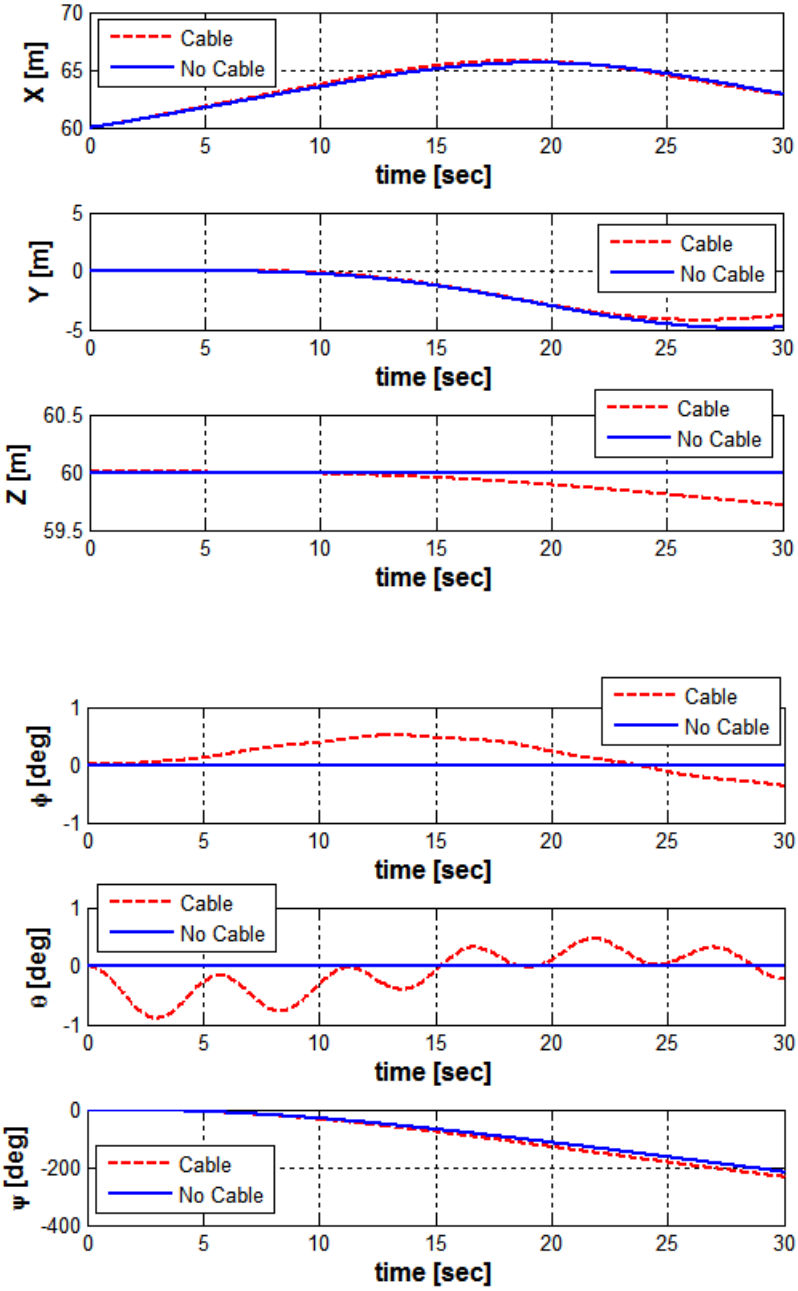
X [m]
Y [m]
Z [m]
ϕ [deg]
θ [deg]
ψ [deg]
time [sec]
Cable
No Cable

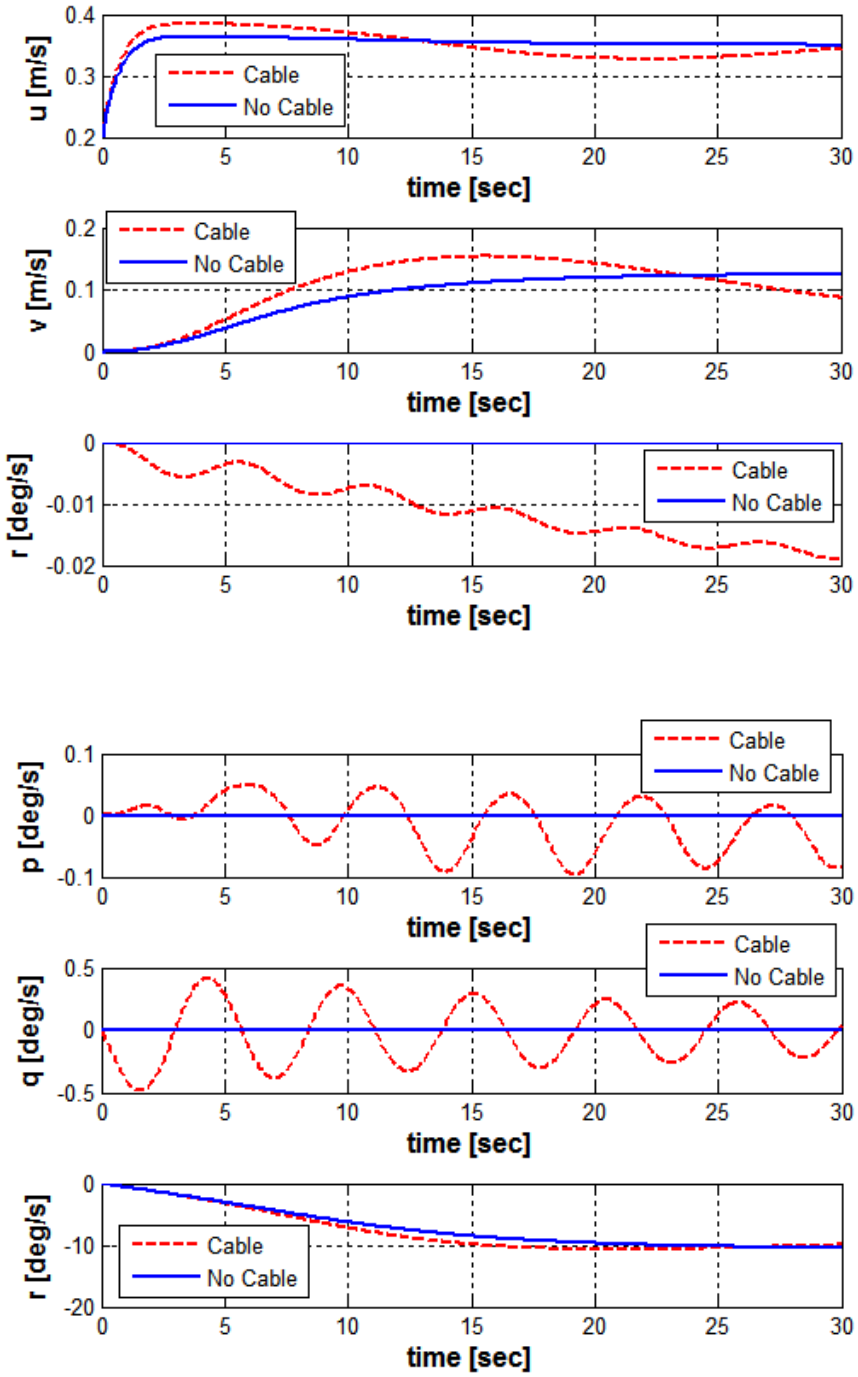

Fig. 8.13 Simulation results of dynamic behaviors of AUV.

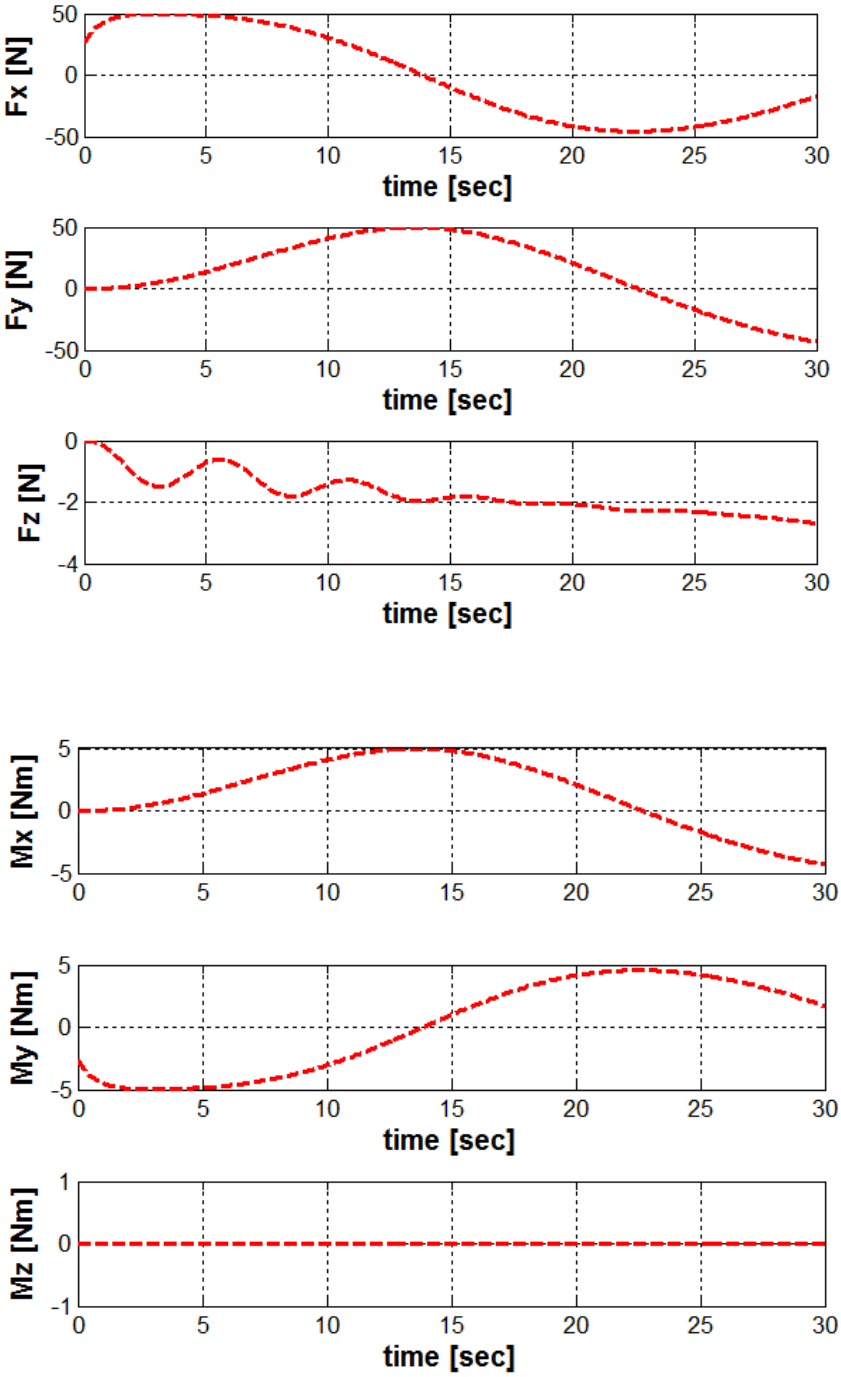

Fig. 8.14 Cable forces effecting to AUV.

8.2.3 Applied Controller to Complete USV -Cable- AUV

It is challenging to control the complete USV-cable-AUV system as it is a poorly damped system and the dynamics are highly nonlinear and unstable. In addition, the AUV is an over-actuated dynamic system which has seven control inputs. As the nonlinear dynamic equations of USV-Cable-AUV are difficult to be solved analytically, the numerical simulation method is adopted to simulate the motion of the AUV and cable system. Based on the simulation scheme introduced in Fig. 8.1, model-based motion simulation is further implemented in the later sections. In this section, we conduct several case studies to investigate the effects of ocean current and cable on AUV motion using model-based simulation. Different motion scenarios have been taken into consideration, including moving in the three-dimensional space (4 waypoints) and moving in the horizontal plane (5 waypoints). Based on the motion analysis, we find that the cable tension causes the extra drag on AUV motion which will affect the motion behavior and endurance capacity of the vehicle. Thus, when deploying the AUV and cable coupling system, one can design the maneuver form of the vehicle to control the cable tension at the tow point within an acceptable range. Table 8.2 shows the cable parameters and connected point to AUV.

A simulation model is made to represent the dynamics in the time domain. The simulation model consists of modeled environmental forces, the USV dynamics, the cable system dynamics, the AUV dynamics, the control laws, and the control allocation. An overview of the simulation model is seen in Fig. 8.15. The block named "USV Dynamic" contains the USV dynamic model presented in Chapter 2. It takes as inputs the cable effects from the block called "Cable Dynamic" and motor thruster force T_{USV} in the block named "Thruster Input USV", then calculates the USV state $\eta = [x, y, \psi]^T$ and $v_r = [u_r, v_r, r]^T$. Similarly, the states of AUV such as; $\eta = [x, y, z, \phi, \theta, \psi]^T$ and $v_r = [u_r, v_r, w_r, p, q, r]^T$ are computed in the block named "HAUV Dynamics" based on three controlled inputs cable force F_{cable}, ocean current effects and thruster input T_{USV}. T_{USV} is calculated by the controller system in block name "Path Following Controller", which contains the robust SMC controller described in Section 6.2. The ocean current is estimated as described in Section 4.8 in the block named "Ocean Currents". Lastly, the desired path is defined in the inertial coordinate system as $\eta_f = \left[x_f, y_f, z_f, \phi_f, \theta_f, \psi_f\right]^T$ and is calculated in the block called "Desired Trajectory".

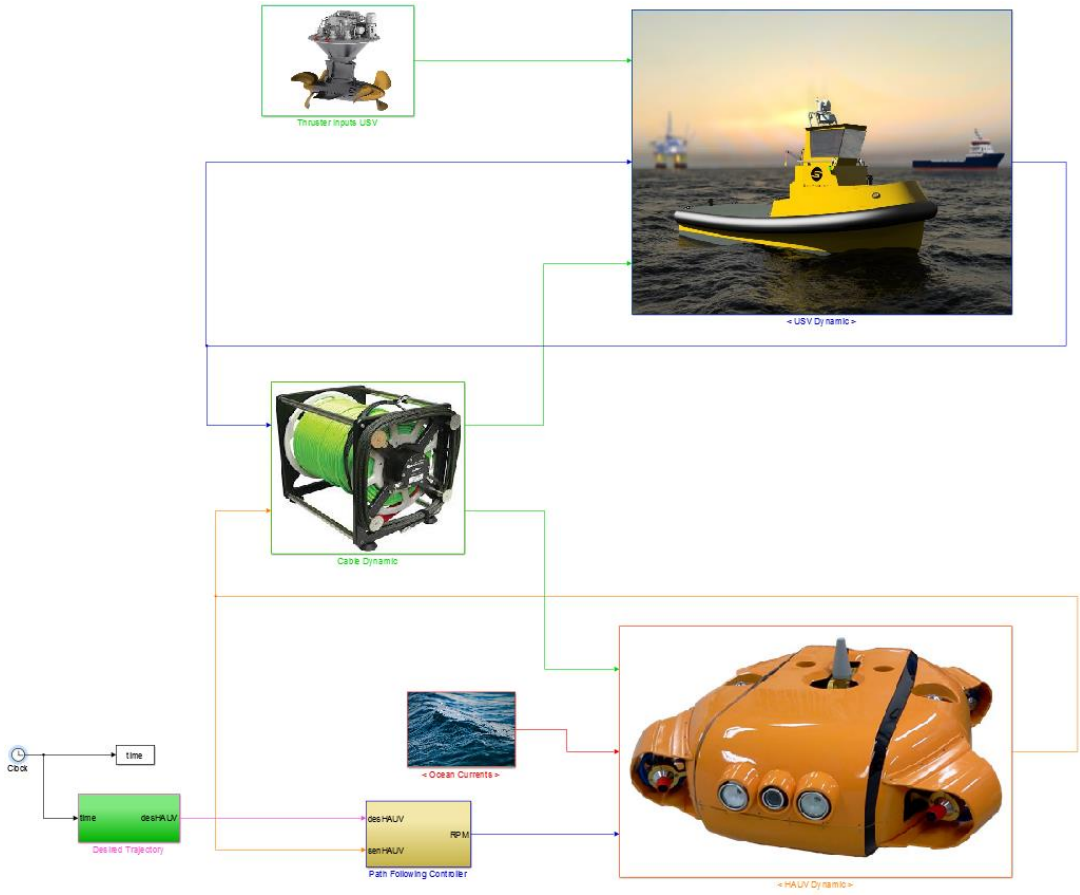

Fig. 8.15 Simulation program for the integrated USV –Cable- AUV systems.

Table 8.2. Cable parameters and connected point to AUV

Cable parameters		
Length of cable	*L*	*100 m*
Constant distribute force	*W*	*W=[-4 3 5] N*
Guess for end force	*Fguess*	*F=[40 0 2] N*
Modulus of elasticity	*E*	*200. 10^9 (200e9)*
Cable diameter	*d*	*0.014 m*
Cable cross-sectional area	*A*	*1.54x10^-4*
Initial mesh	*s*	*S=0:1:L*
Connected points between cable and AUV		

X axis	*x*	*0 m*
Y axis	*y*	*0 m*
Z axis	*z*	*-0.1 m*

8.2.3.1 Four Waypoints Trajectory in 3D

The simulations have been conducted to demonstrate the theoretical performance of the control systems, and to study how dynamics impact the control system performance. To verify the effectiveness of the proposed thruster allocation control and the control algorithms, the USV-cable-AUV model was formed and the necessary above algorithms were applied to this model. In this section, the motion of the cable tethered AUV system in three-dimensional space is presented. The parameters for the underwater vehicle and the controller used in the simulations are shown in Table 8.3. In this study, we consider the current effects on the dynamics of both the AUV and the cable. Also, the model-based simulation is conducted to predict the motion of the coupled system, especially under the disturbance of ocean current. The simulation results are shown in Figs. 8.16-8.25.

Table 8.3. Parameters for 4 waypoints of AUV with cable effects

Time for simulation	
Simulation time	*30 seconds*
Sampling time	*0.01*
Position initial values	
$[X \quad Y \quad Z \quad \phi \quad \theta \quad \psi] = [52 \quad -2 \quad 55 \quad 10 \quad 10 \quad 30]$	
Velocity initial values	
$[u \quad v \quad w \quad p \quad q \quad r] = [0 \quad 0 \quad 0 \quad 0 \quad 0 \quad 0]$	
Waypoints	
Waypoint 1	$(x \quad y \quad z \quad \phi \quad \theta \quad \psi) = (55 \quad 0 \quad 55 \quad 0 \quad 0 \quad 0)$
Waypoint 2	$(x \quad y \quad z \quad \phi \quad \theta \quad \psi) = (60 \quad -4 \quad 58 \quad 0 \quad 0 \quad -30)$
Waypoint 3	$(x \quad y \quad z \quad \phi \quad \theta \quad \psi) = (67 \quad -2 \quad 61 \quad 0 \quad 0 \quad -90)$
Waypoint 4	$(x \quad y \quad z \quad \phi \quad \theta \quad \psi) = (62 \quad 2 \quad 64 \quad 0 \quad 0 \quad 0)$
Current parameters (3D)	

Average speed	*0.5 m/s*
Angle of attack	*10 degrees*
Heading angle of current	*60 degrees*
SMC Controller	
Λ	$\Lambda = \begin{pmatrix} \Lambda_x & \Lambda_y & \Lambda_z & \Lambda_\phi & \Lambda_\theta & \Lambda_\psi \end{pmatrix} = \begin{pmatrix} 10 & 10 & 10 & 40 & 40 & 10 \end{pmatrix}$
K	$K = \begin{pmatrix} K_x & K_y & K_z & K_\phi & K_\theta & K_\psi \end{pmatrix} = \begin{pmatrix} 0.5 & 0.5 & 0.5 & 2.5 & 2.5 & 0.5 \end{pmatrix}$

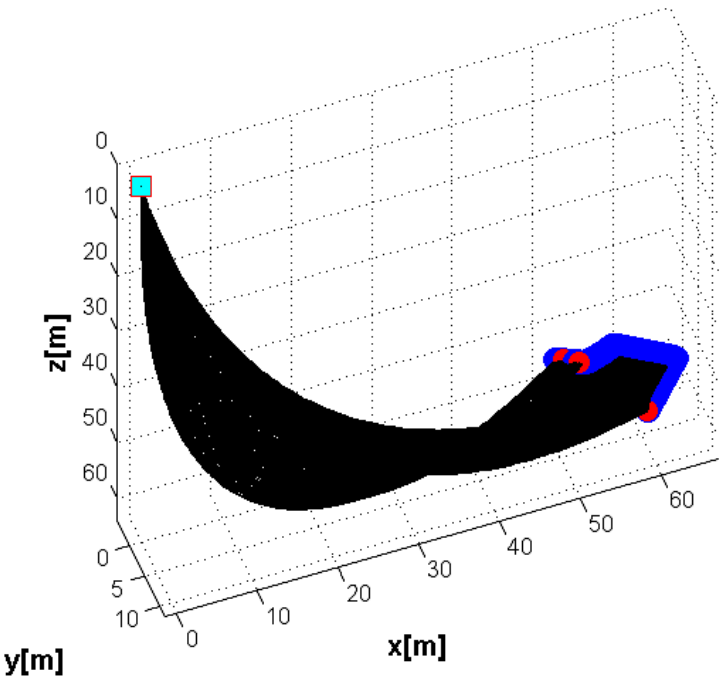

Fig. 8.16 Trajectory of complete systems using SMC controller.

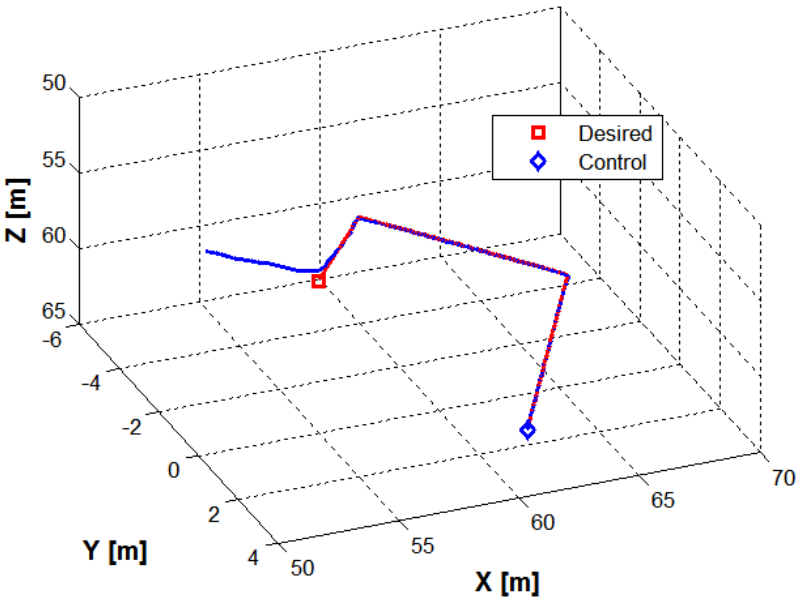

Fig. 8.17 Trajectory of complete systems using SMC controller (no cable configuration).

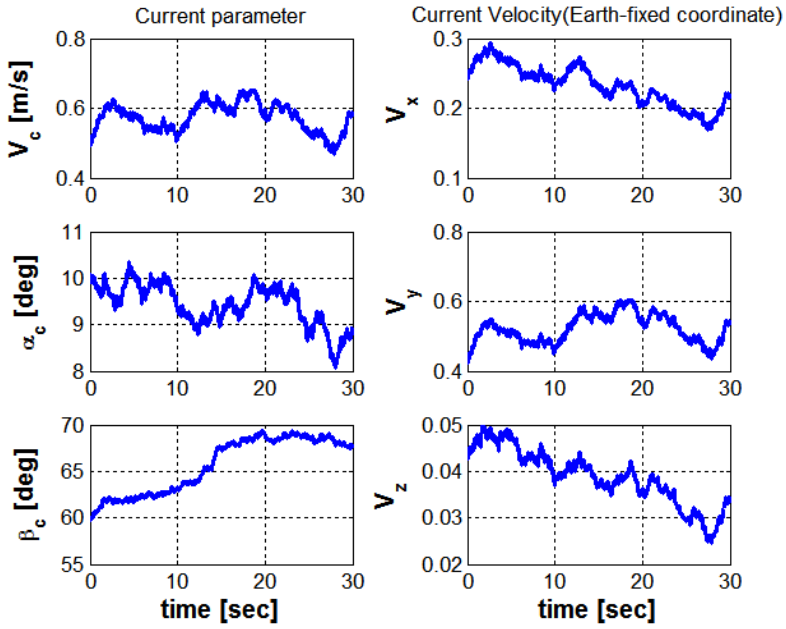

Fig. 8.18 Current forms.

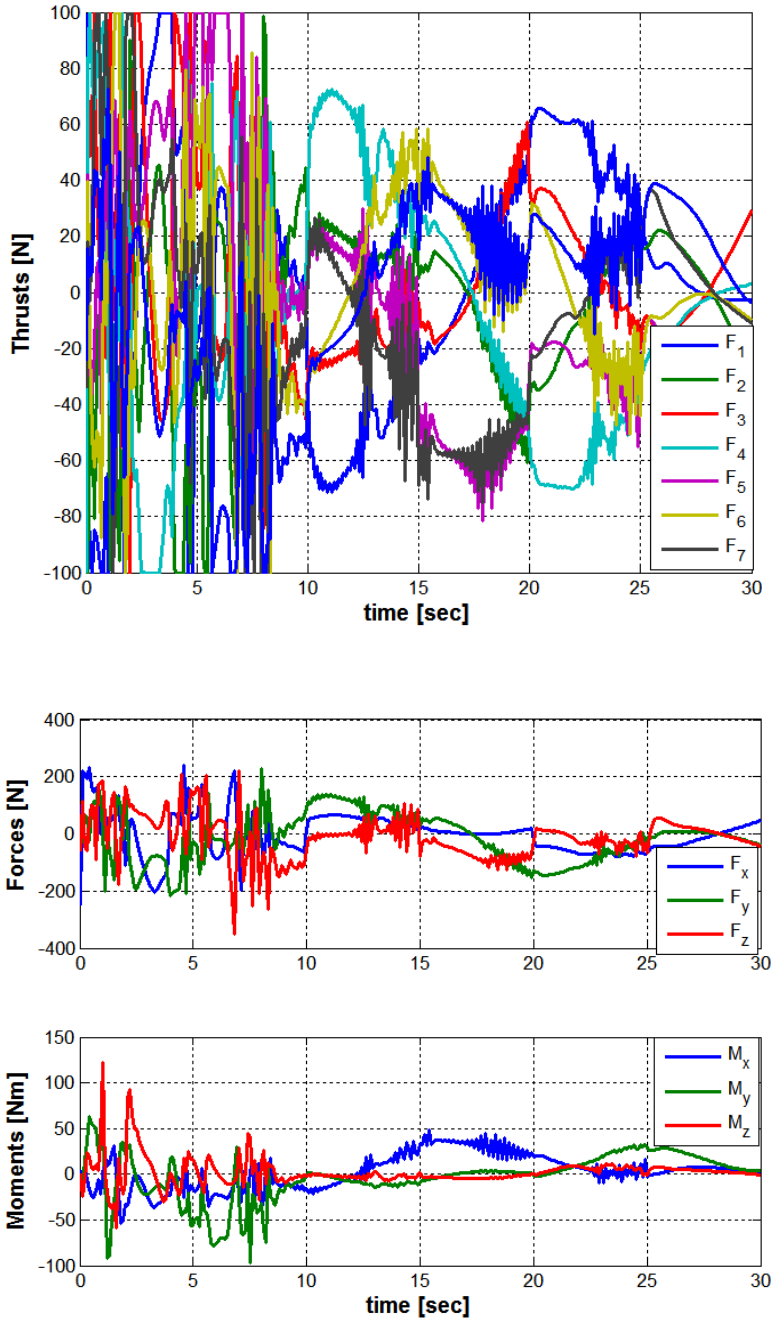

Fig. 8.19 Control inputs using SMC controller.

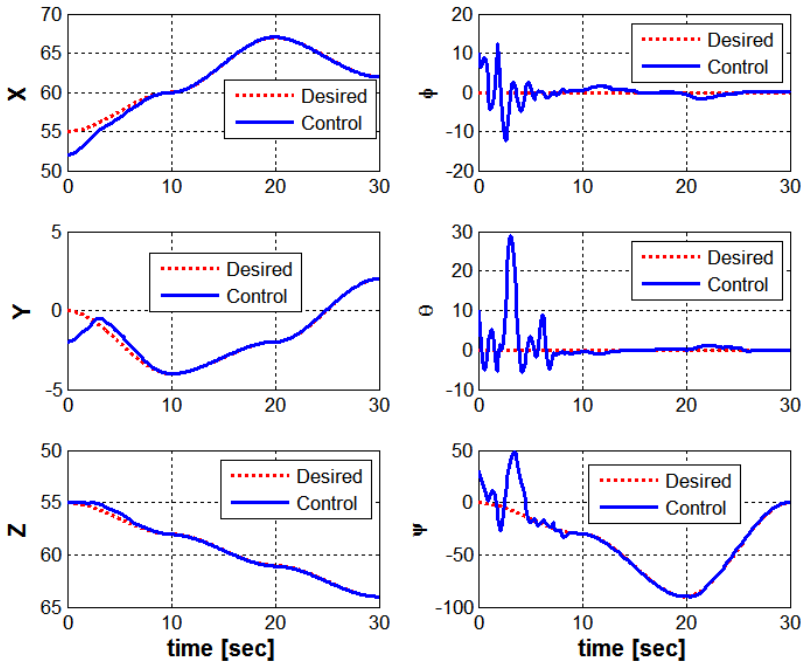

Fig. 8.20 Positions and orientation angles of AUV using SMC controller.

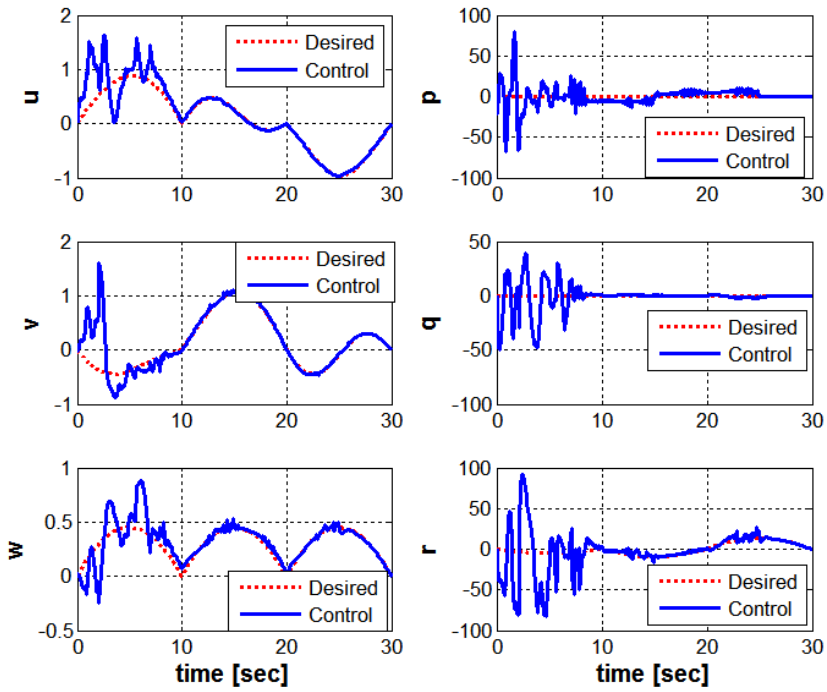

Fig. 8.21 Velocities of AUV using SMC controller.

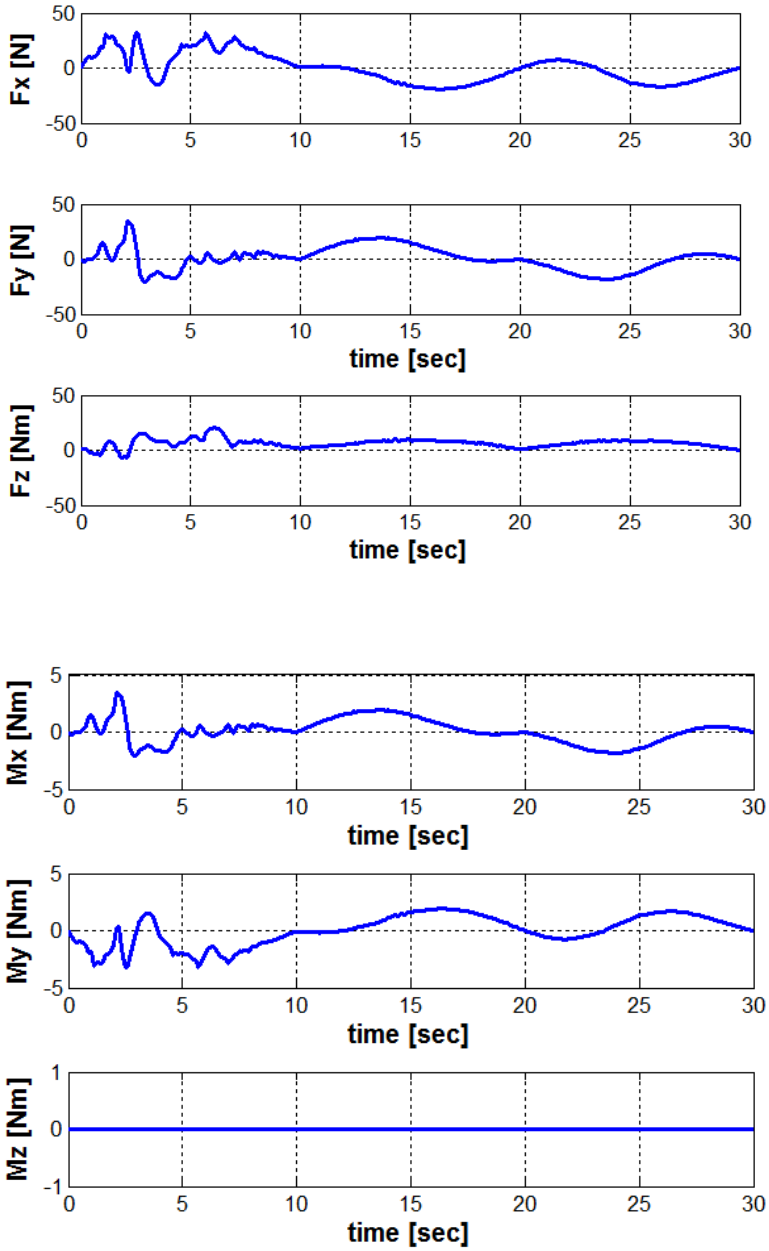

Fig. 8.22 Cable forces and moment w.r.t body frame.

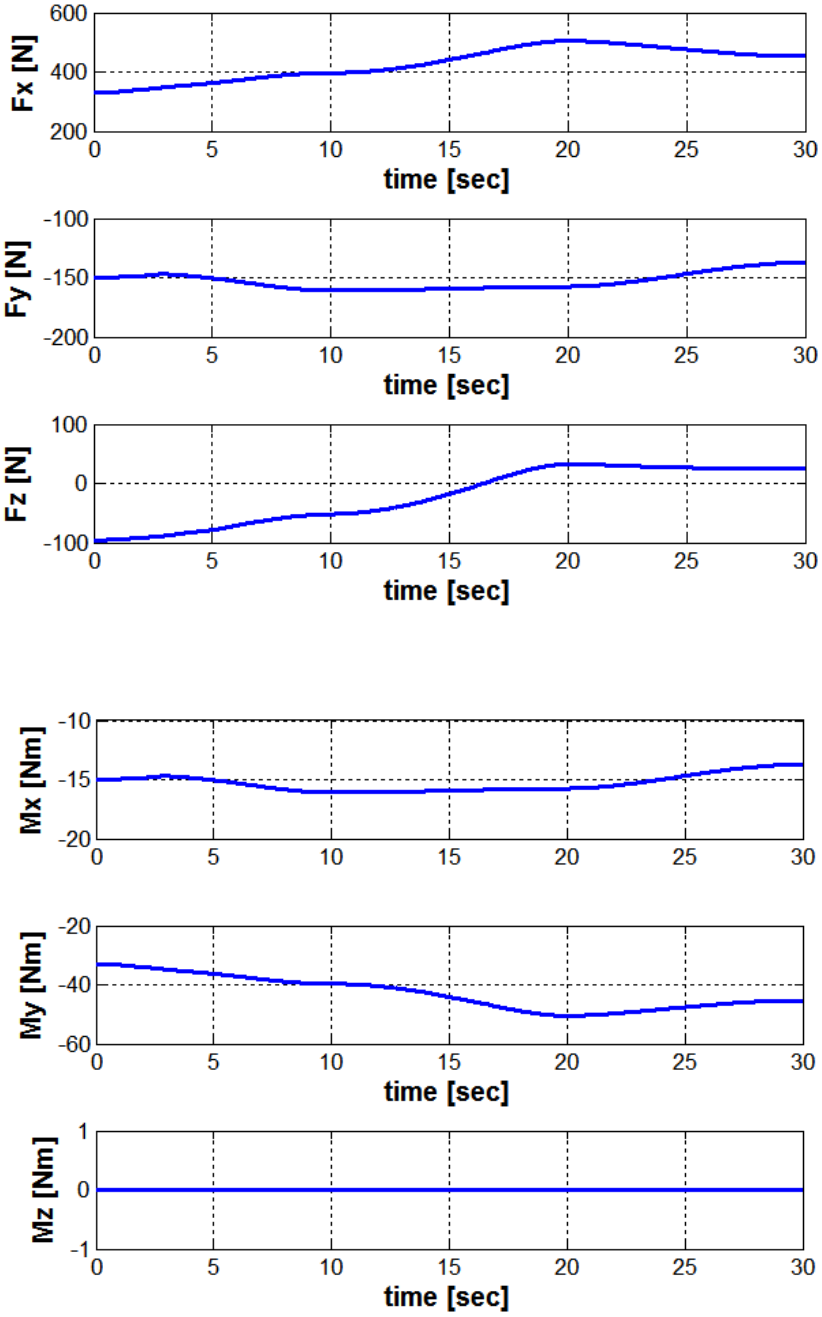

Fig. 8.23 Cable forces and moment w.r.t earth frame.

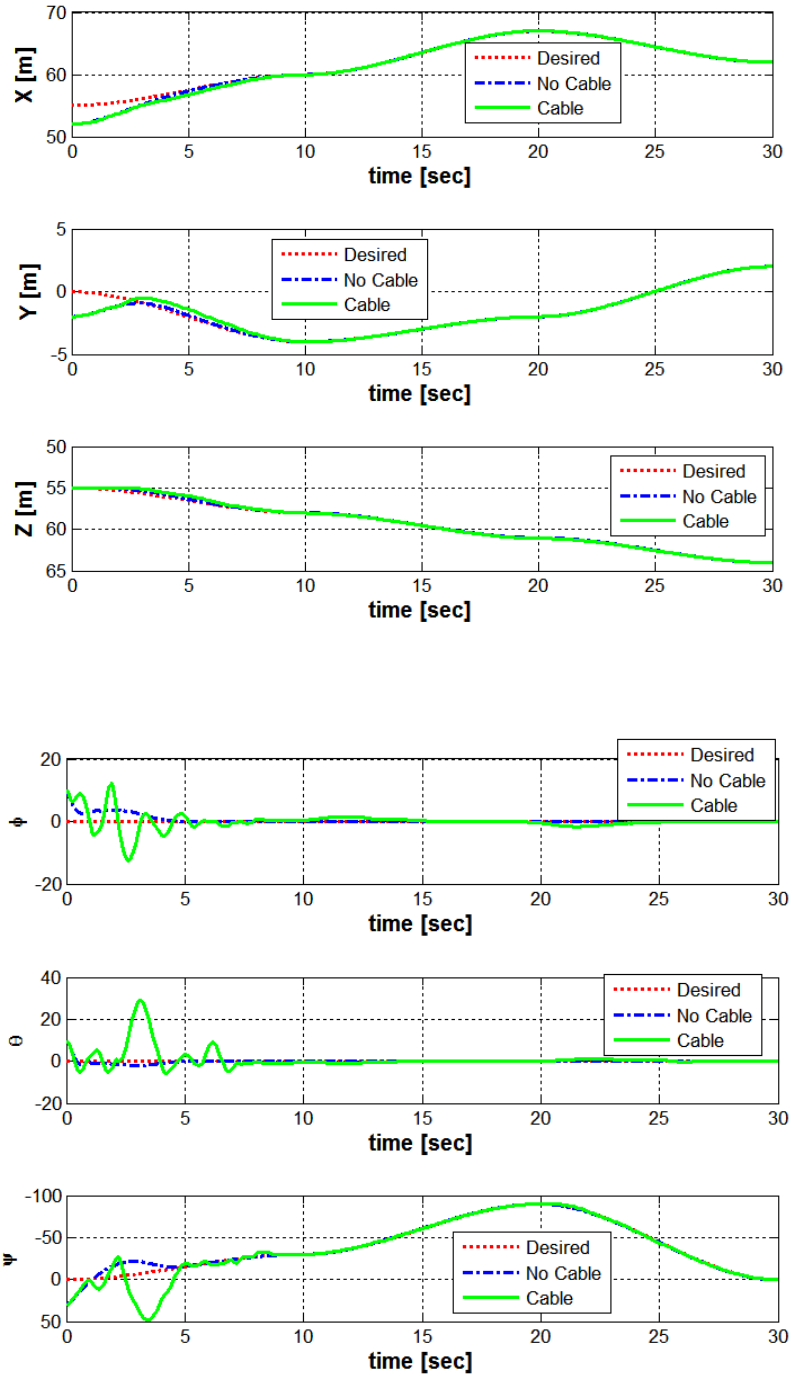

Fig. 8.24 Positions and orientation angles of AUV in both cases: with and without cable.

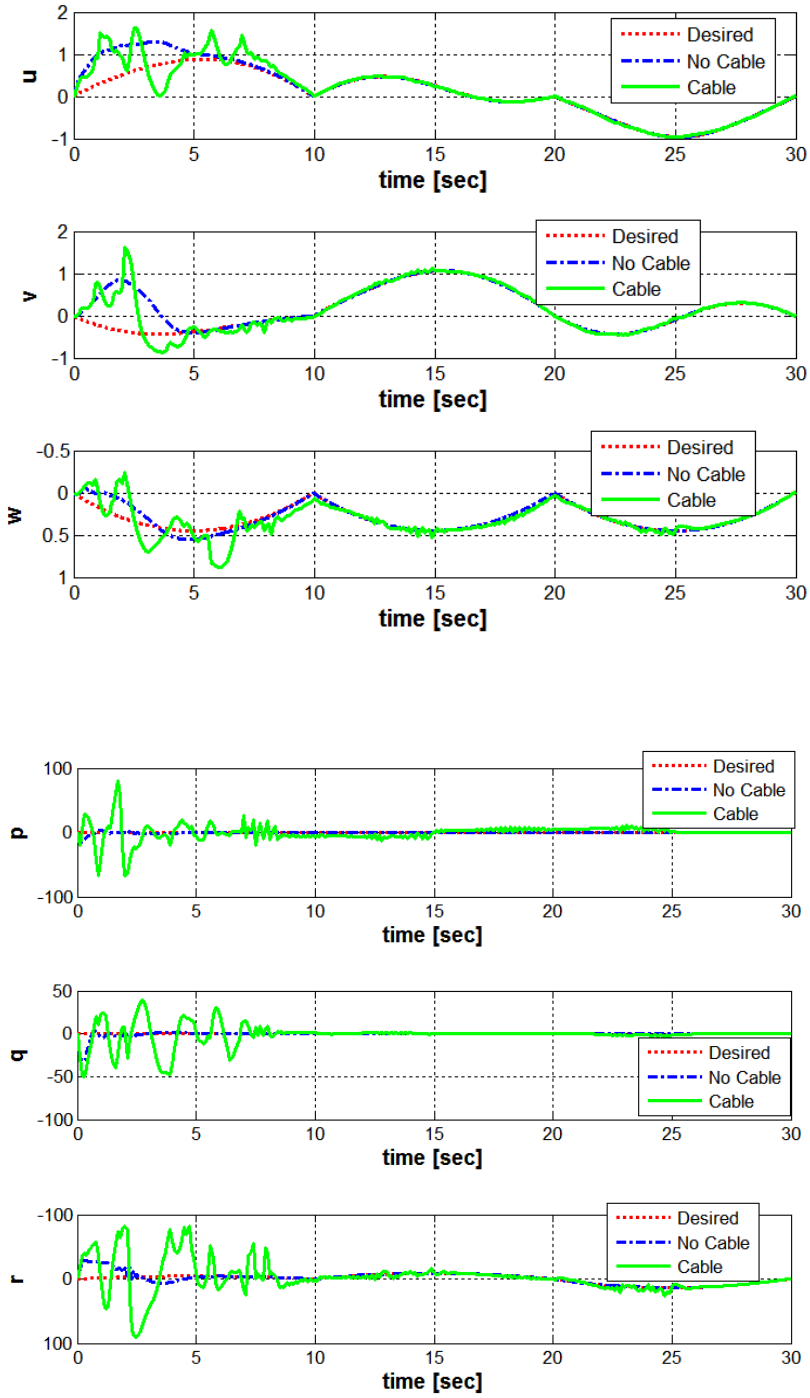

Fig. 8.25 Velocities of AUV in both cases: with and without cable.

The model uncertainty was applied in the same way as in the previous simulation in Section 6.4.2, assuming that a 3-dimensional current model with a reference speed of 0.5 m/s (about 1 knot) and its orientation w.r.t. the inertial frame is 60° acting on the AUV. The variation of AUV trajectory and the configuration of the cable are shown in Figs. 8.16 and 8.17. The simulation results confirm that the actual trajectories could track the desired trajectories efficiently from the start point to the end point by the designed SMC controller and allocation control algorithm despite parameter uncertainties and disturbance effects. This suggests robustness of the SMC scheme over the environmental disturbances and parameter uncertainties.

In the motion analysis, both the variation of the cable tension at the tow point and the configuration of the cable are investigated as shown in Figs.8.22 and 8.23. From the results, the cable tension causes the extra drag on AUV motion which will affect the motion behavior and endurance capacity of the vehicle, while the variation of the configuration of the cable may get the vehicle tangled especially under the disturbance of ocean current as shown in Figs. 8.20-8.23.

The control inputs obtained through the sliding mode motion controller and the thrust distributed to each propeller by the control allocation algorithm are shown in Figs. 8 and 9. As the results are shown, the forces remain within the constraints on the maximum force magnitude. The control system presents a good performance despite the actuators reaching the saturation levels. Therefore, the proposed method can be more advantageous in terms of power saving.

8.2.3.2 Five Waypoints Trajectory in Horizontal Plane

Next simulation, the motion of the coupled AUV and cable system in the horizontal plane is studied. To do so, the AUV is required to follow five waypoints to arrive at the destination. The guidance system will make a path for the AUV to follow based on the waypoints given. After generating the waypoints by the proposed algorithm, waypoint tracking simulations were performed. The tracking controller was implemented using same robust SMC controller. The parameters for the simulations are shown in Table 8.4. The simulation results are shown in Figs. 8.26-8.35. As shown in Fig. 8.28, the current effects are applied to the AUV at a reference speed of 0.5 m/s (about 1 knot) and its orientation w.r.t. the inertial frame is 60°. Also, the model uncertainty was applied in the same way as in the previous simulation. Furthermore, the simulation duration is 40 seconds, with a sampling time of 0.01 sec.

Table 8.4. Parameters for 5 waypoints of AUV with cable effects

Time for simulation	
Simulation time	*40 seconds*
Sampling time	*0.01*
Position initial values	
$[X \quad Y \quad Z \quad \phi \quad \theta \quad \psi] = [58 \quad -2 \quad 57 \quad 10 \quad 10 \quad 30]$	
Velocity initial values	
$[u \quad v \quad w \quad p \quad q \quad r] = [0 \quad 0 \quad 0 \quad 0 \quad 0 \quad 0]$	
Waypoints	
Waypoint 1	$(x \quad y \quad z \quad \phi \quad \theta \quad \psi) = (60 \quad 0 \quad 60 \quad 0 \quad 0 \quad 0)$
Waypoint 2	$(x \quad y \quad z \quad \phi \quad \theta \quad \psi) = (63 \quad 0 \quad 60 \quad 0 \quad 0 \quad -30)$
Waypoint 3	$(x \quad y \quad z \quad \phi \quad \theta \quad \psi) = (66 \quad 3 \quad 60 \quad 0 \quad 0 \quad -90)$
Waypoint 4	$(x \quad y \quad z \quad \phi \quad \theta \quad \psi) = (66 \quad 6 \quad 60 \quad 0 \quad 0 \quad 0)$
Waypoint 5	$(x \quad y \quad z \quad \phi \quad \theta \quad \psi) = (63 \quad 9 \quad 60 \quad 0 \quad 0 \quad 0)$
Current parameters (3D)	
Average speed	*0.5 m/s*
Angle of attack	*10 degrees*
Heading angle of current	*60 degrees*
SMC Controller	
Λ	$\Lambda = (\Lambda_x \quad \Lambda_y \quad \Lambda_z \quad \Lambda_\phi \quad \Lambda_\theta \quad \Lambda_\psi) = (8 \quad 8 \quad 8 \quad 40 \quad 40 \quad 8)$
K	$K = (K_x \quad K_y \quad K_z \quad K_\phi \quad K_\theta \quad K_\psi) = (0.5 \quad 0.5 \quad 0.5 \quad 2.5 \quad 2.5 \quad 0.5)$

Figs. 8.26 and 8.27 represent the desired and the measured trajectory of the complete USV-cable-AUV in the water. The simulation results confirm that the measured trajectory could track the desired trajectory efficiently from the start

point to the end point. Thus, we could verify that the vehicle tracked the waypoints successfully. Moreover, the position and orientation errors between the desired trajectories and measured values with time are shown in Figs. 8.30 and 8.31. The results show that all of the measured values for the vehicle's position and orientation angles followed the desired trajectories without any significant error. The current simulation results are sufficiently verifies the performance of the designed SMC controller with an allocation control algorithm.

The variation of the cable tension at the tow point and the configuration of the cable are investigated as shown in Figs. 8.32 and 8.33. We find that the cable tension causes the extra drag on AUV motion which will affect the motion behavior and endurance capacity of the vehicle, while the variation of the configuration of the cable may get the vehicle tangled especially when the coupled system moves in currents.

The control input of the SMC controller and thrusts distributed to the seven thrusters are shown in Fig. 8.29. As we can see from the results, the forces remain within the constraints on the maximum force magnitude. The control system presents a good performance despite the actuators reaching the saturation levels. In addition, during turns, the thruster actuation increases proportionally with how sharp the turn is, and at the end of the simulation when the AUV has converged to the path the thruster actuation stays at a low even level to keep the forward velocity. Looking at the individual thruster actuation in Fig. 8.29, it is also easy to see that the thruster allocation system tries to optimize the thruster actuation.

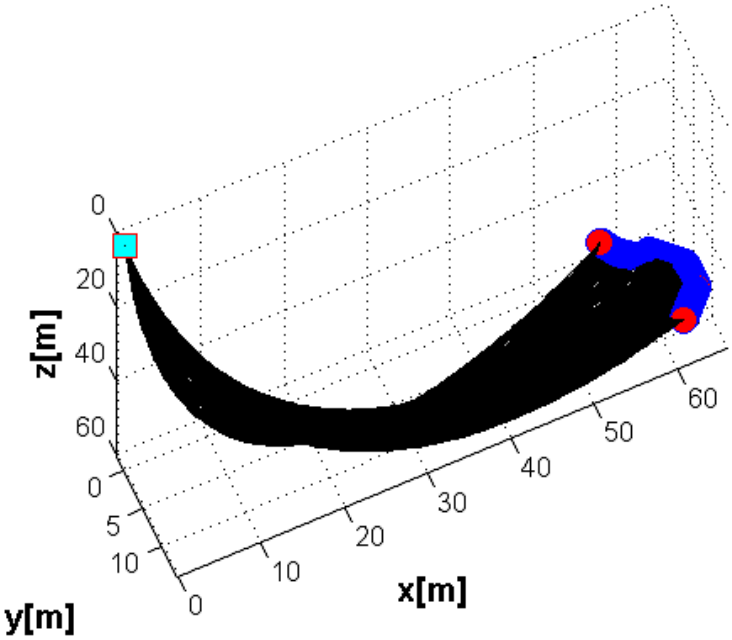

Fig. 8.26 Trajectory of complete systems using SMC controller.

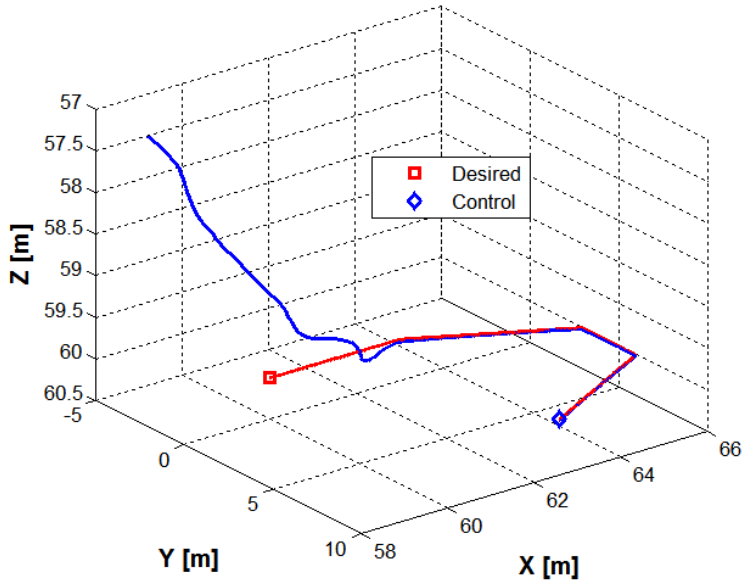

Fig. 8.27 Trajectory of complete systems using SMC controller (no cable

configuration).

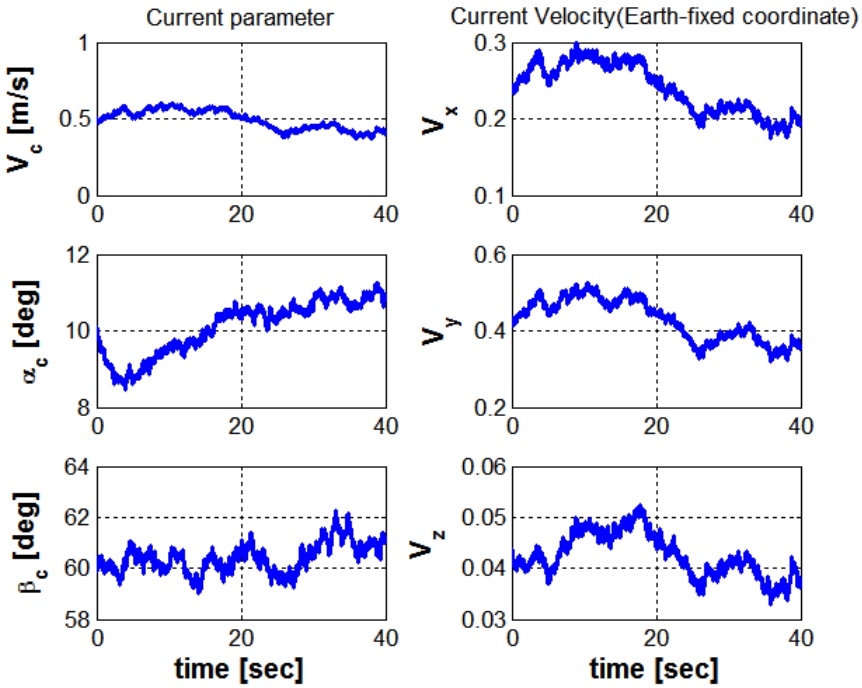

Fig. 8.28 Current forms.

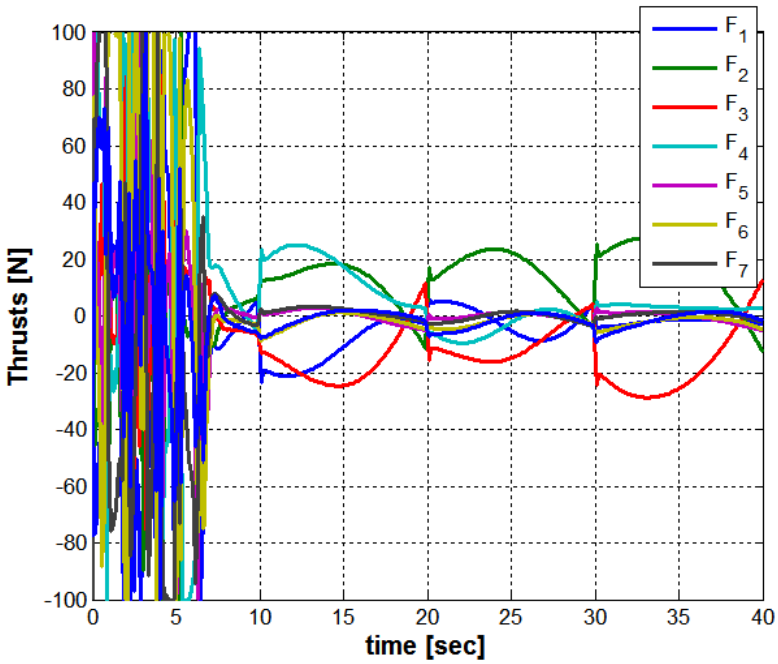

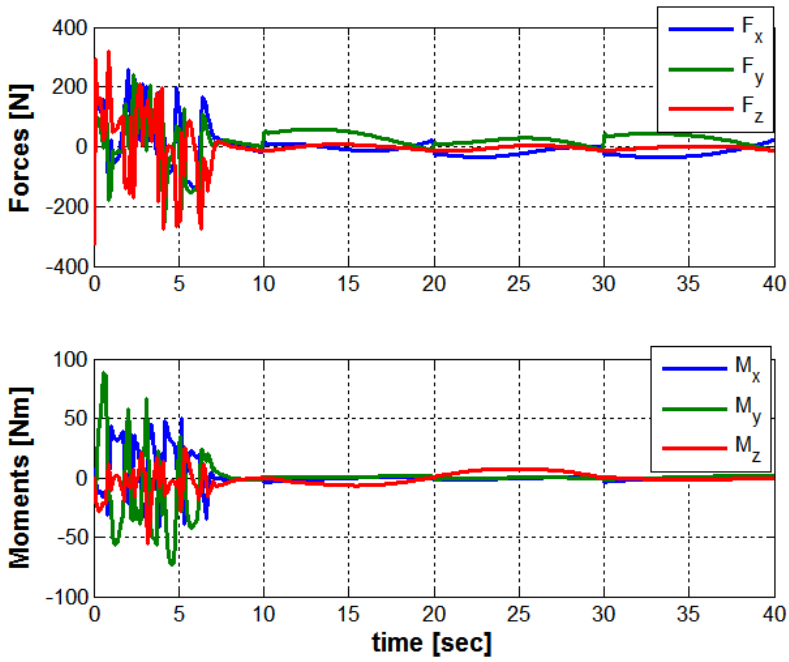

Fig. 8.29 Control inputs using SMC controller.

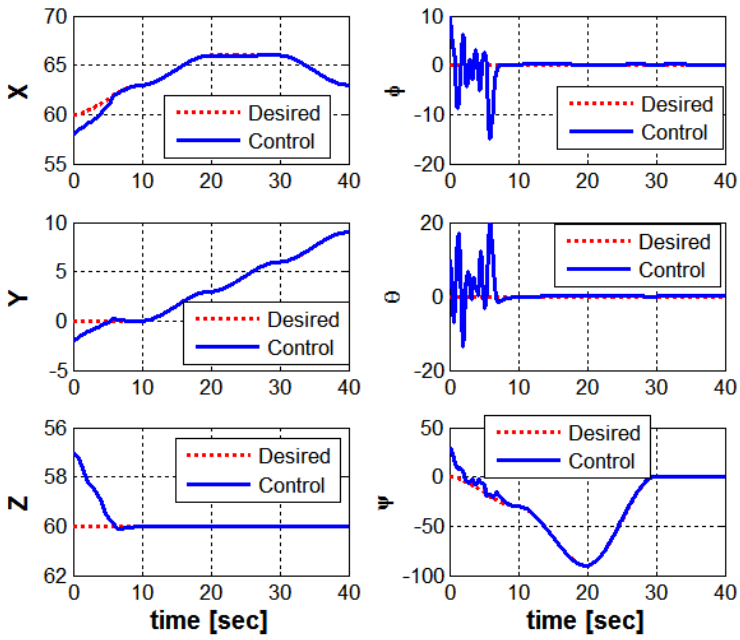

Fig. 8.30 Positions and orientation angles of AUV using SMC controller.

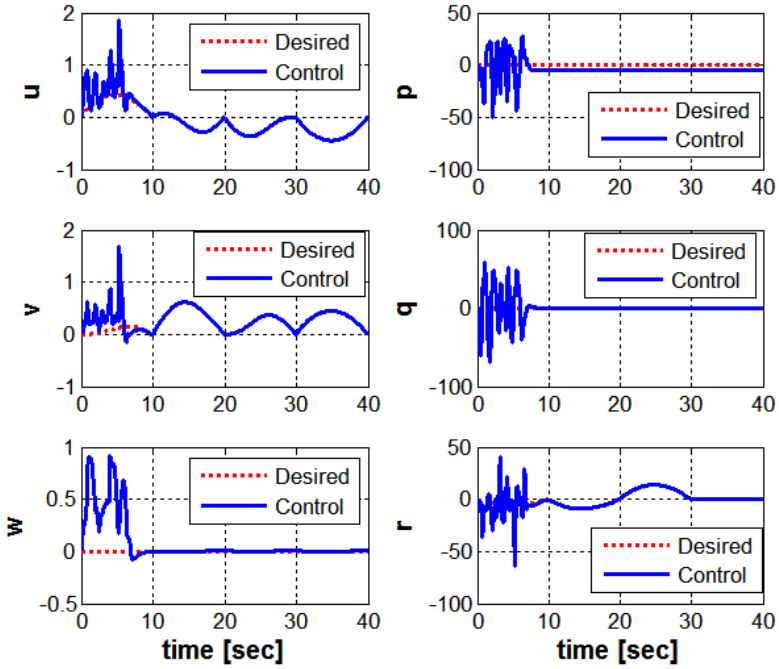

Fig. 8.31 Velocities of AUV using SMC controller.

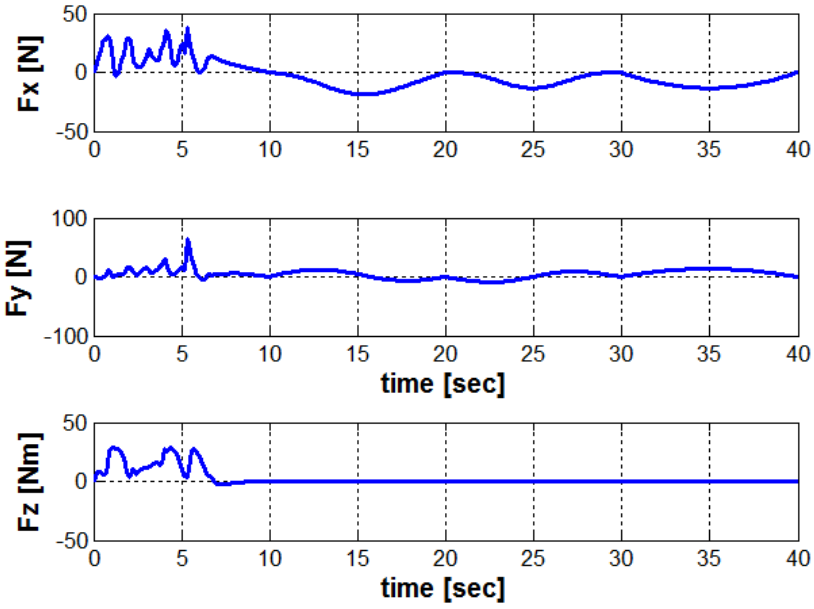

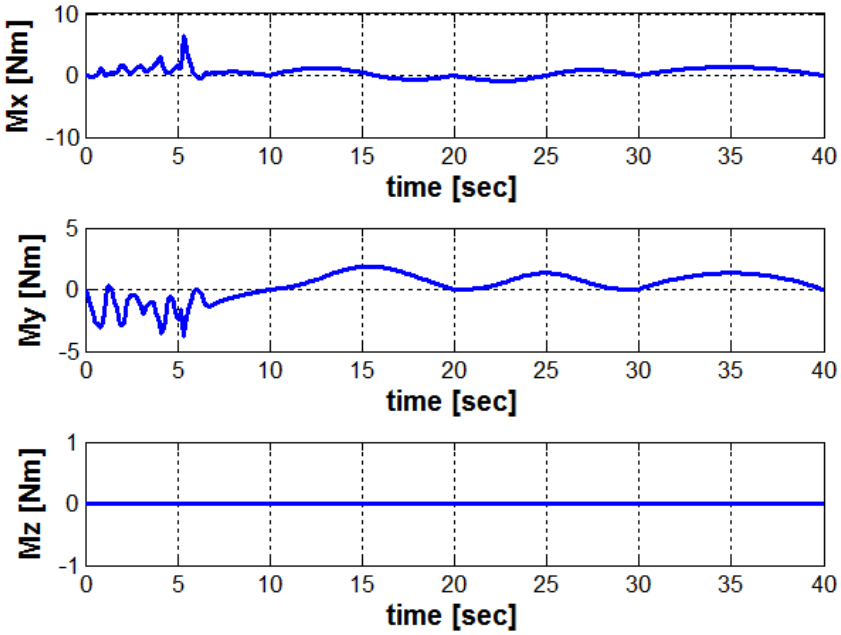

Fig. 8.32 Cable forces and moment w.r.t body frame.

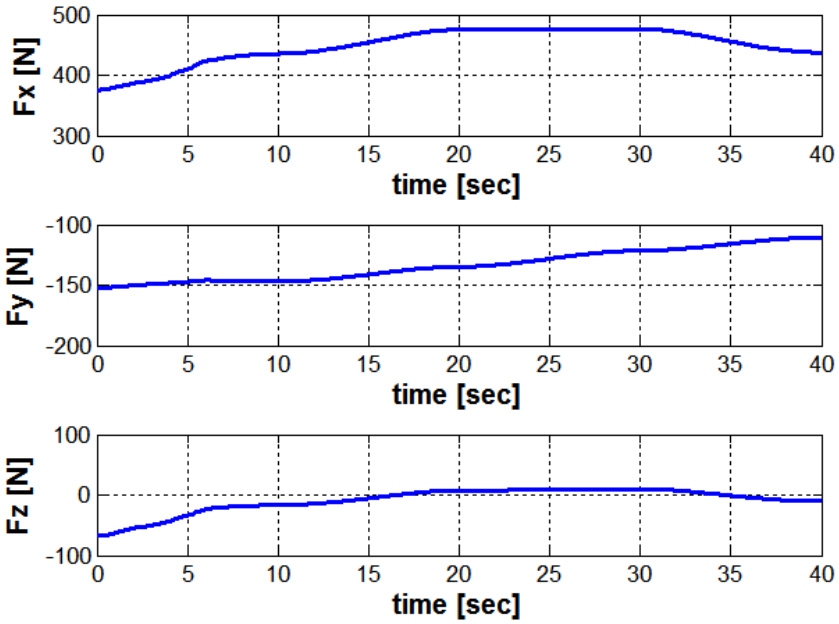

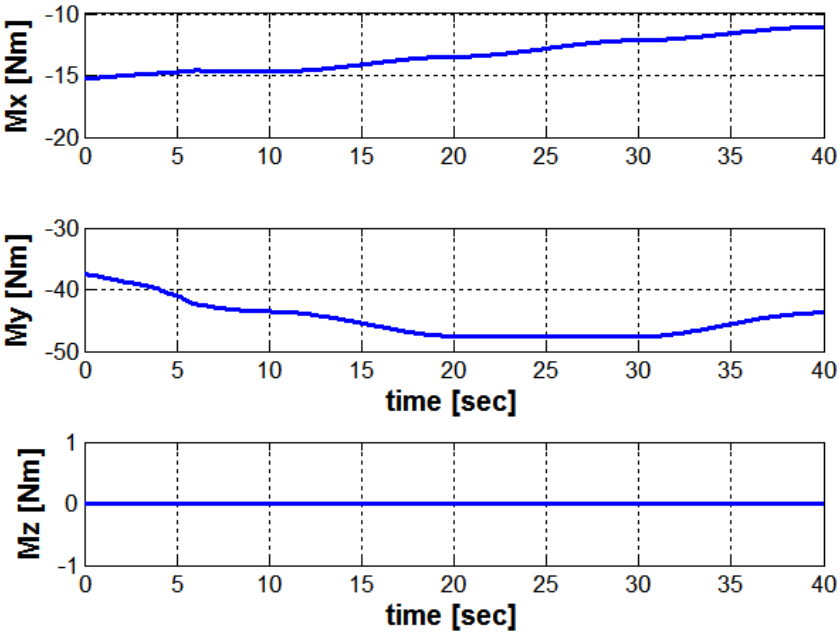

Fig. 8.33 Cable forces and moment w.r.t earth frame.

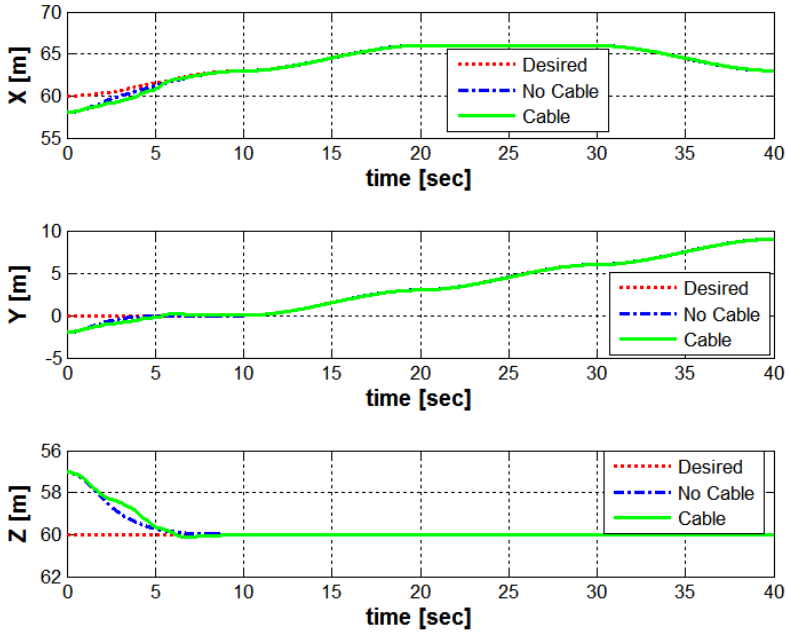

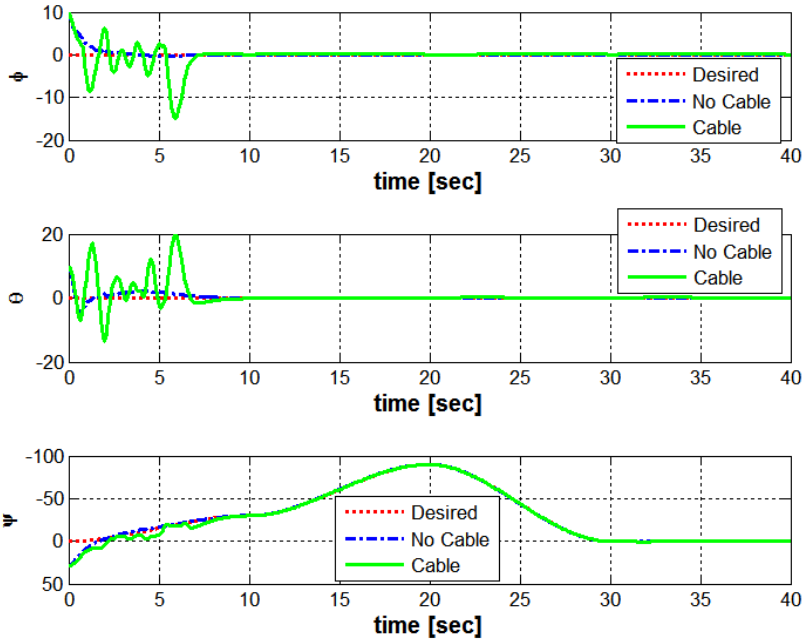

Fig. 8.34 Positions and orientation angles of AUV in both cases: with and without cable.

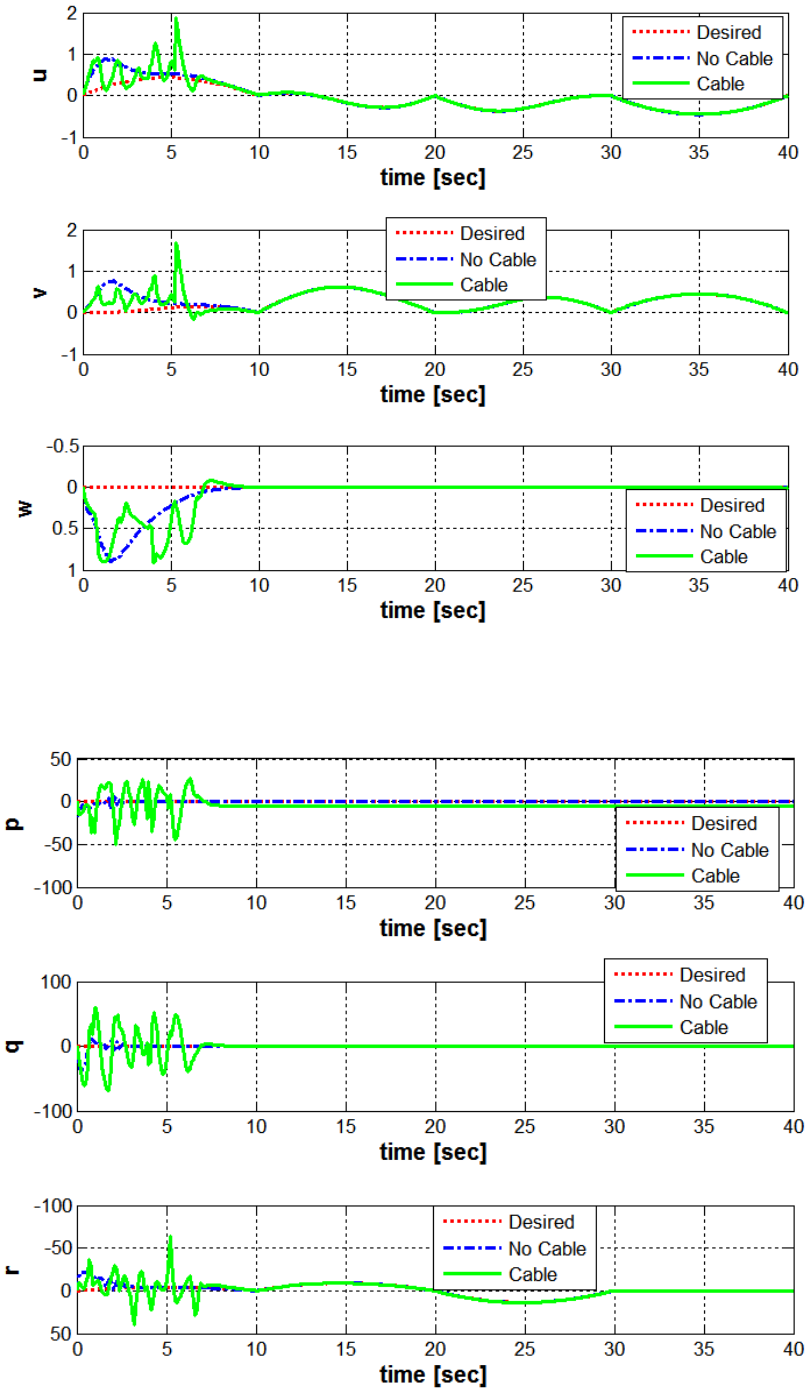

Fig. 8.35 Velocities of AUV in both cases: with and without cable.

Test with and without current effects have been performed to show the significant effects of current and cable to AUV, as shown in Figs. 8.34 and 8.35, where the position and orientation of the AUV under cable effects are represented by blue dotted lines while in the case of without considering the cable effects are shown by green solid lines.

Obviously, using the SMC controller and the allocation control algorithm considering the actuator saturation proposed in this dissertation, the simulation results confirm that the given target trajectory tracking can be successfully performed for the AUV subject to model uncertainty and disturbance.

Chapter 9: Conclusions and Future Works

The major task of an AUV is to collect information from the underwater environment and send the data back to the onshore control center, for which the reliable data transmission is required. However, according to the current technology available, underwater communication has always been an important challenge in the field. In general, there are three kinds of approaches widely applied for underwater communication, which are through acoustic wave, blue light or optical fiber. Due to the different communication mechanisms, each method has both its pros and cons. Acoustic signal can be transmitted over 10 kilometers; however, it has the disadvantage of low transmission rate and could be detected easily; besides, the performance of the acoustic sonar relies on the propagation environment heavily. Blue light can provide higher data transmission rate than the acoustic wave; however, its communication distance is very limited, only within 100 meters. Thus, in order to have the real-time and reliable underwater communication through large range, using an umbilical cable could be a better solution for the real-time surveillance mission of an AUV. In this case, we focus on the development of a modeling and control system of over-actuated, hover-capable AUV-cable-USV, with a primary focus on interconnections between guidance, control and path planning systems.

9.1 Modeling of Complete USV-Cable-AUV System

In this dissertation, we employ a dynamics modeling method for investigating a multi-body dynamics system consisting of an USV, an UC, and an AUV. The AUV, which is towed by a UC for the purposes of exploration or mine hunting, is modeled with a 6-DOF equation of motion that reflects its hydrodynamics characteristics. The 4th-order Runge–Kutta numerical method was used to analyze the motion of the USV with its hydrodynamic coefficients which were obtained through experiments and from the literature. In modeling of the flexible UC dynamics, the governing equations of the UC dynamics are established based on the catenary equation method. The shooting method is applied to solve a two-point boundary value problem of the catenary equation. To reflect the hydrodynamic characteristics of the UC, the hydrodynamic force due to added mass and the drag force are imposed. Several simple numerical simulations were conducted to validate appropriateness of the modeling.

9.2 Motion Control

This dissertation consists of a mathematical modeling of vehicles, mathematical model parameters derivation, autopilot and guidance design, obstacle avoidance, effects of ocean currents on the path and navigation of the complete USV-cable-AUV. This dissertation proposes an autopilot design for automatic takeoff, altitude control and turning control. The autopilot will consist of a guidance system and two different controllers which will be tested against each other. The first will be a PID controller, much used in the industry, and the second a Sliding Mode controller. The last controller is nonlinear and more robust than the PID. The autopilot design is supposed to handle varying current and cable effects. The guidance system will make a path for the AUV to follow based on waypoints given.

9.3 Cable Force and Moment at the Tow Points

This dissertation presents the mathematical model of a cable-tethered AUV system as well as the numerical simulation scheme for the coupled motion analysis. A series of simulations have been conducted to analyze the motion interaction of the coupled AUV and cable system, especially under the disturbance of ocean currents. In our simulation, different motion cases are studied as the vehicle moves in one-, two- and three- dimensional spaces, respectively. The variation of the cable tension at the tow point or the configuration of the cable or both is investigated for each case. We find that the cable tension causes the extra drag on AUV motion which will affect the motion behavior and endurance capacity of the vehicle, while the variation of the configuration of the cable may get the vehicle tangled especially when the coupled system moves in currents. Generally, as for a tethered AUV, it will take the vehicle additional propulsion to compensate the drag caused by the cable and maintain the desired forward speed. In general, the cable drag will increase as the length of the cable increases, so the maximum affordable cable length for the AUV will depend on the propulsion capability and the power capacity of the vehicle. However, if proper maneuvering strategy is adopted, one can control the cable tension to make it within an acceptable range by switching the orientation of the vehicle from time to time. Since the uniform current carries the AUV and cable coupling system as a whole to move forward together, it will cause less effect on the cable tension.

9.4 Path Planning

Path planning deals with what we want to achieve (by defining spatial and temporal constraints), and guidance dictates how we should act in order to achieve it (by generating appropriate reference trajectories to be fed to the corresponding

controllers). Therefore it is important to develop: a) path design methodologies, which will generate feasible and safe paths with several desired properties, and b) guidance laws capable of generating reference trajectories which will lead the vehicle on the desired path, even when unknown disturbances (such as ocean currents) affect the vehicle's motion.

In this dissertation, RRT properties and several RRT path planning algorithms are described. Normal RRT is not an efficient way to find a path between start and goal configurations because the tree wanders the whole space. By selecting the goal point with some probability, the growth of RRT is biased towards the goal instead of exploring the whole space. A greedy variation of the algorithm reduce the planning time by extending trees successively along the ray connecting selected node and random points until a collision occurs. The efficiency of planning algorithm is further enhanced by combining the biased and greedy RRT. Thus, a new synchronized biased-greedy RRT is proposed which leverages the strengths of the biased and greedy RRTs. It combines the advantage of the biased RRT that grows trees towards the goal location, with the ability of the greedy RRT that makes trees traverse the environment in a single iteration. The proposed method achieves performance improvements compared to other RRT variants, not only in computational time but also in the quality of the path. The RRT is a computationally efficient tool for complex online motion planning, but the resulting path contains a lot of wavy redundant nodes. A pruning algorithm is proposed which is able to remove most of the extraneous nodes within a short time. After applying the pruning algorithm, most of the path consists of straight lines and has less jaggy motion.

9.5 Future Works

In this dissertation, only the uniform current is considered for the case studies, while in the real world the ocean environment is much more complicated with unsteady, non-uniform components, in which case the current effect on the cable-tethered AUV should be further investigated in future studies to provide effective and practical guidelines for the safe operation of the AUV and cable coupling system.

References

[1] Breivik, M. (2010). Topics in Guided Motion Control of Marine Vehicles. PhD thesis, Norwegian University of Science and Technology.

[2] Caccia, M., Bruzzone, G., and Bono, R. (2006). Modelling and identification of the Charlie2005 ASC. In 14th Mediterranean Conference on Control and Automation, 2006, pages 1-6.

[3] Miskovic, N., Vukic, Z., Bibuli, M., Bruzzone, G., and Caccia, M. (2011). Fast in-field identification of unmanned marine vehicles. Journal of Field Robotics, 28(1):101–120.

[4] Bibuli, M., Bruzzone, G., Caccia, M., Indiveri, G., and Zizzari, A. (2008). Line following guidance control: Application to the Charlie unmanned surface vehicle. In IEEE/RSJ International Conference on Intelligent Robots and Systems. IROS 2008, pages 3641-3646.

[5] Bibuli, M., Bruzzone, G., Caccia, M., and Lapierre, L. (2009). Path-following algorithms and experiments for an unmanned surface vehicle. Journal of Field Robotics, 26(8):669-688.

[6] Bruzzone, G., Bruzzone, G., Bibuli, M., and Caccia, M. (2011). Autonomous mine hunting mission for the Charlie USV. In OCEANS 2011, pages 1-6, Santander, Spain.

[7] Caccia, M., Bibuli, M., Bono, R., Bruzzone, G., and Spirandelli, E. (2009). Aluminum hull usv for coastal water and seafloor monitoring. In OCEANS 2009 - EUROPE, pages 1-5.

[8] Caccia, M., Bibuli, M., R., B., Bruzzone, G., and E., S. (2007). Unmanned surface vehicle for coastal and protected waters applications: the Charlie project. Marine Technology Society Journal, 41(2):62-71.

[9] Caccia, M., Bibuli, M., Bono, R., Bruzzone, G., Bruzzone, G., and Spirandelli, E. (2008a). Unmanned marine vehicles at CNR-ISSIA. In In Proceedings of IFAC Conference on Control Applications in Marine Systems, pages 3070–3075, Seoul, Korea.

[10] Bibuli, M., Caccia, M., and Lapierre, L. (2007). Path-following algorithms and experiments for an autonomous surface vehicle. In In Proceedings of IFAC Conference on Control Applications in Marine Systems.

[11] Casarella, M.J., Parsons, M. (1970). Cable systems under hydrodynamic loading. Mar. Technol. Soc. J. 4(4) 27-44.

[12] Yoerger, D.A., Grosenbaugh, M.A., Triantafyllou, M.S. (1991). Drag forces and flow induced vibrations of a long vertical tow cable-part1: steady-state towing conditions. J. Offshore Mech. Arct. Eng. 19 (3) 117-127.

[13] Hover, F.S., Yoerger, D.R. (1992). Identification of low-order dynamic models for deeply towed underwater vehicle systems. Int. J. Offshore Polar 2 38-45.

[14] Chai, Y.T., Varyani, K.S. (2002). Three dimensional lump mass formulation of a catenary riser with bending, torsion and irregular seabed interaction effect, Ocean Eng. 29 1503-1525.

[15] Li, Q., Xu, H., Zhang, Q., Wang, X., Li, Z. (2008). Dynamics simulation of remotely operated vehicle fiber optic micro cable system, in: Proceedings of the 7th World Congress on Intelligent Control and Automation, Chongqing, China.

[16] Horner, D.P., Healey, A.J., Kragelund, S.P., “AUV experiments in obstacle avoidance,” Proceedings of MTS/IEEE, OCEANS 2005, Washington, DC, 17-23 Sept. 2005.

[17] Feng, Z., Allen, R. (2004). Evaluation of the effects of the communication cable on the dynamics of an underwater flight vehicle. Ocean Eng. 31 1019-1035.

[18] Milinazzo, F., Wilkie, M., Latchman, S.A. (1987). An efficient algorithm for simulating the dynamics of towed cable systems. Ocean Eng. 14 (6) 513-526.

[19] Hagen, P. E., Størkersen, N., Vestgard, K., and Kartvedt, P. (2003). The HUGIN 1000 autonomous underwater vehicle for military applications. In Proc. MTS/IEEE OCEANS, Volume 2, San Diego, USA, pp. 1141-1145.

[20] Jalving, B. and Gade, K. (1998). Positioning accuracy for the HUGIN detailed seabed mapping. In Proc. MTS/IEEE OCEANS, Volume 1, Nice, France, pp. 108-112.

[21] Pascoal, A., Oliviera, P., Silvestre, C., Bjerrum, A., Ishoy, A., Pignon, J.P., Ayela, G., and Petzeit, C. (1997). MARIUS: An autonomous underwater vehicle for coastal ocenaography. IEEE Robotics & Automation Magazine, 47-59.

[22] Oliveira, P., Pascoal, A., Silva, V., and Silvestre, C. (1998). Mission Control of the MARIUS Autonomous Underwater Vehicle: System Design and Implementation, and Sea Trials. Journal of Systems Science 29 (10). Special issue on Underwater Robotics.

[23] Fossen, T. I. (1994). Guidance and Control of Ocean Vehicles. John Wiley & Sons Ltd.

[24] Abkowitz, M.A. (1969). Stability and Motion Control of Ocean Vehicles. Cambridge, MIT Press.

[25] Newman, J.N. (1997). Marine Hydrodynamics. MIT Press, Massachusetts.

[26] Yuh, J. (1990). Modeling and Control of Underwater Robotic Vehicles. IEEE Transactions on Systems, Man and Cybernetics, vol 20, n 6, pp. 1475-83.

[27] Fossen, T.I. (1991). Nonlinear Modeling and Control of Underwater Vehicles. PhD Thesis, Dept of Engineering Cybernetics, the Norwegian Institute of Technology, Trondheim.

[28] Fossen, T.I., and Fjellstad, O.E. (1995). Nonlinear Modeling of Marine Vehicles in 6 Degrees of Freedom. International Journal of Mathematical Modeling of Systems, vol.1, no.1.

[29] Goheen, K.R. (1991). Modeling Methods for Underwater Robotic Vehicle Dynamics. Journal of Robotic Systems, vol. 8, no.3, pp. 259-317.

[30] Clayton, B.R., and Bishop, R.E.D. (1982). Mechanics of Marine Vehicles. E.&F.N. Spon Ltd.

[31] Egeskov, P., Bjerrum, A., Pascoal, A.,and Silvestre, C. (1994). Design, Construction and Hydrodynamic Testing of The AUV MARIUS. IEEE Symposium on Autonomous Underwater Vehicle Technology, pp. 199-207.

[32] Chiok Ching Chaw. (2000). Modeling and Control of An Autonomous Underwater Vehicle. Master's thesis, NUS, Department of Mechanical and Production Engineering.

[33] Nahon, M. (1996). A Simplified Dynamics Model for Autonomous Underwater Vehicles. Proceedings of the IEEE Symposium on Autonomous Underwater Vehicle Technology, pp. 373-379.

[34] Prestero, T. (2001). Development of A Six-Degree of Freedom Simulation Model for The REMUS Autonomous Underwater Vehicle. MTS/IEEE Oceans 2001, An Ocean Odyssey. Conference Proceedings, vol.1, pt. 1, pp. 450-456.

[35] Prestero, T.J. (2001). Verification of A Six-Degree of Freedom Simulation Model For The REMUS AUV. Master's thesis, MIT, Department of Ocean and Mechanical Engineering.

[36] Yuh, J. (2000). Design and control of autonomous underwater robots: A survey. In Automatic Robots 8, 7-24, Kluwer Academic Publishers.

[37] Jalving, B. (1994). The ndre-auv flight control system. IEEE Journal of Oceanic Engineering, 19(4):497-501.

[38] Yoerger, D.N., and Slotine, J.E. (1985). Robust trajectory control of underwater vehicles. IEEE Journal of Oceanic Engineering, 10(4):462-470.

[39] Healey, A.J., and Lienard, D. (1993). Multivariable sliding mode control for autonomous diving and steering of unmanned underwater vehicles. IEEE Journal of Oceanic Engineering, 18(3):327–339.

[40] Nakamura, Y., and Savant, S. (1992). Nonlinear tracking control of autonomous underwater vehicles. In Proceedings of IEEE Int. Conf. of Robotics and Automation, volume 3, pages A4–A9.

[41] Papoulias, F.A., Cristi, R., and Healey, A. J. (1990). Adaptive sliding mode control of autonomous underwater vehicles in the dive plane. IEEE Journal of Oceanic Engineering, 15(3):152–160.

[42] Tabai, S.S., El-Hawary, F., and El-Hawary, M. (1994). Hybrid adaptive control of autonomous underwater vehicles. In Proceedings of Symposium of Autonomous Underwater Vehicle Technology, pages 275–282.

[43] Caccia, M., and Veruggio, G. (2000). Guidance and control of a reconfigurable unmanned underwater vehicle. In Control Engineering Practice 8, pages 21–37.

[44] Yoeger, D.A., Grosenbaugh, M.A., Triantafyllou, M.S. (1991). Drag forces and flow-induced vibrations of a long vertical tow cable-part1: steady-state towing conditions. Journal of Offshore Mechanics and Arctic Engineering, 19 (3): 117-127.

[45] Hover, F.S., Yoerger, D.R. (1992). Identification of low-order dynamic models for deeply towed underwater vehicle systems. International Journal of Offshore and Polar Engineering, 2:38-45.

[46] Buckham, B., Nahon, M., Cote, G. (2000). Validation of a finite element model for slack ROV tethers. IEEE Journal of Oceanic Engineering, 1129–1136.

[47] Albow, C.M., Schechter, S. (1983). Numerical simulation of undersea cable dynamics. Ocean Engineering 10 (6), 443–457.

[48] Chai, Y.T., Varyani, K.S. (2002). Three Dimensional Lump Mass Formulation of a Catenary Riser with Bending, Torsion and Irregular Seabed Interaction Effect. Ocean Engineering, 29:1503-1525.

[49] Wingnet, J.M., Huston, R.L. (1976). Cable Dynamics - A Finite Segment Approach. Computers and Structures, 6:475480.

[50] Irvine, M. (1981). Cable Structures. Massachusetts Institute of Technology, USA.

[51] Sagatun, S.I. (2001). The Elastic Cable Under the Action of Concentrated and Distributed Forces. Journal of Offshore Mechanics and Arctic Engineering, 123:43-45.

[52] The Society of Naval Architects and Marine Engineers. (1950). Nomenclature for treating the motion of a submerged body through a fluid. Technical and Research Bulletin, No.1-5.

[53] Faltinsen, O.M. (1990). Sea Loads on Ships and Offshore Structures. Cambridge University Press.

[54] Blendermann, W. (1994). Parameter identification of wind loads on ships. Journal of Wind Engineering and Industrial Aerodynamics, 51(3), 339-351.

[55] Triantafyllou, M.S. (1990). Cable Mechanics with Marine Applications, Lecture Notes, Massachusetts Institute of Technology (MIT), USA.

[56] Vu, M.T., Choi, H.S., Kang, J.I., Ji, D.H., and Jeong, S. K. (2017). A study on hovering motion of the underwater vehicle with umbilical cable. Ocean Engineering 135, pp. 137-157.

[57] Shampine, L.F., Kierzenka, J., Reichelt, M.W. (2000). Solving Boundary Value Problems for Ordinary Differential Equations in MATLAB with Bvp4c, Technical Report, MathWorks Inc.

[58] SNAME (1952). Nomenclature for treating the motion of a submerged body through a fluid. Technical report, The Society of Naval Architects and Marine Engineers.

[59] Fjellstad, O.E., and Fossen, T.I. (1994). Position and attitude tracking of auv's: a quaternion feedback approach. Oceanic Engineering, IEEE Journal of, 19(4):512 –518.

[60] Fossen, T. I. (2011). Handbook of Marine Craft Hydrodynamics and Motion Control. John Wiley & Sons, Ltd, Chichester, UK.

[61] Imlay, F. (1961). The complete expressions for added mass of a rigid body moving in an ideal fluid. Technical report, David Taylor Model Basin, Washington D.C.

[62] Sagatun, S.I., and Fossen, T.I. (1991). Lagrangian formulation of underwater vehicles' dynamics. In Conference Proceedings 1991 IEEE International Conference on Systems, Man, and Cybernetics, pages 1029–1034.

[63] Fossen, T. I. (2002). Marine Control Systems: Guidance, Navigation and Control of Ships, Rigs and Underwater Vehicles. Trondheim, Norway: Marine Cybernetics.

[64] Fossen, T. I. and Ross, A. (2006). Nonlinear modelling, identification and control of UUVs. In Roberts, G. N. and Sutton, R., editors, Advances in Unmanned Marine Vehicles, chapter 2, pages 13 – 42. IET, The Institution of

Engineering and Technology, Michael Faraday House, Six Hills Way, Stevenage SG1 2AY, UK.

[65] Korotkin, A. (2009). Added Masses of Ship Structures, volume 88 of Fluid Mechanics and Its Applications. Springer Netherlands, Dordrecht.

[66] Tang, S. (1999). Modeling and simulation of the autonomous underwater vehicle, Autolycus. PhD thesis, Massachusetts Institute of Technology.

[67] Renilson, M. (2015). Submarine Hydrodynamics. Springer Briefs in Applied Sciences and Technology. Springer International Publishing, Cham.

[68] Skjetne, R., Smogeli, Ø. N., and Fossen, T. I. (2004). A Nonlinear Ship Manoeuvering Model: Identification and adaptive control with experiments for a model ship. Modeling, Identification and Control: A Norwegian Research Bulletin, 25(1):3–27.

[69] Yang, R., Clement, B., Mansour, A., Li, M., and Wu, N. (2015). Modeling of a Complex-Shaped Underwater Vehicle for Robust Control Scheme. Journal of Intelligent & Robotic Systems, pages 1–16.

[70] Hong, Y., Teo, K. M., Chitre, M., and Ng, K. M. (2016). Online System Identification of an Autonomous Underwater Vehicle Via In-Field Experiments. IEEE Journal of Oceanic Eng Engineering Engineering, 41(1):5–17.

[71] Butcher, J. C. (2008). Numerical Methods for Ordinary Differential Equations. John Wiley & Sons, Ltd.

[72] Spong, M.W., Hutchinson, S., and Vidyasagar, M. (2006). Robot Modeling and Control. Wiley, New Jersey, USA.

[73] Corneliussen, J. (2003). Implementation of a guidance system for cybership II, Master's thesis, NTNU, Trondheim.

[74] Naeem, W., Sutton, R., Ahmad, S.M., and Burns, R.S. (2003). A Review of Guidance Laws Applicable to Unmanned Underwater Vehicles. The Journal of Navigation, Vol. 56, pp. 15-29.

[75] Antonelli, G., Fossen, T.I., Yoerger, D. (2008). Underwater Robotics. In Handbook on Robotics, Springer-Verlag, pp. 987-1008.

[76] Haghi, P. (2009). Nonlinear Control Methodologies for Tracking Configuration Variables. In Underwater Vehicles (edited by Alexander V. Inzartsev), pp. 152-172.

[77] Do, K.D., Pan, J. (2009). Control of ships and underwater vehicles. Springer.

[78] Brockeet, R.W. (1983). Asymptotic stability and feedback stabilization. In Differential Geometric Control Theory. Pp. 181-191. Boston: Birkhauser.

[79] Skjetne, R., Fossen, T.I., and Kokotovi´c, P. (2002). Output maneuvering for a class of nonlinear systems, in 'Proc. 15th IFAC World Congress on Automatic Control', IFAC, Barcelona, Spain.

[80] Skjetne, R. (2005). The Maneuvering Problem. PhD thesis, Norwegian University of Science and Technology, Department of Marine Technology.

[81] Breivik, M., and Fossen, T. I. (2008). Guidance Laws for Autonomous Underwater Vehicles. In A. V. Inzartsev (Ed.) Underwater Vehicles, chap. 4. I-Tech.

[82] Fossen, T.I. (2010). Guidance and Control of Marine Craft. Norwegian University of Science and Technology.

[83] Breivik, M., and Fossen, T. (2008). Guidance laws for planar motion control. In Decision and Control, 2008. CDC 2008. 47th IEEE Conference on, pp. 570 –577.

[84] Kreyszig, E. (2011). Advanced Engineering Mathematics. John Wiley & Sons, Inc.

[85] Wikipedia - PID. PID controller -wikipedia, the free encyclopedia, 2012. URL http://en.wikipedia.org/w/index.php?title=PIDcontroller&oldid=490210451. [Online; accessed 4-July-2019].

[86] Johansen. I.H. (2011). UAV Autopilot Design for Recce D6.

[87] Lee, J., Roh, M., and Lee, D. Clonal Selection Algorithms for 6-DOF PID Control of Autonomous Underwater Vehicles. Department of Bio and Brian Engineering, KAIST; Key Information: PID control.

[88] Sellers, D. (2003). An Overview of Proportional plus Integral plus Derivative Control and Suggestions for Its Successful Application and Implementation. Portland Energy Conservation Inc.

[89] Kirkeby, M. (2010). Comparison of controllers for dynamic positioning and tracking of ROV Minerva. Master Thesis. Norwegian University of Science and Technology, Department of Marine Technology.

[90] Slotine, J.J.E., and Li, W. (1991). Applied Nonlinear Control. Prentice-Hall Int., Eaglewood Cliffs, New Jersey.

[91] Fossen, T., and Johansen, T. (2006). A survey of control allocation methods for ships and underwater vehicles. In Proc. of the 14th IEEE Mediterranean Conference on Control and Automation. Ancona, Italy.

[92] Peterson, J., and Bodson, M. (2006). Constrained quadratic programming techniques for control allocation. IEEE Transaction on Control System Technology. 14(1):91–98.

[93] Perez, T. (2009). Anti-windup designs for ship dynamic positioning with control allocation. In Proc. of the 8th IFAC International Conference on Manoeuvring and Control of Marine Craft. Guaruja, Brazil.

[94] Ruth, E., Smogeli, O., Perez, T., and Sorensen, A. (2009). Antispin thrust allocation for marine vessels. IEEE Transactions on Control Systems Technology, 2009. 17(6):1257 – 1269.

[95] Tøndel, P., Johansen, T.A., and Bemporad, A. (2003). An Algorithm for Multi-parametric Quadratic Programming and explicit MPC solutions. Automatica, vol. 39, pp. 489-497.

[96] Johansen, T. A., Fossen, T. I., and Tøndel, P. (2005). Efficient Optimal Constrained Control Allocation via Multi-Parametric Programming. AIAA Journal of Guidance, Control and Dynamics, vol. 28, pp. 506-515.

[97] Nilsson, N.J. (1969). A mobile automation: An application of artificial intelligence techniques. The 1st International Joint Conference on Artificial Intelligence, pp. 7-9.

[98] Sleumer, N. H., and Tschichold-Grman, N. (1999). Exact cell decomposition of arrangements used for path planning in robotics. Institute of Theoretical Computer Science Swiss Federal Institute of Technology Zurich, Switzerland, Technical report.

[99] Nash, A., Daniel, K., Koenig, S., and Felner, A. (2007). Theta: Any-angle path planning on grids. Journal of Artificial Intelligence Research, vol. 39, pp. 1177-1183.

[100] Tahir, Z., Ahmed, H.Q., Ayaz, Y., and Nawaz, R. (2018). Potentially guided bidirectionalized RRT for fast optimal path planning in cluttered environments. Robotics and Autonomous Systems, vol. 108, pp. 13-27.

[101] Cao, X. M., Zou, X.J., Jia, C.Y., Chen, M.Y., and Zeng, Z.Q. (2019). RRT-based path planning for an intelligent litchi-picking manipulator. Computers and Electronics in Agriculture, vol. 156, pp. 105-118.

[102] LaValle, S.M., and Kuffner, J. J. (2001). Rapidly-exploring random trees: Progress and prospects. Algorithmic and Computational Robotics: New Directions, pp. 293-308.

[103] Amato, N.M., and Wu, Y. (1996). A randomized roadmap method for path and manipulation planning. Proceeding IEEE International Conference on Robotics and Automation, pp. 113-120.

[104] Boor, V., Overmars, M., and Vander Stappen, A. F. (1999). The Gaussian sampling strategy for probabilistic roadmap planners. Proceeding IEEE International Conference on Robotics and Automation, pp. 1018-1023.

[105] LaValle, S. M., and Kuffner, J. J. (2001). Randomized kinodynamic planning. International Journal of Robotics Research, vol. 20, no.5, pp. 378–400.

[106] Wang, W., Deng, H., and Wu, X. (2018). Path planning of loaded pin-jointed bar mechanisms using rapidly-exploring random tree method. Computers and Structures, vol. 209, pp. 65-73.

[107] Choset, H., Lynch, K.M., Hutchinson, S., Kantor, G., Burgard, W., Kavraki, L.E., and Thrun, S. (2005). Principles of Robot Motion: Theory, Algorithms, and Implementations. The MIT Press.

[108] Kavraki, L.E., and LaValle, S.M. (2008). Motion planning. In Springer Handbook of Robotics, chapter 5, pages 109–131. Springer Berlin Heidelberg.

[109] Latombe, J.C. (1991). Robot Motion Planning. Kluwer Academic Publishers, Boston, MA.

[110] LaValle, S. M. (2006). Planning algorithms. Cambridge University press.

[111] Ferguson, D., Kalra, N., and Stentz, A. (2006). Replanning with RRTs. IEEE International Conference on Robotics and Automation, Orlando, Florida.

[112] Steven M. LaValle. (1998). Rapidly-exploring random trees: A new tool for path planning. TR 98-11, Computer Science Dept, Iowa State University.

[113] Yang, K., and Sukkarieh, S. (2008). Planning Continuous Curvature Paths for UAVs Amongst Obstacles. Australasian Conference on Robotics and Automation, Canberra.

[114] Frazzoli, E. (2003). Quasi-random algorithms for real-time spacecraft motion planning and coordination. Acta Astronautica, vol. 53, pp. 485-495.

[115] D. Obreja, D., Nabergoj, R., Crudu, L., and Popoiu, S.P. (2010). Indentification of hydrodynamic coefficients for manoeuvring simulation model of a fishing vessel. Ocean Engineering, 37 (2010), pp.678-687.